Numerical Analysis of the Ultrarelativistic and Magnetized Bondi–Hoyle Problem

by

Andrew Jason Penner

B.Sc., University of Manitoba, 2002
M.Sc., University of Manitoba, 2004

A THESIS SUBMITTED IN PARTIAL FULFILLMENT OF
THE REQUIREMENTS FOR THE DEGREE OF

DOCTOR OF PHILOSOPHY

in

The Faculty of Graduate Studies

(Physics)

THE UNIVERSITY OF BRITISH COLUMBIA

(Vancouver)

April 2011

ABSTRACT

In this thesis, we present numerical studies of models for the accretion of fluids and magnetofluids onto rotating black holes. Specifically, we study three main scenarios, two of which treat accretion of an unmagnetized perfect fluid characterized by an internal energy sufficiently large that the rest-mass energy of the fluid can be ignored. We call this the ultrarelativistic limit, and use it to investigate accretion flows which are either axisymmetric or restricted to a thin disk. For the third scenario, we adopt the equations of ideal magnetohydrodyamics and consider axisymmetric solutions. In all cases, the black hole is assumed to be moving with fixed velocity through a fluid which has constant pressure and density at large distances. Because all of the simulated flows are highly nonlinear and supersonic, we use modern computational techniques capable of accurately dealing with extreme solution features such as shocks.

In the axisymmetric ultrarelativistic case, we show that the accretion is described by steady-state solutions characterized by well-defined accretion rates which we compute, and are in reasonable agreement with previously reported results by Font and collaborators [1, 2, 3]. However, in contrast to this earlier work, where the computed solutions always had tail shocks, we find parameter settings for which the time-independent solutions contain bow shocks. For the ultrarelativistic thin-disk models, we find steady-state configurations with specific accretion rates and observe that the flows simultaneously develop both a tail shock and a bow shock. For the case of axisymmetric accretion using a magnetohydrodynamic perfect fluid, we align the magnetic field with the axis of symmetry. Preliminary results suggest that the resulting flows remain time-dependent at late times, although we cannot conclusively rule out the existence of steady-state solutions. Moreover, the flow morphology is different in the magnetic case: additional features that include an evacuated region near the symmetry axis and close to the black hole are apparent.

TABLE OF CONTENTS

LIST OF TABLES

LIST OF FIGURES

ACKNOWLEDGEMENTS

First I would like to thank my supervisor Matt Choptuik, without his guidance and determination, I would not be the student that I am today. His continuous efforts to mould us into computational physicists is what will pave the way for future research in physics.

I owe a debt of gratitude to Dr. W. Unruh, Dr. J. Heyl, and Dr. D. Jones for their involvement and support in different aspects of my research project, as well as the various group meetings that expanded my understanding of general relativity and astrophysics. Further to this I would like to thank the astronomers at the University of British Columbia for their input and educational guidance during my stay.

I really do wish I could thank everyone who helped me get where I am today, whether it be my grandparents, Andy and Lorna Moffat, and parents, Jim and Doreen Penner, who showed me that hard work will pay off in dividends. Or if it is the employers who hired me along the way showing me so many life skills that I will continue to use. Unfortunately, due to space considerations, I cannot name all those who helped individually.

I certainly thank my friends, who were there for me through thick and thin, to give advice on life, research, and sometimes just a place to go and vent. Wherever I go from here know that you will never be forgotten.

I owe a special thanks to my friends Anand Thirumalai and Silke Weinfurtner, who were there for me in some of my most troubling times, and some of my best. Although they did their best to help me through the academic side of life, what is most memorable are the times we just hung out and relaxed.

I am happy to thank members of the current and extended research group; Benjamin Gutierrez, Silvestre Aguilar-Martinez, Dominic Marchand, and Ramandeep Gill for all the advice and diversions along the way.

I would be remiss if I did not also acknowledge the efforts of past group members such as Dr. D. Neilsen, Dr. S. Noble, Dr. M. Snajdr, Dr. B. Mundim, and Roland Stevenson for their

advice throughout this research project and my graduate career.

I would also like to thank Gerhard Huisken and the Albert Einstein Institute (MPI-AEI, Germany) for their hospitality and support during the time that I spent there.

I also thank the people in the mathematics department in the University of Southampton, in specifically for their advice in the later stages of my data analysis.

Finally I thank the funding agencies NSERC and CIFAR for their financial support.

DEDICATION

I dedicate this thesis to my mother, she was there for the beginning of this degree, and did not make it to the end. Her love, support, and constant care will never be forgotten. She is very much missed.

CHAPTER 1

INTRODUCTION

One of the more intriguing aspects of physics is the existence of gravitationally compact objects that curve spacetime. These objects include neutron stars and black holes and are thought to be the driving mechanism behind many interesting astrophysical phenomena, including accretion disks. Gravitationally compact objects have a radius, R, close to their Schwarzschild radius, $R_{\rm s} = 2GM/c^2$, where G is Newton's gravitational constant, and c is the speed of light [4]. Many gravitationally compact objects—including many classes of neutron stars—are thought to be surrounded by accretion disks. Realistic modelling of neutron stars involves complicated microphysics, especially in the interactions between their atmospheres and the accreting matter. On the other hand, black holes, while the most extreme class of gravitationally compact objects, have well defined boundaries that can be modelled without an atmosphere. In both cases, however, the compact objects themselves curve spacetime and, as far as the gravitational interaction goes, are thus most appropriately studied using Einstein's theory of general relativity.

In this thesis, we numerically model scenarios involving the gravitationally mediated accretion of matter onto a black hole. Astrophysically, the matter is expected to be a highly ionized fluid, or plasma. In general, direct modelling of the plasma degrees of freedom is prohibitively expensive computationally: a hydrodynamic approximation is thus frequently made, and we will follow this approach here. The effects of magnetic fields are expected to be important in the accretion problems we consider, and we thus include some of these effects via the so called ideal magnetohydrodynamic approximation, wherein the plasma is assumed to have infinite conductivity. We further assume that the spacetime containing the black hole is fixed (non-dynamic), which is tantamount to asserting that the accreting fluid is not self-gravitating.[1]

Of the many types of black-hole-accretion problems that we could consider, we focus on the dynamics of accretion flow onto a moving black hole, where we again emphasize that we assume that the the mass of the accreting matter is insufficient to significantly change the mass of the black

[1] For more examples of general relativistic astrophysical applications of fluid dynamics we refer the reader to Camenzind [5], or Shapiro and Teukolsky [6]

hole. With this assumption, we can describe the gravitational field using a time-independent, or stationary, spacetime. Historically, the roots of the problems that we consider can be traced to the studies of Bondi and Hoyle [7] who investigated non-relativistic accretion flows onto point particles that were moving through the fluid. Extension of such studies to the general relativistic case has been made by several authors—most notably Petrich *et al.* [8] and Font *et al.* [1]. The nomenclature "Bondi-Hoyle accretion" is typically retained in these works, and we adopt that convention here. However, these previous calculations considered only purely hydrodynamical models and, as already stated, we thus extend the earlier research by including some of the effects of magnetic fields in our work. Another departure from previous research is our modelling of the fluid, in some cases, in the so-called ultrarelativistic limit.

As described in more detail in Chap. 2, we study accretion flows for spacetimes describing single spherically symmetric, or single axisymmetric black holes. The remainder of this chapter is devoted to an overview of the thesis. We begin with an outline of the thesis and highlight our main results. We then proceed to brief reviews of hydrodynamics and magnetohydrodynamics, particularly in the context of general relativistic calculations We study the accretion flow in spacetimes for spherically symmetric and axisymmetric black holes, described in more detail in Chap. 2. We proceed by presenting the outline of the thesis project with accompanying results. Then we present a brief history of hydrodynamics and magnetohydrodynamics before introducing our approach to the study of accretion flows.

1.1 Project Outline

The purpose of this thesis is to study the general relativistic Bondi–Hoyle accretion problem in two distinct fluid models. The first part of the study uses an ultrarelativistic fluid model, where the rest mass density of the fluid is neglected. The second part of the study generalizes the relativistic Bondi–Hoyle problem by using a background fluid which is a perfect conductor with a magnetic field embedded in it. The details for these models are found in Chap. 2.

To perform this study we focus on two different fluid descriptions for the uniform fluid background used in the general relativistic Bondi–Hoyle setup.

1. we investigate an ultrarelativistic fluid, and separately,

2. we investigate an ideal magnetohydrodynamic (MHD) fluid.

We use the ultrarelativistic description to model axisymmetric accretion onto an axisymmetric black hole and we also consider ultrarelativistic infinitely thin-disk accretion onto an axisymmetric black hole. The infinitely thin-disk model, the same as studied by Font *et al.* [3], is a highly restricted model; however, it serves the purpose of allowing us to gain an insight into the full three dimensional simulations. During our study of the ultrarelativistic systems we found results that conflict with the general findings of Font *et al.* [1, 2, 3] who found that only a tail shock forms for their hydrodynamic models . Using this new hydrodynamic model, where we neglect the rest mass density of the fluid and the corresponding conservation law, we find the presence of both a bow shock and a tail shock. This is in contrast to the results from the hydrodynamic studies performed by Font *et al.* , where they included the rest mass density. We further find that the boundary conditions for our ultrarelativistic system must be much larger than those proposed in the previous hydrodynamic studies.

When we use the ideal MHD model we study the axisymmetric accretion onto an axisymmetric black hole with an asymptotically uniform magnetic field aligned with the rotation axis. While this geometric setup is highly idealized it reveals a lot of new physical features not seen in the previous studies of a purely hydrodynamic fluid background. One such feature is a region downstream of the black hole that evacuates, forming a vacuum. The depletion region is a phenomenon that appears to be similar to the effects of our sun's solar wind interacting with the earth's magnetosphere. We also find that the presence of a magnetic field only marginally affects the accretion rates relative to a hydrodynamic system where there is no magnetic field present in the fluid.

To investigate our fluid models in the relativistic Bondi–Hoyle accretion problem we focus on three distinct combinations of equations and domain geometries;

1. Axisymmetric ultrarelativistic accretion

2. Non-axisymmetric infinitely-thin ultrarelativistic accretion

3. Axisymmetric magnetohydrodynamic accretion

We developed our own finite-volume high-resolution shock-capturing code. Since the field of numerical magnetohydrodynamics is still very new, there are a lot of advantages to developing our own code, including development a much better fundamental understanding of the methods and techniques used in the field. No existing code at the time of this writing used the ultrarelativistic equations of motion to be described in Chap. 2, nor did any code exist that used our implementa-

tion of the magnetohydrodynamic equations of motion. Further to this we suggest a new method to monitor the physical validity of the magnetic field treatment, in Chap. 4.

1.2 Numerical Relativistic Hydrodynamics: A Brief Review

A plasma is a highly ionized gas, that is, it is a gaseous mixture of electrons protons and neutrons. With current numerical methods and computational facilities there is no efficient way to study the dynamics of every particle in the plasma. Since we are interested in the bulk properties of plasma accretion we approximate the plasma flow using (magneto)hydrodynamic models. In this section we described the hydrodynamic approximation, that we assume the plasma may be treated as a fluid, and that we will be using the Valencia formulation, and integral techniques to solve the resulting system of equations. We also introduce the concept and assumptions needed for an ultrarelativistic fluid.

1.2.1 Ideal Hydrodynamic Approximation

We are interested in accretion of astrophysical plasmas onto black holes, and since we are specifically interested in the gravitational attraction of the fluid to the black hole, we will be concerned with the flow of the heaviest particles. To simplify the model, we will make the assumption that the particles are all baryons which all have identical mass, $m_{\rm B}$. We will further use the hydrodynamic approximation, which means that we assume that the fluid will be adequately described by studying the bulk properties of the particles within fluid elements, or small volumes of fluid. The size of the fluid element is much larger than the mean free path of each particle constituent, and consequently each fluid element is considered to be in local thermal equilibrium. Thermal equilibrium suggests that the velocity distribution in each fluid element is isotropic. An isotropic velocity distribution further implies that the pressure the particles exert on the sides of the fluid elements is also isotropic [9].

Moreover, since the typical velocity of the constituent fluid particles in each fluid element will be of order of the speed of light, at least in some regions of the domain, we must consider relativistic hydrodynamics.

1.2.2 Review

The numerical study of hydrodynamics has its roots in Euler's mathematical analysis of fluid dynamics in 1755 [10]. For a review of non-relativistic hydrodynamics, we refer the reader to Darrigol (2008) [11] and Goldstein (1969) [12]. For a review of the numerical methods used to solve non-relativistic hydrodynamic equations of motion, we refer the reader to Birkhoff (1983) [10].

While numerical hydrodynamics has been applied to many physical systems, the most relevant studies for our current project relates to the development of hydrodynamical models for relativistic astrophysical systems. An early attempt to study astrophysical phenomena using a hydrodynamic model was performed by May and White [13, 14] in their study of the spherically symmetric gravitational collapse of a star. Their study used Lagrangian coordinates wherein the coordinates move with the fluid. To discretize their system of equations, May and White used a finite difference scheme where one replaces the derivatives in an equation with approximate differences. To handle discontinuities that may develop in the fluid variables, they introduced an artificial viscosity by adding a term to the system of equations to mimic the effects of physical viscosity. The viscous term acts to smooth discontinuities so that the fluid variables may be treated as continuous.

Lagrangian coordinates make it difficult to consider problems in general geometries. In spherical symmetry, the matter may only move radially and the co-moving coordinates cannot "pass" each other; however, in more general spacetimes the matter has greater degrees of freedom, which can allow the mixing of coordinates [15]. In contrast to the Lagrangian coordinates, we can use Eulerian coordinates where the coordinates are fixed by some external conditions and the fluids flow through the coordinate system [16]. An early relativistic investigation using Eulerian coordinates to describe a fluid system was performed by Wilson [16, 17], where—in the case of one spatial dimension, x—each fluid unknown, $q = q(x, t)$, satisfies a partial differential equation which takes the form of a so-called advection equation,

$$\frac{\partial q}{\partial t} + v\frac{\partial q}{\partial x} = s \tag{1.1}$$

where $v = v(t, x)$ is the fluid 3-velocity. It is important to note that in this formulation the source term, $s = s(t, x, \partial q/\partial x)$ may contain gradients of the fluid pressure, and thus this is not a so-called conservation equation. Wilson uses a finite difference approximation to numerically evolve the resulting partial differential equations. The use of the finite difference method also required the introduction of an artificial viscosity that would allow the differential equations to be solved in the

presence of a discontinuity such as a shock [18].

The formulation that we use originated with the Valencia group [19], who realized that the fluid equations may be written as a set of coupled conservation equations. The Valencia formulation is similar to the one described by Wilson; however, the equations are now written as,

$$\frac{\partial \mathbf{q}}{\partial t} + \nabla \cdot \mathbf{f}(\mathbf{q}) = \mathbf{s} \tag{1.2}$$

where $\mathbf{q}$ is now a vector of conservative variables and the $\mathbf{f}$ are known as the fluxes associated with the conservative variables. In this description the components of the vector of source functions, $\mathbf{s}$, do *not* contain any spatial derivatives of the fluid variables such as the velocity or the pressure. By using this formulation, Martí *et al.* [19], were able to adopt Godunov-type schemes (also known as high resolution shock capturing, or HRSC, schemes) which will be described in detail in Chap. 3. Godunov-type schemes solve an integral formulation of the conservative equation (1.2), and are therefore also valid across discontinuities in the fluid variables. These methods do not require the use of artificial viscosity to stabilize the resulting evolution. From here on we refer to this approach as the conservative method.

A generalization of the Godunov-type schemes are called finite volume methods. Finite volume methods find "weak" solutions to hyperbolic systems of equations and are capable of solving hyperbolic partial differential equations with discontinuous data sets. We describe this method in more detail in Chap. 3.

Godunov's original scheme is only a first order accurate integral solution; however, using conservative schemes, researchers were able to develop methods that extended the numerical accuracy of the integral solution. This allows for better resolution of the extreme pressure gradients, and other discontinuities, that form in a supersonic fluid. When studying a one dimensional advective equation such as Eqn. (1.2), we refer to a characteristic curve as the path along which values of the field, $\mathbf{q}$, propagates unaltered with a characteristic speed, $\partial\mathbf{f}/\partial\mathbf{q}$. Mathematically, along a characteristic curve, $\tau(x,t)$, Eqn. (1.2) reduces from a partial differential equation (PDE) to an ordinary differential equation (ODE),

$$\frac{\partial \mathbf{q}}{\partial t} + \nabla \cdot \mathbf{f}(\mathbf{q}) = \mathbf{s} \Rightarrow \frac{d\mathbf{q}}{d\tau} = \mathbf{s}. \tag{1.3}$$

The mathematical details behind characteristics are found in Chap. 3.

By formulating the hydrodynamic equations in a conservative form, researchers were able to calculate the characteristics, or characteristic structure, for all the fluid variables. Moreover, since general relativity requires all physical equations of motion to be hyperbolic, due to speed of light constraints on propagation of physical effects, it certainly seems natural to consider the use of conservative methods when studying fluid systems in a general relativistic context.[2]

The influences of hydrodynamics on gravitational systems and vice versa has been the subject of a large amount of research for decades. Researchers have performed detailed surveys of idealized fluid systems in many different configurations, starting as early as the 1970's when Michel studied steady state accretion onto a static spherically symmetric black hole [22]. In the 1980's, Hawley and collaborators, studied accretion tori, donut shaped disks with high internal energies and well-defined boundaries [23], around rotating black holes using a relativistic hydrodynamical code based on Wilson's method [24, 25, 26]. This work is reviewed in Frank, King, and Raine [27]. In Hawley *et al.* 's setup, the stationary black hole is centred in an axisymmetric thick accretion disk and evolved in time. They parameterized their accretion torus by the angular momentum of the entire torus, l, and studied three regimes, one in which initially $l < l_{\rm ms}$, where $l_{\rm ms}$ is the angular momentum of a marginally stable bound orbit, another for $l_{\rm ms} < l < l_{\rm mb}$ where $l_{\rm mb}$ is the angular momentum of the marginally bound orbit, and finally $l_{\rm mb} < l$. The accretion tori were found to flow into the black hole, except for in the second case, where only some of the disk flows into the black hole while the rest remains in orbit. When $l_{\rm mb} < l$ the accretion torus was found to remain orbiting outside the black hole. De Villiers and Hawley extend this study [28] by considering the full three dimensional accretion tori and investigate the effect of the Papaloizou–Pringle instability, an instability found in constant specific angular momentum accretion tori when disturbed by non-axisymmetric perturbations [29].

Before we proceed, we will briefly introduce a concept related to relativistic hydrodynamics, that is ultrarelativistic hydrodynamics. This is one of two particular models that are the focus of this research.

[2] For a review of this method of study please see Living Reviews in Relativity, in particular numerical hydrodynamics and magnetohydrodynamics in general relativity [20]. Interested readers may also wish to read the review numerical hydrodynamics in special relativity [21].

1.2.3 Ultrarelativistic Hydrodynamics

When the characteristic fluid velocities of the particles that make up the fluid elements are *very* close to the speed of light, the thermal energy of the fluid is much greater than the rest mass density, and we say that the fluid is ultrarelativistic. Mathematically, this allows us to consider a limit where the rest mass density of the fluid is ignored. Ultrarelativistic systems are relevant in the early universe where the ambient temperature is thought to be on the order of $T \sim 10^{19} GeV$, and the internal energy of the particles is far too high for the rest mass density to affect the system [30]. The ultrarelativistic model of a fluid is particularly useful in the radiation dominated phase of the universe where we would naturally expect to find radiation fluids such as photon gases [31]. The black holes in this period would be primordial black holes [30]. The algebraic details for this fluid model will be discussed in Chap. 2. Ultrarelativistic fluids have been studied in detail for stellar collapse [32, 33, 34], and have been treated as a model for a background fluid in Bondi–Hoyle accretion for a single set of parameters modelling the fluid [35]. We will expand on the treatment as a background fluid in Sec. 1.6.3.

1.3 Numerical Relativistic Magnetohydrodynamics: A Review

We now introduce the material needed for the second part of the thesis, relativistic magnetohydrodynamics. Specifically the assumptions behind ideal magnetohydrodynamics, and the history

1.4 Ideal Magnetohydrodynamic Approximation

We extend the hydrodynamic approximation, that the accreting plasma may be treated as a single constituent fluid, by imposing the ideal MHD limit. We assume that the fluid is a perfect conductor which imposes this condition, via Ohm's law, that the electric field in the fluid's reference frame vanishes, and that the electromagnetic contributions to the fluid are entirely specified by the magnetic field. This is shown in mathematical detail in Chap. 2. The perfect conductivity condition leads to "flux-freezing", where the number of magnetic flux lines in each co-moving fluid element is constant in time.

1.5 Review

Having reviewed the development of the numerical techniques to solve hydrodynamic models for astrophysical phenomenon, we turn our attention to a review of the material where researchers extend the existing hydrodynamic numerical techniques to include magnetic field effects. In particular, we focus on the material where they take the ideal magnetohydrodynamic limit, so the fluid is treated as a perfect conductor therein no electric fields are present in the fluid's reference frame. This is discussed in greater detail in Chap. 2.

Both the Wilson formulation Eqn. (1.1), and the conservative method Eqn. (1.2), were extended to magnetic-fluids in the ideal magnetohydrodynamic limit in the early 2000's. De Villiers and Hawley (2003) extended the Wilson formulation to include magnetic fields in De Villiers *et al.* [36] where they studied accretion tori on Kerr black holes. Hawley *et al.* studied the hydrodynamic accretion tori in Hawley *et al.* (1984) [25] and added a weak poloidal magnetic field to trigger a magnetorotational instability (MRI) [23]. The flows resulted in unstable tori in which the MRI develops and is later physically suppressed due to the symmetry of the setup. Anninos *et al.* (2005) [37] extended De Villier's work by studying a variation of the Wilson technique when calculating stable magnetic field waves. The magnetohydrodynamic extension of the Wilson method has also been used to study different accretion phenomenon such as tilted accretion disks [38]. As with the original Wilson formulation, the extensions were finite-difference based codes and therefore also required the introduction of artificial viscosity to smooth discontinuities.

All general relativistic magnetohydrodynamic codes are based on developments made in special relativistic magnetohydrodynamics. Notable special relativistic developments include work by Van Putten (1993) [39] who used a spectral decomposition code to solve the equations of motion. He proved the existence of compound waves in relativistic MHD, analogous to the magnetosonic waves found in classical MHD by Brio and Wu [40].[3] Later Van Putten (1995) [42] calculated the fully general relativistic ideal magnetohydrodynamic equations of motion. Both studies by Van Putten's required the use of smoothing operators to stabilize shocks, and consequently were not able to accurately handle problems that contained high Lorentz factors. This is do to the "smearing" caused by the smoothing operators which substantially reduce the accuracy of solutions across strong shocks [43]. Balsara (2001) [44], was the first to calculate the closed form analytic solution of the

[3] We do not introduce spectral methods in this thesis but will refer the reader to textbooks on the subject such as "Spectral Methods for Time-Dependent Problems" [41] as an example.

special relativistic characteristic structure and used a total variation diminishing (TVD) Godunov-type scheme to solve the 1-dimensional magnetohydrodynamic equations of motion. Komissarov (1999) [43] was the first to develop a 2-dimensional second order Godunov-type special relativistic MHD solver. Then del Zanna *et al.* (2003) [45] become the first group to develop a 3-dimensional third order Godunov-type scheme for special relativistic MHD. Although the implementation details vary from code to code, such as the use of spectral methods, TVD methods, and higher order schemes, all are based on conservative formulations of the fluid equations of motion.

The Godunov-type schemes requires that we solve a Riemann problem either exactly or approximately. The Riemann problem consists of a conservation law in conjunction with piecewise constant initial data that contains a single discontinuity. The Riemann problem is the simplest model for discontinuous systems. Martí and Müller (1994) [46] were the first to develop an exact Riemann solver for 1-dimensional relativistic hydrodynamics, later extended to multiple dimensions by Pons *et al.* (2000) [47]. Rezzolla and Giacomazzo (2001) refined this method [48] and later extended it to special relativistic magnetohydrodynamics (2006) [49]. The exact solution is useful in code testing and verification of the different flux approximations that are used for the approximate Riemann solvers. No exact solution exists for a Riemann problem in general relativistic magnetohydrodynamics. The Godunov-type methods described in the previous paragraph use an approximate Riemann solvers where the iterative processes used to solve the exact Riemann problem are replaced with approximations that are faster to solve. The approximate methods are discussed in Chap. 3.

With the special relativistic conservative equations of motion for ideal magnetohydrodynamics developed, work began by Anile [50] on the construction of Godunov-type conservative methods that could include the relativistic equations of motion on a curved spacetime background. Gammie *et al.* (2003) [51] were the first to use this method to develop a general relativistic code called HARM (High-Accuracy Relativistic Magnetohydrodynamics). Komissarov (2005) [52] used conservative methods to describe the magnetosphere of a black hole. Anton (2006) followed up on Martí's 1991 [19] paper by investigating and subsequently calculating the "characteristic-structure" of magnetohydrodynamics in a special relativistic fixed background [53]. The accretion torus problem was studied in the context of a magnetohydrodynamic fluid accretion using conservative methods by Gammie [51], and Montero with Rezzolla [54], which also resulted in a simulation of the MRI. For a review of the magnetized torus problem we refer the reader to papers such as de Villiers *et*

al. (2003) [36].

Now that we have reviewed the development of the techniques used to study general relativistic magnetohydrodynamic (GRMHD) systems with a fixed spacetime background[4], we turn our attention to the applications of GRMHD to astrophysical problems, particularly the accretion process.

When material accretes onto a massive central object the material will begin to reduce its orbital radius. If the material has angular velocity relative to the central object, to conserve angular momentum, the angular velocity will increase as the radius is reduced. In the most extreme cases, such as accretion onto compact objects, the velocity of the accreting material will approach the speed of light. At these limits if the material were to reduce its orbital radius any further, the corresponding increase in angular velocity would exceed the speed of light. Consequently such material would cease to accrete onto the central object, thus researchers were lead to ask questions about how the angular velocity or angular momentum would be transported away from the material closest to the central object. In typical fluids found on earth, one may expect that frictional forces such as viscosity would allow for this mechanism to take place. In large scale astrophysical accretion processes; however, viscosity is too small to be the dominant mechanism for angular momentum transport [23]. Researchers such as Stone, Balbus and Hawley [59, 60] investigated angular momentum transport and found that for steady hydrodynamic flow, there cannot be any angular momentum transport out of the disk, and further that if an instability is present, the angular momentum transport must be inward [23]. Balbus and Hawley (1998) reviewed accretion as well as the effects of magnetic fields in accretion phenomena [23]. In the review they show that a hydrodynamic description of an accretion disk is not capable of allowing angular momentum transport, all explanations using hydrodynamic models such as differential rotation are stable to linear perturbations. Balbus and Hawley encouraged further exploration of the role of magnetic fields in accretion since introducing a magnetic field to the accretion system introduces instabilities that do not exist in a purely hydrodynamic system.

When the accreting fluid contains an embedded magnetic field, Balbus and Hawley show that the accretion disk experiences the so-called magnetorotational instability [61]. Hawley *et al.* [62] explain that the viscous dissipation from magnetic field can come from two possible torques, either external, where a rotating magnetized wind coming off of the disk carrying away angular momen-

[4]There are several other applications and techniques for both hydrodynamic and magnetohydrodynamic matter models including the simulation of core-collapse supernovae and neutron star mergers. As these depend on treating a dynamic spacetime background, and do not relate directly to the thesis topic, I do not discuss them here. Reviews of these topics may be found in papers such as [55], [56], [57] or [58].

tum, or internal, where the magnetic fields carry the angular momentum radially out of the disk by a linear instability in the disk due to an angular momentum transfer process in the presence of a weak magnetic field. The presence of a rotational velocity in the magnetohydrodynamic system allows for an incompressible magnetorotational wave which is unstable for some wavenumbers.

The magnetorotational instability is caused by the magnetic tension transferring angular momentum from fluid elements in low orbits with large angular velocity to fluid elements in higher orbits and smaller angular velocity. To conserve angular momentum, an object accelerated in the direction of its orbit that gains angular momentum moves to a higher orbit, thereby decreasing its angular velocity. The magnetic fields enforce co-rotation between these fluid elements and ultimately decelerate the fluid element in the lower orbit and accelerate the fluid element in the higher orbit. This process transfers angular moment away from the accreting body. This effect is only possible for weak magnetic fields, otherwise the magnetic field force dominates any centrifugal force of the fluid and holds the fluid together [62].

As general relativistic magnetohydrodynamics is a rapidly developing field, there are many outstanding questions, including how magnetic fields affect the accretion rates found in systems that were previously studied using the purely hydrodynamic approximation.

One of the models used to explain a particular type of accretion phenomenon is referred to as Bondi–Hoyle accretion. Bondi–Hoyle accretion is thought to be a good model for accretion inside common envelopes, astrophysical bodies in a stellar wind and bodies inside active galactic nuclei [63]. We briefly describe these below and we refer the reader to texts such as "Introduction to High-Energy Astrophysics" [64] for more details.

In a close binary system mass can transfer from one object to another. When the object transfers mass, it also transfers momentum, and therefore causes a change in the orbital separation [64]. If mass is transfered from an object of lower mass to an object of higher mass, the lower mass object moves in such a way as to increases the orbital separation between the binary bodies so that it conserves the linear momentum of the entire system and angular momentum of the orbiting body. On the contrary, if a larger mass object transfers mass to a smaller mass object, the orbital separation will decrease. If the latter occurs, an unstable mass transfer may ensue [64]. One such outcome will be a common envelope.

When mass is transfered from the more massive donor star to the less massive accreting star or black hole such that the mass transfer is faster than the accretor may accrete it, a hot cloud,

or envelope, of stellar matter forms around the accretor. If the envelope grows large enough it will become larger than the size of the Roche lobe, the region around a star in which orbiting material is gravitationally bound to the star, it will envelope both stars becoming what is known as a common envelope (CE). The CE will then exert a drag force on the orbiting bodies, which will reduce the orbital radius of the binary system. The energy extracted from the binary stars is deposited in the common envelope as thermal energy [64].

Stellar wind is the emission of particles from the upper atmosphere of a star [65]. The amount of matter that makes up the stellar wind will depend on the star producing the wind. Dying stars produce the most stellar wind, but this wind is relatively slow at ~ 400 km/s [66], while younger stars eject less matter but at higher velocities, ~ 1500 km/s [67]. Bondi–Hoyle type accretion occurs when a massive object passes through this material [63].

An active galaxy is a galaxy in which a significant fraction of the electromagnetic energy output is not contributed to by stars or interstellar gas. At the centre of the active galaxy lies the nucleus, commonly known as an active galactic nucleus (AGN), which is on the order of 10 light years in diameter [64]. The radiation from the core of an active galaxy is thought to be due to accretion by a super massive black hole at the core, and generates the most luminous sources of electromagnetic radiation in the universe.

One of the modern applications of Bondi–Hoyle accretion may be seen in Farris *et al.* [68] where they simulate the merger of two binary black holes in a (non-magnetic) fluid background. They simulate both a Bondi-like evolution where the background gas is stationary relative to the binary merger, as well as a Bondi–Hoyle evolution where there is a net velocity of the fluid background relative to the binary merger.

All Bondi–Hoyle accretion models have focused on a purely hydrodynamic model, despite the fact that the phenomenon described above may be treated in a more general sense by allowing for the presence of an electromagnetic field [69].

In this thesis, we address two distinct physical scenarios. First, we study the accretion of a truly ultrarelativistic hydrodynamic fluid onto a black hole in a Bondi–Hoyle model in two distinct geometric configurations: axisymmetric and non-axisymmetric infinitely thin-disk, which are described in more detail in Chap. 2. Second, we investigate Bondi–Hoyle type accretion onto a black hole using an axisymmetric magnetohydrodynamic model. In all of our studies, we are interested in looking for phenomenological effects such as instabilities that may develop, or if the

flow reaches a steady state. To determine if the flow is stable, we will measure the accretion rates of energy, mass, and angular momentum. In the event of a stable accretion flow, the accretion rates will be constant in time.

Now we describe the physical conditions for the systems of interest; namely, the accretion of a relativistic magnetofluid onto a moving black hole, and the accretion of an ultrarelativistic fluid without a magnetic field onto a moving black hole. We follow this with a detailed description the previous studies performed using the Bondi–Hoyle accretion model.

1.6 Bondi–Hoyle Accretion

The Bondi–Hoyle accretion problem, whether it is considered in the gravitationally non-relativistic regime or in the relativistic regime, has the same basic setup. A star, of mass M, moves through a uniform fluid background at a fixed velocity, v_∞, as viewed by an asymptotic observer. We assume that the mass accretion rate is insufficient to significantly alter the spacetime background around the accretor [63]. Likewise, any momentum accretion rates are assumed too small to alter the velocity of the central body. We now give a brief history of the study of the Bondi–Hoyle system in the non-relativistic and relativistic regimes.

For the sake of this review of previous work, when we refer to a non-relativistic fluid, the characteristic velocities of the (magneto)hydrodynamic system is sub-relativistic and the gravity is treated in a Newtonian framework. When a fluid is relativistic, it has characteristic velocities that approach the speed of light, is modelled using either special or general relativity, and the gravity is treated using a general relativistic framework. Our research does not focus on the non-relativistic Bondi–Hoyle accretion problem; however, it is important to understand the features of a non-relativistic system since many of these features appear in the relativistic regime.

1.6.1 Non-relativistic Regime

To understand the non-relativistic Bondi–Hoyle accretion problem, we follow the ballistic trajectory of a streamline as the fluid passes the point mass. The trajectory of the fluid will be affected by the gravitational field of the star. If the kinetic energy of the flow is smaller than the gravitational energy of the mass the trajectory of the flow will be altered and the fluid will ultimately be accreted by the mass. As the fluid caught by the gravitational field passes the star, it becomes caught in the

gravitational field of the star. This results in the fluid flow changing its trajectory and converging behind the star. If the fluid is too close to the star the fluid will be gravitationally bound to the star, reverse direction and accrete onto the star [63]. By studying a ballistic trajectory, we neglect the effects due to pressure within the fluid.

The study performed by Hoyle and Lyttleton (1939) [70] determined the rate of accretion of a massive star as it travelled through a uniform pressureless fluid background. Their proposed closed form analytic model of the mass accretion rate, $\dot{M}_{\rm HL}$, was;

$$\dot{M}_{\rm HL} = \frac{4\pi G^2 M^2 \rho_\infty}{v_\infty^3}. \tag{1.4}$$

This is known as the Hoyle–Lyttleton accretion rate, $\dot{M}_{\rm HL}$. Here, G is Newton's gravitational constant, while M and v_∞ are the mass and the velocity of the massive point-like object as viewed by an asymptotic observer. Likewise, ρ_∞ is the density of the fluid as viewed by an observer at infinity. For the derivation we refer the reader to [70, 71, 72, 73, 63].

When Bondi [74] studied the mass accretion rate onto a spherically symmetric point mass he calculated a mass accretion rate for an object with zero velocity relative to the fluid background with a non-zero pressure,

$$\dot{M}_{\rm B} = 2\pi \frac{G^2 M^2 \rho_\infty}{\left(c_s^\infty\right)^3}, \tag{1.5}$$

where c_s^∞ is the speed of sound in the fluid as viewed by an observer at infinity. Bondi then posited an interpolation formula to connect the mass accretion rate of a point-like body with a fixed velocity to the spherically symmetric accretion problem, formulating an accretion rate $\dot{M}_{\rm B}$ [63, 74],

$$\dot{M}_{\rm B} = 2\pi \frac{G^2 M^2 \rho_\infty}{\left(c_s^{\infty\,2} + v_\infty^2\right)^{3/2}}. \tag{1.6}$$

It is noted that there is a discrepancy in the numerical factors between Eqns. (1.4) and (1.5). Shima *et al.* [75] performed a series of numerical studies of the Bondi and Hoyle–Lyttleton accretion and found that the correct scaling factor for Eqn. (1.6) is twice as large as Bondi's original calculation. The final non-relativistic mass accretion rate was determined to be,

$$\dot{M}_{\rm B} = 4\pi \frac{G^2 M^2 \rho_\infty}{\left(c_s^{\infty\,2} + v_\infty^2\right)^{3/2}}. \tag{1.7}$$

Extensive numerical work was carried out, using the non-relativistic treatment of both the fluid

and the gravitational field, by Ruffert in the mid-nineties [76, 77, 78, 79, 80, 63] and, more recently, in 2005 [81], where he found that the three dimensional evolution was stable. In the non-relativistic 2D simulations, the massive body travels through space with sub-relativistic speeds. As this body travels, it creates an accretion column in its wake. When the flow results in a bow shock, where the accretion column travels upstream to the front of the body and loses physical contact with the body, the point of contact of the accretion column with the point mass would eventually begin to oscillate and eventually wrap the accretion column around the central object. This oscillation was called the flip-flop instability. Later it was discovered that this instability was actually very sensitive to boundary conditions in each simulation. Some, such as Foglizzo *et al.* (2005) [82], argue that the flip-flop instability is an artifact of an incorrect numerical treatment of the boundary conditions, while others Blondin (2009) [83] have recently argued that this instability is real. As stated in Font *et al.* (1998) [2], the 3D simulations by Ruffert (1999) [84] show strong evidence of long term stability of the accretion flows, unlike the simulations performed in two spatial dimensions studied in Sawada (1989) [85], Matsuda (1991) [86], Livio (1991) [87], unless the flow has density gradients at infinity [88]. Since our work is in the relativistic regime, we do not address the issue of the presence of a flip-flip instability in non-relativistic Bondi–Hoyle accretion.

In the non-relativistic system, a bow shock develops depending on the values of the parameters used to specify the flow:

1. the adiabatic constant, Γ for polytropic equations of state,
2. the asymptotic speed of sound in the fluid, $c_{\rm s}^{\infty}$
3. the Mach number, $\mathcal{M} = v/c_{\rm s}$, where v is the speed of the accretor
4. and the radius of the accretor, $r_{\rm a}$.

Ruffert discovered that a bow shock develops in these systems due to a pressure increase in the downstream flow. As the body moves through the background fluid, it will begin to attract material and start compressing the material closest to the upstream side of the accretor. Due to the compression of the upstream matter the internal pressure and density increases, high enough that a shock forms. Studies have shown that the position of the shock is controlled by the value of Γ, and not by the Mach number, $\mathcal{M}$.

We note that non-relativistic Bondi–Hoyle accretion is still under investigation in various configurations, including configurations where the composition of the background fluid is no longer

uniform [89, 90].

1.6.2 Relativistic Regime

Michel (1972) [22], studied a relativistic extension to the Bondi accretion problem, where a uniform fluid surrounds a stationary spherically symmetric stationary black hole and assumes that the background fluid is not sufficiently massive enough to modify the mass of the black hole. He discovered that the relativistic Bondi problem has a closed form solution, depending on two free parameters which are set by specifying the density and pressure at a transonic point, the point where the fluid velocity equals the speed of sound. This solution is explained in more detail in Chap. 4.

The relativistic Bondi–Hoyle accretion problem consists of a black hole travelling at a constant asymptotic velocity through a uniform fluid background. In analogy to the non-relativistic Bondi–Hoyle problem, we assume that the mass of the accreted matter is small relative to the mass of the black hole. This allows us to examine the system using a fixed spacetime background. To date no closed form solution to this problem has been found.

The numerical study of the relativistic Bondi–Hoyle accretion problem was originally performed by Petrich *et al.* (1989) [8]. They numerically studied axisymmetric accretion onto a spherically symmetric black hole using the Wilson method. The fluid was completely specified by the velocity, v_∞, of the travelling black hole viewed by an asymptotic observer, by the adiabatic constant, Γ, used in the equation of state, and by the asymptotic speed of sound, c_s^∞ for the fluid. Petrich *et al.* [8] showed that the evolution of such a system settles down to a steady state flow onto the black hole. In the same study, Petrich *et al.* proceed to calculate the accretion rates for both the mass and angular momentum relative to the relativistic Bondi mass accretion rate (1.6). They discovered a strong agreement between the Bondi–Hoyle theory and their non-relativistic evolution calculations. Their paper also surveys a wide range of parameters, from Newtonian limits up to what they call the ultrarelativistic limit, where the speed of sound and the speed of the black hole are close to the speed of light. The use of a time dependent code allowed them to determine that the resulting steady state flow was both unique and stable [8].

In later works, Font, Ibañéz, and Papadopoulos [1, 2, 3, 91] used conservative methods to solve the hydrodynamic equations of motion, and re-investigated the relativistic Bondi–Hoyle setup. In Font *et al.* (1998) [1], all simulations performed on a wide range of values for both $\mathcal{M}$, $c_{\rm s}^\infty$ and

Γ resulted in a steady evolution, and all but one of their simulations produce a tail shock. In Font *et al.* (1998) [2], they changed their geometric configuration to calculate the solution of non-axisymmetric hydrodynamic accretion onto the equatorial plane of a spherically symmetric black hole using a thin disk approximation. The results of [2] were again steady state solutions each with a tail shock. In Font *et al.* [3], Font *et al.* (1999) study non-axisymmetric accretion onto a rotating black hole using a thin disk approximation where they discovered that these flows also reached a steady state with an attached tail shock, but also that the effects of the rotating black hole were only noticeable within a few Schwarzschild radii, R_s from the black hole, beyond that the flow was essentially unaltered by the rotation.

1.6.3 Ultrarelativistic Fluid Modelling

Past research using ultrarelativistic fluid models mainly focused on gravitational collapse problems, there has been little research into the accretion of an ultrarelativistic fluid onto a compact object itself. Petrich *et al.* [35] studied the special case of ultrarelativistic accretion onto a spherically symmetric compact object for a $\Gamma = 2$ fluid. They found that the problem could be solved in closed form, and that the flow was steady. Polytropic fluids with $\Gamma = 2$ have a speed of sound equal to the speed of light, therefore they are all subsonic. One of our goals is to see what happens as the adiabatic constant decreases and the fluid is allowed to become supersonic? Only numerical treatments appear to be able to solve the complicated system of partial differential equations that arise from using fluid models.

1.7 Thesis Layout

In Chap. 2, we describe the necessary general relativistic formalism to describe spacetimes. We describe the coordinates used for this study and the stress-energy tensors used to calculate the equations of motion of the fluid for this work. We derive the equations of motion for both the magnetohydrodynamic models as well as the ultrarelativistic hydrodynamic models. We also describe the specific geometries of the spacetimes which we considered.

In Chap. 3, we describe our Godunov-type solver and specifically the finite volume method, used to numerically solve a system of hyperbolic partial differential equations. We describe the different flux approximations we implemented, along with the different cell interface techniques used. We

further describe techniques for both handling discontinuities that arise in the fluid evolution, known as shock capturing, as well as maintaining the magnetic field constraint to truncation error.

In Chap. 4, we describe a set of tests that are used to determine the validity of the flux approximations and reconstruction techniques used to measure the shock capturing capabilities of the methods described in chapter 3. This includes one and two dimensional tests. We also describe methods used for code verification, in particular the convergence test, and the independent residual, useful for simulations with no known solution for comparison since they allow us to know whether or not our numerical solution approaches the continuum solution. For the general relativistic magnetohydrodynamic study, we suggest a new method to study the convergence of the magnetic field constraint.

In Chap. 5, we present the results of our current work and we describe the simulations using both axisymmetry and thin-disk approximations for both the ultrarelativistic and magnetohydrodynamic systems. We further go on to describe the results of simulations of axisymmetric fluid flow onto a rotating black hole which include the following simulations,

1. Axisymmetric ultrarelativistic accretion onto an $a = 0$ black hole
2. Axisymmetric ultrarelativistic accretion onto an $a \neq 0$ black hole
3. Thin-disk ultrarelativistic accretion onto an $a = 0$ black hole
4. Thin-disk ultrarelativistic accretion onto an $a \neq 0$ black hole
5. Axisymmetric magnetohydrodynamic accretion onto an $a = 0$ black hole
6. Axisymmetric magnetohydrodynamic accretion onto an $a \neq 0$ black hole.

We found that the ultrarelativistic accretion problem in both the axisymmetry and non-axisymmetric infinitely thin-disk models were sensitive to the location of the outer boundary, this is in contrast to previous studies. We did find in our axisymmetric studies that, once the boundary was extended far enough to prevent boundary effects from disrupting the system, some parameters revealed the presence of a bow shock. In previous relativistic hydrodynamic studies only tail shocks would form for any parameters investigated. The ultrarelativistic non-axisymmetric infinitely thin-disk models revealed the presence of both a tail shock and a bow shock, again a feature not discovered in previous relativistic studies.

We also discovered that the presence of a magnetic field in a perfect conducting fluid background did not disrupt the development of a steady accretion flow. Furthermore new morphological features developed in the flow, which included a region immediately downstream of the black hole where the baryon rest mass density and thermal pressure are depleted. This new feature is not possible in a purely hydrodynamic stystem, so previous studies would have not captured them.
Finally, in Chap. 6 we conclude this work and discuss related future projects.

1.8 Notation, Conventions and Units

We use the following conventions throughout the thesis:

- We used MTW [4] conventions: specifically, Newton's gravitational constant, G, and the speed of light, c are set to unity. $G = c = 1$. The metric signature is $(-+++)$. Greek indices *i.e.* $\mu, \nu = \{0, 1, 2, 3\}$ run over the full spacetime coordinates and Latin indices *i.e.* $i, j, k = \{1, 2, 3\}$ run over the spatial components. The Einstein summation convention applies to both types of indices *i.e.* $v^\mu v_\mu = \sum_{\mu=0}^{3} v^\mu v_\mu$ and $w^i w_i = \sum_{i=1}^{3} w^i w_i$.

- Since we always use a coordinate basis for calculations, we will use a standard tensor notation such that $T^{\mu\nu}$ will represent the components of the tensor. For ease of representation we will use the Penrose abstract index notation [92] and refer to v^μ as a vector rather than the components of a vector.

- We reserve the variable p to be the index which enumerates the equations in a system of conservation laws. *i.e.* $p = 1, 2..8, 9$ for the full general relativistic magnetohydrodynamic system of equations.

- We denote partial differentiation by $\partial_i f = \partial f / \partial x^i$ as well as $f_{,i} = \partial f / \partial x^i$ of a function $f = f(x^i)$.

- In the case of describing a discretized quantity we adhere to the notation that a superscript will denote a discretized time and a subscript denotes a discretized spatial location. Thus $q^n_{ijk} \sim q(t^n, x_i, y_j, z_k)$

- A dot over a variable will denote a derivative with respect to time. For example the mass accretion rate is denoted $\partial m(t)/\partial t = \dot{m}$.

- We will use the acronym UHD to refer to ultrarelativistic hydrodynamics, and
- We will use the acronym MHD to refer to magnetohydrodynamics, and
- The acronym GRMHD has been used in the literature to refer to both the fully dynamic general relativistic magnetohydrodynamics as well as relativistic systems in which the spacetime is fixed. In this dissertation we use GRMHD to refer to the latter.

CHAPTER 2

FORMALISM AND EQUATIONS OF MOTION

2.1 Overview

Most of the visible universe is a plasma, a highly ionized gas (fluid). The solution of the plasma equations of motion, as seen for example in Kulsrud [93], requires us to keep track of too many degrees of freedom for the problem to be tractable. To make the problem tractable, we usually make several assumptions about the properties of the plasma. The first assumption is that the fluid is only comprised of equal mass particles, as described in Chap. 1. Next, we are interested in studying the bulk properties of the fluid, the 3-velocity, v^i, the density, ρ_0, the pressure, P, and the magnetic field $\mathcal{B}^i$ defined in Eq. (2.78). To study the bulk properties we use the hydrodynamic approximation, allowing the bulk fluid properties to be measured by considering finite volumes or elements of the fluid. All particles within the finite element are assumed to be in local thermodynamic equilibrium with isotropic velocities. The isotropic velocity assumption leads to an isotropic pressure within each fluid element. We make this system more realistic by considering the dynamics of the fluid in the presence of a magnetic field, through the study of MHD. In this thesis we are interested in an idealized version of the MHD system, wherein the fluid body has perfect conductivity, and so the local electric field is zero.

The bulk property variables are known as primitive variables and may be recorded as $\mathbf{p} = (\rho_0, v^i, P, \mathcal{B}^i)$. However, when we cast this system of equations in conservative form we consider the relativistic rest mass density D, the energy, E, the 3-momentum S_i. We refer to these variables as the set of conservative variables and for convenience we record them in a compact form as $\mathbf{q} = (D, S_i, E, \mathcal{B}^i)$. Due to the highly nonlinear nature of the relationship between the primitive and conservative variables we are not able to easily write an expression for the primitive variables, $\mathbf{p}$, and a function of the conservative variables, $\mathbf{q}$. The inversion is performed numerically, and is discussed in section 3.3.

We will also study what is known as the ultrarelativistic limit of a hydrodynamic fluid, where

the fluid elements described above have an internal energy that is sufficiently high that the rest mass density of the baryonic particles is negligible. So, the internal energy of the fluid which is generally written,

$$\rho = \rho_0 + \rho_0\epsilon, \tag{2.1}$$

is dominated by the internal energy density, thus the internal energy of the fluid becomes

$$\rho = \rho_0\epsilon. \tag{2.2}$$

We apply the study of both ideal MHD and ultrarelativistic hydrodynamics to accretion onto black holes.

Relativistic fluids are known to develop shocks. In order to capture these shocks we use high-resolution shock-capturing methods to evolve the equations of motion. This technique requires the equations of motion to be written in a conservative form,

$$\partial_t \mathbf{q} + \partial_i \mathbf{f}^i(\mathbf{q}) = \mathbf{s}(\mathbf{q}), \tag{2.3}$$

where

$$\mathbf{q} = (q_1(x^\mu), q_2(x^\mu), ..., q_(x^\mu)) \tag{2.4}$$

is a vector of conserved variables,

$$\mathbf{f}^i = (f_1^i(\mathbf{q}, x^\mu), f_2^i(\mathbf{q}, x^\mu), ..., f_p^i(\mathbf{q}, x^\mu)) \tag{2.5}$$

is the corresponding flux vector, and,

$$\mathbf{s}(\mathbf{q}) = \mathbf{s}(\mathbf{q}(x^\mu)) \tag{2.6}$$

is a vector of source terms. This will be described in more detail in Chap. 3. We will be deriving the equations of motion to take on the conservative form.

We describe the spacetime defined by the presence of a black hole using Einstein's general relativity.

Einstein's theory of general relativity is a geometric theory of gravitation. This theory is most

naturally and elegantly described in a covariant form in terms of geometric objects, or tensors. However, to study a particular problem, such as some astrophysical phenomenon, we use a coordinate dependent form; consequently, we will discuss general relativity in terms of some coordinates x^μ, where μ is an index running over time and the space coordinates, as described in Chap. 1. Numerical relativity is concerned with the solution to the Cauchy problem, where a problem is given by some initial data and some boundary conditions to produce a unique time evolving solution. The Einstein equations do not lend themselves naturally to this type of problem, since they do not naturally separate space and time. Arnowitt, Deser, and Misner (ADM) [94] proposed a formulation for general relativity to allow for the solution of the Cauchy problem. Since we assume a stationary spacetime, we are not interested in the description and equations for a dynamic spacetime. We will; however, make use of the AMD variables, lapse, α, shift vector β_i, and the 3-metric γ_{ij} which will be defined in Sec. 2.2.

In this chapter we describe the spacetimes used to model black holes and derive the equations of motion for two general relativistic fluid systems on a curved spacetime background

1. Ideal Magnetohydrodynamics Sec. 2.5,

2. Ultrarelativistic hydrodynamics Sec. 2.6.2.

In the last section of this chapter, we discuss the different geometries studied in this project.

2.2 3+1 Decomposition

We give an overview of the above mentioned ADM formalism here. For a detailed treatment please see York [95], Choptuik [96], or Camenzind [5].

The full $3 + 1$ decomposition provides us with a formalism through which we may describe the evolution of the spacetime. In our study, we consider fixed though generally curved spacetime backgrounds, so it is sufficient to restrict attention to the decomposition of the spacetime metric $g_{\mu\nu}$.

Assume we have a spacetime manifold and an associated metric used to measure distances between points on this manifold. We slice this spacetime into a foliation of spacelike hypersurfaces, denoted Σ_t, as seen in Fig. 2.1. This slicing defines surfaces of constant time, and on each surface we have three coordinates labelling spatial locations on each surface. This defines a timelike vector quantity, n^ν, that allows us to connect the different hypersurfaces.

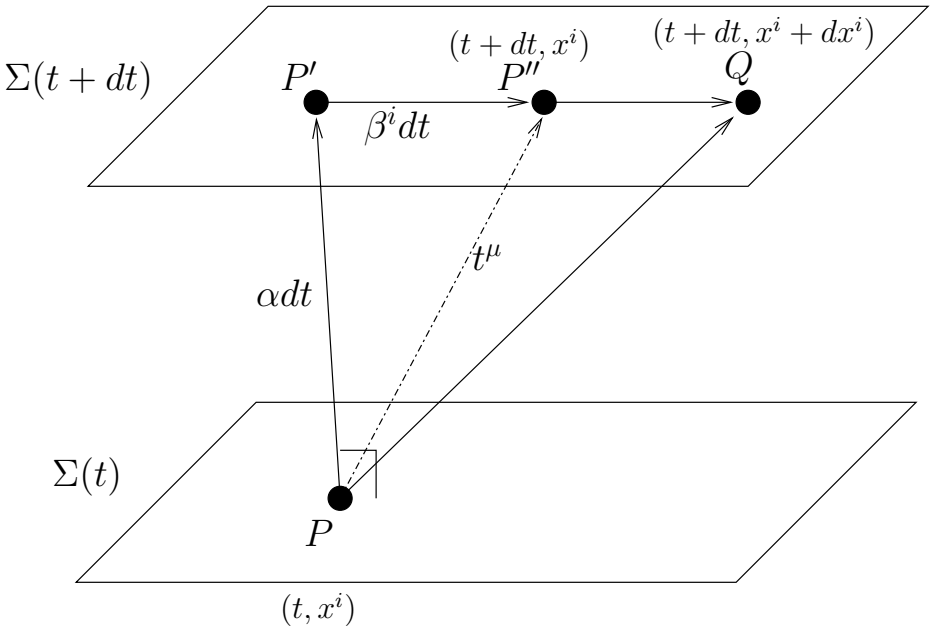

Figure 2.1: The 3+1 decomposition of relativistic spacetime. The spacetime is foliated into space-like hypersurfaces $\Sigma(t)$, here we show two such slices at t and $t + dt$. The vector connecting the coordinate x^i on slice $\Sigma(t)$ to x^i on slice $\Sigma(t + dt)$ may be decomposed into a part orthogonal to the slice αdt, and a part parallel to the slice $\beta^i dt$. To follow the dynamics of an event as it moves from event P at (t, x^i) to a new point Q at $(t + dt, x^i + dx^i)$ requires that we also consider the spatial translation.

If t is the time function, the normalized gradient,

$$n_\mu = \frac{\nabla_\mu t}{\sqrt{g^{\mu\nu}\nabla_\mu t \nabla_\nu t}} \tag{2.7}$$

is an orthogonal unit vector and, $\perp^\mu{}_\nu$, is a projection operator into the surface,

$$\perp^\mu{}_\nu \equiv \delta^\mu{}_\nu + n^\mu n_\nu. \tag{2.8}$$

Where $\delta^\mu{}_\nu$ is the Kronecker delta, and the n^μ, $n_\nu = g_{\mu\nu}n^\nu$ are the normal vectors, and one-forms to the hypersurfaces respectively. *i.e.* If S^μ is any tangent vector, then $\perp^\nu{}_\mu S^\mu$ is a projected tangent vector to a curve lying on the surface $t = \text{const}$.

The induced spatial metric on the hypersurfaces is found by applying, Eqn. (2.8), to the space-time metric,

$$\gamma_{\mu\nu} = g_{\mu\nu} + n_\mu n_\nu. \tag{2.9}$$

The curve defined by constant spatial coordinates and varying t has a tangent vector S^μ which may be written as,

$$S^\mu = \alpha n^\mu + \beta^\mu. \tag{2.10}$$

The general spacetime metric may be written as;

$$ds^2 = \left[-\alpha^2 + \beta^i\beta_i\right] dt^2 + 2\beta_i dx^i dt + \gamma_{ij} dx^i dx^j, \tag{2.11}$$

where γ_{ij} are the spatial components of the projected 4-tensor as defined in Eqn. (2.9).

For fixed spacetime backgrounds, such as those discussed in the next section, we write the metric in the $3+1$ form as follows;

$$\begin{bmatrix} g_{tt} & g_{jt} \\ g_{ti} & g_{ij} \end{bmatrix} = \begin{bmatrix} \beta_s\beta^s - \alpha^2 & \beta_j \\ \beta_i & \gamma_{ij} \end{bmatrix}$$

and

$$\begin{bmatrix} g^{tt} & g^{jt} \\ g^{ti} & g^{ij} \end{bmatrix} = \begin{bmatrix} -1/\alpha^2 & \beta^j/\alpha^2 \\ \beta^i/\alpha^2 & \gamma^{ij} - \beta^i\beta^j/\alpha^2 \end{bmatrix}.$$

We also express the determinant of the 4-metric as g, and the 3-metric γ_{ij} as γ. g and γ are related by $\sqrt{-g} = \alpha\sqrt{\gamma}$. The normal vector from the perspective of stationary observers on the hypersurface are;

$$n_\mu = (-\alpha, 0, 0, 0) \tag{2.12}$$

$$n^\mu = (1/\alpha, -\beta^i/\alpha), \tag{2.13}$$

where n_μ is defined so that we have the normalization condition $n^\mu n_\mu = -1$.

2.3 Black Hole Spacetimes

2.3.1 Minkowski or Special Relativistic Spacetime

The Minkowski metric, the standard metric used in special relativity, is diagonal, with zero shift, and has a trivial lapse function when Cartesian coordinates are used. Explicitly, the line element, ds^2, of this spacetime takes the form,

$$ds^2 = -dt^2 + dx^2 + dy^2 + dz^2. \tag{2.14}$$

The signature of the metric is,

$$g_{\mu\nu} = \eta_{\mu\nu} = \mathrm{diag}(-1, 1, 1, 1). \tag{2.15}$$

This description of spacetime is used to test the development of the methods described in Chap. 3. The results of some of these tests are found in Chap. 4. When we have a black hole present in our spacetime we consider two specific geometries. The first of these is spherically symmetric, while the second is axisymmetric.

2.3.2 Spherically Symmetric Spacetime

When we consider static black holes we use two different coordinates to describe the spacetime, the Schwarzschild coordinates and the Ingoing Eddington–Finkelstein coordinates.

Schwarzschild coordinates:

Using the Schwarzschild coordinates for a spherically symmetric black hole results in the following formulation for the line element,

$$ds^2 = -\left(1 - \frac{2M}{r}\right) dt^2 + \left(1 - \frac{2M}{r}\right)^{-1} dr^2 + r^2 d\theta^2 + r^2 \sin^2\theta d\phi^2. \tag{2.16}$$

The constant M denotes the mass of the black hole as measured by an observer at infinity. There are two important facts about this metric; first, this metric is asymptotically flat, that is, in the limit where $r \to \infty$, we recover flat spacetime written in spherical coordinates. The second is that there are two singularities, one located at the origin, at $r = 0$, and the other is apparent in the metric element g_{rr} when $r = 2M$. If we consider future null infinity, and look at its causal past, any boundaries in the past are known as event horizons. The region inside the event horizon is known as a black hole. For a spherically symmetric spacetime, the event horizon is located at $r = 2M$. This metric produces the ADM variables for the lapse and shift,

$$\alpha = \sqrt{1 - \frac{2M}{r}} \tag{2.17}$$

$$\beta_i = 0. \tag{2.18}$$

The singularity at the event horizon is known to be a coordinate singularity, we consider the existence of a new set of coordinates to circumvent this issue.

Ingoing Eddington–Finkelstein coordinates:

A transformation exists to map the Schwarzschild metric onto coordinates that are referred to as horizon adaptive coordinates. Kruskal coordinates exploit a transformation to remove a coordinate singularity. Let,

$$u = t - r^* \tag{2.19}$$

$$v = t + r^* \tag{2.20}$$

where

$$r^* = \int \frac{dr}{1 - 2M/r} = r + 2M \ln\left|\frac{r}{2M} - 1\right|. \tag{2.21}$$

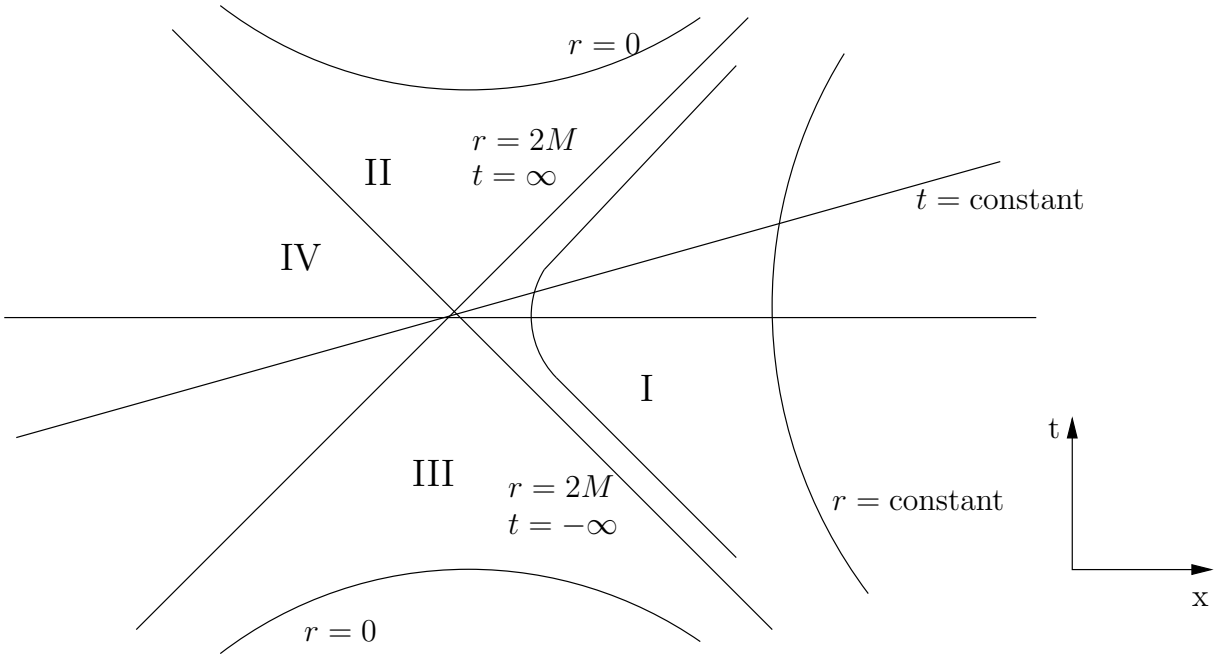

Figure 2.2: The Kruskal diagram for the Schwarzschild spacetime, as described by Wald [31].

Clearly this coordinate transformation is ill-defined at $r = 2M$; however, when using these coordinates we alleviate the singularity in the metric. These are difficult to use in calculations, and some researchers, *e.g.* Poisson [97], suggests the use of what are known as ingoing (v, r) or outgoing (u, r) Eddington–Finkelstein coordinates. Using the ingoing coordinates, we cover the regions of space that we are most interested in modeling. In these coordinates, the spherically symmetric metric takes on the form:

$$ds^2 = -\left(1 - \frac{2M}{r}\right) dv^2 + 2dvdr + r^2 d\theta + r^2 \sin^2\theta d\phi. \tag{2.22}$$

This may be written using a coordinate transformation derived from the null coordinates [98];

$$ds^2 = -\left(1 - \frac{2M}{r}\right) d\bar{t}^2 + \frac{4M}{r} d\bar{t}dr + \left(1 + \frac{2M}{r}\right) dr^2 + r^2 d\Omega^2, \tag{2.23}$$

where $\bar{t}$ is not the same as t in the Schwarzschild coordinates. There is a relation between the two time coordinates

$$\bar{t} = v - r = t + 2M \ln\left(\frac{r}{2M} - 1\right). \tag{2.24}$$

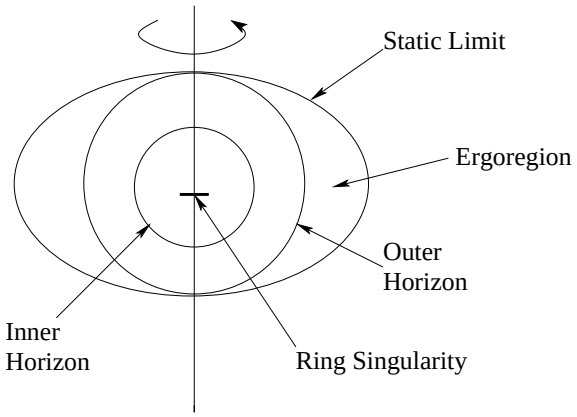

Figure 2.3: A Schematic for the Axisymmetric Spacetime.

Note that the singularity still exists in the coordinate transform itself. Any relation between the two coordinates must be made outside of the event horizon. Here our lapse and shift take the form,

$$\alpha = \sqrt{\frac{r}{r+2M}} \tag{2.25}$$

$$\beta_r = \frac{2M}{r} \tag{2.26}$$

$$\beta_\theta = 0 \tag{2.27}$$

$$\beta_\phi = 0. \tag{2.28}$$

2.3.3 Axisymmetric Spacetime

When the black hole is rotating, we have an axisymmetric spacetime. There are two coordinates commonly used to describe this spacetime, the Boyer–Lindquist coordinates, and the Kerr–Schild coordinates.

Boyer–Lindquist coordinates:

The Boyer–Lindquist coordinates are a generalization of the Schwarzschild coordinates to allow for rotation. The Kerr spacetime written in these coordinates yields the line element,

$$ds^2 = -\left(1 - \frac{2Mr}{\Sigma}\right) dt^2 - \frac{4aMr\sin(\theta)^2}{\Sigma} dt d\phi + \frac{\Sigma}{\Delta} dr^2 + \Sigma d\theta^2 + \mho \sin(\theta)^2 d\phi^2, \tag{2.29}$$

where we use

$$\Sigma = r^2 + a^2\cos(\theta)^2 \tag{2.30}$$

$$\Delta = r^2 - 2Mr + a^2 \tag{2.31}$$

$$\mho = \left(r^2 + a^2 + \frac{2a^2Mr\sin(\theta)^2}{\Sigma}\right). \tag{2.32}$$

ϕ is the angle around the symmetry axis, θ is the polar angle and r is again a radial coordinate. There is one outstanding feature of rotating black holes as opposed to the spherically symmetric black holes: a rotating hole is prone to cause an effect called frame dragging, an effect that is most strongly realized when a particle enters a region known as an ergo-region, as seen in Fig. 2.3. A particle, or light, may enter the ergo-region through a surface called the static limit, defined by

$$r_{\text{static}} = M + \sqrt{M^2 - a^2\cos^2\theta}. \tag{2.33}$$

Inside the ergo-region the time coordinate, t, transitions from a timelike coordinate to a spacelike coordinate [5]. This surface lies outside the outer horizon and any particle that is within this surface must rotate with the black hole. In the case of the Kerr hole, the event horizon coincides with the static limit at two locations, both on the axis of rotation, $\theta = 0$ and $\theta = \pi$. In the Kerr spacetime when the g_{rr} component of the metric goes to zero we have $\Delta = 0$, leading to two roots;

$$r_+ = M + \sqrt{M^2 - a^2} \tag{2.34}$$

$$r_- = M - \sqrt{M^2 - a^2}, \tag{2.35}$$

where the first of these is the outer, or event, horizon. Light cannot escape this horizon just as in the spherically symmetric black hole. The second equation describes the inner horizon, or Cauchy horizon as seen in the diagram 2.3 [99, 5]. Since the second solution is either inside or tangent to the event horizon, it is not discussed further. For more details about the surfaces we refer the reader to Wald [100]. For the horizon to be physical we require that $-M < a < M$. If a exceeds these limits, we have a naked singularity [101], where the singularity of spacetime is not hidden behind an event horizon, and in this case no black hole exists.

When $a = 0$, the static limit, r_{static}, corresponds to the event horizon, r_+ which also corresponds

to the inner Cauchy surface, r_-. Thus we are left with only an event horizon, which corresponds to the event horizon for a spherically symmetric black hole. Just as we did for the spherically symmetric black hole in Schwarzschild coordinates, we use a set of horizon adaptive coordinates. Our choice is a generalization of the Eddington–Finkelstein coordinates known as the Kerr–Schild coordinates that remove the coordinate pathologies found at the event horizon.

Kerr–Schild coordinates:

For the rotating black hole there is a generalization of the ingoing Eddington–Finkelstein coordinates, known as the Kerr–Schild coordinates. Given the coordinate transformation [5, 91];

$$d\phi = d\phi_{BL} + (a/\Delta)dr \tag{2.36}$$

$$dt = dt_{BL} + \left[\frac{1+Y}{1+Y-Z} - \frac{1-Z^k}{1-Z}\right], \tag{2.37}$$

where $Y = a^2\sin^2\theta/\Sigma$, and $Z = 2Mr/\Sigma$, and k is a non-negative integer which is used to parametrize the family. It is common to use $k = 1$ as it is the simplest member of this family of horizon penetrating coordinates. This choice of parameter gives us the Kerr–Schild coordinates.

$$\begin{aligned} ds^2 = & -(1-Z)dt^2 - 2aZ\sin^2\theta dt d\phi + 2Z dt dr + (1+Z)dr^2 \\ & -2a(1+Z)\sin^2\theta dr d\phi + \rho^2 d\theta^2 + \sin^2\theta\left(\rho^2 + a^2(1+Z)\sin^2\theta\right)d\phi^2 \end{aligned} \tag{2.38}$$

2.3.4 Symmetries

When looking for symmetries of spacetime, we look for some obvious features, such as a metric that is independent of any particular coordinate. Take for example the Minkowski spacetime in Cartesian coordinates. This metric is independent of all coordinates, which indicates that there are at least four symmetries (three spatial and one temporal) in that spacetime. To find the symmetries in general we look for Killing vectors, ξ, which is a vector field that obeys the Killing equation;

$$\nabla_\mu \xi_\nu + \nabla_\nu \xi_\mu = 0 \tag{2.39}$$

this shows symmetries of the system, therein implying a conserved quantity [101]. The Killing equation is derived from;

$$\mathcal{L}_\xi g_{\alpha\beta} = 0. \tag{2.40}$$

This is the Lie derivative of the metric along the Killing vector fields. Killing vectors are exploited in Chap. 5.

2.4 Magnetohydrodynamics

Magnetohydrodynamics (MHD) couples a fluid to an electromagnetic field. We present each of these, hydrodynamics, and electrodynamics before proceeding to describe the ideal MHD condition and then our MHD system.

2.4.1 Hydrodynamics, A Perfect Fluid

Fluid models are used to describe continuum systems by their macroscopic thermodynamic properties, including the internal energy and pressure. For a detailed introduction to relativistic fluids, we refer the reader to Schutz [99], Anile [50], Lichnerowicz [102], or Landau and Lifshitz [103].

A perfect fluid does not have shear stresses or dissipation. The stress energy tensor is [4, 101, 99];

$$T^{\mathrm{F}}_{\mu\nu} = (\rho + P)u_\mu u_\nu + P g_{\mu\nu}, \tag{2.41}$$

where ρ is the energy density, P is the pressure, u_μ are the fluid's 4-velocity, and $g_{\mu\nu}$ is the spacetime metric. Both the density and the pressure are evaluated in the rest frame of the fluid. The energy density includes both the rest mass density ρ_0 and the internal energy density $\rho_0\epsilon$,

$$\rho = \rho_0 + \epsilon\rho_0, \tag{2.42}$$

where ϵ is the energy density per baryon. We also express the fluid enthalpy, ω,

$$\omega = \rho + P, \tag{2.43}$$

from which we obtain the specific enthalpy, h,

$$h = \frac{\omega}{\rho_0} = 1 + \epsilon + \frac{P}{\rho_0}. \tag{2.44}$$

The constituent particles of the fluid are characterized by the number density, $n = n(x^\mu)$. If we further assume that the fluid has only one-component, we define the rest mass energy density, ρ_0, by,

$$\rho_0 = m_B n. \tag{2.45}$$

The fluid 4-current, $J^\mu(x^\nu)$, becomes

$$J^\mu = \rho_0 u^\mu. \tag{2.46}$$

The equations of motion for the fluid are derived from two conservation laws; the conservation of baryon number,

$$\nabla_\mu J^\mu = 0. \tag{2.47}$$

and the stress energy,

$$\nabla_\mu T^{\mu\nu} = 0. \tag{2.48}$$

In particular, we consider projections of the conservation of stress-energy along the fluid's 4-velocity, and into the plane perpendicular to the 4-velocity.

$$u_\nu \nabla_\mu T^{\mu\nu} = 0 \tag{2.49}$$

$$h_{\lambda\nu} \nabla_\mu T^{\mu\nu} = 0, \tag{2.50}$$

where $h_{\lambda\nu}$ is the tensor that projects tensor quantities into the plane perpendicular to the fluid's 4-velocity,

$$h_{\mu\nu} = g_{\mu\nu} + u_\mu u_\nu. \tag{2.51}$$

Equations (2.49) and (2.50) are 4 equations with 5 unknowns, ρ_0, ϵ, u^i, P, so we need an equation of state, $P(\rho_0, \epsilon)$ to close the system of equations.

Equation of state

For our system we require the equation of state to relate the pressure, P, the baryon rest mass density, ρ_0, and the energy density ϵ.

$$P \rightarrow P(\rho_o, \epsilon).$$

From the work by Chandrasekhar [104] and Synge [105], we have an ideal gas equation of state for a relativistic non-degenerate adiabatic monatomic gas,

$$P(\rho_0, \epsilon) = (\Gamma - 1)\rho_0\epsilon, \tag{2.52}$$

where Γ is the adiabatic constant. The cases of interest include $\Gamma = 5/3$ for a low energy non-relativistic gas, and $\Gamma = 4/3$ for a high energy relativistic gas [105, 104]. These are limiting cases for the more general equation of state described by Taub [106], where the adiabatic constant depends on the baryon rest mass density. Taub [106] also shows that the ideal gas equation of state is only physically valid below the limit $\Gamma \leq 5/3$ if the system is to remain in agreement with the relativistic kinetic theory of gases [107].

For ultrarelativistic systems, where we take the limit,

$$\rho = \rho_o(1 + \epsilon) \rightarrow \rho_o\epsilon \tag{2.53}$$

the ideal relativistic equation of state is defined as;

$$P = P(\rho) = (\Gamma - 1)\rho, \tag{2.54}$$

where ρ is the internal energy density of the fluid. This is a barotropic equation of state, since the pressure is a function of the internal energy density alone, and the use of this equation of state allows us to determine the equations of motion of a hydrodynamic system by using Eq. (2.48) alone. This is possible because we are assuming the rest mass density conservation, Eq. (2.47), is dynamically unimportant. We use the ultrarelativistic equation of state, Eqn. (2.54) when the internal energy of the fluid is much greater than the fluid's rest mass density, such as expected for

a radiation fluid. The enthalpy for the ultrarelativistic system may be written as

$$\omega = \frac{\Gamma P}{\Gamma - 1}. \tag{2.55}$$

The Speed of Sound

By studying a linearized form of the hydrodynamic equations of motion, we can determine a measure of how fast a disturbance travels in a fluid medium. This speed is referred to as the speed of sound; specifically, given the equation of state, we can determine the speed of sound, c_s, by taking the partial derivative with respect to the internal energy density [103],

$$c_s^2 = \left.\frac{\partial P}{\partial \rho}\right|_s. \tag{2.56}$$

Where ρ is the fluid energy density, and s denotes the entropy per particle. When applying Eqn. (2.56) to the ideal gas equation of state in the form (2.52) we get;

$$c_s^2 = \frac{\Gamma P}{\rho_0 h}. \tag{2.57}$$

In the Newtonian limit $\rho_0 h \to \rho$, we recover the usual speed of sound in an ideal gas, $c_s^2 = \Gamma P/\rho$. For the ultra relativistic fluid equation of state (2.54) we have;

$$c_s^2 = \Gamma - 1. \tag{2.58}$$

In our ultrarelativistic study we restrict our attention to the adiabatic constant $\Gamma = 4/3$. When we study magnetohydrodynamics we will use both $\Gamma = 4/3$ and $\Gamma = 5/3$.

This is the extent of the information that we need from hydrodynamics alone. We now proceed by describing the electromagnetic properties needed to describe magnetohydrodynamics.

2.4.2 Electromagnetism

Since we are considering ideal MHD in this research, we begin by describing the electromagnetic stress-energy tensor, and then describe the relativistic ideal MHD condition, then finally the full ideal MHD stress-energy tensor.

For an electromagnetic field in vacuum, we have the well-known electromagnetic stress-energy

tensor $T^{\rm EM}_{\mu\nu}$ [4, 101, 99, 108];

$$T^{\rm EM}_{\mu\nu} = F_{\mu\sigma}F_{\nu}{}^{\sigma} - \frac{1}{4}g_{\mu\nu}F_{\alpha\beta}F^{\alpha\beta}, \tag{2.59}$$

where $F_{\mu\nu}$ is the Faraday tensor. Adopting a locally inertial frame in Cartesian coordinates we have,

$$F_{\mu\nu} = \begin{pmatrix} 0 & -E_x & -E_y & -E_z \\ E_x & 0 & B_z & -B_y \\ E_y & -B_z & 0 & B_x \\ E_z & B_y & B_x & 0 \end{pmatrix}. \tag{2.60}$$

E_i are the electric field components, and B_i are the magnetic field components. The mixed form of the Faraday tensor is defined as $F^{\sigma}{}_{\nu} = g^{\sigma\mu}F_{\mu\nu}$. Just as with the hydrodynamic stress-energy tensor (2.41), it can be shown that in a local inertial frame, the element $T_{00} = (E^2 + B^2)$ is the local energy density made up of the electric field energy density E^2, and the magnetic field energy density B^2. The elements T_{0j} denote the contributions to the stress-energy from the Poynting flux, the momentum associated with an electromagnetic field. The elements T_{ij} are the elements of the usual non-relativistic Maxwell stress tensor.

It is convenient to define the Maxwell tensor ${}^*F_{\mu\nu} = \epsilon_{\mu\nu\lambda\kappa}F^{\mu\nu}$, where $\epsilon_{\mu\nu\lambda\kappa} = \sqrt{-g}[\mu\nu\lambda\kappa]$, and that $[\mu\nu\lambda\kappa]$ is the Levi–Civita totally antisymmetric tensor, with components $(\pm 1, 0)$, and $F^{\mu\nu} = g^{\mu\gamma}g^{\nu\omega}F_{\gamma\omega}$.

The relativistic electrodynamic equations of motion are completely described by [108],

$$\nabla_{\mu}F^{\mu\nu} = \mathcal{J}^{\mu} \tag{2.61}$$

$$\nabla_{\mu}{}^*F^{\mu\nu} = 0 \tag{2.62}$$

where (2.61) is the generalization of the Maxwell equations that govern the dynamics and constraints of the electric field, and (2.62) is the generalization the Maxwell equations that govern the dynamics and constraints of the magnetic field [108]. $\mathcal{J}^{\mu}$ is the electromagnetic 4-current.

2.4.3 Relativistic Force Free Condition

In ideal MHD, we consider the magnetic field as frozen to the fluid, such that the number of field lines passing through a fluid element is constant. For this behaviour to occur, the electric field in the co-moving frame of the fluid must be zero. This is known as the force free condition, and may be derived by setting the Lorentz force in the rest frame to zero;

$$F_{\mu\nu}u^{\nu} = 0, \tag{2.63}$$

where we have projected the electromagnetic field into the frame of the fluid. The assumption of frozen flux lines is valid for many astrophysical phenomenon since the conductivity in these systems is extremely large. The ideal MHD condition assumes that the electric field is dependent on the velocity and the magnetic field, thus allowing us to eliminate the electric field from the Faraday tensor, and eliminating the need to evolve the electric fields via Eqns. (2.61). This is only true in the ideal MHD limit; the case of infinite conductivity.

The electromagnetic stress-energy tensor (2.59) may now be expressed in terms of the fluid 4-velocity, u^{λ}, and the magnetic fields alone. In the reference frame of the fluid, we have the electromagnetic stress energy contributions $T_{00} = B^2$, $T_{jk} = B_j B_k + B^2/2$, the remaining terms are zero.

When formulating the stress energy tensor for ideal MHD, it is convenient to define the magnetic 4-vector, b^{μ}, by projecting the Faraday tensor into the direction of the fluid 4-velocity [51, 50];

$$b^{\mu} = u_{\nu}\,{}^{*}F^{\mu\nu}, \tag{2.64}$$

where the index on the 4-vector b^{μ} is raised and lowered using the 4-metric $b_{\mu} = g_{\mu\nu}b^{\nu}$. The components of the 4-vector are found seen in (2.100) With this definition we may write the electromagnetic stress-energy tensor (2.59);

$$T^{\mathrm{EM}}_{\mu\nu} = b^2 u_{\mu}u_{\nu} + \frac{b^2}{2}g_{\mu\nu} - b_{\mu}b_{\nu}, \tag{2.65}$$

in analogy to the hydrodynamic stress energy tensor we consider $b^2 = g_{\mu\nu}b^{\mu}b^{\nu}$ to be the magnetic energy, and $b^2/2$ to be the magnetic pressure.

We are now in the position to determine the stress-energy tensor for ideal MHD by adding the

two tensors together;

$$T^{\mathrm{MHD}}_{\mu\nu} = T^{\mathrm{F}}_{\mu\nu} + T^{\mathrm{EM}}_{\mu\nu} = (\rho + P + b^2)u_\mu u_\nu + (P + \frac{1}{2}b^2)g_{\mu\nu} - b_\mu b_\nu. \tag{2.66}$$

Since we assume that the original hydrodynamic model applies to a neutral fluid, any interaction terms between the fluid and the magnetic field are further assumed to be negligable.

We carry on the analogy between the hydrodynamic stress-energy tensor and the MHD stress-energy tensor and define the MHD enthalpy, h^*,

$$h^* = h + \frac{b^2}{\rho_0} \tag{2.67}$$

as well as the MHD pressure, P^*,

$$P^* = P + \frac{b^2}{2}. \tag{2.68}$$

For the remainder of this thesis, when we refer to a stress-energy tensor, we will mean the MHD stress energy tensor (2.66).

Since the local electric field is zero in the ideal MHD approximation, it suffices to include Eqns. (2.62) in the development of the equations of motion for and ideal MHD system.

The coupling between magnetic fields and fluid matter leads to the production of other types of disturbances, known as the Alfvén wave and the magnetosonic waves. We briefly discuss these here.

The Alfvén Speed

By studying a linearization of the MHD equations of motion, Alfvén [109] proved the existence of a wave that arises from the coupling of matter and a magnetic field. This wave comes from oscillations that occur due to the interaction of the compressed magnetic field and the fluid system. It is analogous to the sound waves discussed in the pure hydrodynamic system, and is referred to as the Alfvén wave. The Alfvén wave travels at a speed [50], c_{a},

$$c^2_{\mathrm{a}} = \frac{|b|^2}{\rho_0 h^*}, \tag{2.69}$$

along the magnetic field lines. When we consider the Newtonian limit, we recover, $|b|^2 \to B^2$, and $\rho_0 h^* \to \rho$ so the Alfvén speed reduces to $c_a^2 = B^2/\rho$, which is the Newtonian expression of the

Alfvén speed [93]. The restoring force for the Alfvén wave is the magnetic pressure, and the velocity as defined in Eqn. (2.69) is directly analogous to the speed of sound as presented in Eqn. (2.57).

Magnetosonic Speeds

The magnetosonic waves are longitudinal waves that travel in a direction perpendicular to the magnetic field. These waves arise from the interaction of the magnetic field with the thermodynamic pressure, and allow for the compression of the fluid. The speeds of the magnetosonic waves, $c_{\rm ms}$, are the roots of a quartic function defined in Chap. 3 Eqn. (3.49). Both the magnetic field and the pressure play a role in defining these waves speeds. The four roots to the quartic function are classified as fast, $c_{\rm ms,\,f}$, and slow, $c_{\rm ms,\,s}$ so named because the fast wave has a larger magnitude than the Alfvén speed and, the other, a smaller magnitude.

2.5 Derivation of The Equations of Motion

The fluid equations (2.49) are not readily amenable to the Cauchy problem, so we need to cast them into a form that may be solved numerically. We now derive the conservative form of the equations of motion, using the ADM line element, which, when considering a coordinate system x^μ as defined earlier, may be written;

$$ds^2 = -(\alpha^2 - \beta^i\beta_i)dt^2 + 2\beta_i dt dx^i + \gamma_{ij}dx^i dx^j. \tag{2.70}$$

We follow the derivation of Font [20].

Using the definition of the lapse, α, and shift β^i, S^μ, is tangent to the trajectories of coordinate

$$S^\mu = \alpha n^\mu + \beta^i \delta^\mu{}_i \tag{2.71}$$

as the tangent vectors for stationary observers. The observers in this frame are referred to as Eulerian observers [33]. Observers at rest in the hypersurface, Σ_t, have 4-velocity n^μ. They will measure the fluid velocity as,

$$v_i = \frac{u_i}{-n^\nu u_i}. \tag{2.72}$$

The contravariant components, $v^i = \gamma^{ij} v_j$, are

$$v^i = \frac{u^i}{-n^\mu u_\mu} = \frac{u^i}{W} + \frac{\beta^i}{\alpha}, \tag{2.73}$$

where u^i are the spatial components of the fluid 4-velocity, u^μ. The Lorentz factor, W, is given by the relation $W = -n_\mu u^\mu = \alpha u^t$ which may also be expressed as;

$$W = \frac{1}{\sqrt{1 - \gamma_{ij} u^i u^j}}. \tag{2.74}$$

We define our $3+1$ conservative variables, density, D, energy, E, momentum, S_i, and magnetic field, $\mathcal{B}^\mu$;

$$D = -n_\nu J^\nu \tag{2.75}$$

$$E = T^{\mu\nu} n_\mu n_\nu \tag{2.76}$$

$$S_i = T^{\mu\nu} n_\mu \gamma_{\nu i} \tag{2.77}$$

$$\mathcal{B}^\mu = -n_\nu {}^*F^{\mu\nu}. \tag{2.78}$$

The variables $\mathbf{q}$ are locally conserved quantities, allowing the equations of motion to be written in conservative form, which is essential for the numerical methods described in Chap. 3. Explicit forms for the conservative variables, when considering our normal 4-vector (2.12) are;

$$D = \rho_0 W \tag{2.79}$$

$$E = (\rho_0 h + b^2) W^2 - (P + \frac{1}{2} b^2) - (\alpha b^t)^2 \tag{2.80}$$

$$S_i = (\rho_0 h + b^2) W^2 v_i - \alpha b^t b_i \tag{2.81}$$

$$\mathcal{B}^\mu = \alpha \, {}^*F^{t\nu}. \tag{2.82}$$

It is typical, when studying the relativistic hydrodynamic equations, to define a new variable, τ,

$$\tau \equiv E - D. \tag{2.83}$$

This variable, when taken to in the Newtonian limit, is the classical energy density.

The first fluid equation we calculate is the conservation of baryon density (2.47),

$$\nabla_\mu J^\mu = 0 \Rightarrow \nabla_\mu(\rho_0 u^\mu) = 0, \tag{2.84}$$

which may be reformulated as;

$$(\rho_0 u^\mu)_{,\mu} + (\rho_0 u^\alpha)\Gamma^\mu{}_{\alpha\mu} = 0.$$

$\Gamma^\mu{}_{\alpha\nu}$ are the Christoffel symbols which is determined by [4],

$$\Gamma^\mu{}_{\alpha\nu} = \frac{1}{2} g^{\mu\delta}\left(g_{\delta\alpha,\nu} + g_{\delta\nu,\alpha} - g_{\alpha\nu,\delta}\right) \tag{2.85}$$

There is a well known relation for a Christoffel symbol contracted over the upper and one of the lower indices;

$$\Gamma^\mu{}_{\alpha\mu} = \frac{(\sqrt{-g})_{,\alpha}}{\sqrt{-g}}. \tag{2.86}$$

Using (2.75) and (2.86) we arrive at;

$$\frac{1}{\sqrt{-g}}\left(\sqrt{-g}\rho_0 u^t)_{,t} + (\sqrt{-g}\rho_0 u^i)_{,i}\right) = 0. \tag{2.87}$$

Then using (2.79) and (2.73), we obtain the final form for the conservation of baryon density;

$$\frac{1}{\sqrt{-g}}\left(\partial_t(\sqrt{\gamma}D) + \partial_i\left(\sqrt{-g}D\left(v^i - \frac{\beta^i}{\alpha}\right)\right)\right) = 0 \tag{2.88}$$

We will now explicitly project the equations of conservation of stress-energy into the 3+1 hypersurfaces as described in Sec. 2.2,

$$\nabla_\mu T^{\mu\nu} = 0 \tag{2.89}$$

A typical development of the $3+1$ fluid equations of motion requires the projection of (2.89) into the plane perpendicular to the spacelike hypersurfaces, Σ_t, to give the equation of motion for the energy, and in the plane parallel to the hypersurfaces to give the Euler equations.

$$\gamma_{j\nu}\nabla_\mu T^{\mu\nu} = 0 \tag{2.90}$$

$$n_\nu \nabla_\mu T^{\mu\nu} = 0. \tag{2.91}$$

We write 2.90, 2.91 in conservative form;

$$\nabla_\mu(T^{\mu\nu}\gamma_{j\nu}) = (\nabla_\mu T^{\mu\nu})\gamma_{j\nu} + T^{\mu\nu}\nabla_\mu\gamma_{j\nu} \tag{2.92}$$

$$\nabla_\mu(T^{\mu\nu}n_\nu) = (\nabla_\mu T^{\mu\nu})n_\nu + T^{\mu\nu}\nabla_\mu n_\nu \tag{2.93}$$

where the first term on the right of eqns. (2.92) and (2.93) is zero by conservation of the stress energy tensor (2.89). We will also make use of the two expressions;

$$\nabla_\mu\gamma_{j\nu} = \partial_\mu\gamma_{j\nu} - \Gamma^\delta{}_{\mu\nu}\gamma_{j\delta} - \Gamma^\delta{}_{j\mu}\gamma_{\delta\nu} \tag{2.94}$$

$$\nabla_\mu n_\nu = \partial_\mu n_\nu - \Gamma^\delta{}_{\mu\nu}n_\delta. \tag{2.95}$$

Using (2.94), (2.95) and (2.86) we get

$$\partial_\mu\left(\sqrt{-g}T^\mu_i\right) - \frac{1}{2}\sqrt{-g}T^{\mu\nu}\partial_i g_{\mu\nu} = 0 \tag{2.96}$$

$$\partial_\mu\left(\sqrt{-g}T^\mu_\nu n^\nu\right) - \sqrt{-g}T^{\nu\mu}\partial_\mu n_\nu = 0 \tag{2.97}$$

Equations (2.96) and (2.97) reduce to;

$$\frac{1}{\sqrt{-g}}\left((\sqrt{-g}S_j)_{,t} + (\sqrt{-g}(S_j\hat{v}^i + P\delta^i{}_j - b_j\mathcal{B}^i/W))_{,i}\right) = T^{\mu\nu}(g_{i\nu,\mu} - \Gamma^\delta{}_{\nu\mu}g_{i\delta}) \tag{2.98}$$

$$\frac{1}{\sqrt{-g}}\left((\sqrt{-g}\tau)_{,t} + (\sqrt{-g}(\tau\hat{v}^i + Pv^i - \alpha b^t\mathcal{B}^i/W))_{,i}\right) = -T^{\mu\nu}\Gamma^t{}_{\nu\mu}. \tag{2.99}$$

Here, for notational simplicity, we have defined $\hat{v}^i = v^i - \beta^i/\alpha$. The terms $b_j = g_{j\nu}b^\nu$, and b^k and b^t are the spatial and temporal components of the previously defined magnetic 4-vector, which may be explicitly written as,

$$b^\mu = (b^t, b^j) = \left(\frac{W}{\alpha}(\gamma_{ik}v^i\mathcal{B}^k), \frac{\mathcal{B}^j}{W} + \alpha b^t\hat{v}^j\right). \tag{2.100}$$

Eqns. (2.98) and (2.99) are the general flux conservative form for the momentum and energy respectively.

To determine the evolution and constraint equation for the magnetic field, we project (2.62)

into a component in the hypersurface and the component perpendicular to the hypersurface.

$$n_\nu \nabla_\mu {}^*F^{\mu\nu} = 0 \tag{2.101}$$

$$\perp^i{}_\nu \nabla_\mu {}^*F^{\mu\nu} = 0, \tag{2.102}$$

From (2.101) we get the no-magnetic-monopole constraint

$$\partial_i \left(\sqrt{\gamma}\mathcal{B}^i\right) = 0, \tag{2.103}$$

and from (2.102) the magnetic induction equation

$$\partial_t \left(\sqrt{\gamma}\mathcal{B}^i\right) - \partial_j \left(\sqrt{-g}(\mathcal{B}^i\hat{v}^j - \mathcal{B}^j\hat{v}^i)\right) = 0. \tag{2.104}$$

We define the complete set of conserved quantities:

$$\mathbf{q} = \begin{bmatrix} D \\ S_j \\ \tau \\ \mathcal{B}^k \end{bmatrix} \tag{2.105}$$

We have the corresponding flux terms:

$$\mathbf{f}^i(\mathbf{q}) = \begin{bmatrix} D\hat{v}^i \\ S_j\hat{v}^i + P\delta^i_j - b_j\mathcal{B}^i/W \\ \tau\hat{v}^i + Pv^i - \alpha b^t\mathcal{B}^i/W \\ \mathcal{B}^k\hat{v}^i - \hat{v}^k\mathcal{B}^i \end{bmatrix}, \tag{2.106}$$

where $\hat{v}^i = v^i - \beta^i/\alpha$. We express the source terms on the right hand side of (2.88), (2.98), (2.99), and (2.104) as a source vector.

$$\mathbf{S}(\mathbf{q}; g_{\mu\nu}) = \begin{bmatrix} 0 \\ T^{\mu\nu}\left(g_{j\nu,\mu} - \Gamma^\delta_{\nu\mu}g_{j\delta}\right) \\ \left(T^{\mu t}\alpha_{,\mu} - T^{\mu\nu}\Gamma^t_{\nu\mu}\right) \\ 0 \end{bmatrix} \tag{2.107}$$

Using the above vectors we write the generalized conservative equation;

$$\frac{1}{\sqrt{-g}}\frac{\partial}{\partial x^0}\sqrt{\gamma}\,\mathbf{q} + \frac{1}{\sqrt{-g}}\frac{\partial}{\partial x^i}\sqrt{-g}\,\mathbf{f}^i(\mathbf{q}) = \mathbf{S}(\mathbf{q}; g_{\mu\nu}), \tag{2.108}$$

which has the form necessary for the use of the high resolution shock capturing methods that will be described in Chap. 3.

2.6 Conservation of the Divergence Free Magnetic Field

Since the evolution of the magnetic field has a constraint $\nabla \cdot B = 0$, we have three evolution equations and one constraint equation. This leaves us with an over determined set of equations. Traditionally, the numerical treatment of a constrained system uses free evolution, where the evolution equations are used to evolve the system of equations and there is an implicit assumption that the constraint will be maintained. However, when using free evolution, any numerical errors that arise are often linked to constraint violations, thus we need a method that enforces the constraint as the flow evolves.

Conservation of the $\nabla \cdot \mathbf{B} = 0$ constraint is difficult when studying numerical MHD in general. For MHD evolution in the Newtonian limit, Hawley and Stone [62] have a comprehensive list of the techniques and their advantages and disadvantages. The methods used for general relativistic treatments are the same as those in the Newtonian systems, just written in generalized coordinates. Deviations from the divergence condition arise from the discretization approximation and once produced may lead to unphysical wave transport properties such as transport of Alfvén waves orthogonal to the magnetic field [110]. If we were to evolve the system with no consideration paid to the constraint violations, we would need to ensure that the violations remain bounded and that the error in the divergence is comparable to the truncation error in the numerical approximation. Since we cannot easily control the bounds on the error we focus our attention on techniques that will conserve the constraint during the evolution. The technique we implement to achieve this goal was the diffusive hyperbolic divergence cleaning.[5] We describe the diffusive hyperbolic divergence cleaning method, where the $\nabla \cdot B = 0$ violations are transported out of the domain with a finite speed.

[5] We are aware that other methods such as constrained transport [111], and flux-CT [112] exist, but chose to try a method that allows for the future use of adaptive mesh refinement.

2.6.1 Divergence Cleaning

There are three techniques that are classified as divergence cleaning methods;

1. elliptic divergence cleaning [113, 114],
2. parabolic divergence cleaning method [110, 114], and
3. diffusive hyperbolic divergence cleaning [110, 114].

We focus on the diffusive hyperbolic divergence cleaning method, and outline the technique below.

Diffusive Hyperbolic Divergence Cleaning

Diffusive hyperbolic divergence cleaning was investigated in non-relativistic MHD by Dedner [110] and later in special relativistic MHD by Anderson *et al.* [114]. The diffusive-hyperbolic technique has the advantage that it is local so it does not require averaging over a wider range of cells which is a requirement of other constraint maintenance techniques such as the so-called "flux-CT" method [112]. Another advantage is that it adheres to the hyperbolic form, and consequently the finite volume method. The last advantage is that it is easy to implement numerically [114, 115].

To implement the diffusive hyperbolic method, we add a divergence term acting on an auxiliary field ψ of the form $\nabla_\mu(g^{\mu\nu}\psi)$ to the Maxwell equations,

$$\nabla_\mu \left({}^*F^{\mu\nu} + g^{\mu\nu}\psi\right) = 0. \tag{2.109}$$

We also add a diffusive term, $\kappa n^\mu \psi$ to (2.109) to damp out any $\nabla \cdot B = 0$ violations [116], where κ is a tunable parameter,

$$\nabla_\mu \left({}^*F^{\mu\nu} + g^{\mu\nu}\psi\right) = -\kappa n^\nu \psi. \tag{2.110}$$

To understand why Eqn. (2.110) removes $\nabla \cdot \mathbf{B} = 0$ violations we take the divergence of Eqn. (2.110) [116],

$$\nabla_\nu \nabla_\mu \left({}^*F^{\mu\nu} + g^{\mu\nu}\psi\right) = -\kappa \nabla_\nu (n^\nu \psi), \tag{2.111}$$

and use the fact that the Faraday tensor is anti-symmetric we get,

$$\nabla^2 (\psi) = -\kappa \nabla_\nu (n^\nu \psi). \tag{2.112}$$

To emphasize our point when we consider flat spacetime, Eqn. (2.112), becomes

$$\partial_\nu \partial^\nu \psi = -\kappa \partial_\nu (n^\nu \psi). \tag{2.113}$$

Equation (2.113) has the form of a damped wave equation for ψ travelling at the speed of light provided that $\kappa > 0$ [116]. The wave equation damps ψ to zero which recovers the original induction equation and no-magnetic-monopole constraint.

Projecting equation (2.109) into $3+1$ form, we get,

$$\partial_t \sqrt{\gamma}\Pi^j + \partial_i(\sqrt{-g}(v^i \mathcal{B}^j - v^j \mathcal{B}^i + \alpha g^{ij}\Psi)) = -\alpha\sqrt{-g} g^{\alpha\mu}\Gamma^j_{\alpha\mu}\Psi + \kappa\beta^j\Psi \tag{2.114}$$

$$\partial_t \sqrt{\gamma}\Psi + \partial_i\left(\sqrt{-g}\left(\frac{\mathcal{B}^i}{\alpha} - \frac{\beta^i}{\alpha}\Psi\right)\right) = \alpha\sqrt{-g} g^{\alpha\mu}\Gamma^t_{\alpha\mu}\Psi - \kappa\Psi. \tag{2.115}$$

where we have defined two new fields,

$$\Pi^i = \mathcal{B}^i + \Psi\beta^i, \tag{2.116}$$

$$\Psi = \psi/\alpha \tag{2.117}$$

to maintain the structure of the conservative expressions.

The waves from this new field, Ψ, travel at the speed of light and dissipate at some rate κ, which is a tunable parameter. Some researchers leave the propagation speed of Ψ as a tunable parameter; however, in our system, we found that propagation speed of the violation must be as fast as possible to keep the solution physical, and to transport violations of the constraint out of the domain as fast as possible.

Since the diffusive hyperbolic method augments the original set of conservation equations of motion, we restate the new state vectors, $\mathbf{q}$;

$$\mathbf{q} = \begin{bmatrix} D \\ S_j \\ \tau \\ \Pi^k \\ \Psi \end{bmatrix} \tag{2.118}$$

and their associated flux, $\mathbf{f}^i$ and source vectors, $\mathbf{s}$;

$$\mathbf{f}(\mathbf{q}) = \begin{bmatrix} D\hat{v}^i \\ S_j\hat{v}^i + P\delta^i_j - b_j B^i/W \\ \tau\hat{v}^i + Pv^i - \alpha b^t B^i/W \\ \mathcal{B}^k\hat{v}^i - \hat{v}^k\mathcal{B}^i + \alpha g^{ij}\Psi \\ \mathcal{B}^i/\alpha - \Psi\beta^i/\alpha \end{bmatrix}, \tag{2.119}$$

$$\mathbf{S}(\mathbf{q}; g_{\mu\nu}) = \begin{bmatrix} 0 \\ \sqrt{-g}T^{\mu\nu}\left(g_{i\nu,\mu} - \Gamma^{\delta}_{\nu\mu}g_{i\delta}\right) \\ \sqrt{-g}\left(T^{\mu t}\alpha_{,\mu} - T^{\mu\nu}\Gamma^{t}_{\nu\mu}\right) \\ -\alpha g^{\alpha\mu}\Gamma^{j}{}_{\alpha\mu}\Psi + \kappa\beta^j\Psi \\ \alpha g^{\alpha\mu}\Gamma^{t}{}_{\alpha\mu}\Psi - \kappa\Psi \end{bmatrix}, \tag{2.120}$$

where $\hat{v}^i \equiv v^i - \beta^i/\alpha$.

Now our state vector has the form

$$\mathbf{p} = \begin{bmatrix} \rho_0 & v^j & P & \mathcal{B}^k & \Psi \end{bmatrix}^T. \tag{2.121}$$

Equations (2.118), (2.119), and (2.120) together with (2.108) form our equations of motion for the general relativistic magnetohydrodynamic system.

2.6.2 Ultrarelativistic Equations of Motion

We discussed in the introduction that we would be studying two distinct fluid models, one modelled using ultrarelativistic hydrodynamics, the other modelled using magnetohydrodynamics. We have seen the magnetohydrodynamic equations of motion described above. Now we turn our attention to the ultrarelativistic hydrodynamic description where we are not concerned with fluids with an embedded magnetic field.

When we describe the velocity of a fluid element, we are describing the net velocity of the constituent particles of the fluid cell. For the fluids described so far there have not been any assumptions on the motion of the individual particles. However, when we describe an ultrarelativistic fluid we are describing a fluid made up of elements in which the constituent particles are individ-

ually moving at relativistic velocities. In ultrarelativistic systems the thermal energy of the fluid dominates the rest mass energy. We take the limit

$$\begin{aligned} \rho &= \rho_0 + \rho_0\epsilon \rightarrow \rho_0\epsilon \\ \rho_0 h &= \rho_0 + \rho_0\epsilon + P \rightarrow \rho_0\epsilon + P = \rho + P \end{aligned} \tag{2.122}$$

where ρ is the internal energy of the fluid [117, 115]. The procedure to derive the equations of motion for the ultrarelativistic system is almost identical to the previously outlined procedure for the magnetohydrodynamic equations of motion. Since we take the limit in which we may neglect the rest mass density we neglect the continuity Eqn. (2.88). For simplicity we neglect the magnetic field contributions. The conservative variables are;

$$\mathbf{q} = \begin{bmatrix} S_i \\ \tau \end{bmatrix} = \begin{bmatrix} (\rho + P)W^2 v_i \\ (\rho + P)W^2 - P \end{bmatrix}. \tag{2.123}$$

The flux vectors are;

$$\mathbf{f}^i(\mathbf{q}) = \begin{bmatrix} S_j \hat{v}^i + P\delta^i_j \\ \tau \hat{v}^i + P v^i \end{bmatrix}, \tag{2.124}$$

and the source vector elements are;

$$\mathbf{S}(\mathbf{q}; g_{\mu\nu}) = \begin{bmatrix} \sqrt{-g} T^{\mu\nu} \left(g_{i\nu,\mu} - \Gamma^{\delta}_{\nu\mu} g_{i\delta} \right) \\ \sqrt{-g} \left(T^{\mu t} \alpha_{,\mu} - T^{\mu\nu} \Gamma^{t}_{\nu\mu} \right) \end{bmatrix}, \tag{2.125}$$

with the equation of state $P = (\Gamma - 1)\rho$. The equations of motion remain of the form;

$$\frac{1}{\sqrt{-g}} \frac{\partial}{\partial x^0} \sqrt{\gamma}\, \mathbf{q} + \frac{1}{\sqrt{-g}} \frac{\partial}{\partial x^i} \sqrt{-g}\, \mathbf{f}^i(\mathbf{q}) = \mathbf{S}(\mathbf{q}; g_{\mu\nu}). \tag{2.126}$$

Equations (2.123), (2.124), (2.125), together with (2.126) form the equations of motion for our ultrarelativistic hydrodynamic system.

Dimensionless Parameters

Here we describe the dimensionless control parameters that are used to parametrize the system under study. These are measurable parameters which will be used to characterize the system we

are modeling. There are two parameters that are used to specify our hydrodynamic system, these are;

- asymptotic Mach Number ($\mathcal{M}_\infty$)
- Adiabatic Constant (Γ)

The Mach number is the ratio of the velocity of the fluid and the speed of sound in the fluid.

$$\mathcal{M} = \frac{v}{c_s}. \tag{2.127}$$

The asymptotic Mach number is then the ratio if the asymptotic velocity of the fluid and the asymptotic speed of sound,

$$\mathcal{M}_\infty = \frac{v_\infty}{c_s^\infty}. \tag{2.128}$$

When considering the relativistic systems, the Mach number is defined as [118],

$$\mathcal{M}^R = \frac{Wv}{W_c c_\mathrm{s}} = \frac{W}{W_c}\mathcal{M}, \tag{2.129}$$

and we define the asymptotic relativistic Mach number as,

$$\mathcal{M}^R_\infty = \frac{W_\infty v_\infty}{W_{c\infty} c_\mathrm{s}^\infty} = \frac{W_\infty}{W_{c\infty}}\mathcal{M}_\infty. \tag{2.130}$$

where $W_c = \left(1 - c_s^2\right)^{-\frac{1}{2}}$ is the sound speed equivalent of the relativistic Lorentz factor [1], and $W = \left(1 - v^2\right)^{-\frac{1}{2}}$ is the relativistic Lorentz factor. The relativistic Mach number is the ratio of the proper speed of the fluid with the proper speed of sound in the fluid.

When considering magnetic field contributions, we have one more parameter that may be used to specify the system;

- Plasma beta parameter (β_P)

$$\beta_P = \frac{2P}{|b|^2} \tag{2.131}$$

is the ratio of the hydrodynamic pressure to the magnetic pressure. For the systems we study, this value is determined by the asymptotic values of P, and $|b|^2$ denoted P_∞ and $|b_\infty|^2$ respectively. In Chap. 5 we use $\beta_P^\infty = 2P_\infty/|b_\infty|^2$ a tunable quantity and will be used to parametrize the magnetic fields as we include them in the MHD effects. For typical MHD systems, we have that β_P is

on the order of unity. For weakly magnetized systems $\beta_P \to \infty$, and the MHD treatment is no longer physically necessary as the (electro)magnetic fields would act as test fields on a geometric background. In systems where $\beta_P \ll 1$, the ideal MHD approximation is no longer self consistent, and the coupled fluid-electromagnetic system should be described by force free electrodynamics [116, 119].[6]

2.7 Geometric Configurations

In this thesis, we consider an axisymmetric spacetime.

The computational costs in equipment and time would be too great to do a full $3+1$ calculation so we impose either an axisymmetry, or an infinitely thin-disk approximation on our system. All problems considered here are $3+1$ type systems, but, where by virtue of a coordinate symmetry the geometry may be completely specified by two free spatial coordinates, these, we will refer to as 2D systems where the time dependence is implicit. When considering the motion of a black hole through a homogeneous background fluid, we need to consider the possibility of the fluid having an angular velocity relative to the motion of the black hole, thus this type of motion requires a minimum of two spatial dimensions. We investigate two different geometries where the fluid may have an angular velocity relative to the black hole, an axisymmetric flow, and what is known as the infinitely thin-disk approximation. In previous studies [1, 2], there were problems, such as coordinate singularities, in studying accretion near the event horizon. When so-called horizon penetrating coordinates are used, the coordinate singularities were alleviated. For this study of the Bondi–Hoyle problem, we only use horizon penetrating coordinates.

In the Bondi–Hoyle problem the background fluid is at rest and it is the accretor that is moving through the fluid. We use that setup to describe the different symmetries used in this study.

Axisymmetry

When the flow is considered to be symmetric around the axis defined by the trajectory of the black hole we refer to this as axisymmetric flow. This is in contrast to a stationary spherically symmetric body in a uniform fluid background, which is completely specified by a one spatial dimension, the radius r. Axisymmetry is used for both a spherically symmetric black hole travelling through

[6] Force free electrodynamics assumes the matter contributions to the fluid dynamics are no longer important and that the fluid is no longer a perfect conductor. The motion of the system is determined by the full set of Maxwell equations, as well as the momentum equations in the limit that the fluid density is constant.

the fluid back ground as well as an axisymmetric black hole with the rotation axis aligned with the direction of the trajectory. To describe spacetime in axisymmetry, we use the Kerr–Schild coordinates, (2.38), where we restrict the azimuthal coordinate $\phi = \text{const}$.

Infinitely Thin–Disk Approximation

The infinitely thin–disk approximation is used to restrict the evolution of the flow to the equatorial plane. We assume this geometry for simplicity [2, 3]. We assume the structure of the flow does not depend on the polar coordinate, that the polar pressure gradients and polar velocities are negligible. In non-relativistic models this geometry is considered as wind accretion past an infinite cylinder using cylindrical coordinates [86, 120][7]. We use the Kerr–Schild coordinates to describe this geometry, where in this case we will restrict the polar coordinate $\theta = \pi/2$ thereby restricting the flow to the equatorial plane of the black hole. Since we restrict the polar coordinate, the polar vector elements are constant and the flux out of the plane is zero. The axis of rotation of the rotating black hole is orthogonal to the direction of the fluid flowing from infinity.

The infinitely thin-disk approximation is highly restrictive and is used to gain a basic understanding of the flow morphology. To get a full understanding of the nature of accretion onto a rotating black hole, a full three dimensional evolution will be necessary.

[7] As cited by Font *et al.* [3]

CHAPTER 3

FINITE VOLUME METHODS

3.1 Introduction

In this chapter, we describe the numerical methods used to solve two sets of equations, the ideal magnetohydrodynamic (MHD) equations of motion discussed in Sec. 2.5 and the ultrarelativistic (UHD) equations of motion discussed in Sec. 2.6.2. We define hyperbolic partial differential equations and the characteristics of our systems of equations. We discuss weak solutions to hyperbolic systems, before describing the particulars of the numerical approximations used to solve the hydrodynamic equations of motion, such as Godunov's method and generalizations of Godunov's method used in the finite volume schemes.

In general, the equations for non-dissipative compressible flows will develop discontinuities, which arise from discontinuous changes in the fluid pressure. Since the pressure gradients in such situations are infinite, we require a specially designed numerical technique that would allow for discontinuities in the fluid variables $\mathbf{q}$ or $\mathbf{p}$ as described in the beginning of Chap. 2.

If discontinuities appear in the system, centered finite difference schemes fail, since derivatives across discontinuities are ill-defined. Godunov [121] developed a method to handle the discontinuities, by dividing the domain of integration into small cells and treating each cell as a Riemann problem, defined in 3.6. Godunov's method was later extended to higher accuracy methods, known as high-resolution shock-capturing methods.

Finite volume methods are a generalization of the Godunov method for solving hyperbolic systems of equations over discontinuous initial data. The finite volume method follows Godunov's prescription by breaking the domain of integration into finite volumes or cells. The finite volume method calculates an integral solution to the original PDE problem over each of these cells, the basics of which we present below. This is by no means expected to be a definitive reference for this technique, as there are several good books on this topic. For more details on the finite volume method we refer the reader to LeVeque [122].

3.2 Hyperbolic Partial Differential Equations

The finite volume method requires that the hyperbolic equations be written in a general conservation form for the solution vector, $\mathbf{q} = \mathbf{q}(x^\mu)$,

$$\partial_t \mathbf{q} + \partial_i \mathbf{f}^i(\mathbf{q}) = \mathbf{s}(\mathbf{q}), \tag{3.1}$$

where $\mathbf{f}^i(\mathbf{q}) = \mathbf{f}^i(\mathbf{q}(x^\mu))$ is the flux density vector, and $\mathbf{s} = \mathbf{s}(\mathbf{q}(x^\mu), x^\mu)$ is the source vector. Since the source terms do not have any bearing on the special techniques used in the finite volume method we will drop the source term in the next several sections for convenience.

Hyperbolicity

Expanding the divergence in equations of the type (3.1), we get

$$\partial_t \mathbf{q} + \frac{\partial \mathbf{f}^i}{\partial \mathbf{q}} \partial_i \mathbf{q} = 0. \tag{3.2}$$

This form is known as the quasilinear form of the conservation equations due to the fact that the PDE's are linear in their first derivative; however, the Jacobian $\partial \mathbf{f}^i / \partial \mathbf{q}$ is dependent on the variables $\mathbf{q}$ and is itself nonlinear in our system. We re-write the Jacobian as a matrix $\mathbf{A}^i = \mathbf{A}^i(\mathbf{q})$,

$$\frac{\partial \mathbf{f}^i}{\partial \mathbf{q}} = \mathbf{A}^i. \tag{3.3}$$

Thus we have one Jacobian matrix per spatial dimension. Equation (3.2) becomes

$$\partial_t \mathbf{q} + \mathbf{A}^i \partial_i \mathbf{q} = 0. \tag{3.4}$$

The system of equations (3.4) is hyperbolic if all the eigenvalues of each of the Jacobians are real. The nature of the eigenvalues of each of the Jacobians leads to the definition of several notions of hyperbolicity [122, 123]. These notions apply to the Jacobian of each dimension individually.

- Strongly hyperbolic - the Jacobian is diagonalizable
- Symmetric hyperbolic - the Jacobian is symmetric and diagonalizable
- Strictly hyperbolic - the eigenvalues of the Jacobian are all distinct, and the Jacobian is

diagonalizable

- Weakly hyperbolic - the Jacobian has degenerate eigenvalues, and the Jacobian is diagonalizable.

By diagonalizable we mean that each of the Jacobians A^i can be written in the form,

$$A = R\Lambda R^{-1} \tag{3.5}$$

where Λ is a diagonal matrix, and R is the set of right eigenvectors. If the Jacobian is strongly hyperbolic, it is known to be well-posed. Well-posed problems are mathematical equations that are known to have a solution that is unique and depends continuously on the data. As cited by Putten [124], Friedrichs [125] proves that the ideal hydrodynamic equations of motion for special relativistic systems are well-posed. We assume this will also hold true for general relativistic systems. The advantage of studying hyperbolic partial differential equations is that the solutions are expected to have wavelike behaviour. The solutions to these systems depend on different wave speeds which correspond to the eigenvalues, or characteristics, of the Jacobian of the system of equations. In Sec. 3.4 we describe the spectral decomposition of the Jacobian for the full system of general relativistic magnetohydrodynamic (GRMHD) equations. The calculation of the characteristics in Sec. 3.4 requires that we know both the conservative variables, $\mathbf{q} = \mathbf{q}(\mathbf{p})$, and primitive variables, $\mathbf{p} = \mathbf{p}(\mathbf{q})$ as defined in 2.1. In the next section we outline the procedure used to perform the variable transformation $\mathbf{p} = \mathbf{p}(\mathbf{q})$.

3.3 Calculating the Primitive Variables

When performing magnetohydrodynamic calculations we typically record the equations of motion in terms of the conservation laws of energy-momentum Eqn. (2.48), and matter Eqn. (2.47). Written in this form the variables describing the fluid take on a particular form, we call this form of the variables "conservative". However, when describing fluid flow we rarely directly discuss the energy and momentum of the fluid elements, but rather the pressure, velocities, etcetera. We refer to the latter variables as "primitive". In relativistic magnetohydrodynamics we are often required to use both variables in our calculations. Due to the highly nonlinear nature of this fluid model we are as-of-yet unable to find a closed form solution for the variable conversion and thus rely on

numerical techniques.

We used the method derived by del Zanna, as outlined below [117]. The process of calculating the primitive variables from the conservative variables is known as primitive variable recovery.[8] We define

$$\Omega \equiv \rho_0 h W^2, \tag{3.6}$$

where ρ_0 is the baryon rest mass density, h is the fluid enthalpy, and W is the relativistic Lorentz factor. We also define

$$Q \equiv S_i B^i, \tag{3.7}$$

the scalar product of the fluid's 3-velocity and the magnetic field. The first stage of the primitive variable recovery is to express the conservative variables as functions of Ω, as outlined below.
We write the energy equation (2.83),

$$\tau = E - D = \Omega - P + \left(1 - \frac{1}{2W^2}\right)|B|^2 - \frac{Q^2}{2\Omega^2} - D, \tag{3.8}$$

and using the momentum equation (2.81) we get

$$|S|^2(\Omega) = \gamma^{ij} S_i S_j = (\Omega + |B|^2)^2 \left(1 - \frac{1}{W^2}\right) - \frac{Q^2}{\Omega^2}(2\Omega + |B|^2). \tag{3.9}$$

We solve (3.9) for W

$$W(\Omega) = \left[1 - \frac{Q^2(2\Omega + |B|^2) + |S|^2\Omega}{(\Omega + |B|^2)^2\Omega^2}\right]^{-\frac{1}{2}}, \tag{3.10}$$

then re-formulate the equation of state, $P = (\Gamma - 1)\epsilon\rho_0$ as

$$P(\Omega) = \frac{(\Omega - DW)(\Gamma - 1)}{\Gamma W^2}. \tag{3.11}$$

Using (3.8), we define $f(\Omega)$,

$$f(\Omega) = \Omega - P + \left(1 - \frac{1}{2W^2}\right)|B|^2 - \frac{Q^2}{2\Omega^2} - D - \tau = 0. \tag{3.12}$$

[8] We are aware of other techniques to solve for the primitive variables such as a two variable and 5 variable solver also outlined in Noble *et al.* [117]; however, after testing, the single variable solver was found to be simpler and just as robust for the systems we investigated.

Finally, we use Newton's method to iteratively solve the nonlinear equation (3.12) for Ω,

$$\Omega^{I+1} = \Omega^I - \frac{f(\Omega^I)}{f'(\Omega^I)}, \tag{3.13}$$

$$f'(\Omega^I) = \frac{\partial f}{\partial \Omega}(\Omega^I), \tag{3.14}$$

where I denotes the Newton iteration. To calculate $\partial f/\partial\Omega$, we use the relations listed below

$$\frac{df}{d\Omega} = 1 - P' + \frac{|B|^2}{W^3}\frac{dW}{d\Omega} + \frac{Q^2}{\Omega^2} \tag{3.15}$$

$$\frac{dP}{d\Omega} = \frac{\left(W\left(1+DW'\right) - 2\Omega W'\right)\left(\Gamma - 1\right)}{\Gamma W^3} \tag{3.16}$$

$$\frac{dW}{d\Omega} = -W^3\frac{2Q^2\left(3\Omega^2 + 3\Omega|B|^2 + |B|^4\right) + |S|^2\Omega^3}{2\Omega^3\left(\Omega + |B|^2\right)^3}. \tag{3.17}$$

We perform this procedure at every time step, n. The Newton iteration must be initialized, so as an initial guess for the value of Ω^0 we use the definition of Ω (3.6) and values for ρ_0, h, and W from the previous timestep, $n-1$,

$$\Omega^0 = \rho_0^{n-1}h^{n-1}/(1-\gamma_{ij}v_i^{n-1}v_j^{n-1})^2. \tag{3.18}$$

Using this initial guess we were able to increase the speed at which the solver converged to the correct solution. Occasionally this method may fail to converge to a solution. In such situations another method was used to determine the primitive variables, this is discussed in Sec. 3.9.1.

Now that we have Ω, we solve for the primitive variables. Using (2.81) we express the velocity components as;

$$v_i = \frac{1}{\Omega + |B|^2}\left(S_i + \frac{Q}{\Omega}B_i\right), \tag{3.19}$$

and the Lorentz factor W (3.10) as,

$$W = \left[1 - \frac{Q^2(2\Omega + |B|^2) + |S|^2\Omega}{(\Omega + |B|^2)^2\Omega^2}\right]^{-\frac{1}{2}}.$$

We use the equation of state as expressed above (3.11) to calculate the pressure;

$$P(\Omega) = \frac{(\Omega - DW)(\Gamma - 1)}{\Gamma W^2};$$

we recover the baryon rest mass density, ρ_0,

$$\rho_0 = \frac{D}{W}. \tag{3.20}$$

When using diffusive hyperbolic divergence cleaning, as defined in Sec. 2.6.1, we recover the magnetic field density $\mathcal{B}^i$ by,

$$\mathcal{B}^i = \Pi^i - \Psi\beta^i. \tag{3.21}$$

Ultrarelativistic Primitive Variable Recovery

We use the same definition for Q (3.7) and redefine Ω,

$$\Omega \equiv hW^2. \tag{3.22}$$

where the enthalpy is defined to be, $h = \rho + P$. The only significant change to the remaining primitive variable recovery method is setting the relativistic density, $D = 0$, the magnetic field, $\mathcal{B}^i = 0$, and baryon rest mass density, $\rho_0 = 0$. Otherwise the procedure is identical.

3.4 Characteristics

3.4.1 MHD Wave Mathematical Description

For the following section, we will be using the notation $\mathtt{A}$ to represent a 10×10 array and $\mathtt{V}$ to represent a 1×10 array. In Antón *et al.* [53], the hyperbolic structure of the general relativistic MHD wave equations was investigated. That work is based on the work by Anile [50] for the general relativistic hydrodynamic hyperbolic structure. To determine the hyperbolic nature of the equations, Antón *et al.* defined a variable 1×10 array $\mathtt{V} = (u^\nu, b^\sigma, P, s)$, where u^ν, b^σ, P are as defined in Chap. 2, and s is the specific entropy. They write the equations of motion as a quasi-linear system;

$$\mathtt{A}^{\mu A}_{B} \nabla_\mu \mathtt{V}^B = 0, \tag{3.23}$$

where $A, B = 1, ..., 10$. The 10×10 matrices $\mathtt{A}^{\mu}$ are given by;

$$\mathtt{A}^{\mu} = \begin{bmatrix} \mathcal{C}u^{\mu}\delta^{\alpha_1}{}_{\beta_1} & -b^{\mu}\delta^{\alpha_2}{}_{\beta_2} + P^{\alpha_2\mu}b_{\beta_2} & l^{\alpha_3\mu} & 0^{\mu\alpha_4} \\ b^{\mu}\delta^{\alpha_5}{}_{\beta_5} & -u^{\mu}\delta^{\alpha_6}{}_{\beta_6} & f^{\alpha_7\mu} & 0^{\mu\alpha_8} \\ \rho_0 h\delta^{\mu}{}_{\beta_9} & 0^{\mu}{}_{\beta_{10}} & u^{\mu}/c_s^2 & 0^{\mu} \\ 0^{\mu}{}_{\beta_{11}} & 0^{\mu}{}_{\beta_{12}} & 0^{\mu} & u^{\mu} \end{bmatrix}. \tag{3.24}$$

where α and β with subscripts are unique indices that run over the range $1 \ldots 4$. Antón *et al.* further define,

$$b_{\alpha} = g_{\alpha\beta}b^{\beta} \tag{3.25}$$

$$\mathcal{C} = \rho_0 h + b^2 \tag{3.26}$$

$$P^{\alpha_2\mu} = g^{\alpha_2\mu} + 2u^{\alpha_2}u^{\mu} \tag{3.27}$$

$$l^{\alpha_3\mu} = \left(\rho_0 h g^{\alpha_3\mu} + \left(\rho_0 h - b^2/c_s^2\right) u^{\alpha_3}u^{\mu}\right)/\rho_0 h \tag{3.28}$$

$$f^{\alpha_7\mu} = \left(u^{\alpha_7}b^{\mu}/c_s^2 - b^{\alpha_7}u^{\mu}\right)/\rho_0 h. \tag{3.29}$$

We define for each value of the index $\mu = 0, 1, 2, 3$

$$0^{\mu}{}_{\beta} = [0\ 0\ 0\ 0]\,, \tag{3.30}$$

$$0^{\mu\beta} = [0\ 0\ 0\ 0]^T\,, \tag{3.31}$$

and

$$0^{\mu} = 0. \tag{3.32}$$

Let $\phi(x^{\mu}) = 0$ define a characteristic hypersurface of Eqn. (3.23) [50], such that its gradient locally has the same velocity as the traveling wave [126]. For example if the waves are travelling in the radial direction the gradient of the hypersurface has the form

$$\phi_{\mu} = (-\lambda, 1, 0, 0), \tag{3.33}$$

where λ denotes the wave speed. To calculate the wave equations, we define a characteristic matrix by contracting the 4-gradient of the hypersurface $\phi_\mu = \nabla_\mu \phi$ with the 4 matrices $\mathtt{A}^\mu$;

$$\mathtt{A}^\mu \phi_\mu = \begin{bmatrix} \mathcal{C}a\delta^{\alpha_1}{}_{\beta_1} & m^{\alpha_2}{}_{\beta_2} & l^{\alpha_3} & 0^{\alpha_4} \\ \mathcal{D}\delta^{\alpha_5}{}_{\beta_5} & -a\delta^{\alpha_6}{}_{\beta_6} & f^{\alpha_7} & 0^{\alpha_8} \\ \rho_0 h \phi_{\beta_9} & 0_{\beta_{10}} & a/c_s^2 & 0 \\ 0_{\beta_{11}} & 0_{\beta_{12}} & 0 & a \end{bmatrix}, \tag{3.34}$$

where

$$a = u^\mu \phi_\mu \tag{3.35}$$

$$\mathcal{D} = b^\mu \phi_\mu \tag{3.36}$$

$$l^{\alpha_3} = l^{\alpha_3 \nu}\phi_\nu = \phi^{\alpha_3} + \left(\rho_0 h - b^2/c_s^2\right) a u^{\alpha_3}/\rho_0 h + \mathcal{D} b^{\alpha_3}/\rho_0 h \tag{3.37}$$

$$f^{\alpha_7} = f^{\alpha_7 \nu}\phi_\nu = \left(a b^{\alpha_7}/c_s^2 - \mathcal{D} u^{\alpha_7}\right)/\rho_0 h \tag{3.38}$$

$$m^{\alpha_2}{}_{\beta_2} = \left(\phi^{\alpha_2} + 2a u^{\alpha_2}\right) b_{\beta_2} - \mathcal{D}\delta^{\alpha_2}{}_{\beta_2}. \tag{3.39}$$

We define,

$$0_\beta = [0\ 0\ 0\ 0]\,, \tag{3.40}$$

$$0^\beta = [0\ 0\ 0\ 0]^T\,. \tag{3.41}$$

To calculate the characteristic wave velocities we calculate the roots of the characteristic equation defined by the determinant of the characteristic matrix Eqn. (3.34). This leaves us with the equation;

$$\det \mathtt{A}^\mu \phi_\mu = \mathcal{C} a^2 \mathcal{A}^2 \mathcal{N}_4 = 0, \tag{3.42}$$

where

$$\mathcal{A} = \mathcal{C}a^2 - \mathcal{D}^2 \tag{3.43}$$

$$\mathcal{N}_4 = \rho_0 h \left(\frac{1}{c_s^2} - 1\right) a^4 - \left(\rho_0 h + \frac{b^2}{c_s^2}\right) a^2 \phi^2 + \mathcal{D}^2 \phi^2. \tag{3.44}$$

$\mathcal{C}$ is defined in Eqn. (3.26) and a is defined in Eqn. (3.35). We wish to calculate the waves for the MHD in their physical directions along a coordinate x^i. To do this, we choose a form for the

characteristic hypersurface;

$$\phi_\mu = (-\lambda, 1, 0, 0) \tag{3.45}$$

$$\phi_\mu = (-\lambda, 0, 1, 0) \tag{3.46}$$

$$\phi_\mu = (-\lambda, 0, 0, 1) \tag{3.47}$$

for the radial, polar, and azimuthal waves respectively. By substituting these expressions into Eqn. (3.42) we have the characteristic polynomial for waves traveling in the respective directions [53]. By using Eqns. (3.45), (3.46) or (3.47), separately, for ϕ_μ in Eqns. (3.35), (3.43) and (3.44) we get the characteristic velocities for the MHD waves for each of the spatial directions. We describe the different MHD waves in detail in the following section.

3.4.2 MHD Waves and Characteristic Velocities

One of the fundamental properties of our expression of the ideal MHD equations of motion is the exposure of the dependence of the system on the waves of the different constituent fields generated by the flow. We have seen above that these consist of a matter wave, sound waves, two Alfvén waves, and four magnetosonic waves, which come in pairs, *i.e.* there are two fast waves and two slow waves so named due to their relative magnitudes when compared to the Alfvén wave speed. We have explicit calculations for the eigenvalues for the Jacobian matrices for ideal MHD [44]. We list the results for the waves travelling in the coordinate x^i-direction.

Matter waves propagate disturbances in the density of the fluid at the speed of the fluid. These waves are stationary in the frame of the fluid and are also called contact discontinuities, meaning the fluid variables are smooth but there is a jump in the density. The speed of the matter waves, $\lambda_{\rm M}$, are found by evaluating the $a = 0$ root for Eqn. (3.42), or setting (3.35) to zero,

$$\lambda_{\rm M} = \alpha v^i - \beta^i. \tag{3.48}$$

When taken to the flat spacetime limit in Cartesian coordinates, ($\alpha = 1$, $\beta^i = 0$), this wave is dragged along by the fluid.

Sound waves are longitudinal velocity perturbations that propagate parallel to the magnetic field. They result from a small disturbance in the density field of the fluid medium, such as a local

compression. The sound waves propagate this disturbance through the fluid medium [127]. Like sound waves, magnetosonic waves are longitudinal, parallel to the velocity of the fluid. There are two types of magnetosonic waves, the fast and slow magnetosonic waves. The difference between the fast and slow waves is the relative motion of the wave to the magnetic field lines. When the magnetosonic wave is perpendicular to the magnetic field lines the magnetic field acts to enhance restoring forces found in sound waves and thus the presence of the magnetic field acts to enhance the speed of the wave [128]. The slow magnetosonic waves are also parallel to the fluid flow; however, these waves are parallel to the magnetic field. The magnetosonic waves are also known as magneto-acoustic waves. The fast and slow magnetosonic waves were originally investigated by Spitzer in 1962 in a Newtonian system [93]. These waves develop due to a nonlinear coupling between the Alfvén waves and the sound waves. This coupling is seen in the dispersion relation for this particular set of fields, as seen in section 3.4.1. In the absence of the magnetic field the magnetosonic waves reduce to the sound wave.

The magnetosonic wave speeds, $\lambda_{\rm MS}$, are the roots of the fourth degree polynomial (3.44) in (3.42), $\mathcal{N}_4 = 0$

$$\lambda_{\rm MS} = N_4 = \rho h \left(\frac{1}{c_s^2} - 1\right) a^4 - \left(\rho_0 h + \frac{b^2}{c_s^2}\right) a^2 G + B^2 G = 0 \tag{3.49}$$

where

$$a = \frac{W}{\alpha}\left(-\lambda + \alpha v^i - \beta^i\right) \tag{3.50}$$

$$B = b^i - b^t \lambda \tag{3.51}$$

$$G = \frac{1}{\alpha^2}\left(-(\lambda + \beta^i) + \alpha^2 \gamma^{ii}\right) \tag{3.52}$$

and c_s is the speed of sound as described in Chap. 2 Eqn. (2.57).

Like the magnetosonic waves, the Alfvén waves also arise from the coupling of matter to the magnetic fields. In the ideal MHD limit, as the fluid flows, it drags the magnetic field with it. Since we have compressible flow and the frozen-in condition, the magnetic fields will compress, and will consequently push against each other. This push is the magnetic pressure. The pressure within the magnetic fields eventually overcomes the compression of the fluid and the density of the fluid begins to decrease. This pressure will then exceed the original compression where the fluid will continue to compress the magnetic field and start the process all over again. The described

oscillatory behaviour is the origin of the Alfvén waves. These waves result from perturbations that are perpendicular to the fluid velocity and parallel to the magnetic field, and are sometimes known as intermediate waves due to their relation to the magnetosonic waves. The Alfvén wave speeds, $\lambda_{\rm a}$ may be calculated by setting $\mathcal{A}$, Eqn. (3.43), to zero

$$\lambda_{a-} = \frac{b^i + \sqrt{\rho_0 h + b^2} u^i}{b^t + \sqrt{\rho_0 h + b^2} u^t}, \tag{3.53}$$

$$\lambda_{a+} = \frac{b^i - \sqrt{\rho_0 h + b^2} u^i}{b^t - \sqrt{\rho_0 h + b^2} u^t}. \tag{3.54}$$

Ultimately, when studying an MHD system with hyperbolic divergence cleaning, (Sec. 2.6.1), two more waves arise from treating the numerical divergence violations as fluxes for the auxiliary variable Ψ in Eqn. (2.114). The wave velocities for the auxiliary field are fixed parameters, and for our system are set to $\pm c$, the speed of light.

The wave speeds calculated in Eqns. (3.48) to (3.54) are also the eigenvalues of the Jacobian matrix in Eqn. (3.3). While we define the Jacobian as the derivative with respect to the conservative variable, the relativistic flux variables are given as a nonlinear combination of conservative and primitive variables, and the conservative variables are a known function of the primitive variables. Calculating the Jacobian is not a one-step process. To find the eigenvalues, we first reformulate the Jacobian matrix [9];

$$\mathbf{A}^i = \frac{\partial \mathbf{f}^i}{\partial \mathbf{q}} = \frac{\partial \mathbf{f}^i}{\partial \mathbf{p}} \left(\frac{\partial \mathbf{q}}{\partial \mathbf{p}} \right)^{-1}. \tag{3.55}$$

Recall that we define $\mathbf{q}$ to be the conservative variables, $\mathbf{f}^i$ to be the flux contributions, and $\mathbf{p}$ to be the primitive variables. To calculate the eigenvalues and eigenvectors numerically we make the following definitions;

$$\mathbf{A}_0 \equiv \frac{\partial \mathbf{q}}{\partial \mathbf{p}} \tag{3.56}$$

$$\mathbf{A}_1^i \equiv \frac{\partial \mathbf{f}^i}{\partial \mathbf{p}} \tag{3.57}$$

and solve the generalized eigenvalue problem,

$$\left(\mathbf{A}_1^i - \mathbf{A}_0 \lambda^i \right) \mathbf{x}^i = 0. \tag{3.58}$$

The superscript i denotes the direction of the eigenvalue equation. For example, to calculate the radial eigenvalues we use the radial fluxes in Eqn. (3.57) and solve the eigenvalue problem in Eqn. (3.58) with $i = r$. We solve Eqn. (3.58) three times once for each dimension. In the case of symmetries we will have a trivial solution, $\lambda = 0$ for all waves since net fluxes in a symmetric direction will be zero, we do not need to solve (3.58) for the symmetric dimension(s). The eigenvalues, λ^i, of (3.58) are no different than those for the system,

$$\mathbf{A}^i \mathbf{y} = \lambda^i \mathbf{y} \tag{3.59}$$

where $\mathbf{A}^i$ is defined in Eqn. (3.55). We relate (3.58) and (3.59) by [9],

$$\left(\mathbf{A}_1^i - \mathbf{A}_0 \lambda^i\right) \mathbf{x} = 0 \tag{3.60}$$

$$\left(\mathbf{A}_1^i \mathbf{A}_0^{-1} - \mathbf{I}\lambda^i\right) \mathbf{A}_0 \mathbf{x} = 0 \tag{3.61}$$

where $\mathbf{I}$ is the identity matrix. Then the eigenvectors, $\mathbf{x}$, of (3.58) are related to the eigenvectors, $\mathbf{y}$, of (3.59) by,

$$\mathbf{A}_0 \mathbf{x} = \mathbf{y}. \tag{3.62}$$

The eigenvectors $\mathbf{y}$ are the eigenvectors for the system of interest. There is no known closed form solution for the eigenvectors for the GRMHD system; thus, we use LAPACK [129] to perform the spectral decomposition.[9] We solve the eigensystem (3.58) and (3.62) for each spatial dimension, i. In the event of a symmetry the number of eigensystems solved is reduced. For example in the case of axisymmetry we do not need to calculate the $i = \phi$ system.

3.5 Conservative Methods

When there are discontinuities in the initial data set, solving equation (3.1) requires special treatment for the discretization of the equations of motion. An older approach used finite differencing of the equations with additional terms to introduce artificial viscosity[10]; however, we pursue a less diffusive technique that is specially developed for conservation laws and discontinuities in the domain, the high resolution shock capturing (HRSC) algorithms. HRSC methods have the advantage

[9] Specifically we used the generalized eigenvalue and eigenvector solver DGGEV.
[10] This form of solution is not treated here, for more details we refer the reader to [8, 25, 26]

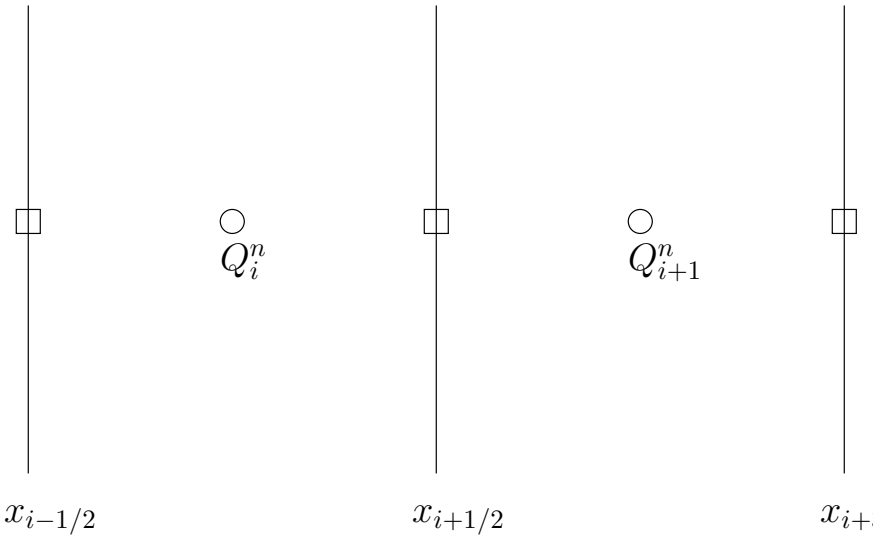

Figure 3.1: A graphical representation of a finite volume, Q_i denotes the state vector, averaged over a cell defined by $x_{i-1/2} \leq x \leq x_{i+1/2}$. The flux is assumed to enter or leave a cell, Q_i through the cell interface at $x_{i+1/2}$.

of ensuring the conservation of the variables $\mathbf{q}$, and that discontinuities such as shocks are well resolved.

To capture the discontinuities that may develop in a fluid flow, we use an integral form of the conservation equations, which is known as the weak solution. We consider Eqn. (3.1),

$$\partial_t \mathbf{q} + \partial_i \mathbf{f^i}(\mathbf{q}) = \mathbf{s}(\mathbf{q}). \tag{3.63}$$

Where $\mathbf{q}$ are the conserved variables, $\mathbf{f}^i(\mathbf{q})$ is the flux density vector, and $\mathbf{s}(\mathbf{q})$ are the source terms.

As shown in Fig. 3.1, we integrate this equation over a finite volume ΔV_i with the domain $x_{i-1/2} \leq x \leq x_{i+1/2}$,

$$\int_{\Delta V_i} \left(\partial_t \mathbf{q} + \partial_x \mathbf{f}(\mathbf{q})\right) dV = \int_{\Delta V_i} \mathbf{s} dV. \tag{3.64}$$

Using Gauss' Theorem,

$$\int_{\Delta V_i} \partial_i \mathbf{f}^i(\mathbf{q}) = \oint_{S_i} \mathbf{f}^i dS_i \tag{3.65}$$

we can re-write the integral over the flux terms,

$$\frac{\partial}{\partial t}\int_{\Delta V_i}\mathbf{q}+\oint_{S_i}\mathbf{f}^j(\mathbf{q})dS_j=\int_{\Delta V_i}\mathbf{s}dx. \tag{3.66}$$

This equation shows us that the change in time for the quantity $\mathbf{q}$ in a volume V_i is from the flux through the volumes surface, as well as from the source within V_i.

Now, to finalize the integral form we integrate over a time interval $t^n \leq t \leq t^{n+1}$ to get;

$$\int_{t^n}^{t^{n+1}}\frac{\partial}{\partial t}\int_{\Delta V_i}\mathbf{q}(t,x^i)dV+\int_{t^n}^{t^{n+1}}\oint\mathbf{f}(\mathbf{q}(t,x^i))dS_j dt=\int_{t^n}^{t^{n+1}}\int_{\Delta V_i}\mathbf{s}(\mathbf{q}(t,x^i))dS_j dt \tag{3.67}$$

Equation (3.67) is the preferred mathematical form of a conservation laws, since it does not depend on continuity of the state vectors. This means that in the presence of a discontinuity, the integral form will still be satisfied [33].

The finite volume method described above involve the use of approximate Riemann solvers to handle discontinuities in the fluid variables. To understand the approximate methods it is beneficial to understand the Riemann problem and the exact solutions. In the following two sections we discuss the Riemann problem in general along with the possible solutions, then the exact Riemann solvers implemented by Martí [46] and Giacomazzo [49].

3.6 The Riemann Problem

The most elementary problem involving discontinuities, as illustrated in Fig. 3.2, has two distinct constant states separated by a discontinuity. This is known as the Riemann problem. For simplicity, we restrict our attention to a problem in one spatial dimension. In Fig. 3.2 we have an example of a a discontinuous initial data set for the state vector $\mathbf{q}=(q_1,q_2,...,q_p)$, which is used for the conservation equation (3.1). The initial data is expressed as,

$$\mathbf{q}(0,x)=\begin{cases}\mathbf{q}_{\mathrm{L}}, & x<0;\\ \mathbf{q}_{\mathrm{R}}, & x>0,\end{cases} \tag{3.68}$$

where $\mathbf{q}_{\mathrm{L}}$ and $\mathbf{q}_{\mathrm{R}}$ are distinct constant values. If we were to study the advection equation as seen in Eqn. (1.1), with $s=0$ and $v=$ Const., we have the simple solution,

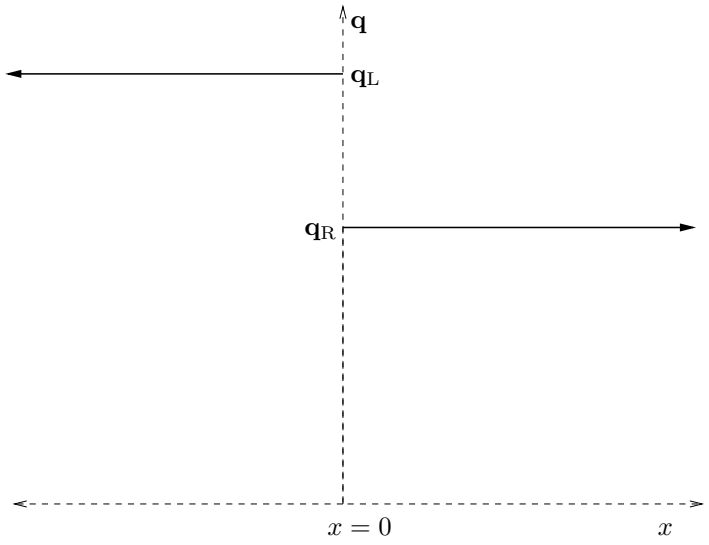

Figure 3.2: A scalar example of an initial data set for the Riemann Problem. The $\mathbf{q}_{\mathrm{L}}$ and $\mathbf{q}_{\mathrm{R}}$ are constant state vectors. Each of these vectors are not a function of the coordinates and are generically separated by a discontinuity at the origin at $t = 0$. When the divider is removed, Riemann's solution described the resulting interaction of the two states.

$$q(t,x) = \begin{cases} q_{\mathrm{L}}, & x - vt < 0; \\ q_{\mathrm{R}}, & x - vt > 0. \end{cases} \tag{3.69}$$

Any information on the left of the discontinuity seen in Fig. 3.2 would propagate upstream with a fixed velocity v, likewise for the information on the right of the discontinuity. In the advection equation example the characteristic line $x - vt = 0$ denotes the location of the discontinuity for all time.

The Riemann problem becomes more complicated in equations where the fluxes are nonlinear, such as in hydrodynamic systems of hyperbolic equations. In particular, considering our magnetohydrodynamic system, we expect to have a minimum of eight characteristics. If our system is strictly hyperbolic each characteristic will be distinct. The set of characteristics for a (magneto)hydrodynamic system are known as a characteristic fan. We refer the reader to figure 3.3 for a sample characteristic fan.

With our system we have two extreme waves denoted $\lambda_{\mathrm{MS^{Fast}}}$. Any part of the domain to the left of the left-most $\lambda_{\mathrm{MS^{Fast}}}$ will simply be the initial data $\mathbf{q}_L$, and the domain to the right of the

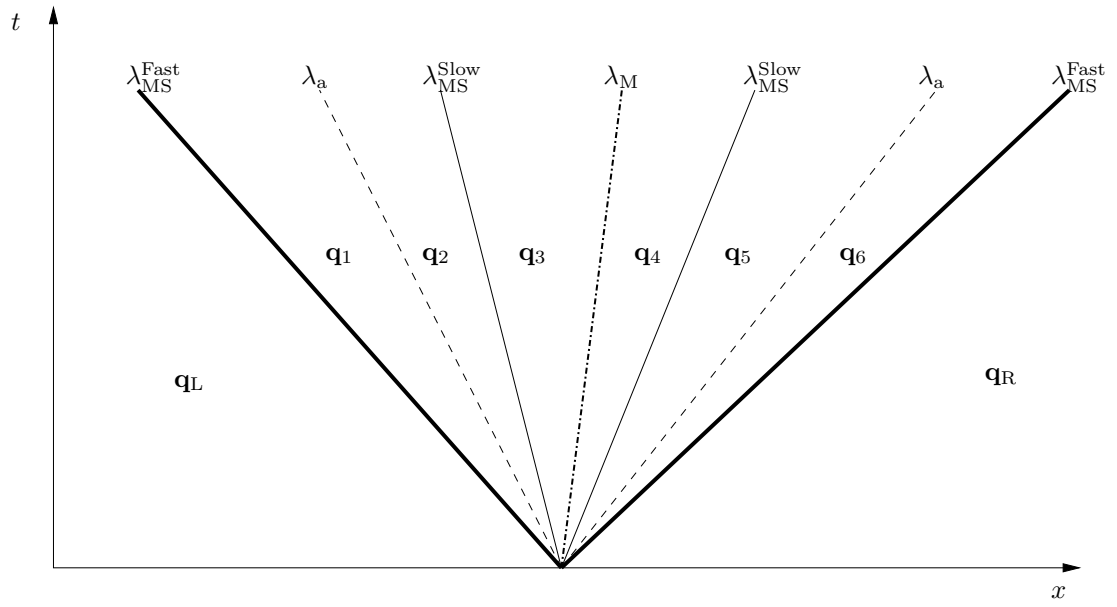

Figure 3.3: The general magnetohydrodynamic characteristic fan. We see the two Alfvén waves, λ_{a}, the fast $\lambda^{\text{Fast}}_{\text{MS}}$ and slow $\lambda^{\text{Slow}}_{\text{MS}}$ magnetosonic waves, and the contact discontinuity λ_{M}. These waves decompose the Riemann problem into 8 regions denoted $\mathbf{q}_{\text{L}}$, $\mathbf{q}_1 \rightarrow \mathbf{q}_6$, and $\mathbf{q}_{\text{R}}$. The treatment of the different regions for an exact solution is described in [49]. When solving the Riemann problem either exactly or approximately the region around the contact discontinuity are typically referred to as star-regions and are denoted q^*_{L} and q^*_{R} on the left and right respectively.

right-most $\lambda_{\mathrm{MS}^{\mathrm{Fast}}}$ will be $\mathbf{q}_R$. The region between these waves is often referred to as the star region and is denoted $\mathbf{q}^*$. The solution in this region is complicated by the interaction of the different waves described in Sec. 3.4. The simplest interactions of the different waves come in three general forms. The first we will define and discuss are shock waves. Then we will discuss rarefaction waves, and finally contact discontinuities which always arise from the presence of matter waves λ_{M}.

For the next several sections, for simplicity, we assume that the conservation vector $\mathbf{q}$ is comprised of one element, $q = q(t, x)$. As we have seen, the advection equation has a constant flux and is therefore not suitable to use as an example for more complicated waves. We use an illustrative example of the shock and rarefaction solutions by using the one dimensional inviscid Burger's equation [122],

$$\partial_t q + \partial_x \frac{q^2}{2} = 0. \tag{3.70}$$

The Burger's equation has characteristics $\lambda = q$.

3.6.1 Shocks

One class of solution to the Riemann problem are known as shock waves. Shocks are defined as locations where characteristic lines converge. To produce a shock in Burger's equation (3.70), we use initial data (3.68) with $\mathbf{q}_{\mathrm{L}} > \mathbf{q}_{\mathrm{R}}$. We see that in this case the characteristics on the left move faster than those on the right, and thus the characteristic lines will converge. An example of a shock forming from discontinuous initial data can be seen in Fig. 3.4, where the shock (green line) originates at $x = 0$ with slope $s = 0.5$.

Physically, shock waves are thin transitions from supersonic to subsonic flow which involve compression and dissipation [130]. A propagating wave in an ideal compressible fluid may lead to an infinite gradient within a finite amount of time. The part of the domain where the gradient blows up is referred to as a shock. The fluid close to either side of the shock may be considered uniform due to the thinness of the shock region.

Shock waves have velocities that may be determined by the so-called Rankine–Hugoniot jump condition, which are the conditions that relate the flux of the state quantities across a discontinuity [93, 122]. For relativistic fluid systems the Rankine–Hugonoit jump conditions are described in detail in Majorana [131], or Anile [50].

The Rankine–Hugoniot jump condition for an ideal fluid considers a steady flow across a jump in

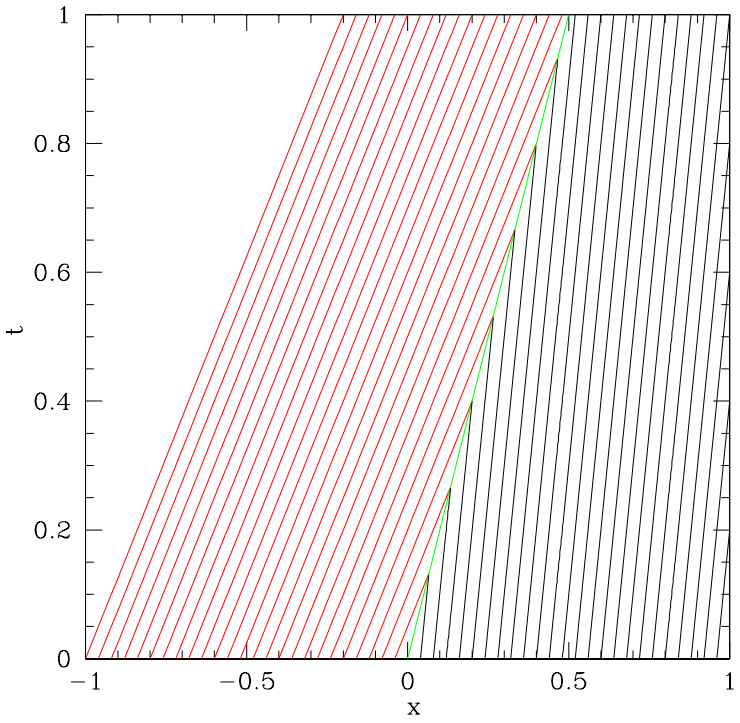

Figure 3.4: An example of a shock wave characteristic diagram for Burger's equation $\partial_t q + \partial_t(q^2/2) = 0$, with initial data; $q(x,0) = 0.8$ if $x < 0$, $q(x,0) = 0.2$, if $x \geq 0$. In this case the shock wave moves with speed, s, determined by the Rankine–Hugonoit jump conditions. For the Burger's equation we have, $s = \frac{f(q_{\rm R}) - f(q_{\rm L})}{q_{\rm R} - q_{\rm L}} = 0.5$ which is evident since the characteristic lines converge on the $t = x/s$ line (green).

initial data demanding a conservation of baryon density Eqn. (2.47), energy-momentum Eqn. (2.48). We consider the integral solution (3.67); if we let the the interval of integration be small enough such that the variation of the variables and flux over the integrals is small we can write

$$\Delta x\, \mathbf{q}_{\mathrm{L}} - \Delta x\, \mathbf{q}_{\mathrm{R}} = \Delta t\, \mathbf{f}(\mathbf{q}_{\mathrm{R}}) - \Delta t\, \mathbf{f}(\mathbf{q}_{\mathrm{L}}) + O(\Delta t^2). \tag{3.71}$$

The term $O(\Delta t^2)$ includes the variations of the conserved quantities and the flux. Looking at an infinitesimal time step, Δt, we have a velocity, $s = \frac{dx}{dt}$. The velocity may be re-written as $\Delta x = s\Delta t$. This leaves us with

$$s(\mathbf{q}_{\mathrm{L}} - \mathbf{q}_{\mathrm{R}}) = \mathbf{f}(\mathbf{q}_{\mathrm{L}}) - \mathbf{f}(\mathbf{q}_{\mathrm{R}}), \tag{3.72}$$

from which the shock speed, s, may be determined. This is the only allowable shock speed. In general the shock speed will be a function of time; however, in this development the time step was assumed to be small enough that we can ignore this variation.

Using this information we then have the solution for the Burger's equation with discontinuous initial conditions that lead to a shock wave,

$$q(t,x) = \begin{cases} q_{\mathrm{L}}, & x - st < 0; \\ q_{\mathrm{R}}, & x - st > 0. \end{cases} \tag{3.73}$$

For the Burger's equation the shock speed (3.72), is determined to be,

$$s = \frac{1}{2}\frac{q_{\mathrm{L}}^2 - q_{\mathrm{R}}^2}{q_{\mathrm{L}} - q_{\mathrm{R}}} = \frac{1}{2}\left(q_{\mathrm{L}} + q_{\mathrm{R}}\right). \tag{3.74}$$

3.6.2 Rarefaction Waves

Another class of solution to the Riemann problem are known as rarefaction waves. The characteristics of a rarefaction wave emanate from the discontinuity, spreading out, as illustrated by the blue lines that originate at the origin in Fig. 3.5. Rarefaction waves expand with time, reducing pressure, and usually follow in the wake of a shock wave. For a rarefied wave solution to Burgers equation we use initial data as seen in Eqn. (3.68) with $\mathbf{q}_L < \mathbf{q}_R$. We see that in this case the

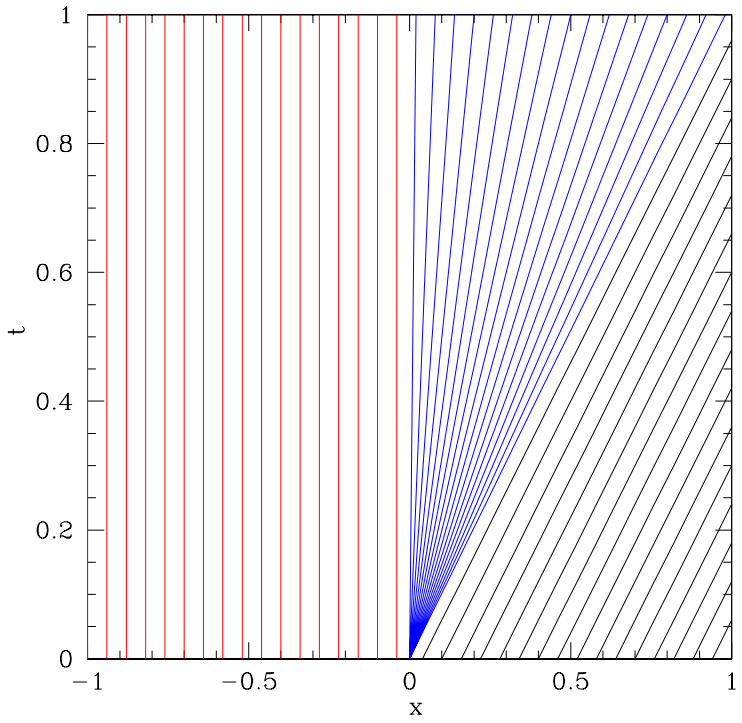

Figure 3.5: A rarefaction wave characteristic diagram for Burger's equation $\partial_t q + \partial_t(q^2/2) = 0$, with initial data $q(x,0) = 0.2$, if $x < 0$, $q(x,0) = 0.8$, if $x \geq 0$. In this case the characteristic structure obeys $q(x,t) = 0.2$, if $x < 0$, $q(x,t) = x/t$ if $0 \leq x \leq t$, or $q(x,t) = 0.8$, if $x \geq 0.8t$. The rarefaction is coloured blue.

characteristics on the left move slower than those on the right, and thus the characteristic lines will diverge. If we attempt to use the Rankine–Hugoniot jump conditions with this initial data the result will be shock waves emanating from the discontinuity. This solution is both unphysical and mathematically unstable. For a discussion on the unstable solution we refer the reader to [122, 132]. To derive the physical solution, we change the initial data to introduce a smooth interpolated region connecting the left and right data. We depict the modified data in Fig. 3.6.

The initial data is now,

$$q(0,x) = \begin{cases} q_{\mathrm{L}}, & x \leq x_{\mathrm{L}}; \\ q_{\mathrm{L}} + \frac{q_{\mathrm{L}} - q_{\mathrm{R}}}{x_{\mathrm{L}} - x_{\mathrm{R}}}(x - x_{\mathrm{L}}), & x_{\mathrm{L}} < x < x_{\mathrm{R}}; \\ q_{\mathrm{R}}, & x \geq x_{\mathrm{x}}. \end{cases} \tag{3.75}$$

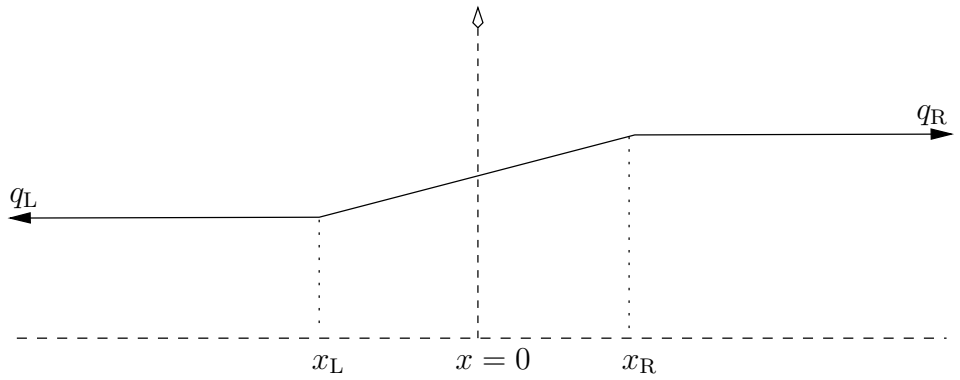

Figure 3.6: We change the initial data for a rarefied wave. Instead of a sharp discontinuity at the origin we introduce interpolated data connecting the two sides. We recover the original initial data by taking the limit as $x_{\mathrm{L}} \to 0$ and $x_{\mathrm{R}} \to 0$.

The wave on the left side is the head of the rarefaction wave, and is governed by the usual characteristic equation,

$$x = x_{\mathrm{L}} + \lambda(q_{\mathrm{L}})t, \tag{3.76}$$

while the right is the tail of the rarefaction wave with the characteristic equation,

$$x = x_{\mathrm{R}} + \lambda(q_{\mathrm{R}})t. \tag{3.77}$$

The full solution of the system is then,

$$q(t,x) = \begin{cases} q_{\mathrm{L}}, & x - x_{\mathrm{L}} < \lambda_{\mathrm{L}} t; \\ \frac{x - x_{\mathrm{L}}}{t}, & \lambda_{\mathrm{L}} t < x - x_{\mathrm{L}} < \lambda_{\mathrm{R}} t; \\ q_{\mathrm{R}}, & x - x_{\mathrm{R}} > \lambda_{\mathrm{R}} t. \end{cases} \tag{3.78}$$

This is the solution to the interpolated problem. To get the solution to the original problem with the discontinuity at the origin, we take the limit $x_{\mathrm{L}} \to 0$ and $x_{\mathrm{R}} \to 0$. The structure of the rarefaction solution is unaltered in this limit [132],

$$q(t,x) = \begin{cases} q_{\mathrm{L}}, & x < \lambda_{\mathrm{L}} t; \\ \frac{x}{t}, & \lambda_{\mathrm{L}} t < x < \lambda_{\mathrm{R}} t; \\ q_{\mathrm{R}}, & x > \lambda_{\mathrm{R}} t. \end{cases} \tag{3.79}$$

This solution is both physical and stable [132]. We may interpret this solution as the value of q being all solutions between q_{L} and q_{R} at the discontinuity. Thus the characteristics λ take on all values between λ_{L} and λ_{R}. Larger values propagate faster than lower values so the discontinuity degrades immediately to a centered rarefied wave [132].

Centered rarefied waves are also known as similarity solution. Similarity solutions have the form;

$$q(x,t) = \hat{q}\left(\frac{x}{t}\right) = \hat{q}\left(\tilde{x}\right), \tag{3.80}$$

and are constant along any ray $x/t = \mathrm{Const}$. Using the similarity solution we substitute Eqn. (3.80) into the linearized conservation equation (3.2) to get;

$$\partial_t q(t,x) + \frac{df}{dq}\partial_x q(t,x) = -\frac{x}{t^2}\hat{q}' + \frac{df}{dq}\frac{1}{t}\hat{q}' = 0, \tag{3.81}$$

where $\hat{q}' = \partial\hat{q}/\partial\tilde{x}$.

Equation (3.81) has two possible solutions,

$$\hat{q} = \mathrm{Const}, \tag{3.82}$$

or

$$\frac{df}{dq}\left(\hat{q}\left(\tilde{x}\right)\right) = \frac{x}{t}. \tag{3.83}$$

Using Eqn. (3.83) we can determine the solution for a centered rarefaction wave [122].

3.6.3 Contact Discontinuities

The last solution to the Riemann problem that we discuss are known as contact discontinuities. A contact discontinuity is defined by an abrupt jump in fluid density with no pressure gradient across the jump. When a contact discontinuity forms it is stationary in the fluid's reference frame.

Contact discontinuities arise when the characteristics for the system are parallel, neither diverging or converging, and do not create entropy, but rather separate regions of different entropic value. Due to the fact that contact discontinuities separate the regions of different entropy they are often referred to as entropy waves, since they carry information about the entropy increase. Physically, these will occur when two opposing shocks intersect [133].

These are all the possible basic waveforms for the simple Burger's equation. When studying systems with nonlinear fluxes combinations of these waves may exist in a single problem. This is typical in shock tube tests studied in hydrodynamics. We discuss these further in Chap. 4 when we apply tests to our code. An example of such a solution may be seen in Fig. 4.3. We now briefly describe the numerical solution of the exact Riemann problem.

3.7 The Riemann Problem: Exact Solutions

We present a simplified description of the exact solution here, a full description may be found in [49]. The exact solution to the special relativistic hydrodynamic Riemann problem was first found by Martí *et al.* [46], followed by Giacomazzo *et al.* [49], who derived the exact solution for special relativistic magnetohydrodynamics. To solve for the magnetohydrodynamic system of equations exactly, they use the shock and rarefaction behaviour of the system of equations at each the discontinuities. If the discontinuity is a shock the solution is determined by a relatively simple set of algebraic expressions. In the event of a rarefaction wave the solution is more complicated since they were required to solve a system of ODEs. The final step is to use matching conditions to connect the fluid variables across the discontinuity. In Fig. 3.3 only $\lambda_{\rm M}$ will be a contact discontinuity. The matching conditions will determine the value of the intermediate state, $\mathbf{q}^*_{\rm L} = \mathbf{q}_3$, $\mathbf{q}^*_{\rm R} = \mathbf{q}_4$, that exists on either side of the contact discontinuity seen in Fig. 3.3.

Giacomazzo *et al.* call this approach the P_t-method, since the intermediate state and the determination of the discontinuity type (shock or rarefaction) is dependent only on the total pressure (magnetic pressure plus thermal pressure). They switch methods when they come to the contact discontinuity due to the complicated nature of MHD waves. By continuing to use the total pressure they find that the method needed to solve the matching conditions are too sensitive to the initial guesses. To rectify this they specify the values of the variables on either side of the contact discontinuity in terms of the transverse components of the magnetic field. For complete details

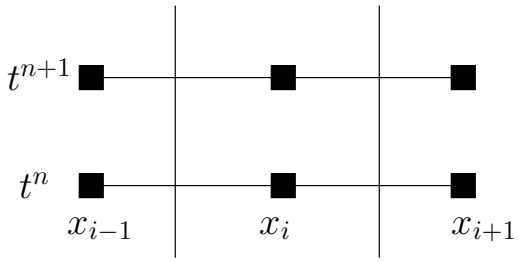

Figure 3.7: A sample one dimensional discretization, the temporal discretization is denoted by the current time step, t^n, and the advanced time step t^{n+1}. The spatial discretization denotes the current spatial location, x_i. The solid vertical lines denote a cell interface.

including the system of equations used for the exact special relativistic MHD method we refer the reader to [49].

The exact solver is computationally expensive [48, 134], so to perform a parameter survey more efficiently we use approximate Riemann solvers as discussed in Sec. 3.8.3. The exact solver is useful for testing how well approximate Riemann solvers capture shocks. We do not implement our own exact solver, but use Giacomazzo *et al.* 's solver to test the shock capturing capabilities of our code. The results from these tests may be seen in Chap. 4.

3.8 The Godunov Method

Methods that break down the domain into finite volumes and treat the interface between each volume as a Riemann problem are known as Godunov methods. We give a general overview of the Godunov method below, and the specific details are described in Sec. 3.8.1. For simplicity we outline the problem using two dimensions, such that, $\mathbf{q} = \mathbf{q}(t, x)$. We use the discretization notation described in Chap. 1, and seen in Fig. 3.7 such that the current discrete time level is denoted, t^n and the advanced time level is denoted t^{n+1}. The spatial discretization is denoted x_i. The cell centers are located at x_i, while the cell interfaces surrounding that cell are locates at $x_{i\pm1/2}$.

To solve Eqn. (3.67) using Godunov-type methods, we start by dividing the computational domain, V (of arbitrary spatial dimension), into finite volumes, ΔV_m, such that $V = \bigcup_m \Delta V_m$. The next step is to define cell averaged quantities, $\mathbf{Q}_i^n$ at the cell centers for time level t^n,

$$\mathbf{Q}_i^n \equiv \frac{1}{\Delta V} \int_{\Delta V} \mathbf{q}(t^n, x) dV. \tag{3.84}$$

Then we extrapolate the variables at the cell centre to the cell interface. In Fig. 3.1 this would require that we extrapolate the data from cell centre $Q(t^n, x_i)$ to the right side of the interface located at $x_{i+1/2}$, denoted $Q_{\mathrm{R}}(t^n, x_{i+1/2})$, and the values at $Q(t^n, x_{i+1})$ to the left side of the cell interface located at $x_{i-1/2}$, denoted $Q_{\mathrm{L}}(t^n, x_{i-1/2})$. The techniques used to perform the interpolation are discussed in Sec. 3.8.2. We now focus on discretizing the surface integral using the surface of the cell.

The temporal integrals over the flux integrals are not, in general, easily solved. Godunov [121] proposed a first order method to approximate the flux integrals by replacing the conservative quantities $\mathbf{Q}(t, x)$ with piecewise constant functions. His approach treats each cell interface as an individual, or local, Riemann initial value problem. As long as the waves from adjacent cells do not interact, each local Riemann problem can be solved exactly. The solutions to the local Riemann problems are treated as constant in time which allows us to approximate the flux integrals, $F^n_{i+1/2}$,

$$\int_{t^n}^{t^{n+1}} \oint \mathbf{f}^j(\mathbf{q}(t, x_{i+1/2}) dS_j dt = \Delta t \oint \mathbf{F}^j_{i+1/2} dS_j. \tag{3.85}$$

We discretize the surface integrals in Eqn. (3.67) and (3.85),

$$\oint_{\Delta S_j} F^j dS_j = \sum F^j \Delta S_j \tag{3.86}$$

for an arbitrary cell index. The sum is over all surfaces bounding the cell. We approximate the source integral as

$$\hat{\mathbf{s}}^n_i \Delta x \Delta t = \int_{\Delta t} \int_{\Delta V} \mathbf{s}(\mathbf{q}(t^n, x_i)) dx dt. \tag{3.87}$$

We perform the temporal integral in (3.67),

$$\int_{\Delta t} \frac{d\mathbf{Q}(t, x_i)}{dt} = \mathbf{Q}(t^{n+1}, x_i) - \mathbf{Q}(t^n, x_i) = \mathbf{Q}^{n+1}_i - \mathbf{Q}^n_i, \tag{3.88}$$

where t^{n+1} denotes the advanced time step.

We then write the complete discretized form of (3.67) in one dimension using Eqns. (3.84), (3.85), (3.86), (3.87), and (3.88) to get,

$$\mathbf{Q}^{n+1}_i = \mathbf{Q}^n_i - \frac{\Delta t}{\Delta x} \left(F_{i+1/2} - F_{i-1/2} \right) + \Delta t \, \hat{s}. \tag{3.89}$$

Where in one dimension in Cartesian coordinates $\Delta S = 1$, and $\Delta V = \Delta x$. Eqn. (3.89) is the final discretized form for the Godunov method.

For full details on the Godunov method we refer the reader to LeVeque [122] or Font [20].

The logical flow of the Godunov method and the generalized methods based on the Godunov method goes as follows;

- First, using the cell averaged quantities, we construct a piecewise constant function, used to approximate the value of the cell at each interface depending on the values of surrounding cells. In the literature this is known as reconstruction.
- Next, we solve the Riemann problem at the cell interfaces.
- Finally, we time evolve the state $Q(t^n, x)$ to the solution $Q(t^{n+1}, x)$ using an explicit numerical integration technique.

This is the basis of the Godunov method, and as long as we adhere to these steps, we may modify any of them to extend Godunov's method to higher order methods. The benefits of Godunov's method are that this method is stable, conservative, and handles shocks. There are two drawbacks to using Godunov's original method; first, by itself, this method is only first order accurate, and the second drawback is that the solution of the full Riemann problem may be computationally expensive, particularly when studying general relativistic magnetohydrodynamics. To circumvent these limitations we consider more sophisticated high-resolution shock-capturing methods. To increase computational efficiency of the method, we introduce approximate Riemann solvers. We outline three such methods in section 3.8.3; the Roe solver, a relativistic Harten–Lax–van Leer (HLL) solver, and the Lax–Friedrichs method.

We now explicitly describe the relativistic form used for the Godunov-type schemes, they are more complicated than the method outlined above.

3.8.1 The Relativistic Godunov Scheme

Due to the subtleties when extending the Godunov scheme to relativistic systems, we outline the method here.

In (2.108) we saw the set of nonlinear conservation laws for general relativistic magnetohydro-

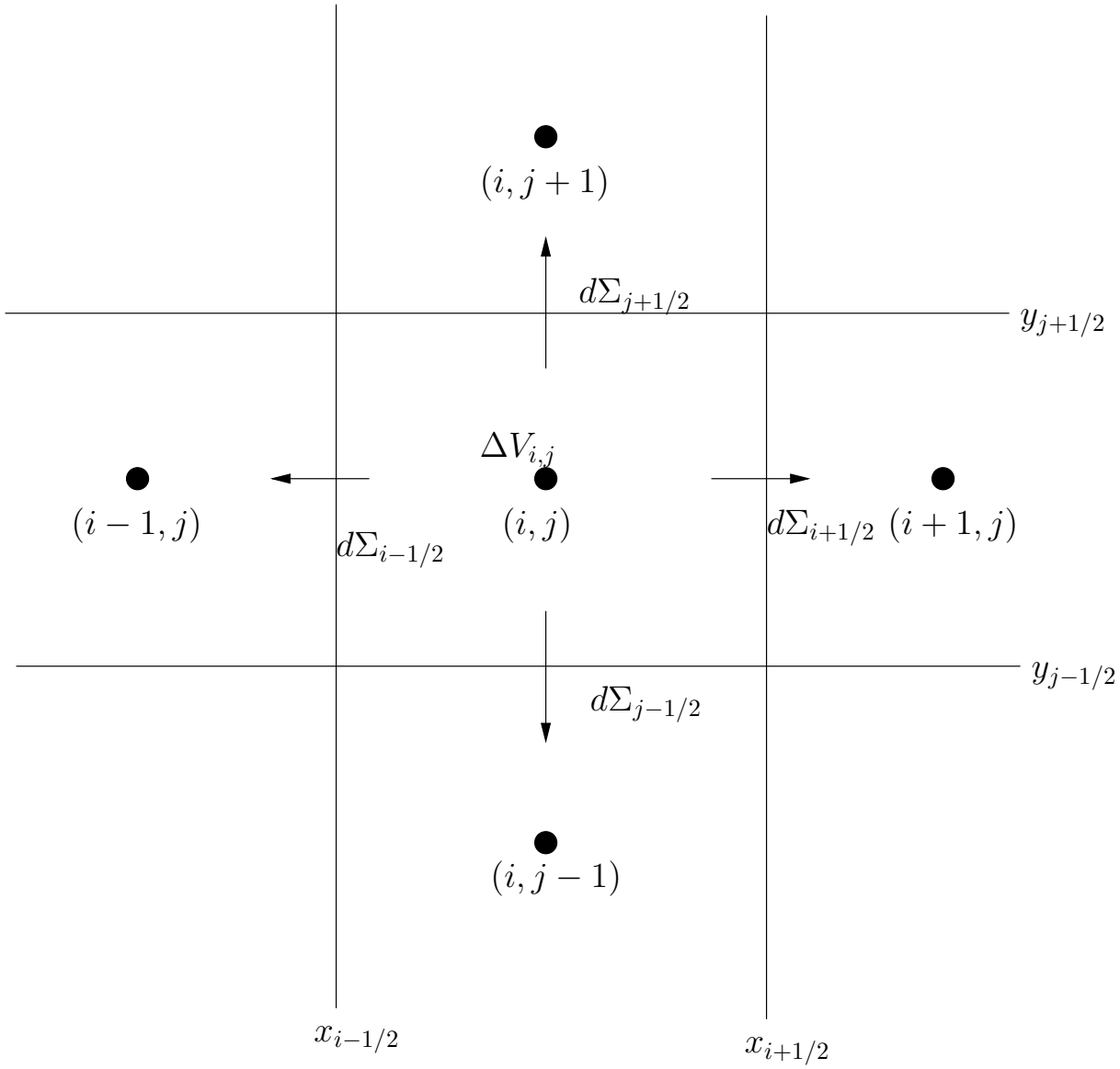

Figure 3.8: The 2D cell for the finite volume method. The cell volume $\Delta V_{i,j} = (x^1_{i+1/2} - x^1_{i-1/2})(x^2_{j+1/2} - x^2_{j-1/2})$, is defined for the cell containing the point (i, j) with a cell surface elements $d\Sigma$ bounding the cell as labelled above. The flux of the conservative equations are calculated at the centre of the cell interfaces, denoted by the location of the arrows.

dynamics are written in general as:

$$\frac{1}{\sqrt{-g}}\frac{\partial}{\partial t}\sqrt{\gamma}\,\mathbf{q} + \frac{1}{\sqrt{-g}}\frac{\partial}{\partial x^i}\sqrt{-g}\,\mathbf{f}^i(\mathbf{q}) = \mathbf{s}(\mathbf{q}), \tag{3.90}$$

where g is the determinant of the 4-metric, γ is the determinant of the 3-metric as defined in Chap. 2. $\mathbf{q}$ is the vector of conservative variables, $\mathbf{f}$ is the set of fluxes for the corresponding conserved variable, and $\mathbf{s}$ is the vector of source terms also defined in Chap. 2. We require the integral form of this equation, so just as in the general method presented in Sec. 3.8.1 we integrate Eqn. (3.90) over some small cell or volume, ΔV, of spacetime,

$$\int_{\Delta V}\frac{1}{\sqrt{-g}}\frac{\partial}{\partial t}\left(\sqrt{\gamma}\,\mathbf{q}\right)dV^{(4)} + \int_{\Delta V}\frac{1}{\sqrt{-g}}\frac{\partial}{\partial x^i}\left(\sqrt{-g}\,\mathbf{f}^i(\mathbf{q})\right)dV^{(4)} = \int_{\Delta V}\mathbf{s}(\mathbf{q})dV^{(4)}, \tag{3.91}$$

where $dV^{(4)} = \sqrt{-g}dx_0dx_1dx_2dx_3$. For relativistic systems the cell average is defined to be [20],

$$\mathbf{Q} \equiv \frac{1}{\Delta V^{(3)}}\int_{\Delta V}\mathbf{q}\Delta V^{(3)}, \tag{3.92}$$

with $\Delta V^{(3)} = \sqrt{\gamma}\Delta x_1\Delta x_2\Delta x_3$. We re-write the first term in Eqn. (3.91) as,

$$\int_{\Delta V}\frac{1}{\sqrt{-g}}\frac{\partial}{\partial t}\left(\sqrt{\gamma}\,\mathbf{q}\right)dV^{(4)} = \Delta V^{(3)}\int_{\Delta x_0}\frac{\partial}{\partial t}\mathbf{Q}\Delta V^{(3)}dx_0. \tag{3.93}$$

Next, using the divergence theorem, we re-write the second term in Eqn. (3.91) as,

$$\int_{\Delta V}\frac{1}{\sqrt{-g}}\frac{\partial}{\partial x^i}\left(\sqrt{-g}\,\mathbf{f}^i(\mathbf{q})\right)dV^{(4)} = \int_{\Delta x_0}\oint_{\partial V}\mathbf{f}(\mathbf{q})d\Sigma dx_0, \tag{3.94}$$

where $d\Sigma$ is normal to the surface of the finite volume ΔV. We approximate the surface integral,

$$\oint_{\partial V}\mathbf{f}^j(\mathbf{q})d\Sigma_j = \sum\mathbf{F}^j\Delta\Sigma_j \tag{3.95}$$

where the sum is over all surfaces bounding the volume element. We define $\Delta\Sigma_j = \sqrt{-g}dx_idx_k\epsilon_{ijk}$ such that the direction of the surface element is outward to the surface area in question. $\epsilon_{ijk} = \sqrt{-g}[ijk]$ is the relativistic Levi–Civita totally antisymmetric tensor. We have also defined

$$\mathbf{F}^i(\mathbf{q}) = \frac{1}{\Delta x_0}\int_{\Delta x_0}\mathbf{f}^i(\mathbf{q})dx_0, \tag{3.96}$$

the time averaged flux.

Our last step with respect to the spatial integrals, is to approximate the integral of the source term,

$$\int_{\Delta V} \mathbf{S}(\mathbf{q}) dV^{(4)} = \int_{\Delta x_0} \hat{\mathbf{S}}(\mathbf{q}) \Delta V^{(4)} dx_0, \tag{3.97}$$

where we write $\hat{\mathbf{S}}(\mathbf{q})\Delta V^{(4)} = \int_{\Delta V^{(3)}} \mathbf{S}(\mathbf{q})\sqrt{-g} dx_1 dx_2 dx_3$. Now we approximate the time integration

$$(\mathbf{Q}\Delta V^{(3)})^{n+1}_{i,j} - (\mathbf{Q}\Delta V^{(3)})^{n}_{i,j} + \Delta x_0 \sum_j \Delta\Sigma_i \mathbf{F}^i_j(\mathbf{q}) = \hat{\mathbf{S}}^n_{i,j} \Delta V^{(4)}, \tag{3.98}$$

and assumed that the evolution is over such a short period of time that the sources and fluxes remain constant in time. The sum over j in (3.98) is the sum of the fluxes over all cell faces, $d\Sigma_{i+1/2}$, $d\Sigma_{i-1/2}$, $d\Sigma_{j+1/2}$, $d\Sigma_{j-1/2}$ as seen in Fig. (3.8). When considering stationary spacetime metrics, the volume elements are independent of time, so we can easily write the final form of the approximate solution of Eqn. (3.90),

$$\mathbf{Q}^{n+1}_{i,j} = \mathbf{Q}^n_{i,j} - \frac{\Delta x_0}{\Delta V^{(3)}} \sum_{i,k} \Delta\Sigma_i \mathbf{F}^i_k(\mathbf{q}) + \hat{\mathbf{S}}(\mathbf{q}) \frac{\Delta V^{(4)}}{\Delta V^{(3)}}. \tag{3.99}$$

The quantity $\mathbf{Q}^{n+1}_{i,j}$ is the advanced time value of the cell average quantity for cell (i, j). To handle the flux time integral in Eqn. (3.96) without explicitly performing the integral, we rely on approximations such as the Roe solver, Harten–Lax–van Leer, or the Lax–Friedrichs methods. These methods are described in Sec. 3.8.3.

In the remaining parts of this section, we describe the different cell interface reconstruction techniques used, as well as implementation notes, followed by the flux approximations used to solve the system described by Eqn. (3.99), also with implementation notes. We then describe the integration methods used and the different boundary conditions used along with implementation notes. We end this chapter with a discussion of other numerical techniques that are often needed to ensure a viable solution.

3.8.2 Variable Reconstruction at Cell Boundaries

Before we can evaluate the flux approximations described above, we require the values of the state vectors, $\mathbf{q}$, at the cell interface. First we introduce the piece-wise constant method used by Godunov. To obtain the values of the state vectors for our system we use the piecewise linear

method[11] for the cell reconstruction. This method typically uses one of two techniques to prevent spurious oscillations from appearing during the reconstruction; the minmod limiter or the monotised central limiter.[12]

Piecewise Constant Method

The piecewise constant method is the simplest way to reconstruct the cell interface. Consider Fig. 3.1: to reconstruct the cell value on the left and right of the interface at x_{i+1}, we use,

$$\mathbf{q}^{\mathrm{L}}_{i+1/2} = \mathbf{q}_i \tag{3.100}$$

$$\mathbf{q}^{\mathrm{R}}_{i+1/2} = \mathbf{q}_{i+1}. \tag{3.101}$$

This method was used by Godunov in his original prescription [121] and results in first order accurate solutions. To increase spatial accuracy, higher order techniques are used for the cell reconstruction, but all of them revert to the piecewise constant method when reconstructing cells that are in the presence of extrema and shocks.

Piecewise Linear Method

The algorithm for piecewise linear method looks for the minimum slope within surrounding cells to extrapolate the value of the state vector $\mathbf{q}$ at the cell centre to the cell interface. By choosing the minimum slope to extrapolate the variables we smooth the data used to calculate the fluxes while minimizing the possibility of introducing unphysical oscillations into the system.

Looking at Fig. 3.9, when using this method to reconstruct a cell interface, we require information of the states in four surrounding cells. To find the reconstructed state at the interface $x_{i-1/2}$, the left interface of cell q_i, we use the cells labeled q_{i-1}, q_i, q_{i+1} to calculate the slopes s_2, s_3, then uses the minmod algorithm (Eqn. (3.102)) to determine which slope is a minimum of the two. The line with the minimal slope is used to reconstruct the variable at that interface. The concise algorithm is shown in Eqn. (3.102). In the event that we are reconstructing a state near an extremum, the minmod algorithm returns a zero slope which indicates that the reconstruction reduces to the piecewise constant method described above. Likewise, to find the reconstructed

[11] We are aware of the higher order piecewise parabolic method [135], but chose not to implement it in this study.
[12] Other techniques do exist but are not as commonly used in relativistic studies. We refer the reader to LeVeque [122] for a detailed discussion of the existing methods.

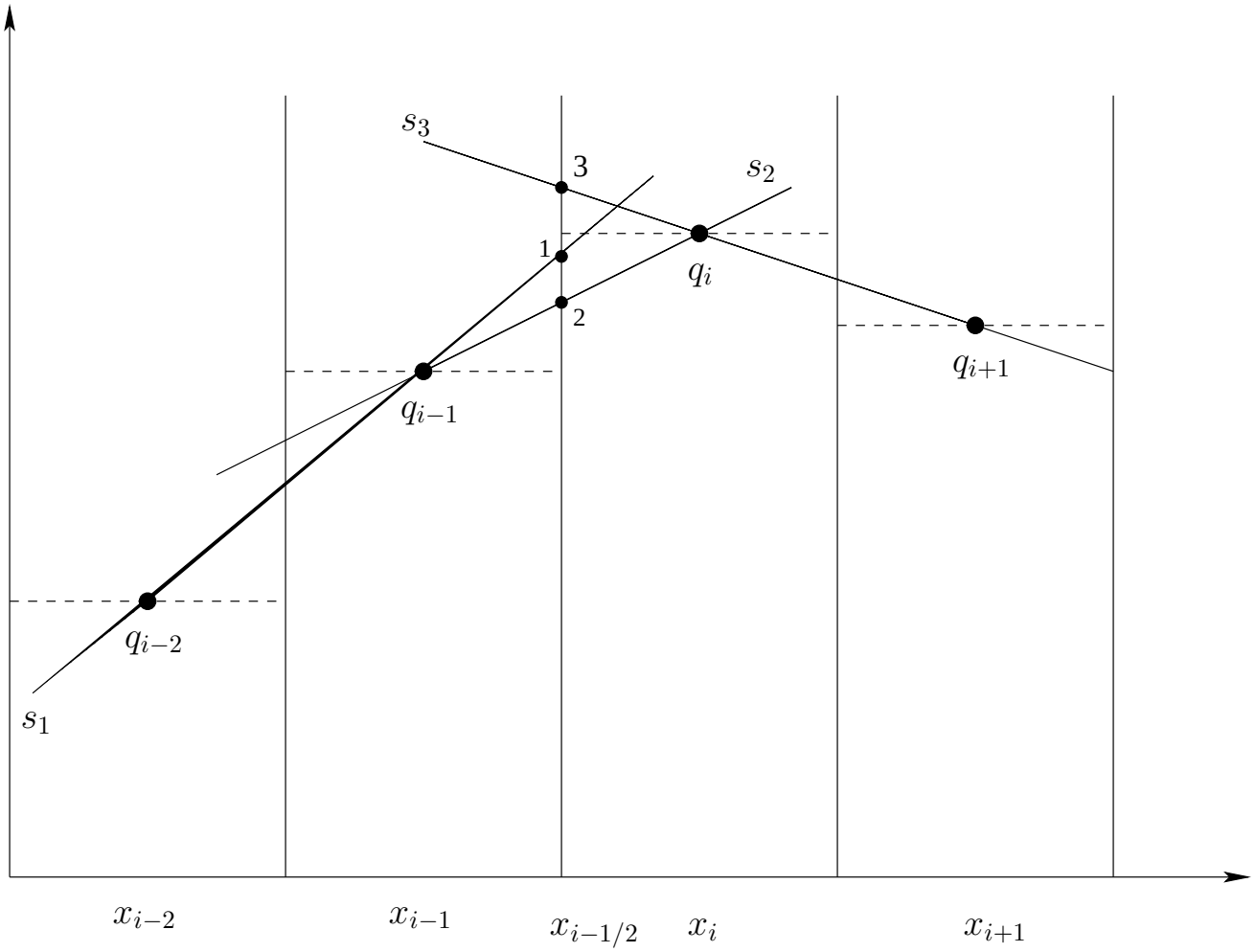

Figure 3.9: To reconstruct the value at the cell face denoted $x_{i-1/2}$ from the left, we use the cells q_{i-2}, q_{i-1} to calculate the slope of the line s_1, and q_{i-1}, q_i to calculate the slope of the line s_2. When we have the slope we determine which of the two has the minimum slope. The line with the minimum slope is used to calculate the quantity $q_{i-1/2}$ of the left side of the cell interface $x_{i-1/2}$. In the diagram above, the quantity $q_{i-1/2}$ is determined at the point labeled 2, as calculated using the line labeled s_2. To calculate the cell face $x_{i-1/2}$ from the right, we follow a similar procedure using the cell values q_{i-1}, q_i, q_{i+1}. In this case, the slopes of the lines s_2 and s_3 are of opposite signs, so we take the value of the cell q_i to be the value of the cell interface from the right, to prevent the production of local extrema in this method. This special case occurs near shocks and extrema, which reduces the order of the method to first order. See the text for a detailed description.

value of the $x_{i-1/2}$ interface for the cell q_{i-1}, we use cells q_{i-2}, q_{i-1}, q_i to find slopes s_1, s_2, then use the minmod limiter to select the correct slope;

$$\text{minmod(a, b)} = \begin{cases} a, & \text{if } |a| < |b|; \\ b, & \text{if } |b| < |a|; \\ 0, & \text{if } ab \leq 0. \end{cases} \tag{3.102}$$

The limiters are introduced to prevent the oscillations that will occur when the reconstruction produces new local maxima. Referring to Fig. 3.9, we see that the reconstructed value q_{L} at the coordinate point $x_{i-1/2}$ is calculated by

$$q_{\text{L}} = q_{i-1} + \sigma_1(x_{i-1/2} - x_{i-1}) \tag{3.103}$$

and the value q_{R} at the same coordinate point is

$$q_{\text{R}} = q_i - \sigma_2(x_{i-1/2} - x_i), \tag{3.104}$$

where $\sigma_1 = \text{minmod}(\text{s}_1, \text{s}_2)$ and $\sigma_2 = \text{minmod}(\text{s}_2, \text{s}_3)$. In this particular configuration, we see that if we were to consider linear extrapolations alone, we are at risk of producing a non-monotonic value such as the point labelled 3. The minmod limiter will reconstruct that value by using the piecewise constant reconstruction value q_i for that cell.

Instead of using the minmod limiter we can use the monotized central difference (MC) limiter. This method acts with the same arguments but is modified such that it does not reduce the slope as dramatically as the standard minmod method.

$$\text{MC(a, b)} = \begin{cases} 2a, & \text{if } |a| < |b| \text{ and } 2|a| < |c|; \\ 2b, & \text{if } |b| < |a| \text{ and } 2|b| < |c|; \\ c, & \text{if } |c| < 2|a| \text{ and } |c| < 2|b|; \\ 0, & \text{if } ab \leq 0, \end{cases} \tag{3.105}$$

where

$$c = \frac{(a+b)}{2}.$$

We compare the minmod and MC algorithms in chapter 4, Figs. 4.6 and 4.7.

With the variables reconstructed at the cell interfaces, we can now calculate the flux across the cell interface, where we perform the flux approximations.

3.8.3 Flux Approximations

There are several different techniques used to approximate flux calculations in Eqn. (3.96), to replace the exact Riemann solver. The techniques we used through this research were the Roe solver, Harten–Lax–van Leer, and Lax–Friedrichs. We describe these methods below. For simplicity we assume the system we are approximating is one dimensional, and expressed in Cartesian coordinates. All flux approximations will be calculated at the cell interfaces, *e.g.* $x_{i+1/2}$, we drop the grid index for notational simplicity.

Roe's Method

Roe's linearized solver approximates the conservation equations by using the linearized form,

$$\partial_t \mathbf{q} + \partial_i \mathbf{f}^i(\mathbf{q}) = 0 \rightarrow \tag{3.106}$$

$$\partial_t \mathbf{q} + A^i \partial_i \mathbf{q} = 0 \tag{3.107}$$

where $A^i = \partial \mathbf{f}^i / \partial \mathbf{q}$ is the Jacobian for the i-th direction flux vector. Roe's method treats the Jacobian for the system as a constant Jacobian matrix. This matrix is a function of the data states $\mathbf{q}_\mathrm{L}$ and $\mathbf{q}_\mathrm{R}$. We will denote the Roe approximate Jacobian matrix as a function of the initial state vectors $\mathbf{q}_\mathrm{L}$ and $\mathbf{q}_\mathrm{R}$ by $\bar{A}^i = \bar{A}^i(\mathbf{q}_\mathrm{L}, \mathbf{q}_\mathrm{R})$. The original system is replaced by an approximate Riemann problem,

$$\partial_t \mathbf{q} + \bar{A}^i \partial_i \mathbf{q} = 0 \tag{3.108}$$

Since the Jacobian matrix $\bar{A}^i$ is treated as a constant the linearized equation can be reduced to a set of scalar advection equations by diagonalizing the Jacobian;

$$\bar{A}^i = R^i \Lambda^i R^{-1i} = R^i \Lambda^i L^i, \tag{3.109}$$

$$R^{-1i} = L^i \tag{3.110}$$

where R^i denotes the matrix of right eigenvectors

$$R^i = \left[r^1|...|r^p\right] \tag{3.111}$$

such that $A^i r^p = \lambda r^p$ for a system of p equations. Likewise, L^i denote the matrix of left eigenvectors

$$L^i = \left[l_1|...|l_p\right]^{\mathrm{T}} \tag{3.112}$$

such that $l_p A^i = \lambda l_p$. We have also defined Λ^i,

$$\Lambda^i = \mathrm{diag}(\lambda_p^i) \tag{3.113}$$

as the diagonal matrix consisting of the eigenvalues of the Jacobian matrix. The relationship between the right, r^p, and left, l_p eigenvectors is $r^j \cdot l_i = \delta_i^j$.
Now we have

$$\partial_t \mathbf{q} + R\Lambda R^{-1}\partial_i \mathbf{q} = S(\mathbf{q}) \tag{3.114}$$

$$R^{-1}\partial_t \mathbf{q} + \Lambda R^{-1}\partial_i \mathbf{q} = R^{-1}S(\mathbf{q}) \tag{3.115}$$

$$\partial_t \omega + \Lambda \partial_i \omega = \mathcal{S}(\omega), \tag{3.116}$$

where the last expression is a decoupled set of linear equations which each have solution;

$$\omega^p(x,t) = \omega^p(x - \lambda_p t). \tag{3.117}$$

Each variable ω^p is known as a characteristic variable and is introduced only to produce a decoupled system of equations. In general, the ω^p will not have a direct physical interpretation. The full solution of (3.2) is a linear combination of the solutions in Eqn. (3.117) [122],

$$\mathbf{q}^j(x,t) = \sum_{p=1}^{n} R^{pj}\omega^p. \tag{3.118}$$

where R^{pj} denotes the jth element of the pth right eigenvector. Equation. (3.118) is an exact solution to the approximate Riemann problem. For this analysis to hold Roe [136] recorded criteria

for the construction of a Jacobian matrix;

1. $\bar{A}$ must be a linear mapping from $\mathbf{q}$ to $\mathbf{f}^i$
2. $\bar{A}(\mathbf{q}_\mathrm{L}, \mathbf{q}_\mathrm{R}) \rightarrow \partial\mathbf{f}/\partial\mathbf{q}$ smoothly as $\mathbf{q}_\mathrm{R}, \mathbf{q}_\mathrm{L} \rightarrow \mathbf{q}$
3. $\bar{A}(\mathbf{q}_\mathrm{L}, \mathbf{q}_\mathrm{R}) \cdot (\mathbf{q}_\mathrm{R} - \mathbf{q}_\mathrm{L}) = \mathbf{f}(\mathbf{q}_\mathrm{R}) - \mathbf{f}(\mathbf{q}_\mathrm{L})$
4. eigenvectors of $\bar{A}(\mathbf{q}_\mathrm{L}, \mathbf{q}_\mathrm{R})$ are linearly independent (diagonalizable with real eigenvectors)

where $\mathbf{q}_\mathrm{L}$ and $\mathbf{q}_\mathrm{R}$ are the left and right state vectors across a cell interface. Item two states that the approximate Jacobian must be consistent with the true Jacobian in the appropriate limit. The first, second, and fourth criteria are satisfied by defining the Jacobian matrix at the cell interface as a function of the average of the two states at the cell interface [33],

$$\bar{\mathbf{q}} = (\mathbf{q}_\mathrm{R} + \mathbf{q}_\mathrm{L})/2 \tag{3.119}$$

$$\bar{A}(\mathbf{q}_\mathrm{L}, \mathbf{q}_\mathrm{R}) \rightarrow \bar{A}(\bar{\mathbf{q}}). \tag{3.120}$$

This setup does not necessarily satisfy the third condition [136], but due to the relative simplicity, it is implemented in relativistic fluid codes [33] also used in the studies by Font *et al.* [1, 2, 3]. Once the criterion above is met the Jacobian may be treated as a matrix with constant coefficients, so we may diagonalize and solve the system of equations as outlined above in Eqns. (3.109) to (3.118).

With the solution of the approximate Riemann problem we can go on to determine the corresponding flux functions,

$$\mathbf{F} = \frac{1}{2}\left(\mathbf{f}(\mathbf{q}_\mathrm{R}) + \mathbf{f}(\mathbf{q}_\mathrm{L})\right) - \frac{1}{2}\sum_p |\lambda_p| \Delta\omega_p r_p, \tag{3.121}$$

where λ_p are the eigenvalues of the Jacobian and r_p are the associated eigenvectors [122]. $\Delta\omega_p$ are defined by jumps in the fluid variables along the interface;

$$(\mathbf{q}_\mathrm{R} - \mathbf{q}_\mathrm{L})^j = \Delta\omega_i R^{ij}, \tag{3.122}$$

which is easily solved when we invert the matrix of right eigenvectors, R^{pj} to obtain the matrix of

left eigenvectors $L^{jp} = \left(R^{pj}\right)^{-1}$,

$$\Delta\omega_i = (\mathbf{q}_\mathrm{R} - \mathbf{q}_\mathrm{L})^j R^{-1}_{ij}. \tag{3.123}$$

We can consider the flux approximation, (3.121), as an arithmetic average for the left and right flux, while adding a stabilizing correction term

$$-\frac{1}{2}\sum_p |\lambda_p| \Delta\omega_p r_p, \tag{3.124}$$

providing viscous dissipation [122]. The Roe scheme is the most costly of the approximate Riemann solvers we used, due to the fact that it requires a full spectral decomposition. This is particularly true for the general relativistic magnetohydrodynamic systems, where the eigenvectors are not known in closed form as they are in special relativistic hydrodynamics. We use numerical routines such as LAPACK [129] to perform the spectral decomposition. Despite the computational cost, this approximation is the approximate method that is least diffusive; consequently, it captures the discontinuities the best. This point is made clear in Chap. 4 when we use different methods to capture the Kelvin–Helmholtz instability using a setup described by Frank *et al.* [137] and Stone.[13]

The other flux approximations used in this work make use of only a few of the wave speeds, ignoring the information contained in the eigenvectors. By neglecting eigenvector information these flux calculations are much faster to compute, but only by sacrificing detailed knowledge of all the waves in the GRMHD system. We also note that in our implementation the Roe method breaks down when the eigenvectors become nearly degenerate, and cannot be used to handle all physical situations; in particular, we found that the method breaks down for extremely low pressure values. Thus in chapter 4 we were unable to use the Roe solver to solve the initial conditions used for Fig. 4.6 and 4.7.

HLL

The Harten–Lax–van Leer method is much faster than the Roe solver and still allows for a sharp capture of a shock or rarefaction [138]. This is seen in the Riemann shock tube tests performed by [122, 115] as well as our own code verification tests shown in Chap. 4 (*i.e.* Fig. 4.2). In this approximation, we use the two fastest characteristic velocities of the system to separate the system into three regions. The information about the other waves is not used for the flux approximations.

[13] http://www.astro.princeton.edu/~jstone/tests/kh/kh.html

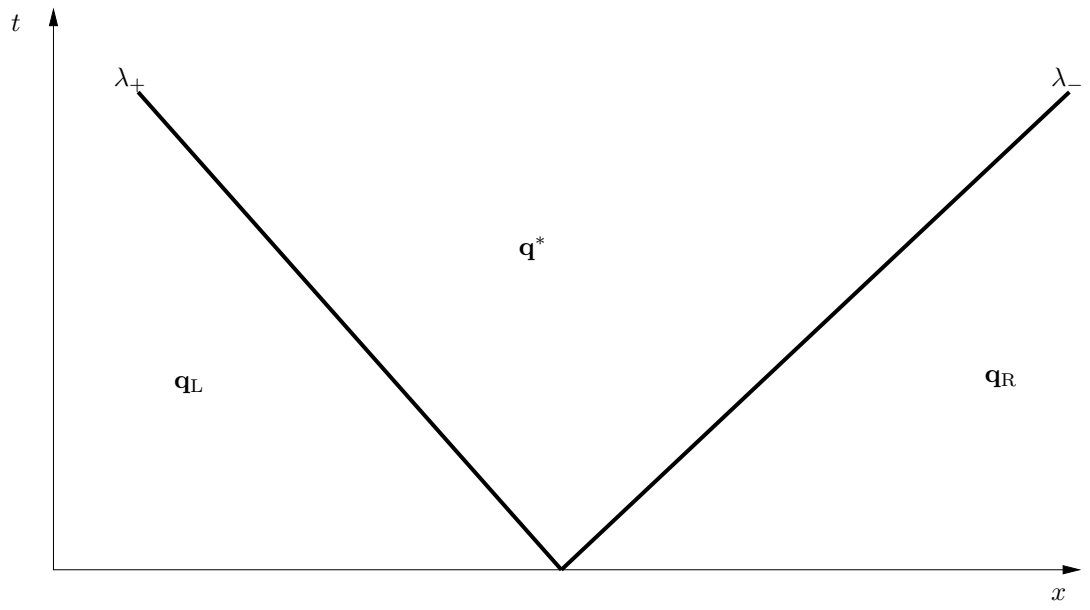

Figure 3.10: The characteristic fan for the HLL flux approximation. We only keep the extreme waves, which for the GRMHD case correspond to the fast magnetosonic waves. These waves split the solution into the left $\mathbf{q}_\mathrm{L}$ and right $\mathbf{q}_\mathrm{L}$ states, and a "star" state defined by Eqn. (3.126).

Referring to Fig. 3.3 we treat the information in the regions $\mathbf{q}_1 \rightarrow \mathbf{q}_6$ as a single state denoted $\mathbf{q}^*$. The characteristic fan used for the HLL flux approximation is found in Fig. 3.10 The disadvantage of this method is that it treats all waves travelling slower than the extreme wave speeds with lower resolution. In particular, for fluid systems, all the details for contact discontinuities (entropy waves) are ignored [122]. This solver separates the solution into three states; the left and right $(\mathbf{q}_\mathrm{L}, \mathbf{q}_\mathrm{R})$ as well as an intermediate or "star" state $\mathbf{q}^*$,

$$\mathbf{q}(x,t;\mathbf{q}_\mathrm{L},\mathbf{q}_\mathrm{R}) = \begin{cases} \mathbf{q}_\mathrm{L}, & \text{if } x < \lambda_- t; \\ \mathbf{q}^*, & \text{if } \lambda_- t \le x \le \lambda_+ t; \\ \mathbf{q}_\mathrm{R}, & \text{if } x > \lambda_+ t, \end{cases} \tag{3.125}$$

where

$$\mathbf{q}^* = \frac{\lambda_+ \mathbf{q}_\mathrm{R} - \lambda_- \mathbf{q}_\mathrm{L} - \mathbf{f}(\mathbf{q}_\mathrm{R}) + \mathbf{f}(\mathbf{q}_\mathrm{L})}{\lambda_+ - \lambda_-} \tag{3.126}$$

denotes the value of the intermediate state, the state in the region between the fastest right and fastest left wave. Implementing this algorithmically, we define,

$$\lambda_+ = \max(0, \lambda_\mathrm{R}, \lambda_\mathrm{L}) \tag{3.127}$$

$$\lambda_- = \min(0, \lambda_\mathrm{R}, \lambda_\mathrm{L}), \tag{3.128}$$

where λ_+ is a right-going wave characteristic, and λ_- is a left-going wave characteristic. λ_L are the eigenvalues of $A(\mathbf{q}_\mathrm{L})$ the Jacobian evaluated using the state values from the left reconstruction. λ_L are the eigenvalues of $A(\mathbf{q}_\mathrm{R})$ evaluated using the state values $\mathbf{q}_\mathrm{R}$ determined from the right-reconstruction. The 0's are included to allow for the case where there are either no right-going or left-going waves, *i.e.* in the instance that all characteristic velocities are travelling in the same direction. Using these characteristics we reconstruct the flux [138],

$$\mathbf{F}^\mathrm{HLL} = \frac{\lambda_+ \mathbf{f}(\mathbf{q}_\mathrm{L}) - \lambda_- \mathbf{f}(\mathbf{q}_\mathrm{R}) + \lambda_+ \lambda_- (\mathbf{q}_\mathrm{R} - \mathbf{q}_\mathrm{L})}{\lambda_+ + \lambda_-}. \tag{3.129}$$

This method is known to be very diffusive, but has proven to handle extreme shocks very well (*e.g.* pressures may vary between neighbouring cells by several orders of magnitude). This method is well suited for our surveys.

Lax–Friedrichs

The final flux calculation we used was the classic Lax–Friedrichs (LF) method which may be interpreted as an integral average within a cell [132] and has the form,

$$\mathbf{q}^* = \frac{1}{2}(\mathbf{q}_\mathrm{L} + \mathbf{q}_\mathrm{R}) - \frac{\Delta t}{2\Delta x}\left[\mathbf{f}(\mathbf{q}_\mathrm{R}) - \mathbf{f}(\mathbf{q}_\mathrm{L})\right]. \tag{3.130}$$

We then calculate the flux to be

$$\mathbf{F} = \frac{1}{2}\left[\mathbf{f}(\mathbf{q}_\mathrm{L}) + \mathbf{f}(\mathbf{q}_\mathrm{R})\right] - \frac{a}{2}(\mathbf{q}_\mathrm{R} - \mathbf{q}_\mathrm{L}). \tag{3.131}$$

where the value a may be determined by,

$$a = \max_p |\lambda_p| \frac{\Delta x}{\Delta t}, \tag{3.132}$$

where λ_p are the local eigenvalues for the system. This reduces to the simple LF method when the maximum eigenvalues tend to unity.

This equation has the form of an average of the two fluxes at an interface with an additional term in the equation that takes on the form of a numerical diffusion to damps out instabilities [122]. This method is very diffusive and "smears" badly, only giving usable results for very fine meshes.

In practice, this method is used when the eigenvalues are approximately unity [115]. The final form of the flux approximation is;

$$\mathbf{F} = \frac{\mathbf{f}(\mathbf{q}_\mathrm{L}) + \mathbf{f}(\mathbf{q}_\mathrm{R}) + a\,(\mathbf{q}_\mathrm{R} - \mathbf{q}_\mathrm{L})}{2}. \tag{3.133}$$

This is the most dissipative shock-capturing method of those considered in this study, and is best used for code development.

Before we proceed to the discussion of the remaining parts of the solution algorithm we discuss limitations of the different flux approximations.

3.8.4 Limitations of Approximate Riemann Solvers

The methods listed above are approximations to the full Riemann problem. These are used for maximum efficiency, as the full Riemann solver is numerically expensive and takes too long to perform parameter surveys for different fluid configurations. We have mentioned that each of the methods have different strengths and weaknesses. For the study at hand we use the Roe solver and the HLL solver as these methods produced the best results. The other solvers were implemented for their simplicity and for code testing purposes only, as they were too diffusive. Quirk [139, 33] discusses limitations of each of the techniques, and found that there were two modes of failure when using the Roe method; first, that it allowed for entropy violations; and second, that near vacuum it had difficulty preventing negative internal energy/negative pressure from forming. There have been proposed entropy fixes that will ensure that the internal energy will be positive. He does warn that these procedures are diffusive and tend to be no better than the artificial viscosity methods, in which we change the fundamental equations of motion by adding dissipative terms in order to retain the use of finite difference techniques. Quirk went on to say that the HLL methods were the best for shock handling while still maintaining positive pressures. Our experience has been that

it will depend on what physical properties we are trying to study as to which method needs to be used. By implementing enough tests for solutions that violate physics in the code, the entropy violations and negative internal energies could be caught and prevent the production of unphysical results.

3.8.5 Basic Algorithm

The algorithm used to perform the two dimensional evolution goes as follows;

1. Calculate the state value of the cell at the interfaces along one spatial dimension, say x^1 from cell values $\mathbf{Q}^n$
2. Calculate the flux integrals in Eqn. (3.96) using an approximate Riemann solver for fluxes along the x^1-direction
3. repeat step 1 along a second spatial dimension, say x^2
4. Calculate the flux integrals in Eqn. (3.96) using an approximate Riemann solver for fluxes along the x^2-direction
5. Calculate the source integral in Eqn. (3.97).
6. Perform the time step to determine $\mathbf{Q}^{n+1}$ using (3.99).

These are the steps we follow when solving our multidimensional magnetohydrodynamic system of equations. The actual time integration is performed using explicit ODE integration techniques discussed in Sec. 3.8.7. Before we discuss the conditions and methods that we use to perform the time integration. We briefly introduce some a condition, known as the CFL condition, required for the stability of the time integration of the numerical solver.

3.8.6 The Courant–Friedrichs–Lewy (CFL) Condition

The CFL condition is a requirement originally posed for finite closed form mathematics, [140][14] to prove the existence of solutions for different PDEs. They prove that a sequence of approximate solutions, as a smaller and smaller grid is used, converge to the continuum solution. Since the original concept, numerists have used this as a necessary condition for their approximate solutions to be convergent to the true solution.

[14] The original paper is written in Russian [141]

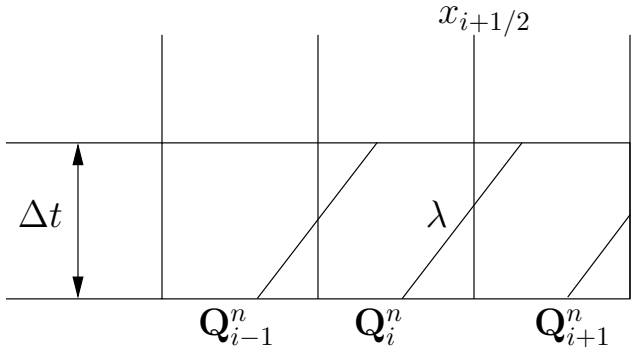

Figure 3.11: The CFL condition for one dimensional cell. For the solution of the conservation equations (3.1) to be convergent we require that the time step, Δt, be small enough that the characteristics do not have enough time to interact with cells beyond the adjacent cell. This condition must be met for convergence to be possible; however, satisfying this condition alone does not guarantee convergence.

If we consider a solution of the general system Eq. (3.1) at some coordinate in space and time, say $\mathbf{Q}^n_i$, it depends on the data at different spatial coordinates in a previous timestep. In particular, if we consider the variable reconstruction techniques used, we know any flux value will depend on at least three cells. The characteristic values, λ as described in Eqns. (3.48, 3.49, 3.53), in the centre cell (Fig. 3.11) give the wave speeds and any information carried by the waves will propagate a distance $\lambda\Delta t$. If the time step is too large, the waves from the centre cell will propagate beyond the adjacent cells [122].

The CFL or Courant factor, ν, for a (magneto)hydrodynamic system is defined to be,

$$\nu = \frac{\Delta t}{\Delta x} \max_p |\lambda_p|, \tag{3.134}$$

where p is the index that runs over all possible characteristics for the GRMHD system. For flows of higher dimension, the overall maximum characteristic from the Jacobians of all dimensions is used; for example, in two spatial dimensions,

$$\nu = \frac{\Delta t}{\Delta x} \max_p \left(|\lambda_p^{x^1}|, |\lambda_p^{x^2}| \right) \tag{3.135}$$

where $\lambda_p^{x^i}$ denotes the set of eigenvalues from the $\partial \mathbf{f}^i / \partial \mathbf{q}$ Jacobian. From this condition we know the CFL condition is governed by the largest overall characteristic wave speed.

To perform the explicit time integration we use the method of lines as described in the following

subsection.

3.8.7 Method of Lines

We calculate the time integration by using an explicit method where we split the temporal and spatial differencing. Using the method of lines we re-write the partial differential conservation equations as a set of first order ordinary differential equations,

$$\frac{d\mathbf{q}}{dt} = \mathcal{L}(\mathbf{q}), \tag{3.136}$$

where $\mathcal{L}$ contains all spatial differential operations.

Based on our flux approximations the exact form for this ODE is,

$$\frac{d\mathbf{Q}_i}{dt} = \mathbf{F}_{i+1/2} - \mathbf{F}_{i-1/2} + \mathbf{s}(\mathbf{Q}_i, g_{\mu\nu}), \tag{3.137}$$

where, as before, $\mathbf{Q}_i$ is the cell average of the i-th cell, $\mathbf{F}_{i+1/2}, \mathbf{F}_{i-1/2}$ are the numerical fluxes as described in Sec.3.8.1, and $\mathbf{s}$ is the source term evaluated at $\mathbf{Q}_i$. Now that the flux form is written as an ODE, we use standard solution techniques for ODE's. Below we outline two methods, Euler and Runge–Kutta, used to solve the equations of motion.

Euler

This is a first order accurate method. For an ordinary differential equation of the form $y' = f(t, x(t))$, the algorithm is:

$$\mathbf{Q}_i^{n+1} = \mathbf{Q}_i^n + \Delta t \left(\mathbf{F}_{i+1/2} - \mathbf{F}_{i-1/2} + \mathbf{S}(\mathbf{Q}_i^n, g_{\mu\nu}) \right). \tag{3.138}$$

This method is explicit, with the local error proportional to Δt^2. We also see that it comes from a simple finite difference approximation to the original ODE.

Runge–Kutta

The Runge–Kutta method is outlined below;

$$\mathbf{Q}_i^{(1)} = \mathbf{Q}_i^n + \Delta t \left(\mathbf{F}_{i+1/2}(\mathbf{Q}^n) - \mathbf{F}_{i-1/2}(\mathbf{Q}^n) + \mathbf{S}(\mathbf{Q}_i^n, g_{\mu\nu})\right) \tag{3.139}$$

$$\mathbf{Q}_i^{(2)} = \mathbf{Q}_i^{(1)} + \Delta t \left(\mathbf{F}_{i+1/2}(\mathbf{Q}^{(1)}) - \mathbf{F}_{i-1/2}(\mathbf{Q}^{(1)}) + \mathbf{S}(\mathbf{Q}_i^{(1)}, g_{\mu\nu})\right) \tag{3.140}$$

$$\mathbf{Q}_i^{n+1} = \mathbf{Q}_i^n + \frac{1}{2}(\mathbf{Q}_i^{(1)} + \mathbf{Q}_i^{(2)}) \tag{3.141}$$

This method uses a trial time step evaluated at the midpoint of each time step. Using this information, it corrects the final solution of each time step.

3.9 Boundaries

The finite volume method as described above is defined to work inside the body of a domain. The boundaries of the domain must be treated as special cases. We use extra cells around the domain, commonly referred to as ghost cells, and update these cells based on the physical setup of the problem at hand. The ghost cells are not part of the physical domain, and are introduced for algorithmic simplicity. For the following, $\mathbf{q}_1$ and $\mathbf{q}_N$ denote the quantities in the cells at the edge of the domain, while $\mathbf{q}_0$ and $\mathbf{q}_{N+1}$ denote the values of the quantities in the ghost cells. Typically, the boundary updates will be some combination of the following:

- Periodic boundary conditions (BC's)

$$\mathbf{q}_0 = \mathbf{q}_N \tag{3.142}$$

$$\mathbf{q}_{N+1} = \mathbf{q}_1 \tag{3.143}$$

  - these are not really boundaries, but for computational implementation we simply match the values of the ghost cells to the values of opposite side of the domain.

- Simple Outflow BC's

$$\mathbf{q}_{N+1} = \mathbf{q}_N \tag{3.144}$$

$$\mathbf{q}_0 = \mathbf{q}_1 \tag{3.145}$$

- these are used when a wave is expected to leave the domain and not return. Once out of the domain, the wave has no other impact on the system, thus the name outflow. We use zeroth order extrapolation to calculate the value of the ghost cells [122].

- Extrapolated outflow BC's

$$\mathbf{q}_0 = 2\mathbf{q}_1 - q_2 \tag{3.146}$$

$$\mathbf{q}_{N+1} = 2\mathbf{q}_N - q_{N-1} \tag{3.147}$$

- these are used when a wave is expected to leave the domain and not return, this modification prevents waves from artificially reflecting from of the outflow boundary. In this case we use a first order extrapolation to determine the value of the ghost cells [122].

- Inflow BC's

$$\mathbf{q}_{N+1} = \text{Const} \tag{3.148}$$

- here the boundary cells are held constant through the entire simulation. This boundary is also known as a prescribed boundary condition.

- Reflective (Wall) [33]

$$v_\perp(x_{\text{Wall}}) = 0 \tag{3.149}$$

$$B_\perp(x_{\text{Wall}}) = 0 \tag{3.150}$$

$$v_\perp(x_{\text{Wall}} + \Delta x) = -v_\perp(x_{\text{Wall}} - \Delta x) \tag{3.151}$$

$$B_\perp(x_{\text{Wall}} + \Delta x) = -B_\perp(x_{\text{Wall}} - \Delta x) \tag{3.152}$$

$$\mathbf{q}(x_{\text{Wall}} + \Delta x) = \mathbf{q}(x_{\text{Wall}} - \Delta x) \tag{3.153}$$

- here a vector component perpendicular to the boundary say, $v_\perp$, is zero at the "wall", any ghost cell beyond the "wall" will take on the negative of the value of a cell adjacent to the wall. In essence this treatment will look as though two fluid elements are headed towards each other near the wall. We take the wall to be located at $x = x_{\text{Wall}}$. For simplicity, we consider functional dependence on one spatial coordinate only. All other quantities are reflected, including the components of the velocity that are parallel to the wall. Note that

the magnetic field components are treated in the same way as the velocity field components.

The boundary conditions presented above are sufficient for all physical setups used in this thesis, including the Bondi–Hoyle accretion problem that will be discussed in Chap. 5.

3.9.1 The Floor

For relativistic fluids, one of the possible outcomes of the physical system could be two adjacent cells with dominant velocity components that face away from each other. This occurrence will produce a physical vacuum, a state in which the density goes to a value near zero. On occasion the cell interface reconstruction will produce a negative pressure, likewise, the primitive variable solver as discussed in section 3.3, is known to experience difficulties finding the correct root. The result is typically an unphysical solution, such as a state with negative pressure. When the unphysical states occur we check the value of the energy, compared to the baryon density. To circumvent this issue we use a numerical floor to impose a lower bound on the pressure and density. This floor is typically imposed on the conservative variables before calculating the primitives.

The concept of a floor is discussed in many different physical setups, and there does not appear to be a general solution that works for all cases. In our implementation, we found it fruitful to fix the floor to some constant low value, regardless of the coordinate location, such as those discussed in Noble *et al.* [117].

The method of floor decided upon for this project, after a discussion with Nielsen [142], was to determine a maximum between a floor value and the conservative density, and at the same time between the floor and the energy, τ,

$$D = \begin{cases} D, & \text{if } D > \text{floor;} \\ \text{floor}, & \text{otherwise.} \end{cases} \tag{3.154}$$

$$\tau = \begin{cases} \tau, & \text{if } \tau > \text{floor;} \\ \text{floor}, & \text{otherwise.} \end{cases} \tag{3.155}$$

After the primitive variable recovery has been performed, we perform a second set of tests on the primitive density and pressure,

$$\rho_0 = \begin{cases} \rho_0, & \text{if } \rho_0 > \text{floor;} \\ \text{floor}, & \text{otherwise.} \end{cases} \tag{3.156}$$

$$P = \begin{cases} P, & \text{if } P > \text{floor;} \\ \text{floor}, & \text{otherwise.} \end{cases} \tag{3.157}$$

In the case when the primitive variables were altered, the conservative variables are recalculated to ensure self consistency.

It is important to understand that the floor is not a physical quantity, but rather a numerical control. It has been observed in our system that this quantity is only necessary in ultrarelativistic systems, and does not interfere with any measurements, since any floored regions only occurred in the downstream region and were found to propagate downstream out of the domain. In our study we found that the floor is only necessary for the ultrarelativistic flows with speeds close to the speed of light.

In this chapter we have explained the characteristics and hyperbolicity conditions of a system of partial differential equations. We explained the algorithm, and techniques used to calculate each step we are able to calculate the evolution of the fluid equations of motion. Finally we explored limitations of our implementation of this algorithm. We now describe the methods we used to test the code developed, and present the results.

CHAPTER 4

NUMERICAL ANALYSIS AND TESTS

The purpose of numerical code testing is to ensure that the numerical results reflect a true solution of the equations being solved. We use three approaches to this, the first of which is convergence testing, where we run the simulation at a minimum of three different resolutions to determine if the solution is showing a trend to the continuum solution. The second is an independent residual test where we take the solution as determined by a numerical method and substitute it into an alternative numerical approximation. As the solution approaches the continuum solution, the independent residual is expected to tend to zero. The previous two tests are general numerical tests which are applied to determine if the numerical solution tends toward the continuum solution. The last set of tests of our solver are specific to the finite volume method, and test the shock capturing properties of the code by looking at specific situations where the solutions are known. There are a battery of tests that may be applied for verification of the shock capturing properties [44, 49, 51]; in particular, we consider one dimensional shock tube tests and blast waves. We also consider tests in two spatial dimensions including the hydrodynamic double shock wave, or Riemann test, and the magnetized strong blast wave. As a stronger comparison between the different flux approximations we use, we also investigate the Kelvin–Helmholtz instability [137]. Finally, we consider the relativistic Bondi accretion problem as a steady state problem, used to test our ability to handle time evolution of a steady system in a general relativistic context.

4.1 Convergence

The following are based on notes written by Choptuik [143], as well as the paper [144]. We can write a differential equation in a general form,

$$\mathcal{L}[u] = f \tag{4.1}$$

where $\mathcal{L}$ represents the differential operators. This representation hides all dependence of the equations on the variables and parameters in the differential equation. $u = u(t, x^i)$ represents a solution vector and $f = f(t, u, x^i)$ is a source term. If we let L^h be a discretized differential operator for some grid spacing h, we further write the discretized equation,

$$\mathcal{L}^h[u^h] = f^h, \tag{4.2}$$

where $u^h = u^h(t, x^i)$ and $f^h = f^h(t, u^h, x^i)$ are the discretized solution and source vectors, respectively. The continuum solution, u even evaluated at discrete points, is not a solution of (4.2). The degree to which the continuum solution fails to satisfy the discrete equation defines the truncation error, τ^h,

$$\tau^h = \mathcal{L}^h[u] - f^h. \tag{4.3}$$

This error may be found from the Taylor series expansion of the difference operators. Since we are actually interested in the solution u, we require that our approximate solution tends to the true solution $u^h \to u$ as the resolution increases.

We further define a solution error, $e^h = e^h(t, x^i)$, containing all error that arises from the substitution of the continuous problem with the discrete problem,

$$e^h = u - u^h. \tag{4.4}$$

One error that is present in all finite precision numerical analysis is round-off error. This error can play a large role in fluid evolution due to the strongly coupled nature of the equations, and the fact that each field can vary over several orders of magnitude relative to each other. The wide range of magnitudes indicates that rounding errors may quickly overwhelm a numerical solution.

Using the Richardson expansion [144], we are able to make a connection between the solution error order and the order of the truncation error, resulting in;

$$u^h = u + h^2 e_2 + h^4 e_4 + O(h^6). \tag{4.5}$$

To determine the convergence of a differencing scheme to the continuum problem, we must test the results at different resolutions and determine the convergence of the solution u^h to the true solution u, without knowing what it is.

To proceed with the discussion of our convergence we need to introduce two additional concepts, a vector or array norm, as well as a convergence factor.

4.1.1 Norms

When investigating convergence, we require techniques that allow us to represent arrays of data as single data points. Typically this is done by measuring a norm of a data set. In numerical analysis, when we refer to a norm, we consider a p-norm. Say we have a vector solution u^h of a discrete equation such as in equation (4.1)

$$L_p(u^h) = \left(\frac{1}{N} \sum_{i=i}^{N} |u_i^h|^p \right)^{\frac{1}{p}} \equiv \|u^h\|_p, \tag{4.6}$$

where N denotes the number of elements in the solution vector. To extend this to higher dimensions, we use;

$$L_p(u^h) = \left(\frac{1}{N_1 N_2 N_3} \sum_{i=i,j,k}^{N_1,N_2,N_3} |u_{ijk}^h|^p \right)^{\frac{1}{p}} \equiv \|u^h\|_p, \tag{4.7}$$

where N_i denotes the number of elements of the solution array u_{ijk} in the ith direction. In this study, unless otherwise specified, when we discuss the norm of a solution we mean the L_2-norm *i.e.* $p = 2$ and drop the subscript.

4.1.2 Convergence Factor

If at a minimum we have three different resolutions $h_1 < h_2 < h_3$, then we evaluate the Richardson extrapolation, Eqn. (4.5) as,

$$\begin{aligned} u^{h_1} &= u + h_1^2 e_2 + h_1^4 e_4 + O(h^6) \\ u^{h_2} &= u + h_2^2 e_2 + h_2^4 e_4 + O(h^6) \\ u^{h_3} &= u + h_3^2 e_2 + h_3^4 e_4 + O(h^6). \end{aligned} \tag{4.8}$$

When we discuss the order of a polynomial expansion in this context we refer to the powers on the expansion parameter, h. If the power on the expansion parameter, h is one, the system is said to be first order. The equations (4.8) are second order.

We then define a convergence factor, Q, to be

$$Q \equiv \frac{\|u^{h_3} - u^{h_2}\|}{\|u^{h_2} - u^{h_1}\|}. \tag{4.9}$$

With the expansions (4.8) and keeping only lowest orders in h, this reduces to

$$Q = \frac{\|h_3^2 e_2 - h_2^2 e_2\|}{\|h_2^2 e_2 - h_1^2 e_2\|} = \frac{\|h_3^2 - h_2^2\|}{\|h_2^2 - h_1^2\|} = \frac{\|(h_3/h_2)^2 - 1\|}{\|1 - (h_1/h_2)^2\|}. \tag{4.10}$$

Typical analysis of this type uses grids that are scaled by factors of two *i.e.* $h_1 = h$, $h_2 = 2h$, and $h_3 = 4h$. In this case we expect that the convergence factor $Q = 4$. Using the above method does not produce an integer convergence factor but does allow us to study the convergence properties of the numerical routine.

For the systems that we study, we extend this analysis to two and three dimensions. Since we keep the relative sizes of the mesh uniform, *i.e.* when we increase the resolution in one dimension we likewise increase resolution in all other dimensions, we are free to choose the lowest resolved dimension of the system to determine the error in our system.

Due to the variable reconstruction method discussed in Chap. 3, we expect that the solution of the system of equations to reduce to first order accuracy near discontinuities and extrema.

4.2 Independent Residual

To ensure that the solution of the given set of equations is the correct solution, we can also use an independent residual.

To use this method we solve the equations of motion using one method of discretization, then discretize the same equations with a second independent technique, and look at the error left when applying the second method to the solution from the first. The error is referred to as the residual. We check the rate of convergence of the residual to zero, which depends on the methods used. For example If we use a second order solver to obtain the solution, and check our solution using a first order independent technique the rate of convergence of the idependent residual will be first order. If the solutions do not converge, then we know there is a problem with the implementation. In short, we consider a linear discretized differential operator $\bar{L}^h$ which is different from the original

discretization L^h. We then calculate the residual, r^h,

$$r^h = \bar{\mathcal{L}}^h(u^h) - f^h, \tag{4.11}$$

where u^h is the solution of the system $\mathcal{L}^h(u^h) = f^h$. If $\mathcal{L}^h$ and $\bar{\mathcal{L}}^h$ are the same continuum operator, then the residual will converge as expected with the Richardson extrapolation [33]. In fluid dynamics, the equations of motion are highly nonlinear. In the following we will switch notation for clarity. Since we are interested in two dimensional problems which may not use equal grid spacing, for clarity we use Δx and Δy in lieu of h to represent the grid spacing in different dimensions. We further denote temporal grid spacing using Δt. We use the following first-order finite-difference discretization to evaluate the independent residual;

$$\mathbf{r} = \frac{\frac{1}{2}(\mathbf{q}^{n+1}_{i+1} - \mathbf{q}^{n}_{i+1}) + \frac{1}{2}(\mathbf{q}^{n+1}_{i} - \mathbf{q}^{n}_{i})}{\Delta t} + \left(\frac{\mathbf{f}^n_{i+1} - \mathbf{f}^n_i}{\Delta x}\right) - \frac{\mathbf{S}^n_{i+1} + \mathbf{S}^n_i}{2} \tag{4.12}$$

where $\mathbf{r}$ are the independent residuals for each of the corresponding state variables $\mathbf{q}$. Recall that $\mathbf{f}^n_{i,j} = \mathbf{f}(\mathbf{q}^n_{i,j})$ and $\mathbf{S}^n_{i,j} = \mathbf{S}(\mathbf{q}^n_{i,j})$. For two dimensional systems, the above independent residual is;

$$\begin{aligned}\mathbf{r} \quad = \quad & \frac{\frac{1}{4}(\mathbf{q}^{n+1}_{i+1,j} - \mathbf{q}^{n}_{i+1,j}) + \frac{1}{4}(\mathbf{q}^{n+1}_{i,j} - \mathbf{q}^{n}_{i,j}) + \frac{1}{4}(\mathbf{q}^{n+1}_{i,j+1} - \mathbf{q}^{n}_{i,j+1}) + \frac{1}{4}(\mathbf{q}^{n+1}_{i+1,j+1} - \mathbf{q}^{n}_{i+1,j+1})}{\Delta t} \\ & + \left(\frac{\mathbf{f}^n_{i+1,j} - \mathbf{f}^n_{i,j}}{\Delta x}\right) + \left(\frac{\mathbf{f}^n_{i,j+1} - \mathbf{f}^n_{i,j}}{\Delta y}\right) - \frac{\mathbf{S}^n_{i+1,j} + 2\mathbf{S}^n_{i,j} + \mathbf{S}^n_{i,j+1}}{4},\end{aligned} \tag{4.13}$$

which is also first order. To evaluate the independent residual above we use the cell centred values for each variable. We used the algebraic form of the fluxes found in Eqns. (2.119) and (2.124) to calculate the finite differenced fluxes for the magnetohydrodynamic and ultrarelativistic systems respectively. Because the independent residual is only a first order approximation to the partial differential equations we can only expect our test to converge to zero to first order.

We expect some difficulty using this method to test global convergence because this difference scheme is not defined across discontinuities. Although we only be use this method to verify the solution array, not solve for it, we will still have poor resolution of any discontinuous variable in the domain. Recall that using a finite difference approximation to solve for solution across a discontinuity leads to unphysical oscillations. Using a finite difference technique as outlined above to check for convergence of a solution that contains shocks may lead to misleading error estimates when calculating global errors such as those calculated using Eqn. (4.9). We applied the

independent residual test for systems that had smooth solutions and terminated the test before the shocks form.

To determine how well our numerical scheme could handle shocks, we used different shock tests which are described in the next several sections.

4.3 Shock and Symmetry Capabilities

Due to the number of different Riemann approximation schemes as well as magnetic field constraint handlers, we need a set of problems that test the shock capturing properties of, and constraint violations of the schemes in fluid systems. The first set of tests we describe are one dimensional and are performed using Minkowski spacetime in Cartesian coordinates. They are designed to test the different flux approximations for their ability to preserve the sharp discontinuities experienced at a shock interface. These tests are commonly referred to as the shock tube tests and are tests of the hydrodynamic codes. Balsara [44] extended these tests to include magnetic field contributions. For the following sections, unless stated otherwise, we use Cartesian coordinates and restrict our attention to the spatial domain $x = [-0.5, 0.5]$.

4.3.1 Sod Shock Tube Tests

The Sod shock tube [122] is one of the original systems investigated using the finite volume method in one dimensional hydrodynamics. A shock tube contains a removable membrane that separates two regions, denoted left, L and right R where the fluid state variables, $\mathbf{p}(0, x)$ of the two halves are of different pressure and density. Both fluids are initially at rest. We choose the location of the membrane to be the origin, $x = 0$. We initialize the primitive variables;

$$(\rho_0(0,x), v^x(0,x), P(0,x)) = \begin{cases} (\rho_{0\mathrm{L}}, 0, P_{\mathrm{L}}), & \text{if } x < 0; \\ (\rho_{0\mathrm{R}}, 0, P_{\mathrm{R}}), & \text{if } x \geq 0; \end{cases} \tag{4.14}$$

Where $\rho_{0\mathrm{L}}, \rho_{0\mathrm{R}}, P_{\mathrm{L}}, P_{\mathrm{R}}$ are all constant. By judicial choices of $\rho_{0\mathrm{L}}, P_{\mathrm{L}}$ and $\rho_{0\mathrm{R}}, P_{\mathrm{R}}$ we set the speed of sound to be the same for both sides of the discontinuity. This model tests the shock capturing properties of a hydrodynamic code since the solution contains three different types of waves; a shock wave, a rarefaction wave, and a contact discontinuity. Results of this test may be seen in Fig. 4.1.

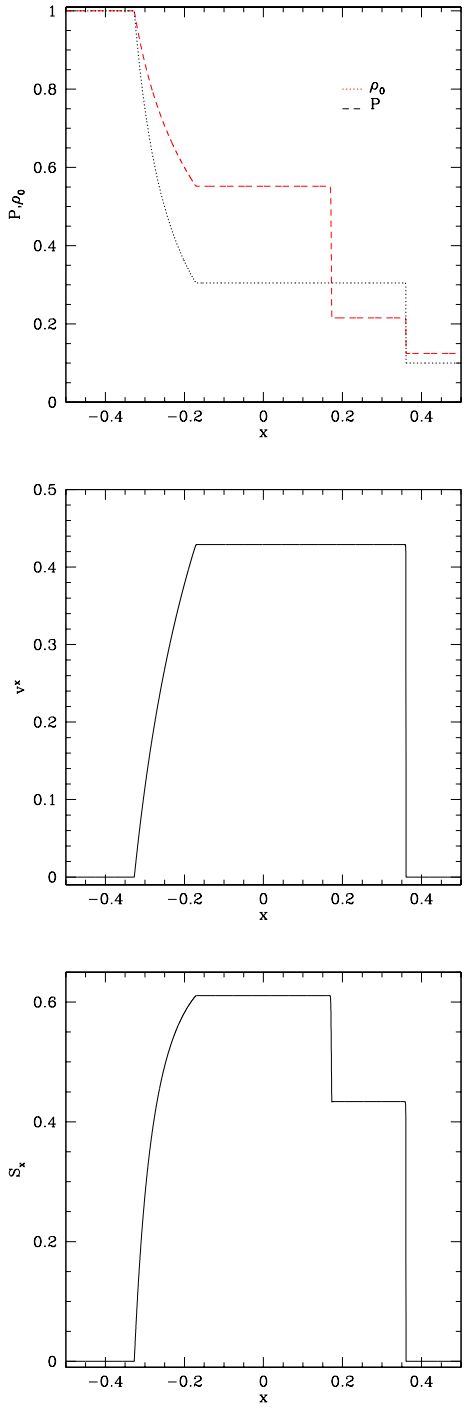

Figure 4.1: The Sod tube test [122]. Plotted are the pressure, density, v^x (middle), and S_x (bottom). The interesting parts of this plot include the existence of a rarefaction wave, a shock wave, and a contact discontinuity where the pressure is constant but the density exhibits a sharp discontinuity. This is a result of using the HLL solver with $c_h = 1.0$, and $N_x = 6400$. The solution shown here is at $t = 0.4$, initial data is in the first two rows of table 4.1.

Test		ρ	P	v_x	v_y	v_z	B_x	B_y	B_z
Sod	L	1.0	1.0	0.0	0.0	0.0	0.0	0.0	0.0
	R	0.125	0.1	0.0	0.0	0.0	0.0	0.0	0.0
Balsara	L	1.0	1.0	0.0	0.0	0.0	0.5	1.0	0.0
	R	0.125	0.1	0.0	0.0	0.0	0.5	-1.0	0.0
1D Blast Wave	L	1.0	1000.0	0.0	0.0	0.0	2.0	7.0	7.0
	R	1.0	0.1	0.0	0.0	0.0	2.0	0.7	0.7

Table 4.1: Initial conditions for the 1D relativistic Balsara blast wave, and the 1D strong blast wave [44].

Since we want the code to handle magnetic field contributions as well, we focus on further tests which probe the the magnetic field contributions. These are the Balsara blast wave [44] and the strong shock blast wave which are based on the hydrodynamic Sod Shock tube as described above.

4.3.2 Balsara Blast Wave

In this test, magnetic fields are introduced to a Sod shock tube by using a constant B_x component and a discontinuous B_y component. In the Balsara blast wave, the shock capturing properties of a magnetohydrodynamic code are tested, as the solution contains all of the relevant types of waves, including coupled magnetosonic waves. The initial data for a test in the $\hat{x}$-direction was,

$$(\rho_0(x,0), v^x(x,0), P(x,0), B^x(x,0), B^y(x,0)) = \begin{cases} (\rho_{0\mathrm{L}}, 0, P_\mathrm{L}, B^x(x,0), B^y_\mathrm{L}), & \text{if } x < 0; \\ (\rho_{0\mathrm{R}}, 0, P_\mathrm{R}, B^x(x,0), B^y_\mathrm{R}), & \text{if } x \geq 0; \end{cases} \tag{4.15}$$

where $\rho_{0\mathrm{L}}, \rho_{0\mathrm{R}}, P_\mathrm{L}, P_\mathrm{R}, B^x(x,0), B^y_\mathrm{L}(x,0), B^y_\mathrm{R}(x,0)$ are all constant. The magnetic field, B^x is uniform over the entire domain and constant in time. The quantities used to initialize the variables can be found in table 4.1.

The results of the Balsara blast wave at time $t = 0.4$ for the initial date in 4.1 are seen in Fig. 4.2. They are in agreement with solutions found in the literature [114, 44]. This test was applied in both spatial directions as a verification that the flux approximations used are valid.

4.3.3 Magnetized Strong Blast Wave

In an extension to the Balsara blast wave, we test the numerical solver's ability to capture strong shocks. This one dimensional test is configured as seen in table 4.1. Using the HLL solver with both the MC and minmod limiter, we are able to capture the strong shocks. The HLL method is a

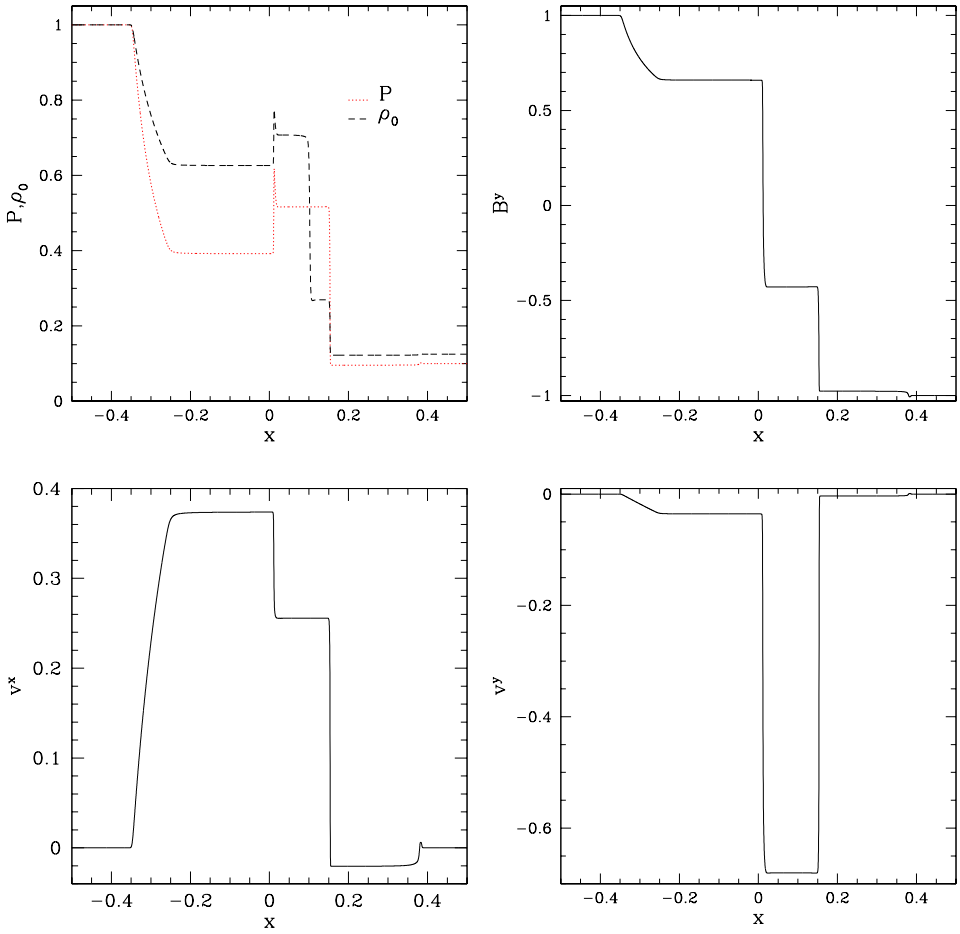

Figure 4.2: The Balsara blast wave test as designed by Balsara [44]. Plotted are the pressure, density (top), v^x (bottom left), B^y (top right), and v^y (bottom right). The interesting parts of this plot include the existence of a shock wave, a rarefaction wave, Alfvén wave and a contact discontinuity where the pressure is constant but the density exhibits a sharp discontinuity. This is a result of using the HLL solver with $c_h = 1.0$, and $N_x = 6400$. The solution shown here is at $t = 0.4$, initial data is in the second two rows of table 4.1.

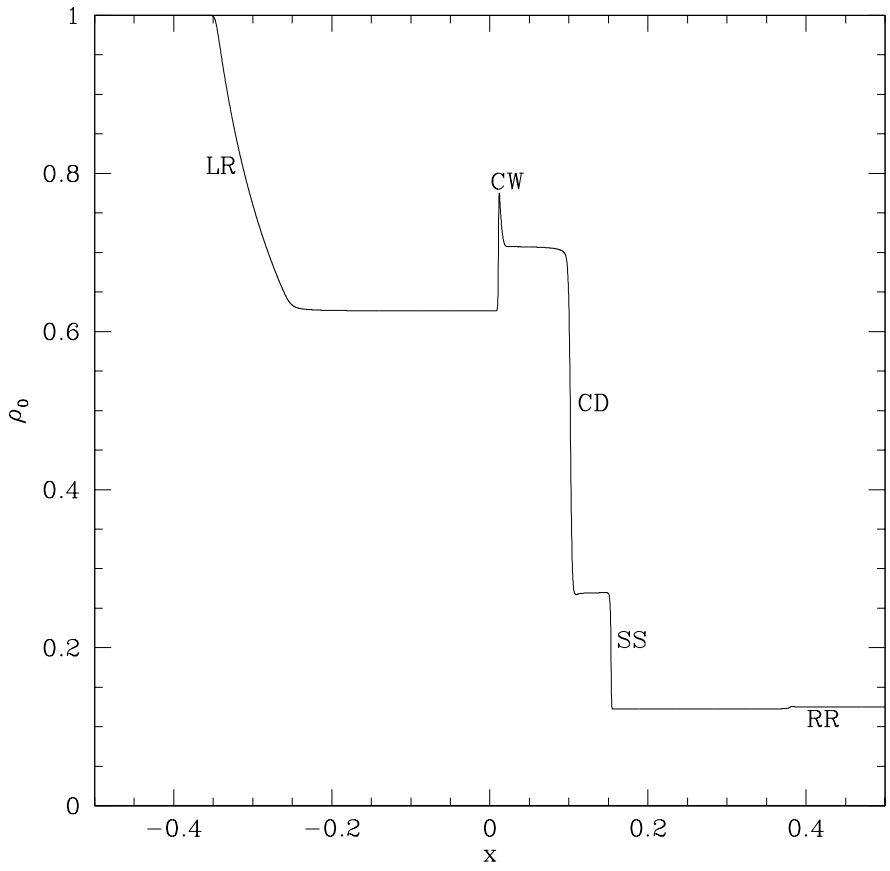

Figure 4.3: The density plot of the relativistic Balsara blast wave test [44]. When compared to Fig. 4.2, we label the different wave forms that develop. It is noted that some of the wave combinations are unique to magnetohydrodynamic systems. The labels are as follows; LR denotes a left moving rarefaction wave and CW denotes a compound wave. The compound wave is unique to MHD systems and consists of an over-compressive shock, and a rarefaction wave. CD denotes a contact discontinuity which is easily recognized by noticing that the pressure is constant across this discontinuity as seen in Fig. 4.2. SS denotes a slow shock and RR denotes a right moving rarefaction [145, 146].

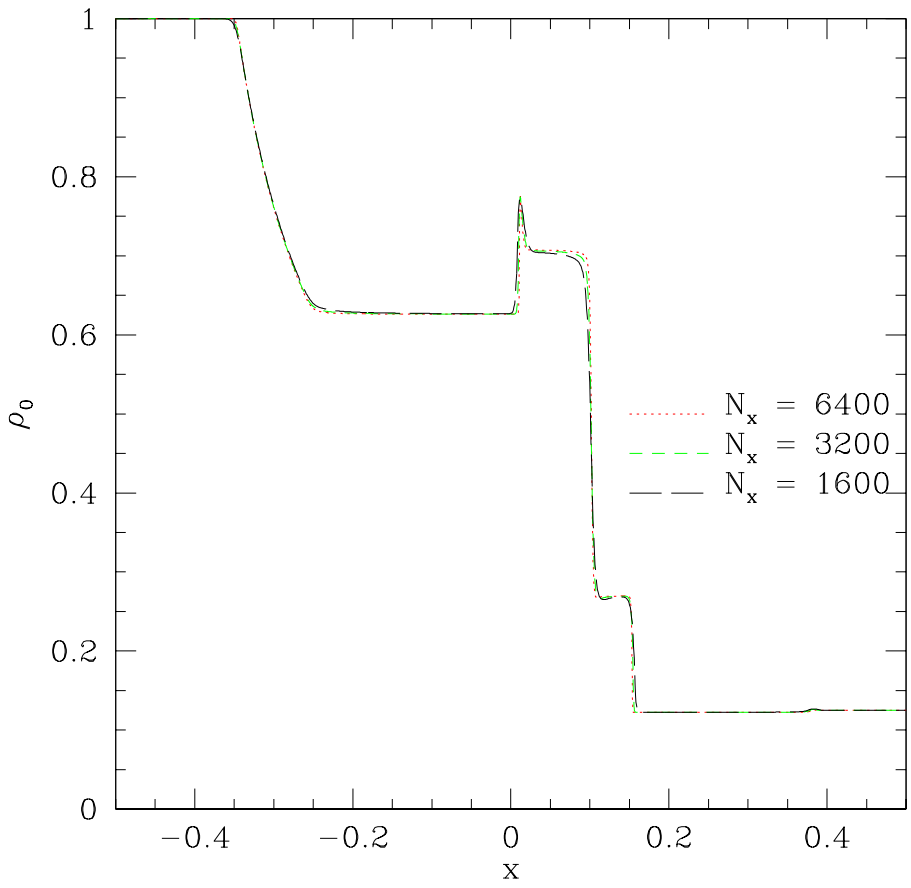

Figure 4.4: The Convergence properties of the Balsara blast wave test. The green line uses $N_x = 1600$, red denotes $N_x = 3200$, and black denotes $N_x = 6400$. We see that the discontinuities are becoming sharper as the resolution increases. The regions $-0.01 \leq x \leq 0.15$, and $0.1 \leq x \leq 0.16$ are shown with greater magnification in Fig. 4.5.

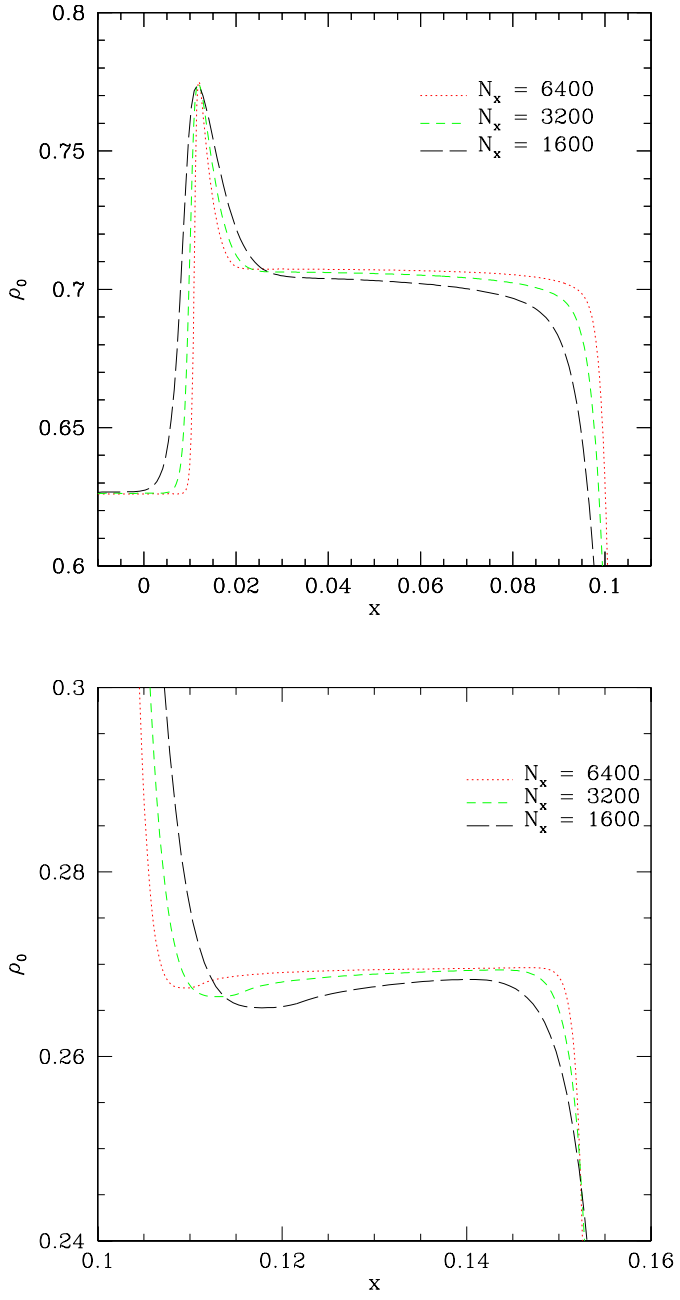

Figure 4.5: The convergence properties of the Balsara blast wave. Level 1 uses $N_x = 1600$, level 2 uses $N_x = 3200$, and black denotes $N_x = 6400$. Here we focus our attention on the regions $-0.01 \leq x \leq 0.15$ (top) and $0.1 \leq x \leq 0.16$ (bottom). As the resolution increases we are able to better approximate the sharp discontinuities and extrema in the profile.

diffusive flux approximation method. The diffusion is shown near strong shocks in particular when we use the minmod limiter. When we use the HLL flux approximation with the MC limiter we see less diffusion in the same region. This is clearly displayed in Figs. 4.6 and 4.7.

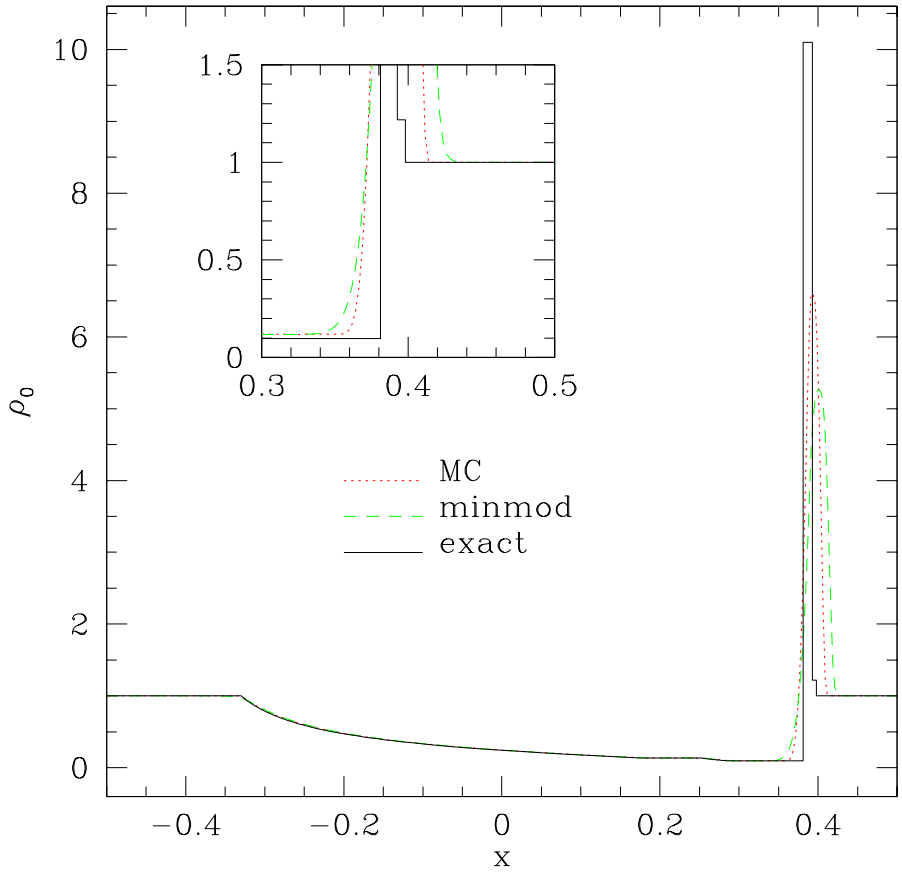

Figure 4.6: The one dimensional strong blast wave. We use the domain $-0.5 \leq x \leq 0.5$, with a resolution $N_x = 401$. The dotted line represents the results while using of the MC limiter, while the dashed line represent the result of using the minmod limiter. The exact solution is represented by the solid line [49]. This shows evidence that the MC limiter offers a better representation of shocks. This is evident, not only due to the larger density amplitude, but also in the region around $x = 0.4$ as seen in the inset plot.

4.3.4 Two Dimensional Riemann Tests

We present the case where shocks are present in multiple directions. Unfortunately, a simple double shock system, such as a two dimensional Balsara type setup, does not exist for the magnetic field case, due to the necessity of the no-divergence constraint in the initial conditions. In Fig. 4.8 we

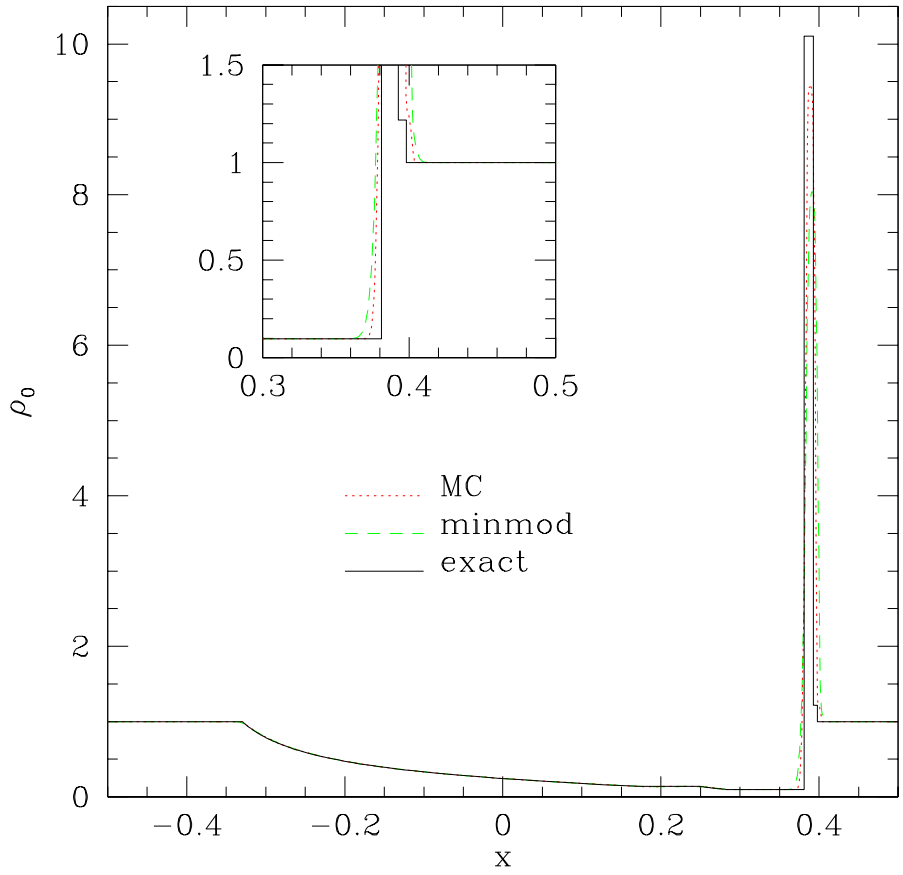

Figure 4.7: The one dimensional strong blast wave at a higher resolution. We use the domain $-0.5 \leq x \leq 0.5$, with a resolution $N_x = 1601$. The dotted line represents the results while using of the MC limiter, while the dashed line is the result of using the minmod limiter. The exact solution is the solid line. The higher resolution test shows evidence that the MC limiter offers a better representation of shocks than the midmod limiter. Once again the density amplitude while using the MC limiter is closer to the exact solution [49], but also in the blown up region around $x = 0.4$ we see that the MC limiter begins to capture the contact discontinuity that the minmod limiter is too diffusive to capture.

Test	Location	ρ	P	v_x	v_y
2D Riemann Shock Test	BL	0.5	1.0	0.0	0.0
	BR	0.1	0.01	0.0	0.99
	TL	0.1	1.0	0.99	0.0
	TR	0.1	0.01	0.0	0.0

Table 4.2: Initial conditions for the 2D relativistic Riemann shock wave. BL = Bottom-Left, TL = Top-Left, BR = Bottom-Right, and TR = Top-Right. These initial conditions are provided by FLASH, http://flash.uchicago.edu/website/codesupport/flash3_ug_3p2/node31.html.

present the result of the 2D shock test for a purely hydrodynamic system (*i.e.* $B_x = B_y = 0$), at time $t = 0.7$. We restrict our attention to Cartesian coordinates, with domain, $-0.5 \leq x \leq 0.5$, $-0.5 \leq y \leq 0.5$.

4.4 Kelvin Helmholtz Instability

Fluids may become unstable when the gradient of any of the constituent fields, (ρ_o, v^i, P, B^j), exceed certain thresholds. As is discussed in Biskamp [147], when the convective transport of the field flux is more efficient than the diffusive transport due to viscous effects, this threshold is reached. These instabilities are categorized as Kelvin–Helmholtz, Rayleigh–Taylor, and the tearing mode instability. It is also known that the presence of magnetic fields may stabilize these instabilities. Since we consider ideal fluids, the fluid does not experience viscous effects which leads the way for any of the previously stated instabilities.

The Kelvin–Helmholtz instability (KHI) occurs when there is a large enough gradient of the state variables across a shear flow within a fluid. If we perform a Fourier analysis of the momentum equations of motion, the dispersion relation reveals a growing mode proportional to the gradient across the velocity field. Further analysis indicates that the presence of a sufficiently strong parallel magnetic field is expected to stabilize the system. Astrophysical fluids may experience differential rotation, which corresponds to a shear flow. When performing this investigation we used the same setup as described within the ATHENA website.[15] Since this is not the focus of this thesis, we will only go into implementation details, for a full treatment of this phenomenon please see [137, 147, 148, 149, 150].

The initial conditions are reproduced in Table 4.3. We use periodic boundary conditions in

[15] http://www.astro.princeton.edu/~jstone/tests/index.html

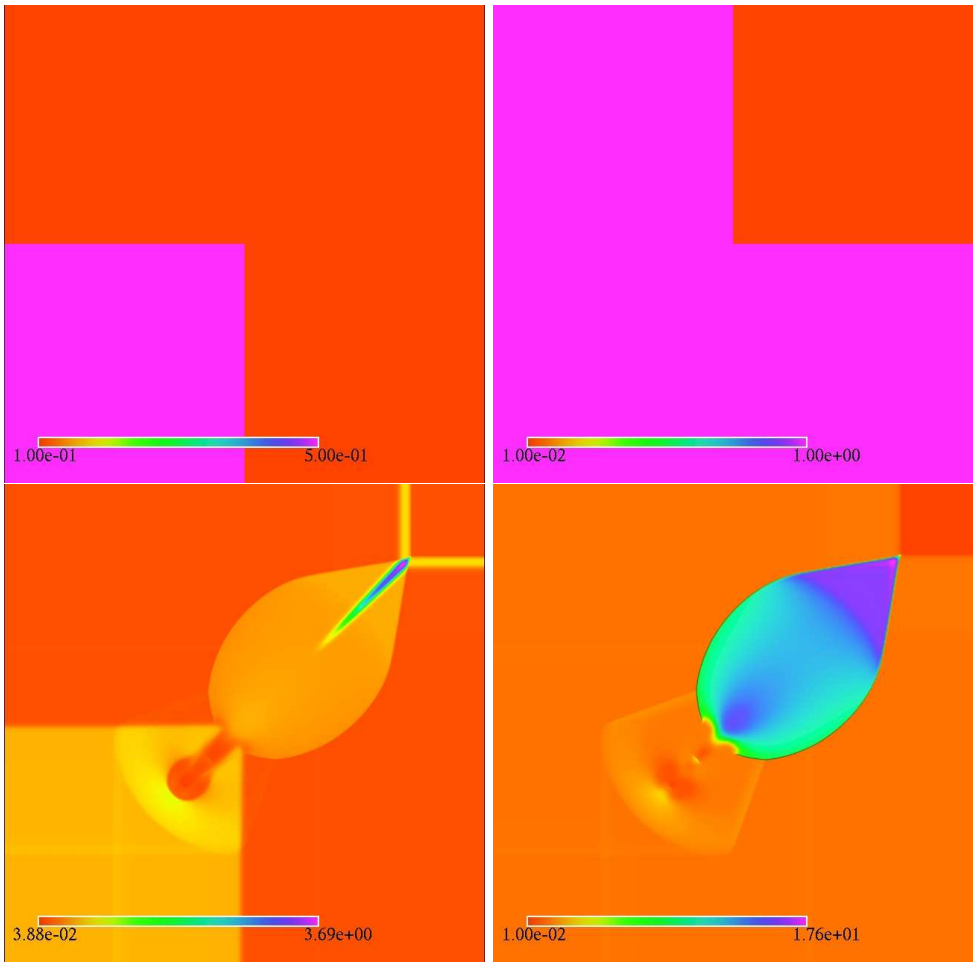

Figure 4.8: The two dimensional Riemann shock test. We present the baryon rest mass density, ρ_0 (left) and the pressure, P (right). The top plot shows the initial conditions, while the bottom plot shows the result of an evolution at $t = 0.7$. We used a resolution of 1025×1025. The initial conditions are seen in Table 4.2. This shows the codes capability for capturing shocks while also maintaining symmetry. Even with using a second order scheme, we are able to capture a lot of the features of this system including the jet that protrudes out the back of the shock. The domain is $(x, y) = [-1, 1] \times [-1, 1]$.

		ρ	P	v^x	v^y	B^x	B^y	β_p
Weak	L	1.0	2.5	0.5	0.0	0.5	0.0	20
	R	2.0	2.5	-0.5	0.0	0.5	0.0	20
Strong	L	1.0	2.5	0.5	0.0	5.0	0.0	0.2
	R	2.0	2.5	-0.5	0.0	5.0	0.0	0.2

Table 4.3: Initial conditions for the 2D Kelvin–Helmholtz tests. When the magnetic field is not considered, B^x is set to zero. The domain, $(x, y) = [-0.5, 0.5] \times [-0.5, 0.5]$, was broken into three regions for $-0.5 \leq y < -0.25$ and $0.25 < y \leq 0.5$ we used the parameters labelled L, for $-0.25 \leq y \leq 0.25$ we used the parameters labelled R.

both the x and y direction. All the state variables;

$$(\rho_0, v^x, v^y, P, B^x, B^y) = (\rho_0(t,x,y), v^x(t,x,y), v^y(t,x,y), P(t,x,y), B^x(t,x,y), B^y(t,x,y)) \quad (4.16)$$

are now functions of two spatial dimensions and time. The setup at $t = 0$ is as follows;

$$(\rho_0, v^x, v^y, P, B^x, B^y) = \begin{cases} (\rho_{0\mathrm{L}}, v^x_{\mathrm{L}}, P, B^x, B^y_{\mathrm{L}}), & \text{if } -0.25 < y < 0.25; \\ (\rho_{0\mathrm{R}}, v^x_{\mathrm{R}}, P, B^x, B^y_{\mathrm{R}}), & \text{otherwise.} \end{cases} \quad (4.17)$$

A uniform pressure, P, and magnetic field, B^x, cover the entire domain. In the centre of the domain the fluid velocity, v^x, and density are discontinuous in the $\hat{y}$-direction. The vertical velocity, v^y, is initially zero. We refer the reader to Table 4.3 for the exact values used. For all velocity fields, we use a periodic perturbation to trigger the instability; the amplitude of the velocity perturbation, v_p, is set to 1% of the original field strength.

$$v^x = v^x_0 + v_p \cos(2\pi y l) \cos(2\pi x l) \quad (4.18)$$

$$v^y = v_p \cos(2\pi y l) \cos(2\pi x l) \quad (4.19)$$

where l is used to control the frequency, and v^x_0 represents the original uniform velocities v^x_{L} and v^x_{R}. The instability that develops is known as the Kelvin–Helmholtz instability (KHI). For the study of non-relativistic form of this instability, we refer the reader to Frank *et al.* [137]. The study of this setup is relevant when testing the numerical diffusion that occurs when using different flux approximations. The only flux approximation that we developed that captures this instability is the Roe solver. All other flux approximations are too diffusive and damp out the instability.

When the magnetic field is embedded in the fluid system, the flow is more stable and the strong

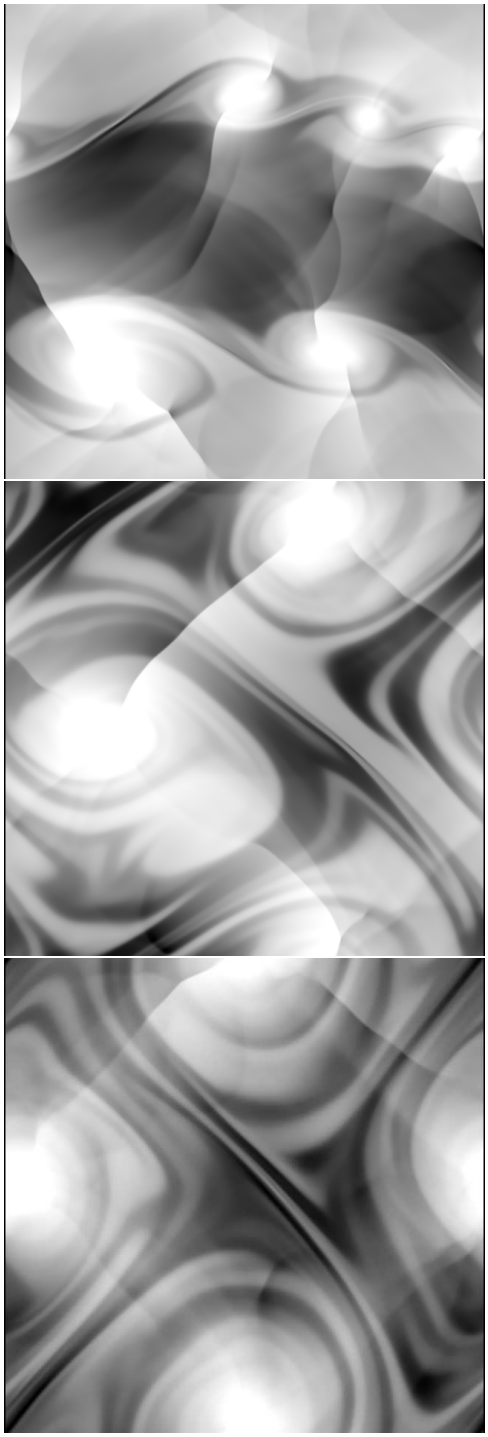

Figure 4.9: Baryon density evolution results of the Kelvin–Helmholtz initial conditions in a special relativistic system. 512×512 resolution using a periodic velocity field perturbation. From top to bottom, $T = 5, 10, 15$. The formation of the "cat's eye" is apparent.

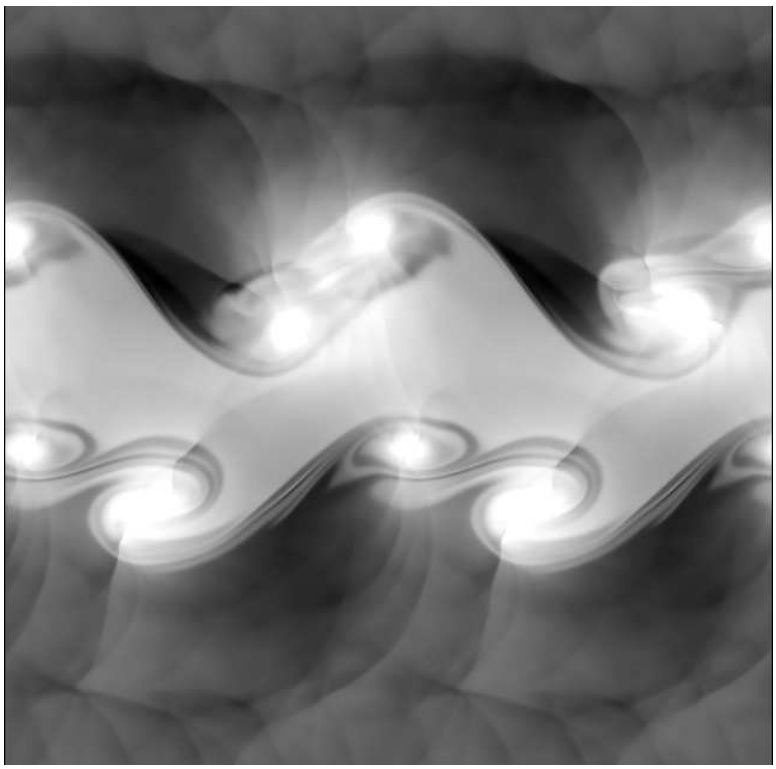

Figure 4.10: Baryon density evolution results of the Kelvin–Helmholtz initial conditions in a special relativistic system. 1024×1024 resolution using a periodic velocity field perturbation. When we compare this to the 512×512 simulation there is a noticeable increase in detail as well as an increase in the number of vortices. This is a feature of unstable systems, the larger the resolution the greater the number of features, which might lead us to believe the system is not convergent. Higher resolution will result in capturing even more vortices.

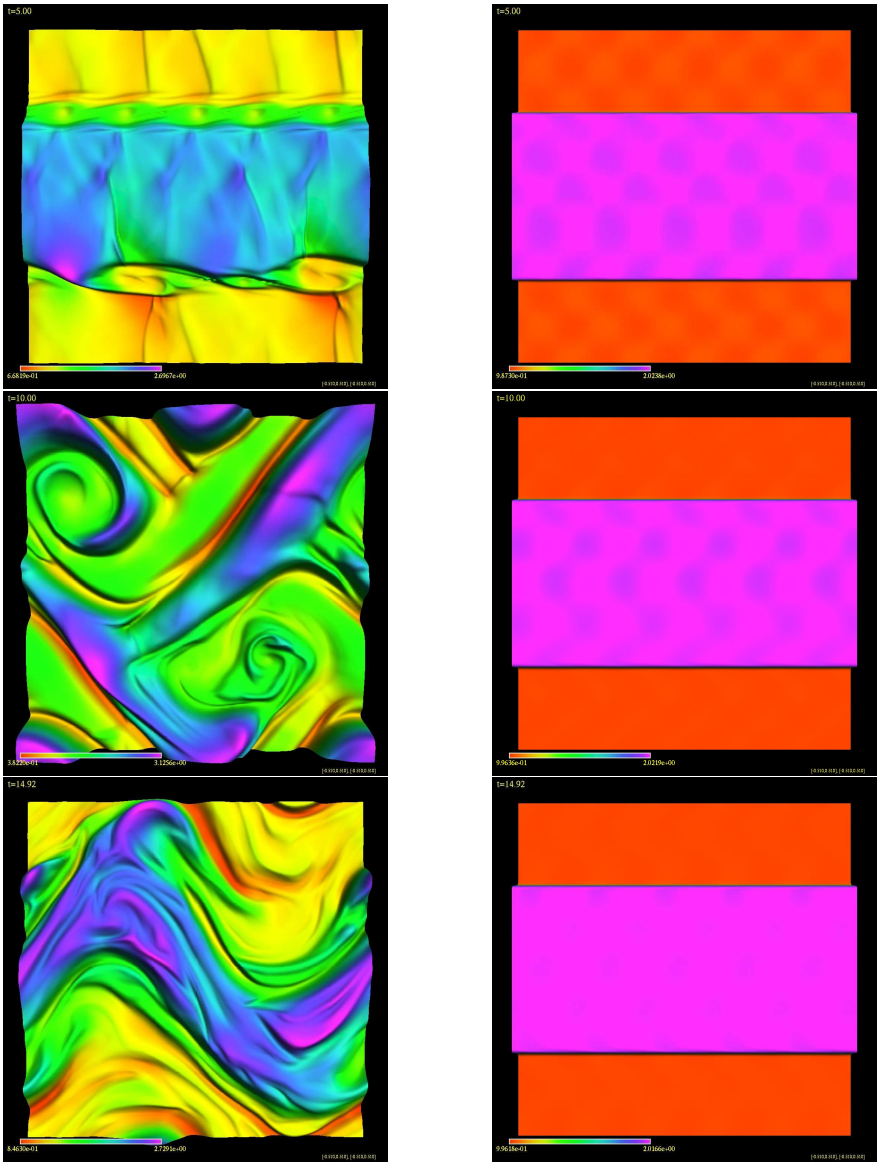

Figure 4.11: Baryon density evolution results of the magnetized Kelvin–Helmholtz initial conditions (table 4.3) in a special relativistic system. 512×512 resolution using a sinusoidal velocity field perturbation to prevent $\nabla \cdot \mathbf{B} = 0$ violations in the initial steps. From top to bottom $T = 5, 10, 15$, left column uses $B^x = 0.5$, the right column uses $B^x = 5.0$. Note that the presence of a relatively strong magnetic field suppresses the instability entirely, offering an example where the presence of a magnetic field stabilizes a flow. The initial plasma beta for the left column is $\beta_p \sim 20$, while on the right $\beta_p \sim 0.2$.

vortices seen in the hydrodynamic system are reduced. If the magnetic field is weak, as in the left column of Fig. 4.11, the instability persists, but takes longer to fully develop. If the magnetic field is sufficiently strong in the direction of the fluid flow, as seen in the right column of Fig. 4.11, the instability is suppressed entirely. The result is a smoother flow as the instability is suppressed by the embedded magnetic field. In the case where the embedded magnetic field is in a direction orthogonal to the fluid flow, the instability is completely suppressed.

4.5 Rigid Rotor

The rigid rotor is a two dimensional special relativistic MHD test which evolves an initially rigidly rotating fluid in the presence of a magnetic field [115, 45]. We show the results using an HLL solver with a minmod limiter. The divergence constraint handling is monitored by measuring two different quantities, we consider the L_2-norm of both the divergence of the magnetic field, and the auxiliary field Ψ as seen in Fig. 4.12. The resulting density evolution may be seen in Fig. 4.13.

To calculate the divergence of the magnetic field as described by (2.103), we use a spatially centred second order finite difference approximation. This discretization may be difficult to calculate across a shock and may consequently show strong violations as resolution increases (shocks become sharper). We used the second order finite difference approximation seen below,

$$\begin{aligned}\nabla\cdot\mathbf{B} \quad\rightarrow\quad & \frac{1}{\sqrt{\gamma}}\left(\frac{\left(\sqrt{\gamma}\mathcal{B}^{x_1}\right)_{i+1,j,k}-\left(\sqrt{\gamma}\mathcal{B}^{x_1}\right)_{i-1,j,k}}{2\Delta x_1}\right.\\ & +\frac{\left(\sqrt{\gamma}\mathcal{B}^{x_2}\right)_{i,j+1,k}-\left(\sqrt{\gamma}\mathcal{B}^{x_2}\right)_{i,j-1,k}}{2\Delta x_2}\\ & \left.+\frac{\left(\sqrt{\gamma}\mathcal{B}^{x_3}\right)_{i,j,k+1}-\left(\sqrt{\gamma}\mathcal{B}^{x_3}\right)_{i,j,k-1}}{2\Delta x_3}\right).\end{aligned} \tag{4.20}$$

In the smooth regions of the solution space, this approximation is second order accurate. The above approximation will break down when a shock occurs in the solution. We will need to consider another method to monitor the no-divergence constraint for the magnetic field, which will be discussed in section 4.6. The results of this test may be seen in the right image of Fig. 4.12. As we can see, discretizing $\nabla\cdot\mathbf{B}=\mathbf{0}$ using a finite difference stencil leads to misleading error estimates.

In addition to the convergence of the magnetic field constraint, we also plot the convergence of

the density cross section of the rigid rotor on both the x and y axis, as seen in Fig. 4.14.

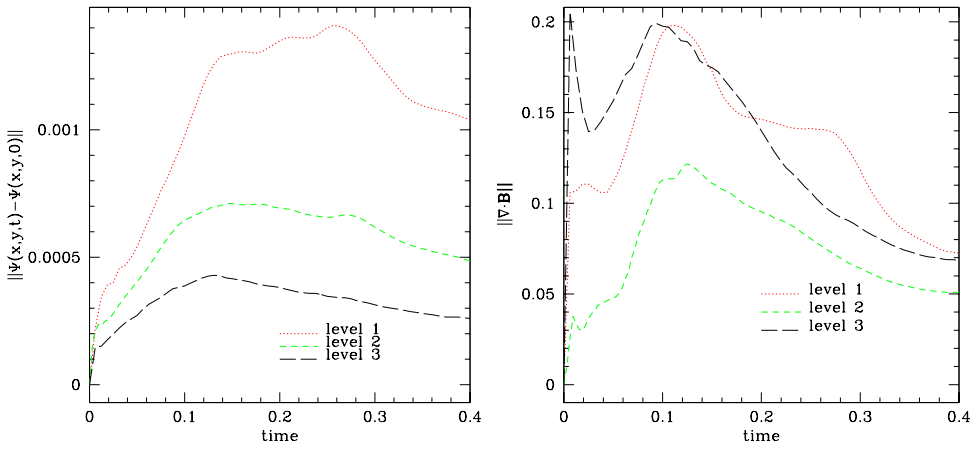

Figure 4.12: The convergence of the magnetic divergence constraint for the relativistic rigid rotor simulation. The base resolution is 321×321 (dotted line). It should be noted that the L_p-norms of the derived quantity $\nabla \cdot \mathbf{B} = \mathbf{0}$ may not be the most useful test for this particular constraint since the magnetic constraint violations are strongest near discontinuities. Other analysis techniques have been considered, but only the L_p norms appear to be universally accepted; therefore, these are the only techniques presented. The left shows the L_2 norm of the deviation of auxiliary field Ψ from the expected continuum solution $\Psi(x, y, 0)$, the right shows the L_2 norm of the magnetic field constraint. If either of these fields blow up we know the evolution has become unphysical. In these evolutions, the quantities are bounded so the evolution variables may still be considered physical. These plots indicate that monitoring the constraint may be better performed by monitoring the auxiliary field Ψ, which is enforced by the fact if Ψ were to experience unbounded growth, the magnetic field constraint would experience strong violations. Due to the presence of shocks and extrema seen in this evolution, the convergence rate of this problem is less than second order.

4.6 Steady State Accretion

When developing time dependent GRMHD codes, we use steady state problems as a test that the code and all methods used are functioning properly [25, 26, 51, 151]. The final two sections discuss the tests used to determine how well we can approximate a steady state solution using a time dependent code. Ultimately this tests the stability of the time evolution.

4.6.1 Spherical Relativistic Bondi Accretion

The relativistic Bondi accretion problem consists of a spherically symmetric black hole accreting asymptotically stationary matter. This problem reduces to a simple ODE, and can be readily

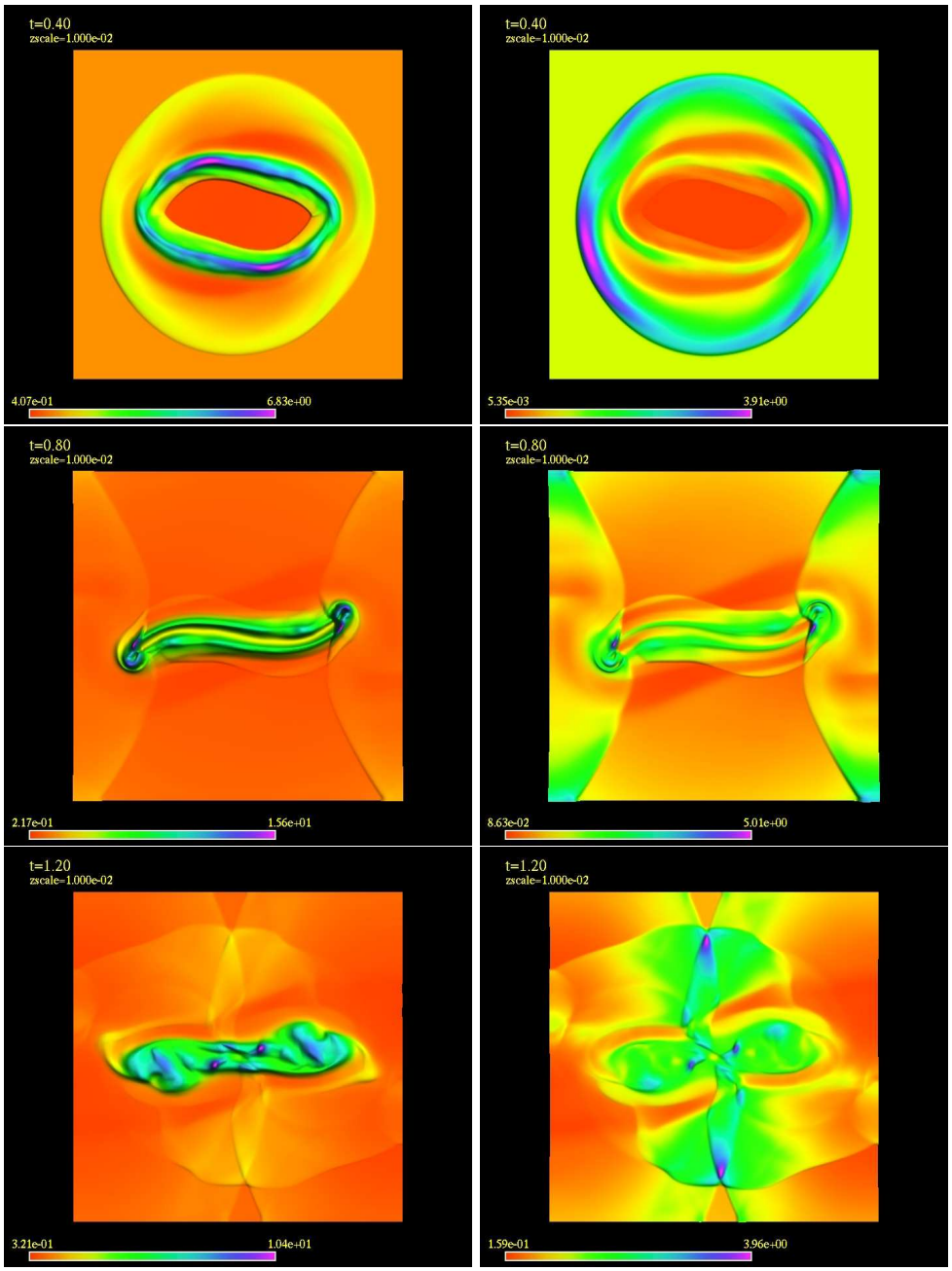

Figure 4.13: The results of the rigid rotor initial conditions 128×128, from top to bottom $T = 0.4, 0.8, 1.2M$, the left column shows the results for the baryon density ρ_o, the right column shows the results for the thermodynamic pressure P. The presence of a magnetic field is apparent in the first frame, where we see a flattened rotating fluid disk.

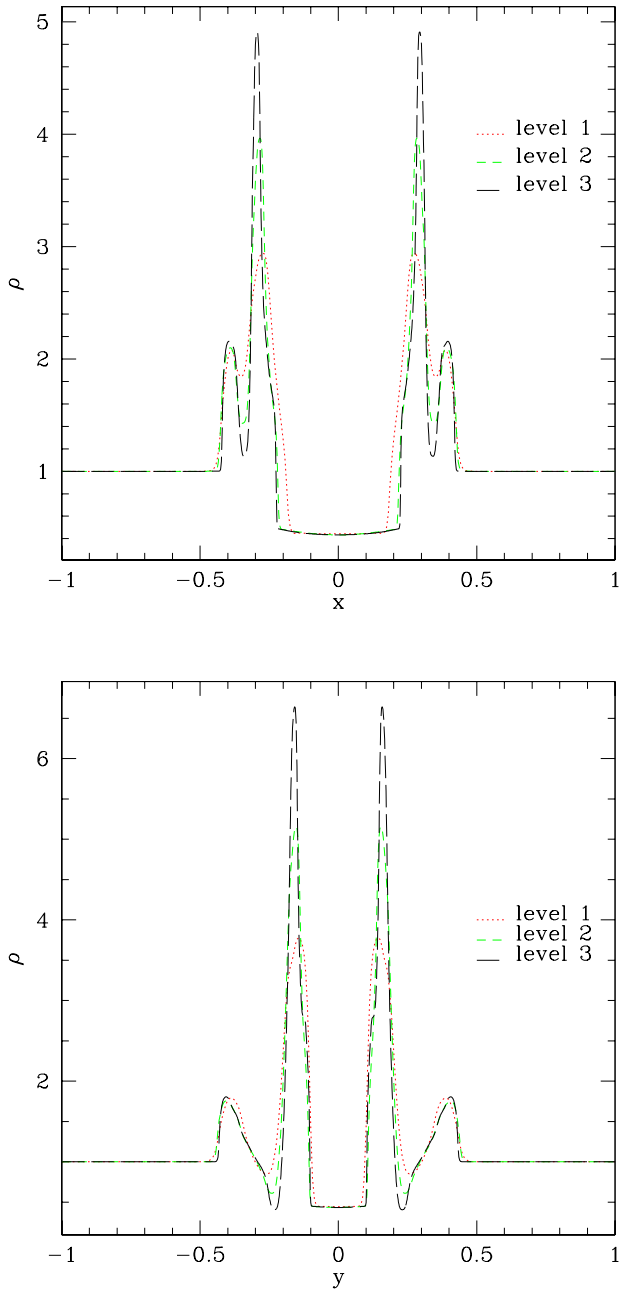

Figure 4.14: The convergence of the relativistic rigid rotor simulation. The top shows the density cross section along the y-axis, the bottom shows the density cross section along the x-axis. The level 1 resolution (dotted line) is $(N_x, N_y) = 321 \times 321$, level 2 $(N_x, N_y) = 641 \times 641$, and level 3 $(N_x, N_y) = 1281 \times 1281$. We see that the base features of the evolution remain the same, becoming more pronounced and sharper peaked. All cross sections are recorded at time $t = 0.4$.

		ρ	P	v_x	v_y	v_z	B_x	B_y	B_z
Rigid Rotor	I	10.0	1.0	$-\omega_z y$	$\omega_z x$	0.0	1.0	0.0	0.0
	O	1.0	1.0	0.0	0.0	0.0	1.0	0.0	0.0

Table 4.4: Initial conditions for the rigid rotor test. The I row denotes values inside a particular radius, while O denotes values outside of that radius. The rigid rotor is set to have zero velocity outside the radius 0.1, while inside the radius 0.1 the fluid is set to experience differential rotation defined by $\vec{v} = \vec{\omega} \times \vec{r}$, where we use $\omega = (0, 0, 9.95)$.

solved using standard numerical ODE solvers. This tests how well the time dependent code will solve a known time independent (steady state) problem.

Here we work in spherical polar coordinates (t, r, θ) and assume that all state variables depend only on r. This reduces the PDE equations of motion to a set of ODEs;

$$\partial_r \left(\sqrt{-g}(D\hat{v}^r)\right) + \partial_\theta \left(\sqrt{-g}(D\hat{v}^\theta)\right) = 0 \tag{4.21}$$

$$\partial_r \left(\sqrt{-g}(S_r\hat{v}^r + P)\right) + \partial_\theta \left(\sqrt{-g}(S_r\hat{v}^\theta)\right) = \sqrt{-g}\frac{1}{2}T^{\mu\nu}g_{\mu\nu,r} \tag{4.22}$$

$$\partial_r \left(\sqrt{-g}(S_\theta\hat{v}^r)\right) + \partial_\theta \left(\sqrt{-g}(S_\theta\hat{v}^\theta + P)\right) = \sqrt{-g}\frac{1}{2}T^{\mu\nu}g_{\mu\nu,\theta} \tag{4.23}$$

$$\partial_r \left(\sqrt{-g}(\tau\hat{v}^r + Pv^r)\right) + \partial_\theta \left(\sqrt{-g}(\tau\hat{v}^\theta + Pv^\theta)\right) = \sqrt{-g}\left(\alpha_\mu T^{\mu t} - \alpha\Gamma^t{}_{\mu\nu}T^{\mu\nu}\right). \tag{4.24}$$

For the spherically symmetric black hole in either ingoing Eddington–Finkelstein or Schwarzschild coordinates, we have $\sqrt{-g} = r^2 \sin\theta$. We also assume that the fluid does not have any initial angular velocity, so $v^\theta = 0$ which leads to $S_\theta = 0$, reducing our set of ODEs (4.21-4.24) to,

$$\partial_r \left(\sqrt{-g}(D\hat{v}^r)\right) = 0 \tag{4.25}$$

$$\partial_r \left(\sqrt{-g}(S_r\hat{v}^r + P)\right) = \sqrt{-g}\frac{1}{2}T^{\mu\nu}g_{\mu\nu,r} \tag{4.26}$$

$$\partial_\theta \left(\sqrt{-g}P\right) = \sqrt{-g}\frac{1}{2}T^{\mu\nu}g_{\mu\nu,\theta} \tag{4.27}$$

$$\partial_r \left(\sqrt{-g}(\tau\hat{v}^r + Pv^r)\right) = \sqrt{-g}\left(\alpha_\mu T^{\mu t} - \alpha\Gamma^t{}_{\mu\nu}T^{\mu\nu}\right). \tag{4.28}$$

Following Michel [22] and Hawley *et al.* [25] we define a temperature $T = P/\rho_o$, and integrate (4.25) to get;

$$T^{\frac{1}{\Gamma-1}}u^r r^2 = C_1, \tag{4.29}$$

where u^r is the radial component of the fluid 4-velocity. Then we integrate (4.26) to get

$$\left[1+(1+\frac{1}{\Gamma-1})T\right]^2\left(1-\frac{2M}{r}+u^{r2}\right)=C_2. \tag{4.30}$$

This gives us enough information to solve for $T(r)$ and $u^r(r)$ if we know the constants of integration C_1, C_2. To specify C_1, C_2 we consider the transonic point, r_c, the point through which the fluid speed transitions from subsonic (less than the speed of sound) to supersonic (faster than the speed of sound). With the information specified at the transonic point we are able to solve for the critical radial component of the 4-velocity, $u_c = u_c(r_c)$ and the critical temperature $T_c = T(r_c)$. For a detailed explanation, we refer the reader to [25, 26].

The steady state accretion test was performed in both one (r) and two (r,θ) dimensions. Although the phenomenon is one dimensional in nature, by performing the simulation with a free polar coordinate we will test the code's capability of making angular approximations [51]. When we consider Eqn. (4.27) using Schwarzschild coordinates, the closed form solution reveals that the left side becomes,

$$\partial_\theta(\sqrt{-g}P) = Pr^2\cos\theta \tag{4.31}$$

while the right side is,

$$\sqrt{-g}\frac{1}{2}T^{\mu\nu}g_{\mu\nu,\theta} = Pr^2\cos\theta, \tag{4.32}$$

comparing (4.31) and (4.32) we see that (4.27) is satisfied trivially if calculated in closed form.

In calculating the numerical solution to Eqns. (4.25–4.28) we use approximate solutions to the differentials as described in Chap. 3. The numerical solution of the left side of (4.31) is only approximately equal to the right side Eqn. (4.32). Solving (4.25–4.28) in two spatial dimensions reveals how well our techniques handle the approximate angular differentiation. expression for the angular momentum. If the code is developed properly, the divergence of the flux for the angular momentum term (4.31) will cancel the source term (4.32) within truncation. We show the evolution at time 100 and the L_2 norm for the time derivative of the radial velocity to show the steady state behaviour.

The results of this simulation may be seen in Fig. 4.16. For the simulation we used the Schwarzschild coordinates, and $\Gamma = 5/3$, $r_c = 8$ to specify the problem.

A final observation for the hydrodynamic code is that this initial condition proved to be a

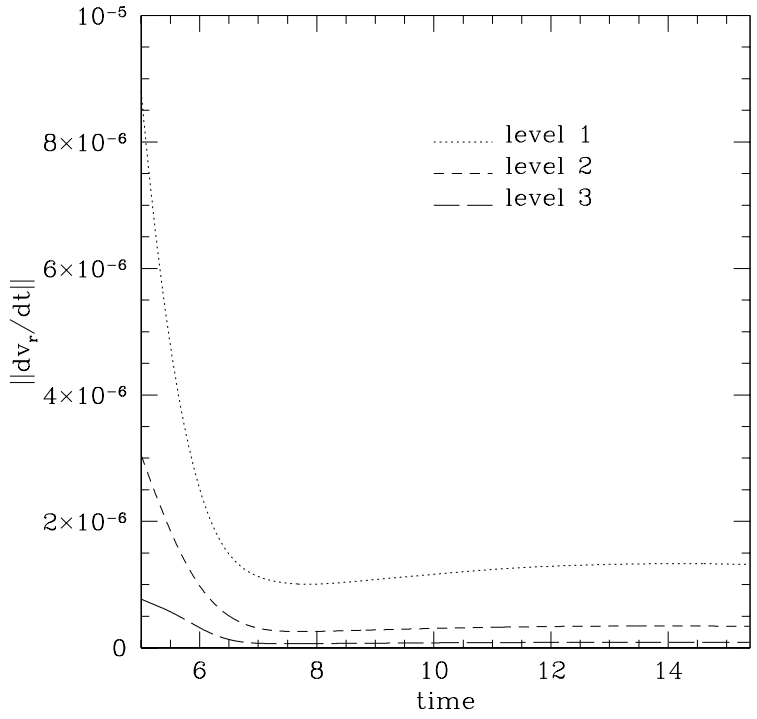

Figure 4.15: Convergence of the L_2-norm of the time derivative of the radial velocity for the relativistic spherical accretion, showing the convergence of the time derivative of the radial velocity. We note that despite the fact that the problem is fixed to a steady state initial condition, some numerical error occurs near the event horizon due to boundary conditions. After some transient time, the evolution maintains a steady state solution. The time derivative of the radial velocity is converging to zero. Only $5 \leq t \leq 15$ is shown for emphasis.

valuable test for the outflow boundary conditions. If we use the simple outflow boundary condition as described in Sec. 3.9, the evolution results in the radial velocity reflecting back from the event horizon due to the high pressure and density [53]. The extrapolated outflow boundary conditions prevent sharp unphysical reflections from occurring at this boundary.

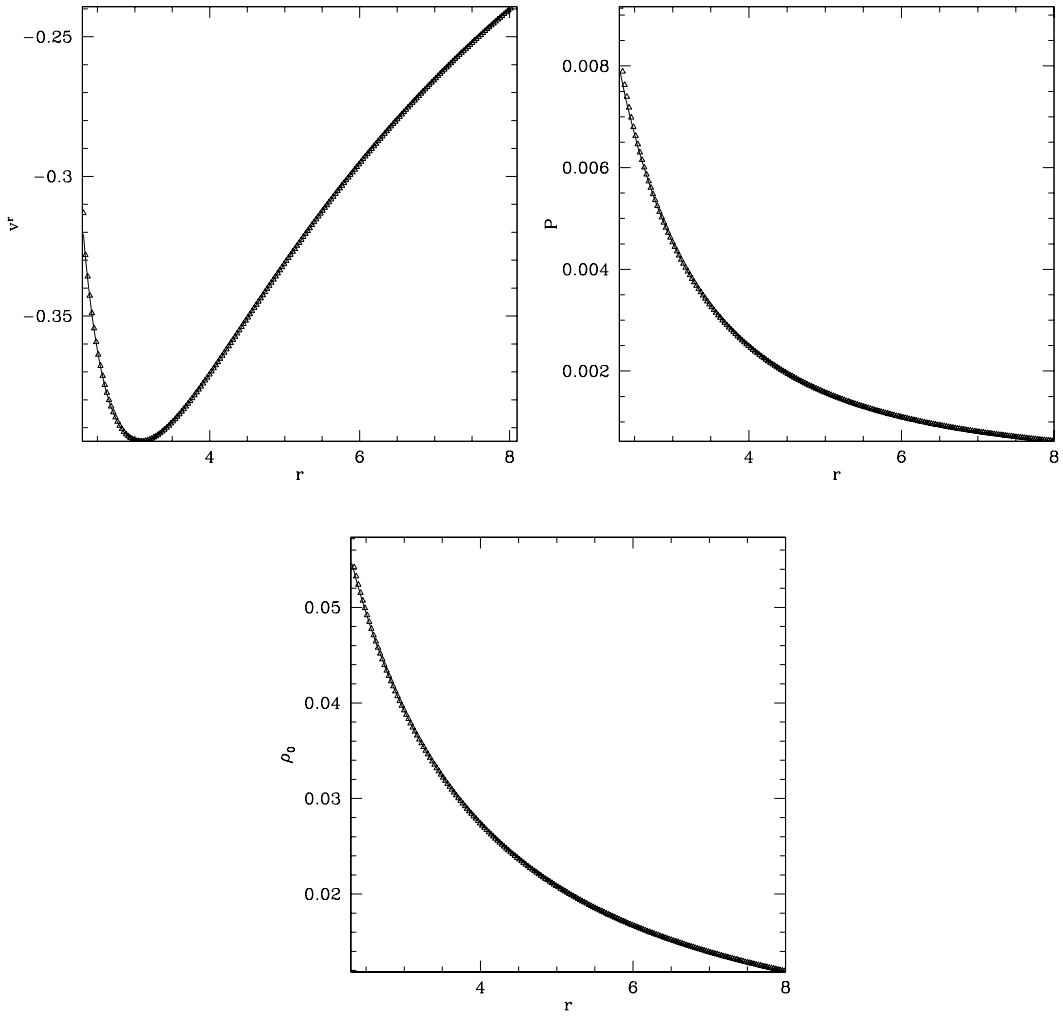

Figure 4.16: Relativistic spherical Bondi accretion. The top left is the radial velocity v^r, the top right shows the thermodynamic pressure P, and the bottom shows the baryon rest mass density ρ_0. These results show the evolution at time ~ 100. The exact solution is represented by the solid line. The only deviation from the exact solution occurs near the boundary; however, the simulation quickly settled to a steady state.

4.6.2 Magnetized Spherical Accretion

We have seen that our numerical solution to the steady state spherical accretion problem is satisfactory, but this only tests the hydrodynamic solver. To test the full magnetohydrodynamic numerical solution against a steady state problem, we impose a radial magnetic field on the spherical accretion and obtain a steady solution [53]. First we ensure that the magnetic field will be divergence free. Thus we solve the ODE;

$$\partial_r \left(\sqrt{\gamma}\mathcal{B}^r(r)\right) = 0. \tag{4.33}$$

For a Schwarzschild spacetime in either Schwarzschild or ingoing Eddington–Finkelstein coordinates, this results in

$$\mathcal{B}^r(r) = \frac{64C}{r^2}, \tag{4.34}$$

where C is an integration constant which is determined by assigning a value to $\mathcal{B}^r$ at the critical radius.

$$\mathcal{B}^r_{\rm c} = \mathcal{B}^r(r_{\rm c}) = \frac{64C}{r_{\rm c}^2}. \tag{4.35}$$

We use the plasma beta, β_p, to parametrize the magnetic field amplitude;

$$\beta_p = \frac{2P}{b^2}. \tag{4.36}$$

Recall from (2.100) that $b^2 = g_{\mu\nu}b^\mu b^\nu$ where;

$$b^\mu = (b^t, b^j) = \left(\frac{W}{\alpha}(\gamma_{ij}v^i\mathcal{B}^j), \frac{\mathcal{B}^i}{W} + \alpha b^t\hat{v}^i\right).$$

Given that $b^\mu = (b^t, b^r, 0, 0)$, as defined by (2.100), we have,

$$b^2 = g_{tt}(b^t)^2 + g_{tr}b^tb^r + g_{rr}(b^r)^2. \tag{4.37}$$

Using Schwarzschild coordinates, we have $g_{tr} = 0$ which simplifies the expression.

To determine the magnitude of the magnetic field at the critical point, we solve for C;

$$2P_c(\beta_p)^{-1} = \left(1 - \frac{2M}{r_c}\right)(b^t)^2 + \left(1 - \frac{2M}{r_c}\right)^{-1}(b^r)^2 = \left(1 - \frac{2M}{r_c}\right)(B^r_c)^2. \tag{4.38}$$

This configuration cannot be reached using an arbitrary initial condition due to the one dimen-

sional nature of this steady state problem. The magnetic flux is exactly zero in the closed form solution; therefore, we cannot have a time dependent magnetic field. Despite the fact that this problem is not physical, it does prove to be a useful test to determine the limitations of a numerical scheme, as such this setup is only being used for code evaluation. Examination of the closed form of the system of equations shows that the magnetic field of this form does not change the equations of motion.

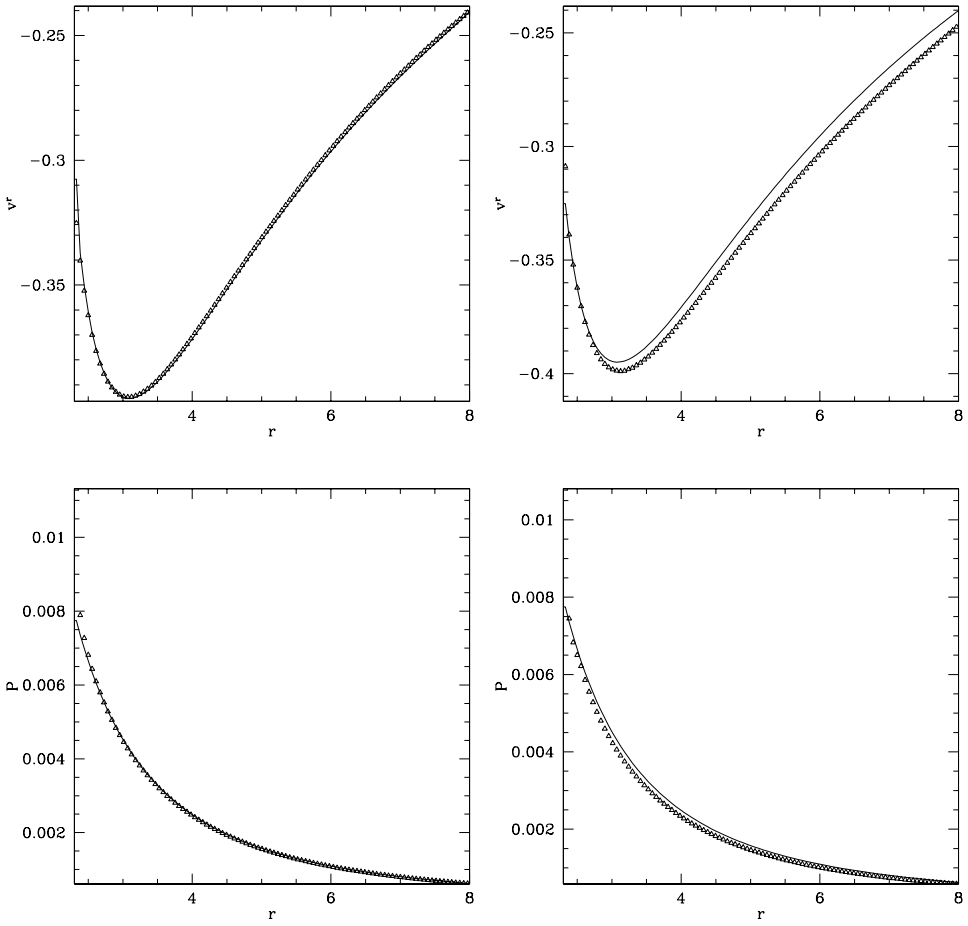

Figure 4.17: Magnetized relativistic spherical Bondi accretion. The results shown are at time $t \sim 100M$. The left column is the result of plasma $\beta_P = 10$, the right column is $\beta_P = 1$. The top shows the radial velocity, the bottom the thermodynamic pressure. We see that we experience difficulty when trying to evolve fluids with a smaller β_P, although the profile of the flow variables remains similar, the magnitudes all disagree with the exact solution. With higher resolution this problem begins to decrease; however, since we are ultimately interested in two dimensional simulations the resolutions demands are too great for the problem to be tractable for small β_P. Larger β_P returned results similar to the $\beta_P = 10$ case.

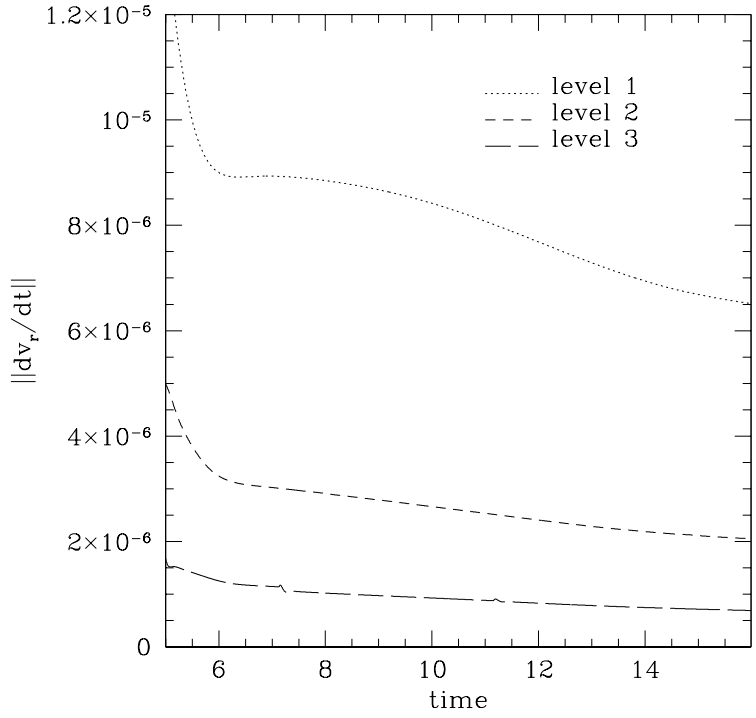

Figure 4.18: Convergence of dv^r/dt for the relativistic magnetized spherical accretion problem. density. The convergence of the time derivative of the radial velocity. We see that the solution is converging to zero. As with the hydrodynamic spherical accretion problem we see that the solution is converging to the steady state, $dv^r/dt = 0$. Only $5 \leq t \leq 16$ is shown for emphasis.

Although the magnetic field flux is identically zero in closed form, we will require the use of a constraint enforcing technique due to the numerical errors, especially when larger magnetic fields are studied. When larger β_p was considered, it was found that the magnetic field constraint could be freely evolved; however, for smaller β_p, the magnetic field constraint violations were much more obvious and without enforcement the system behaved unpredictably. Tests show that there are limitations on the magnitude of the magnetic field that can be evolved using our code. Therefore, in this study we will need to restrict our attention to plasma beta, $\beta_P > 1$.

CHAPTER 5

RESULTS

We investigate the relativistic Bondi–Hoyle problem in the ultrarelativistic and magnetohydrodynamical fluid background. We present new results for 6 different configurations.

1. Axisymmetric ultrarelativistic hydrodynamic accretion onto an $a = 0$ black hole.
    - The fluid flow at infinity is uniform in the $\hat{z}$-direction.
    - The internal energy of the fluid is sufficiently large that we may neglect the rest mass density.
    - The fluid is flowing past a stationary, non-rotating black hole.
2. Axisymmetric ultrarelativistic hydrodynamic accretion onto an $a \neq 0$ black hole.
    - The fluid is as described above, but the black hole is rotating with a rotation axis aligned with the asymptotic fluid velocity.
3. Infinitely thin-disk ultrarelativistic hydrodynamic accretion onto an $a = 0$ black hole.
    - The fluid is similar to the first case except that the fluid is restricted to flow in the equatorial plane.
    - The fluid is flowing past a stationary, non-rotating black hole.
4. Infinitely thin-disk ultrarelativistic hydrodynamic accretion onto an $a \neq$ black hole.
    - The Fluid is similar to the previous case except that the fluid is flowing past a rotating black hole with an axis of rotation orthogonal to the fluid plane.
5. Axisymmetric magnetohydrodynamic accretion onto an $a = 0$ black hole.
    - The fluid is now embedded with a magnetic field that is uniform and parallel to the $\hat{z}$-direction at infinity.
    - The rest mass density contributes to this fluid.

- The fluid is flowing past a stationary, non-rotating black hole.

6. Axisymmetric magnetohydrodynamic accretion onto an $a \neq 0$ black hole.

   - The fluid is the same as above, but this time flowing past a rotating black hole whose rotation axis is parallel to the $\hat{z}$-direction.

The ultrarelativistic studies show a range of fluid flow patterns, referred to as the flow morphology, that differs from the previously studied hydrodynamic flows for some parameters. In particular, when Font *et al.* [1], [2], and [3], hereafter referred to as FI981, FI982, and FI99 respectively, studied a similar setup, they consider the relativistic set of hydrodynamic equations of motion including the contributions of the baryon rest mass density. In our study we assume that the rest mass density is negligible when compared to the internal energy of the fluid and we neglect any conservation of the baryon density.

Our studies present a new condition where we include the magnetic field contributions in the axisymmetric configuration. Including the evolution of the embedded magnetic field makes our results more general, and perhaps more broadly applicable to astrophysical phenomenon than existing models.

Before we proceed to present our results, we introduce the mathematical description of the measurements made. We consider monitoring different accretion rates including mass accretion, energy accretion, and momentum accretion rates, described below.

5.1 Accretion Phenomenon and Accretion Rates

To determine the behaviour of the accretion solution, we consider the accretion rates for several different fluid quantities into the black hole. In particular, we consider the accretion rates for the energy, the radial momentum, the angular momentum, and, when studying the GRMHD system, the mass [8, 1, 2, 3, 91]. In the cases where the magnetic field is embedded in the background fluid, we also consider the energy and momentum accretion of the magnetic fields alone. Below we describe the methods of calculating these properties for any given system.

5.1.1 Rest Mass Accretion Rate

The rest mass accretion rate is calculated from the gauge invariant mass [1, 2]. This quantity is derived from the volume integral of the relativistic density of the fluid, $D = D(t, r, \theta)$ over a given proper volume, $\mathcal{V}$,

$$m(t) = \int_{\mathcal{V}} \sqrt{\gamma} D dV. \tag{5.1}$$

If we differentiate with respect to time and then substitute the conservation of baryon number (2.88), we have an expression for the baryon accretion rate, across a closed surface;

$$\frac{dm}{dt} = \dot{m} = \int_{\mathcal{V}} \partial_t \sqrt{\gamma} D dV = -\int_{\mathcal{V}} \partial_i \sqrt{-g} D v^i dV = -\oint \sqrt{-g} D v^i dS_i. \tag{5.2}$$

We would then scale this expression with the mass per baryon. In our case we choose this mass to be unity, leaving the expression unaltered. In the event that the fluid accretes in a steady state the closed integral may be evaluated over any spatial surface in the domain. For simplicity, we use the surface defined by the Schwarzschild radius, $R_s = 2\mathrm{M}$, for all measurements, since this point is the same for all equally massive black holes studied in this survey. This will allow us to compare the accretion rates for all black holes in our survey. We use geometric units in which we set $G = c = M = 1$, where M is the mass of the black hole.

5.1.2 Stress-Energy Accretion Rates

In relativistic systems, Killing vectors arise from symmetries and imply the existence of conserved quantities, as discussed in Chap. 2. The conserved quantities we are interested in are determined by,

$$Q^{(\iota)}(t) = \int_{\mathcal{V}} \sqrt{-g} T^{\mu\nu}\, {}^{(\iota)}\xi_\mu n_\nu dV, \tag{5.3}$$

where ${}^{(\iota)}\xi_\mu$ are the Killing vectors, n_ν is the 3+1 normal covector as seen in (2.12), and $\mathcal{V}$ is some proper volume of spacetime. In the case of a Kerr and Schwarzschild spacetimes, we have a temporal and an azimuthal Killing vector. The temporal Killing vector indicates that the energy of the system is conserved and the azimuthal indicates a conservation of angular momentum.

5.1.3 Energy Accretion Rate

Using the temporal Killing vector, ${}^{(t)}\xi_\mu$ in (5.3) we get;

$$E(t) = \int_{\mathcal{V}} \sqrt{-g} T^{tt} \alpha dr d\theta d\phi = \int_{\mathcal{V}} \sqrt{-g} \frac{E}{\alpha^2} \alpha dr d\theta d\phi = \int_{\mathcal{V}} \sqrt{\gamma} E dr d\theta d\phi. \tag{5.4}$$

by differentiating with respect to time we get the energy accretion rate through some spatial surface. We are specifically interested in the energy accretion rate into the black hole, so we define our surface to be the surface defined by the Schwarzschild radius.

$$\begin{aligned}
\frac{dE}{dt}(t) = \dot{E} &= \int_{\mathcal{V}} \partial_t \left(\sqrt{\gamma} E\right) dr d\theta d\phi \\
&= \int_{\mathcal{V}} \partial_i \left(\sqrt{-g} \left(E\hat{v}^i + Pv^i - \alpha b^t \mathcal{B}^i / W\right)\right) dr d\theta d\phi + \int_{\mathcal{V}} \sqrt{-g} \left(T^{\mu t} \alpha_{,\mu} - T^{\mu\nu} \Gamma^t_{\nu\mu}\right) dr d\theta d\phi \\
&= \int_{\partial\mathcal{V}} \sqrt{-g} \left(E\hat{v}^i + Pv^i - \alpha b^t \mathcal{B}^i / W\right) d\theta d\phi + \int_{\mathcal{V}} \sqrt{-g} \left(T^{\mu t} \alpha_{,\mu} - T^{\mu\nu} \Gamma^t_{\nu\mu}\right) dr d\theta d\phi.
\end{aligned} \tag{5.5}$$

Where we use Eqn. (2.97) to express the temporal energy derivative in terms of the energy flux and the geometric source term, and recall that we define $\hat{v}^i = v^i - \beta^i/\alpha$. We also use Gauss' theorem to convert the volume integral of the divergence of the flux to a surface integral. $\partial\mathcal{V}$ denotes the surface of the volume $\mathcal{V}$ that is defined by the Schwarzschild radius. When we discuss the energy flux in the ultrarelativistic system we set $\mathcal{B}^i = 0$.

5.1.4 Azimuthal Angular Momentum Accretion Rate

The angular momentum transfer from the fluid background onto the black hole is defined in a similar fashion as the energy accretion rate. In this calculation we use the azimuthal Killing vector ${}^{(\phi)}\xi_\mu$, which gives us,

$$\frac{dQ^{(\phi)}}{dt} = \dot{P}_\phi(t) \quad = \quad -\int_{\partial\mathcal{V}} \sqrt{-g} T^r{}_\phi d\theta d\phi + \int_{\mathcal{V}} \sqrt{-g} T^{\mu\nu} \left(g_{\nu\phi,\mu} - \Gamma^\lambda{}_{\mu\nu} g_{\lambda\phi}\right) dr d\theta d\phi. \tag{5.6}$$

We use the azimuthal component of Eqn. (2.96) to describe the temporal derivative of the azimuthal angular momentum in terms of the divergence of the flux, then use Gauss' theorem to convert the volume integral of the divergence of the flux to a surface integral.

In each of the accretion rates defined above we have a flux contribution that is an integral over

the surface of a volume which we will denote T_1, and a volume integral of the geometric source terms, denoted T_2. All accretion calculations then have the form,

$$\dot{P}_j = T_1 + T_2. \tag{5.7}$$

The spatial volume over which we take this integral is the volume between the event horizon, $r_{\rm EH}$ and the radial location of which we make our calculation, R_s.

$$T_2 = \int_0^{\pi} \int_0^{2\pi} \int_{r_{\rm EH}}^{R_s} \text{Source dV}. \tag{5.8}$$

We have used Source to represent the expression inside the volume integral from Eqns (5.5) and (5.6).

5.1.5 Radial Momentum Accretion Rate

As the black hole travels through the fluid background it focuses the matter not immediately accreted behind it by the gravitational interaction between the matter and the black hole. The accumulated matter could begin to have its own gravitational effect on the black hole. This would be realized through gravitational drag. Chandrasekhar referred to this effect as dynamical friction [152, 153, 154, 155, 30]. In previous papers by Font *et al.* [2, 3] relativistic drag has been defined to be,

$$\dot{P}_r(t) = -\int_{\mathcal{V}} \partial_t \left(\sqrt{-g} T^t{}_r\right) dr d\phi d\theta \tag{5.9}$$

$$= -\int_{\partial\mathcal{V}} \sqrt{-g} T^r{}_r d\theta d\phi + \int_{\mathcal{V}} T^{\mu\nu} \left(g_{\nu r,\mu} - \Gamma^{\lambda}{}_{\mu\nu} g_{\lambda r}\right) dV, \tag{5.10}$$

where $\mathcal{V}$ is the proper volume enclosed by the proper surface $\partial\mathcal{V}$.

Unfortunately, this is a misconception as this calculation would necessarily require that in the asymptotic limit we have a radial Killing vector, and even then this would not correspond to a relativistic drag. While referring to this calculation as a measure of drag is unphysical, this integral does provide another calculation that may expose instabilities in the flow. We perform this calculation so that we may compare our results to those from previously published works. We refer to the results from Eqn. (5.10) as the radial momentum accretion rate, but caution the reader

that no physical information can be extracted from this calculation.

Rescaling

The various accretion rates in this chapter were rescaled with respect to the asymptotic Bondi accretion rate. Petrich *et al.* [8] calculated their accretion rates at the accretion radius, and scaled their calculated accretion rates by using the Bondi accretion rate as evaluated at the transonic radius. Since our measurements were recorded at the Schwarzschild radius we needed to use a different scaling value. For each geometric configuration described below, the calculation was repeated using $v_\infty = 0$ which corresponds to the static Bondi accretion problem. For the cases with rotating black holes the rescaling factor was taken to be the Bondi solution for the non-rotating black hole, as the Bondi accretion problem does not take into account the rotation of a black hole.

This ends our description of the accretion rates studied. We now present the initial conditions and results for the different geometric configurations introduced in Chap. 2. First, we investigate the ultrarelativistic hydrodynamic (UHD) systems in four different configurations;

- axisymmetric accretion onto a spherically symmetric black hole, ($a = 0$, $\Gamma = 4/3$, $\phi = \text{const}$)
- axisymmetric accretion onto a axisymmetric black hole, ($a \neq 0$, $\Gamma = 4/3$, $\phi = \text{const}$)
- non-axisymmetric infinitely thin-disk accretion onto a spherically symmetric black hole, ($a = 0$, $\Gamma = 4/3$, $\theta = \pi/2$)
- infinitely thin-disk accretion onto an axisymmetric black hole, ($a \neq 0$, $\Gamma = 4/3$, $\theta = \pi/2$).

Recall that we define Γ to be the adiabatic constant, and that the black hole is parameterized by its mass M which for our purposes is set to unity, as well as its spin parameter $0 \leq a < 1$. When we state $\phi = \text{const}$ it means that we are describing the space time using only the radial and polar coordinates (r, θ) and choosing to set the ϕ coordinate to be constant. In axisymmetric systems setting $\phi = 0$ is a matter of convenience, and is not a restriction on the system. When $\theta = \pi/2$ we are describing the matter in spacetime using the radial and azimuthal coordinates (r, ϕ) and holding the polar coordinate fixed at $\pi/2$ so all matter is in the equatorial plane of the black hole. Unlike axisymmetry, holding θ fixed is a restrictive assumption.

In the last part of this chapter, we discuss the axisymmetric accretion of a magnetohydrodynamic fluid;

- axisymmetric accretion onto a spherically symmetric black hole, ($a = 0$, $\Gamma = 4/3, 5/3$, $\phi =$ const)
- axisymmetric accretion onto a axisymmetric black hole, ($a \neq 0$, $\Gamma = 4/3$, $\phi =$ const)

In all simulations we will choose a set of asymptotic velocities for the fluid flowing past the black hole. The values used are referenced in the appropriate sections.

5.2 Axisymmetric Bondi–Hoyle UHD Accretion Onto a Black Hole

In this configuration, our state variables $\mathbf{q}$ as defined in Eqn. (2.123) take on the coordinate dependence; $\mathbf{q} = \mathbf{q}(t, r, \theta)$. See Fig. 5.1 for a graphical representation of this geometry.

Initially, an infinite uniform fluid medium surrounds the black hole. We parametrize the properties of the surrounding fluid by the asymptotic speed, v_∞, the adiabatic constant Γ, and the asymptotic speed of sound c_s^∞ [8, 1]. We write the initial conditions for the fluid 3-velocity, v^i in the Kerr–Schild coordinates as [1];

$$v^r(0, r, \theta) = \frac{1}{\sqrt{g_{rr}}} v_\infty \cos\theta \tag{5.11}$$

$$v^\theta(0, r, \theta) = -\frac{1}{\sqrt{g_{\theta\theta}}} v_\infty \sin\theta \tag{5.12}$$

$$v^\phi(0, r, \theta) = 0. \tag{5.13}$$

where $g_{\theta\theta} = g_{\theta\theta}(r)$ and $g_{rr} = g_{rr}(r)$ are elements of the metric tensor. This velocity configuration corresponds to a black hole travelling with a velocity v_∞ in the Cartesian $\hat{z}$-direction, as seen by an observer at infinity. We can easily verify that the square of the velocity as expressed above reduces to $v^2 = v_\infty^2$. We define our speed of sound to correspond to the ultrarelativistic system (2.58) [33, 9, 1];

$$c_s^\infty = \sqrt{\Gamma - 1}. \tag{5.14}$$

Although the speed of sound is constant through the entire UHD domain, we keep the superscript denoting the asymptotic value for consistency with other works such as those presented in FI981.

Since the characteristics of the system are independent of the pressure, the solution to the

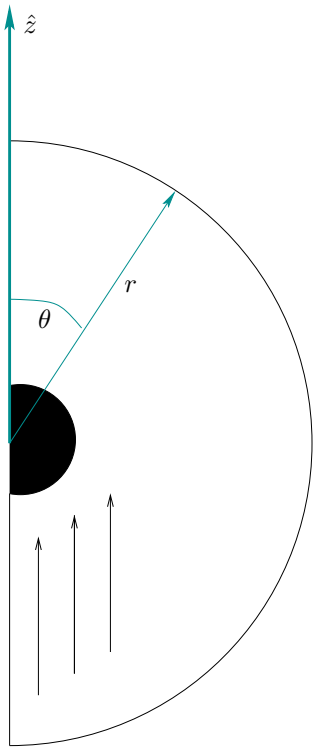

Figure 5.1: The axisymmetric Bondi–Hoyle accretion setup. The radial coordinate increases away from the "centre" of the black hole. The angular coordinate increases from top ($\theta = 0$) to bottom ($\theta = \pi$). The arrows inside of the the half-disk show the direction of fluid flow. This geometry is valid for any $\phi = \text{const}$. Events in the black shaded region are inside the event horizon/black hole. The flow is in the positive $\hat{z}$ direction. We use inflow boundary conditions at $r_{\max}$ for $\pi/2 \leq \theta \leq \pi$. For the boundary $r_{\max}$, $0 \leq \theta < \pi/2$ we use extrapolated outflow boundary conditions. The boundary at $r_{\min}$ was also treated using extrapolated outflow. The angular boundaries $\theta = 0$ and $\theta = \pi$ used reflective boundary conditions.

Model	v_∞	$\mathcal{M}$	$\mathcal{M}^R$
U1	0.3	0.5	0.4
U2	0.6	1.0	1.1
U3	0.7	1.2	1.4
U4	0.9	1.6	2.9

Table 5.1: The parameters used for systems studied in the ultrarelativistic ($a = 0$, $\Gamma = 4/3$, $\phi = \text{const}$) regime. We consider four specific cases in detail, when the flow is asymptotically subsonic (U1), the flow is marginally supersonic (U2), and when the flow is supersonic (U3 and U4). The adiabatic constant $\Gamma = 4/3$, corresponds to $c_s^\infty = \sqrt{1/3} \sim 0.57$. The third column records the asymptotic Mach number for the flow, and the last column records the relativistic Mach number as described in Eqn. (2.129).

equations of motion will scale with the pressure. Thus, without loss of generality, we take $P_\infty = 1$. When the simulation is turned on, the system undergoes a transition period until a steady state is reached. Once this transition time has passed, we expect to see the various accretion rates become constant if the flow stabilizes.

For the radial boundary condition in the upstream side of the domain ($r = r_{\rm max}$, $\pi/2 < \theta \leq \pi$), we used an inflow boundary condition. Recall that the inflow condition holds the values of all variables constant to the values prescribed at initialization. For the radial boundary located inside the event horizon, $r = r_{\rm min}$ as well as in the downstream region ($r = r_{\rm max}$, $0 \leq \theta \leq \pi/2$) we used extrapolated outflow for all state variables. To treat the polar boundaries numerically, we used reflection symmetry, also known as a wall boundary condition. The techniques for evaluating these boundaries are described in Chap. 3. We also note that the value of $r_{\rm max}$ is twice as large as those considered in Font *et al.* [1]; this was necessary to capture the physics while ensuring the solutions of the equations of motion are not being adversely affected by boundary conditions.

All simulations were performed using 400×160 resolution for 10^5 time steps, utilizing parallel techniques via PAMR [156] and the message passing interface (MPI)[16] to increase the speed of the individual runs. We use the domain $r_{\rm min} \leq r \leq r_{\rm max}$, $0 \leq \theta \leq \pi$.

All ultrarelativistic fluids are parameterized using parameters the spin parameter of the black hole, a, the asymptotic speed of the fluid, v_∞, and the adiabatic constant, Γ. In our study we restrict our attention to $\Gamma = 4/3$ fluids as mentioned in Sec. 2.6.2.

5.2.1 Axisymmetric Accretion: a=0

We perform a parameter survey over the asymptotic flow velocity, v_∞, in the ultrarelativistic regime, investigating the parameters listed in Table 5.2. The previous work presented in FI981 considered the mass accretion rate as one of the measures to determine a steady state flow. We consider a system in which the baryon rest mass density, ρ_0, is negligible compared to the energy of the fluid, so we are not able to directly measure the mass accretion rate. Instead, we take advantage of the timelike Killing vector and measure the energy accretion rate.

When we simulate model U2 in Table 5.1, we end up with a system where the tail shock, which is present for a brief period during the transient solution, detaches from the black hole as the high pressure region in the downstream region slowly migrates around to the front and makes contact with the axis of symmetry. By performing convergence testing and using different boundary conditions, we determined that this was a physical feature of the simulation. We refer the reader to the appendix Fig. A.1 for a time evolution of this system. Model U2 develops a steady bow shock just beyond the upstream side of the black hole.

Although some of the fluid falls into the black hole, there is a pressure build-up around the black hole, most dominantly on the downstream side. On the upstream side this resembles the spherical accretion as seen in Chap. 4. As the simulation proceeds the fluid pressure downstream overwhelms the fluid flowing on the upstream side and begins to wrap around the black hole, forming a pressure build-up in the upstream side as seen in the appendix in Fig. 5.8.

In the moderately supersonic and subsonic cases, the built-up pressure eventually overcomes the pressure from the fluid at the front of the black hole, pushing the fluid back upstream. This is displayed in figure Fig. A.1 for model U2. If the black hole travels at subsonic speeds, such as in model U1, an initial wave propagates out of the system, leaving the domain we calculate, and the resulting flow reaches a steady state, with no shock.

When the black hole has a faster asymptotic velocity, as in models U3 and U4, we again have a tail shock and the system behaves much like the hydrodynamic counterparts investigated by FI981 [1]. See Fig. A.2 for a time evolution of model U4. For model U4, the fluid flowing past the black hole puts enough pressure on the matter behind the black hole to maintain an accretion column. A cross section of the pressure profile may be seen in figure 5.2, where we see that the pressure profile upstream does not appear to smoothly reach the upstream boundary condition. To ensure that

[16] https://computing.llnl.gov/tutorials/mpi/

this propagation of internal effects to the boundary does not alter the interior physics, we repeated the simulation using a value of $r_{\max} = 100$. Using the larger maximum radius, the upstream and downstream profiles show that the pressure at the boundary matches the asymptotic pressure. The resulting flow is stable. The steady state pressure profile may be seen in Fig. 5.9.

The morphology of our results for models U3 and U4 agree with the behaviour of the relativistic hydrodynamic accretion process observed in FI981 [1].

The resulting energy and radial momentum accretion rates for models U2, U3, and U4 are seen in Fig. 5.3. A convergence test is performed using slices through the domain across defining features such as shock fronts or the angle of attachment of the tail shock to the black hole. The results of these tests for model U4 and U2 may be seen in Figs. 5.5 and 5.6 respectively. These tests indicate that the code used to simulate the fluid evolution converges, with respect to resolution, to a physical solution. Fig. 5.5 shows that as the resolution of the simulation is increased, the opening angle of the Mach cone converges to a fixed value, a requirement of a steady state accretion flow. Fig. 5.6 converges, with resolution, to a bowshock. The convergence tests presented indicate that the features in the fluid is not merely a numerical artifact, but a real physical feature of the system under investigation.

A snapshot of the evolution of the pressure field at time $t = 1000$ for velocities $v_\infty = 0.6$, 0.9 may be seen in Figs. 5.8 and 5.9. We see in Fig. 5.8 the bowshock present in the upstream region of the calculated domain. This shock front stabilizes and reaches a steady state. In previous simulations such a phenomenon was not present [1]. It was speculated that the formation of a bow shock was a necessary condition for the presence of instabilities, which did not occur in previous studies. We have found a system (model U2) where bowshocks are present. Although model U2 was determined to reach a steady state, a wider parameter survey may reveal other similar systems that do experience instabilities. For $v_\infty = 0.3$, the flow produced a wave travelling upstream which interfered with the upstream boundary conditions, this simulation was terminated earlier at $t = 300M$. Models U3 and U4 exhibit similar flow morphologies as seen in [1].

5.2.2 Axisymmetric Accretion: a≠0

In this series of simulations, we extend the axisymmetric accretion problem to allow the black hole to rotate along the axis of the flow. Accretion onto an axisymmetric rotating black hole has been performed in the specialized case for the adiabatic constant $\Gamma = 2$ by Petrich [35]. For $\Gamma = 2$ fluids

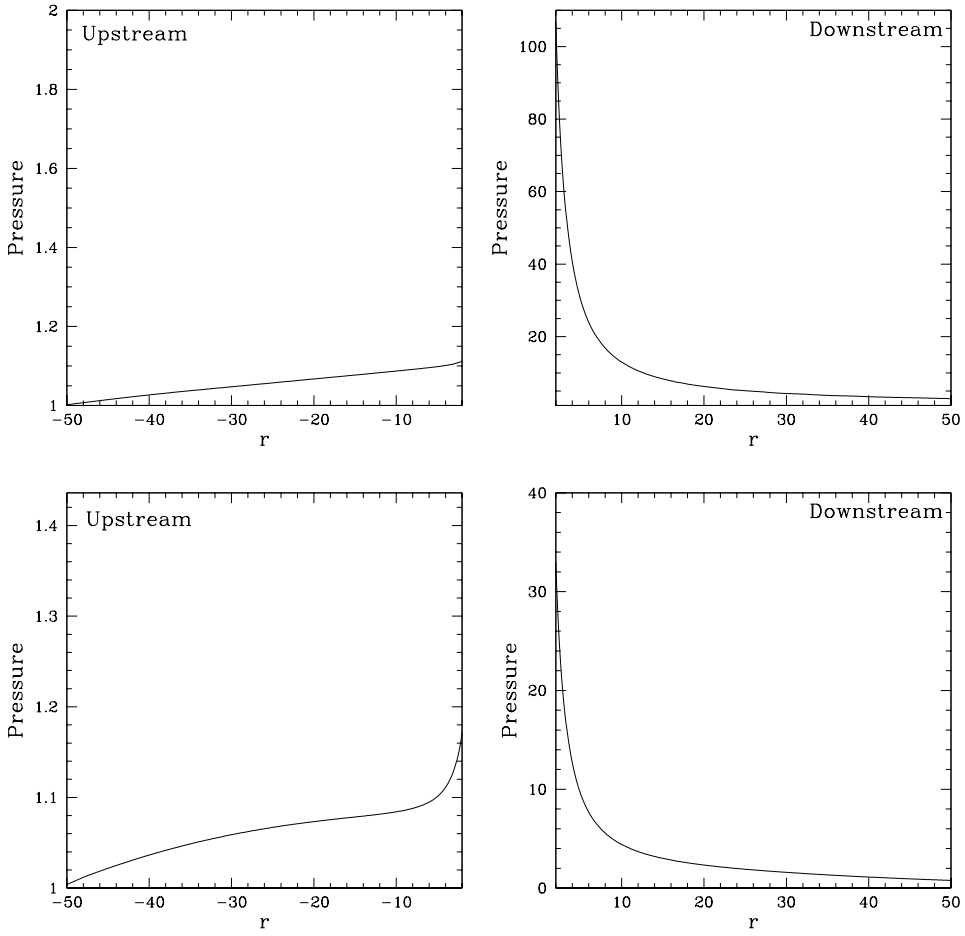

Figure 5.2: Ultrarelativistic pressure profile in the upstream (left column) and downstream (right column) regions for model U3 (top) and U4 (bottom). We see that the pressure in the upstream region of the black hole is small by comparison to the pressure in the wake in the downstream region. The image on the left is magnified to show that there is a slight increase in pressure as the fluid reaches the black hole. As the asymptotic velocity of the black hole increases the upstream pressure deviates less from the pressure defined at the boundaries. Since the upstream pressure profile does not smoothly agree with the upstream boundary condition, a larger domain was required for simulations of slower black holes.

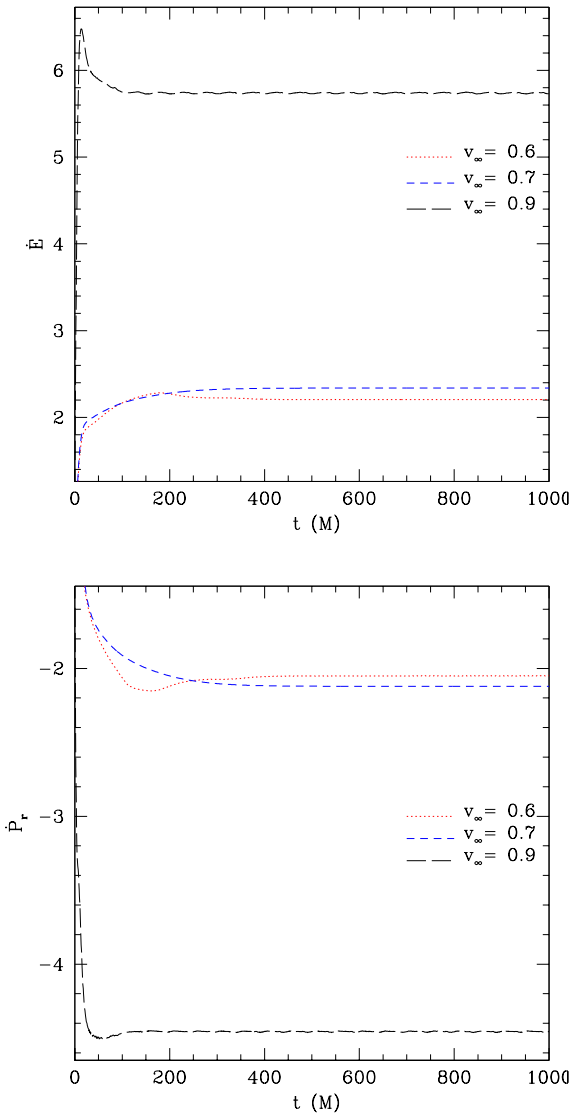

Figure 5.3: Axisymmetric ultrarelativistic energy accretion (top) and radial momentum accretion (bottom) rates for $\Gamma = 4/3$ for models U2, U3, and U4. The faster the black hole is travelling the more energy it accretes, and the larger the radial momentum accretion rate becomes. This is in agreement with the results from Font *et al.* [2].

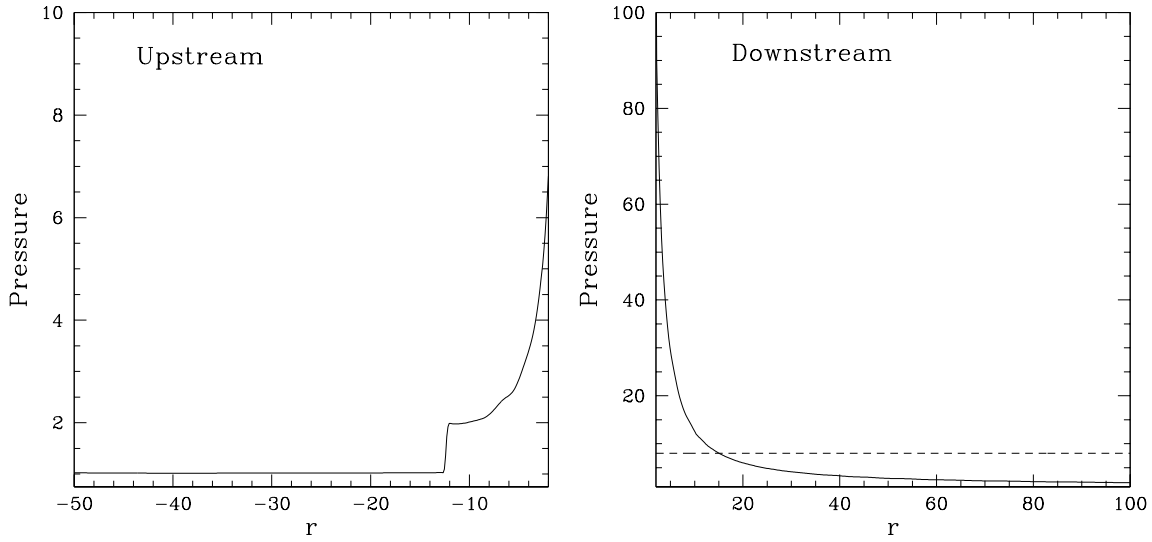

Figure 5.4: Ultrarelativistic pressure profile upstream (top) and downstream (bottom) for model U2 with radial domain $r_{\rm S} \leq r \leq 100$. We see that the pressure in the upstream region of the black hole is small by comparison to the pressure in the downstream region, or wake. The pressure profile in the upstream region indicates that there is a shock in the upstream region of the black hole. This detached shock is a bow shock that forms when the black hole is travelling at marginally supersonic speeds, $v_\infty \sim c_s^\infty$. This bow shock does not exist when we investigate black holes with a larger asymptotic speed as seen in the upstream profile for the black hole with $v_\infty = 0.9$, as seen in Fig. 5.9. The above profiles were taken at $t = 1000M$. With the larger radial domain, we see that the pressure profile smoothly matches the upstream boundary conditions. The dashed line in the downstream profile emphasizes the maximum pressure of the fluid surrounding the black hole in the upstream side.

Model	a	v_∞	$\mathcal{M}$	$\mathcal{M}^R$
U6	0.5	0.6	1.04	1.06
U7		0.9	1.56	2.91
U8	0.9	0.6	1.04	1.06
U9		0.9	1.56	2.91
U10	0.99	0.6	1.04	1.06
U11		0.9	1.56	2.91

Table 5.2: The parameters used for systems studied in the ultrarelativistic ($a \neq 0$, $\Gamma = 4/3$, $\phi = \text{const}$) regime. We consider two specific cases in detail, when the flow is marginally supersonic ($v_\infty = 0.6$), and when the flow is supersonic ($v_\infty = 0.9$). The adiabatic constant $\Gamma = 4/3$, corresponds to the speed of sound $c_s^\infty = \sqrt{1/3} \sim 0.57$. As in table 5.1 we record the Mach numbers for reference.

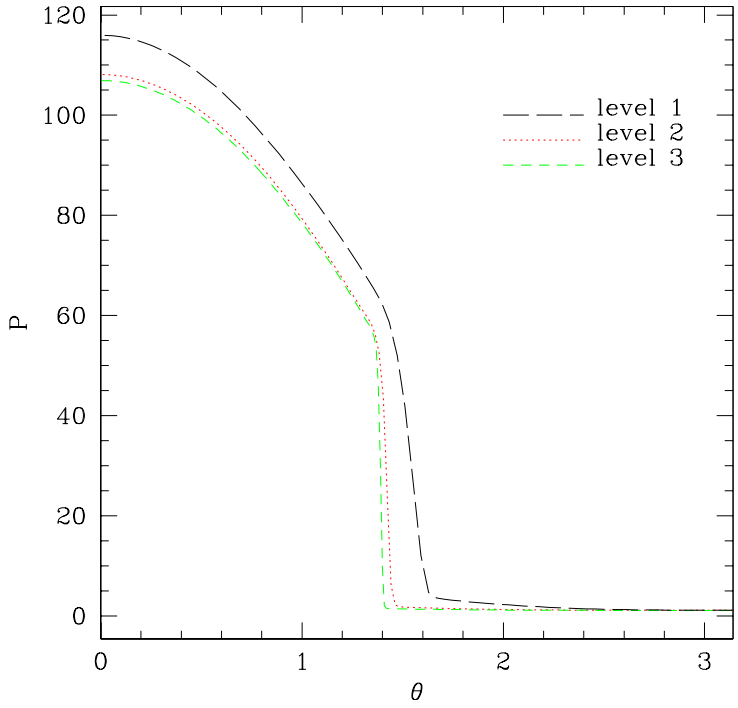

Figure 5.5: Ultrarelativistic pressure profile at the event horizon for the axisymmetric evolution model U4 for three different resolution levels. We see that the attachment angle at the event horizon is converging on the solution $\theta \sim 1.4$. The resolution changes are $4:2:1$. The lowest resolution (level 1) is $N_r \times N_\theta = 200 \times 80$. For our convergence testing, we simultaneously scale both spatial dimensions by two for each level whereas previous authors only consider scaling the resolution of the angular dimension.

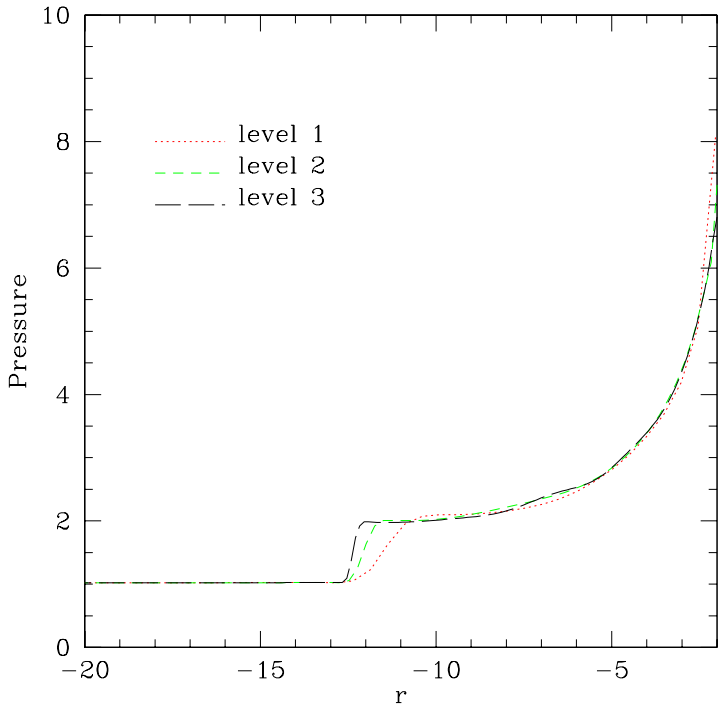

Figure 5.6: Ultrarelativistic pressure profile in the upstream region for the axisymmetric evolution model U2 for three different resolution levels. We see that the front of the bow shock converges to $r \sim 13$ at time $t = 1000M$. The resolution changes are $4 : 2 : 1$. The system is converging on a solution. The lowest resolution (level 1) is 200×80. Only the radial domain $2 \leq r \leq 20$ is plotted to show more detail.

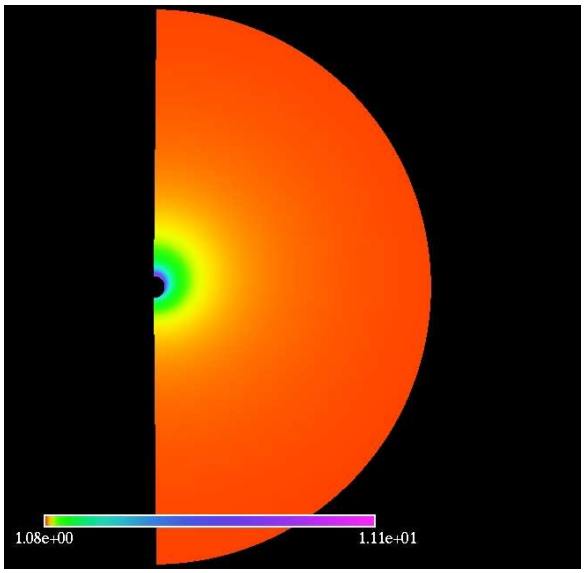

Figure 5.7: Ultrarelativistic pressure profile for model U1. This configuration does not have a shock wave, which is in agreement with other subsonic studies [8, 1].

the speed of sound is unity, and thus supersonic flows for these fluids are impossible. Other studies are mentioned in several papers [8, 1], but we have found no evidence that this problem has been studied numerically for less stiff fluids *i.e.* smaller Γ. Polytropic fluids with an adiabatic constant $\Gamma = 2$ can be used to represent baryons travelling though meson vector fields, or are also commonly used for some neutron star models [9]. In this thesis, we are considering fluids with large internal energy, but not sufficiently high that $c_s^\infty = 1$.

The initial conditions as presented in (5.2) can also be used for a fluid around a rotating black hole. We investigate the parameters used in the previous section for models U2 and U4, with the addition of a rotation parameter taking the values of $a = 0.5$, $a = 0.9$, and $a = 0.99$. These are summarized in Table 5.2.

For the parameters investigated, we found that the accretion rates reach a steady state. The energy accretion rates for models U6, U8, and U10 may be seen in Fig. 5.13, while the energy accretion rates for models U7, U9, and U11 are seen in Fig. 5.14. We see that the higher velocity configurations reach a steady state solution faster, which is in agreement with the studies performed with $a = 0$ as well as the hydrodynamic non-rotating study performed in FI981. Just as in FI981 we find that the accretion rates oscillates around some central value, but as the resolution increases the amplitude of the oscillations diminish. We turn the reader's attention to Fig. A.3 for a time

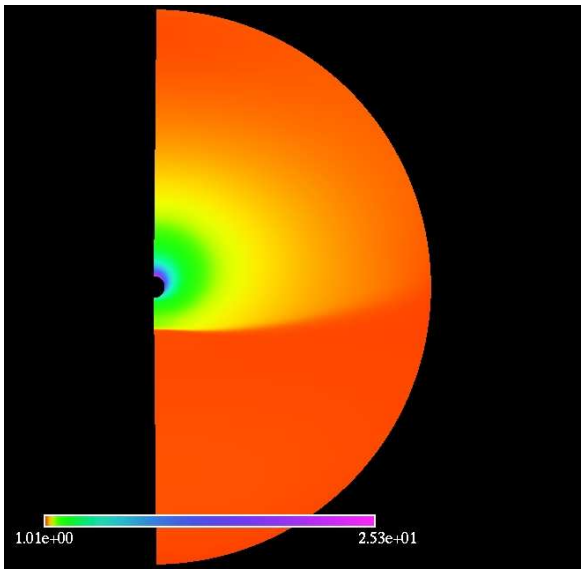

Figure 5.8: Ultrarelativistic pressure profile onto a spherically symmetric black hole. This image is a marginally supersonic evolution model U2. Note the presence of the bow shock close to the front of the black hole. The profile of the bow shock is investigated in more detail in Figs. 5.4 and 5.6.

evolution of model U7, and Fig. A.5 for model U11.

In Fig. 5.10 we see a cross section of the pressure field at $\theta = \pi$ (upstream), and $\theta = 0$ (downstream). We compare the upstream and downstream profiles for models U4, U7, and U9. The effects of rotation are only truly distinguishable from models with $a = 0$ for models with spin parameter $a > 0.5$. When we consider a cross section through $r = 4$ in Fig. 5.11, we compare the opening angles of the tail shock. As with the upstream and downstream profiles, we can only marginally distinguish the cross section for models U4 and U7, while model U9 has a wider opening angle. Convergence tests for this geometry may be seen in figure 5.12.

This concludes our work in axisymmetric ultrarelativistic accretion onto a black hole. We now turn our attention to the non-axisymmetric infinitely thin-disk model introduced in Sec. 2.7.

5.3 Non-axisymmetric Infinitely Thin-Disk Ultrarelativistic Accretion Onto a Black Hole

In this configuration the black hole is travelling through an infinitely thin uniform fluid background. The orientation of the black hole is such that the rotation axis is orthogonal to the direction of

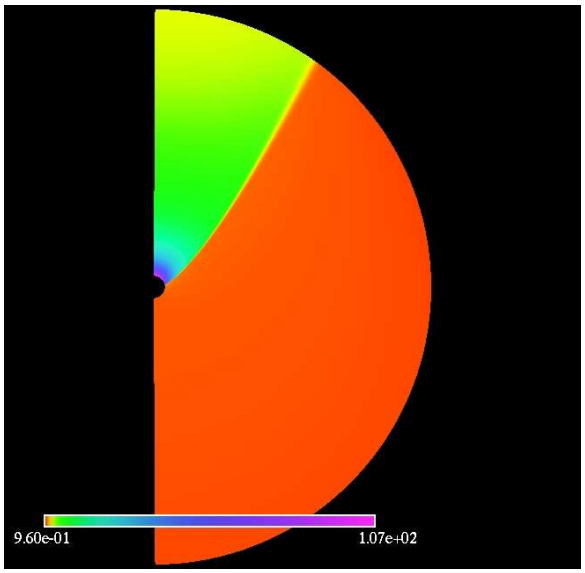

Figure 5.9: Ultrarelativistic energy accretion onto a spherically symmetric black hole. Here we have a snapshot of the black hole in model U4 at time $t = 1000M$. The black hole is in the highly supersonic regime. This plot shows evidence of the typical tail shock experienced in this type of flow [1].

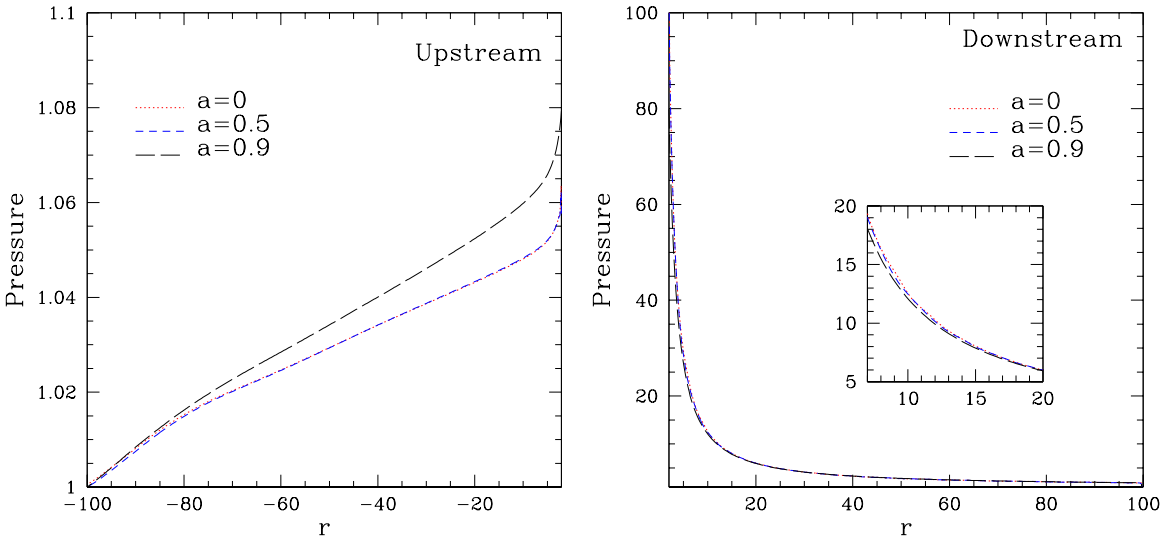

Figure 5.10: Ultrarelativistic pressure profiles for the rotating axisymmetric accretion problem for $v_\infty = 0.9$, models U4, U7, U9. We see that for black hole spin parameters $a = 0$ and $a = 0.5$ the downstream (bottom) pressure profiles are only marginally distinguishable. As the spin is increased to $a = 0.9$, we see a much larger pressure in the upstream region of the black hole (top). The profiles on the downstream region become slightly sharper when the spin parameter in increased.

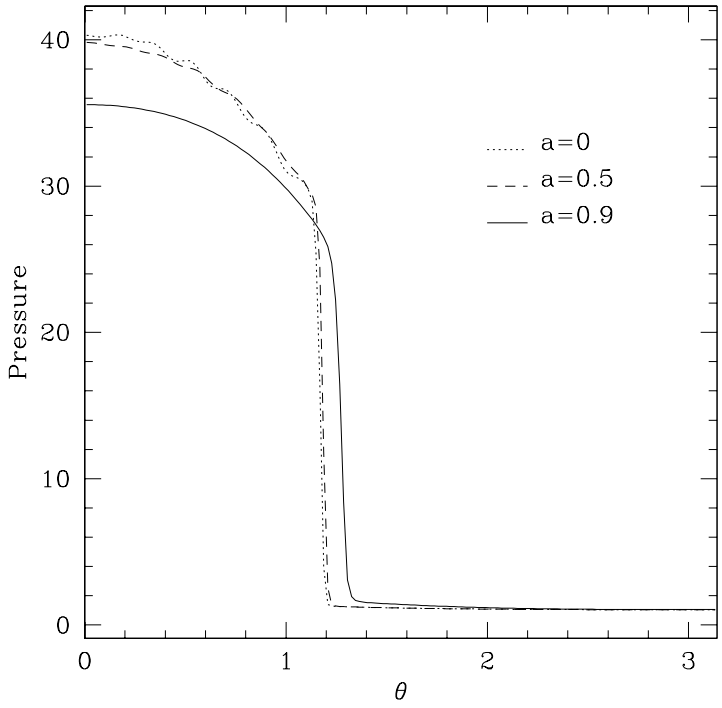

Figure 5.11: Ultrarelativistic axisymmetric pressure profile $P(1000, 4, \theta)$ for a section through the tail shock at $r = 4$M and asymptotic velocity $v_\infty = 0.9$, models U4, U7, U9. We see the opening angle of the tail shock widens as the spin parameter in increased. Just as in the pressure profile along the $\theta = 0, \pi$ lines are altered by the spin parameter. The opening angle changes slightly for a spin $a = 0.5$ (dashed line) black hole as compared to a spin $a = 0$ (dotted line) black hole, but when we consider an $a = 0.9$ (solid line) black hole we see a larger shock opening angle. We also see that as the spin increases the pressure profile on $r = 4$M becomes smoother and the amplitude decreases.

Model	v_∞	$\mathcal{M}$	$\mathcal{M}^R$
U12	0.6	1.04	1.06
U13	0.9	1.56	2.91

Table 5.3: The parameters used for systems studied in the ultrarelativistic ($a = 0$, $\Gamma = 4/3$, $\theta = \pi/2$) regime. We consider two specific cases in detail, when the flow is marginally supersonic (U12), and when the flow is supersonic (U13). The adiabatic constant $\Gamma = 4/3$, corresponds to $c_s^\infty = \sqrt{1/3} \sim 0.57$. The last two columns record the Mach number and relativistic Mach number for the flow.

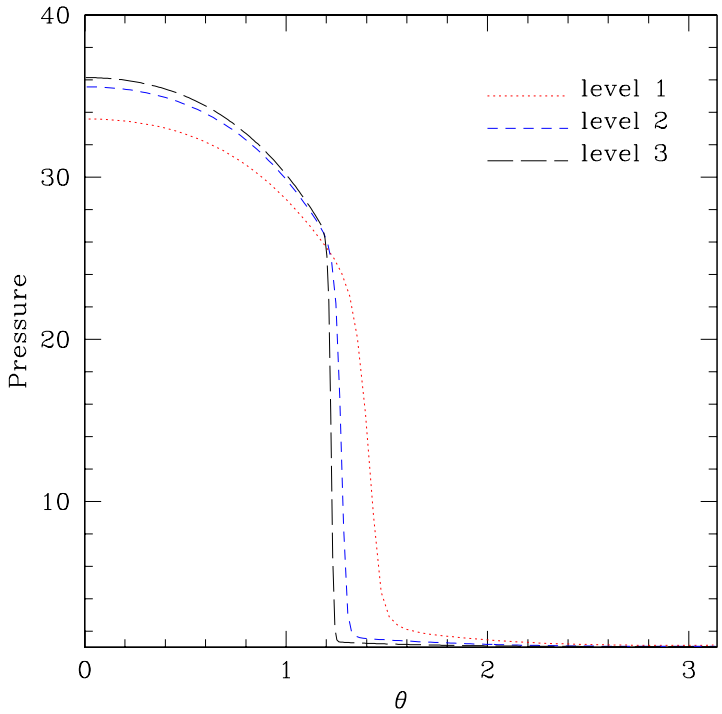

Figure 5.12: Ultrarelativistic axisymmetric pressure profile $P(1000, 4, \theta)$ for a section through the tail shock at $r = 4$ for model U9. We see the opening angle of the tail shock converges to $\theta \sim 1.2$. The pressure tends to a maximum of $P_{\max} \sim 36$.

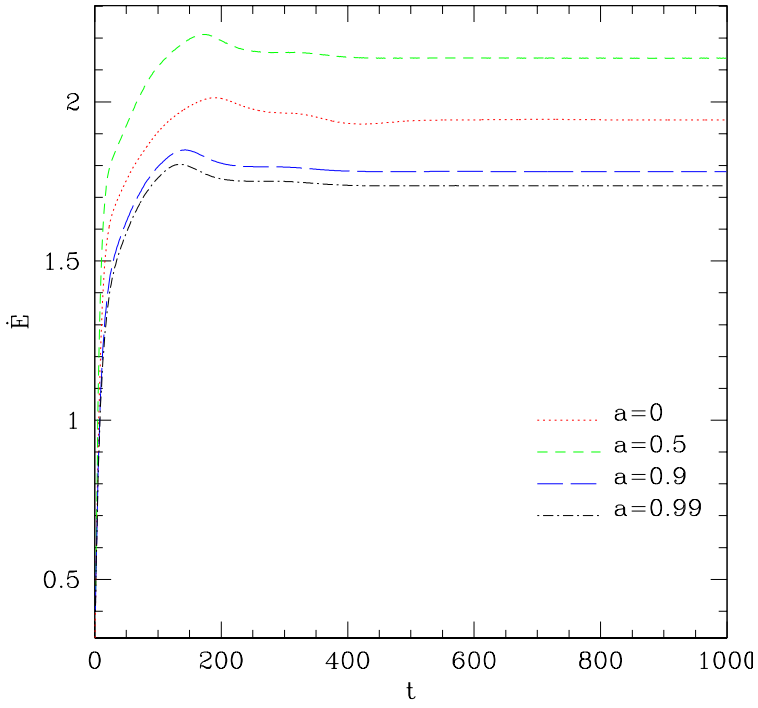

Figure 5.13: Energy accretion rates, models U2, U6, U8, U10, for the axisymmetric configuration. We see that the energy accretion rate as measured at the Schwarzschild radius actually increases for an $a = 0.5$ black hole and decreases for larger spin parameters.

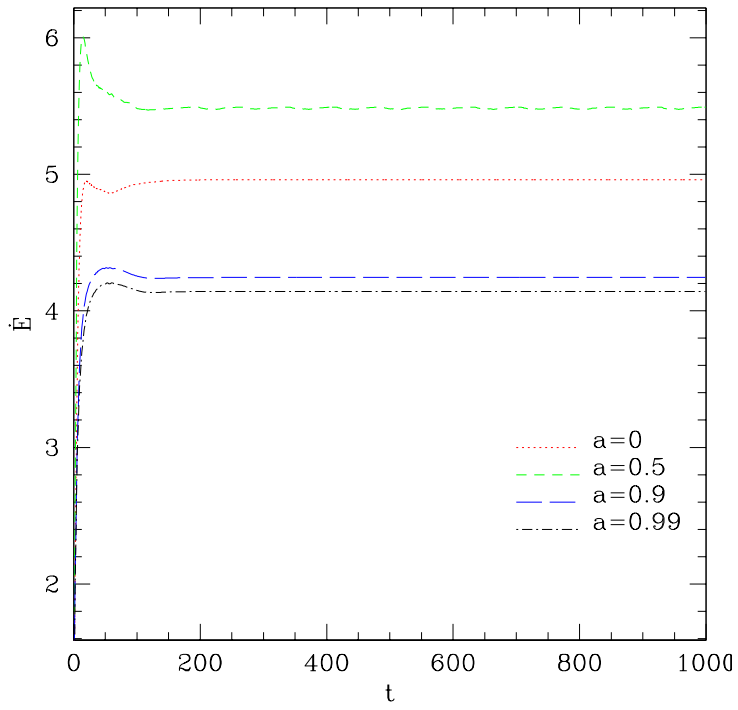

Figure 5.14: Energy accretion rates, models U4, U7, U9, U11, for the axisymmetric configuration. These results are in agreement with those seen in Fig. 5.13, we see that the energy accretion rate of an $a = 0.5$ black hole is a maximum out of the parameters considered in this study. This is directly related to the fact that the spin $a = 0.5$ black hole has the widest attachment angle and the largest wake when compared to other spins considered.

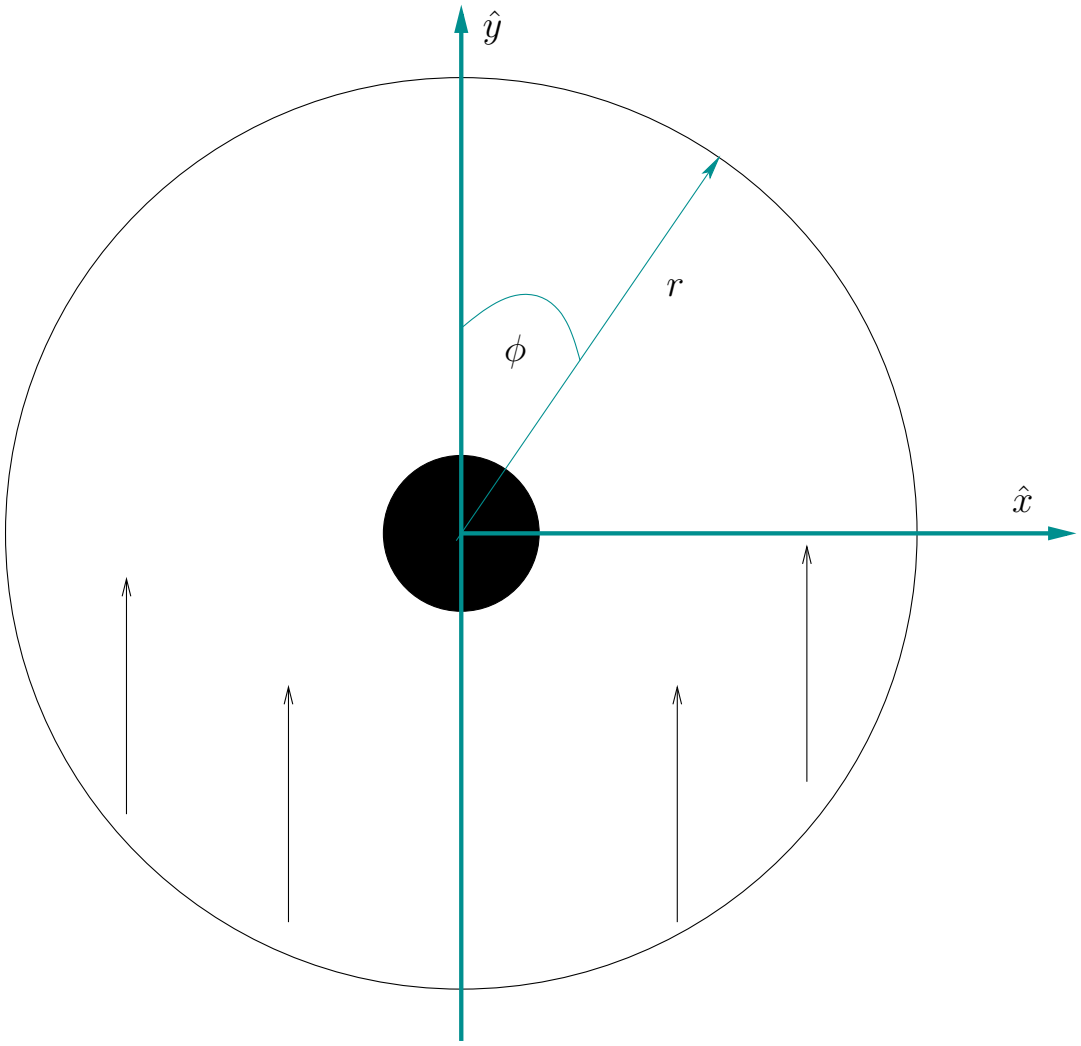

Figure 5.15: The non-axisymmetric infinitely thin-disk accretion setup. The radial coordinate increases away from the "centre" of the black hole. The angular coordinate increases from top to bottom. The arrows inside of the the disk show the direction of fluid flow as viewed by an observer at infinity. The boundary of the shaded region in the centre denotes the event horizon, the area inside the event horizon is a black hole. The boundary at $r_{\rm max}$ and $\pi/2 \leq \phi \leq 3\pi/2$ are treated with inflow boundary conditions. The remaining radial boundaries are treated using extrapolated outflow. The angular boundaries at $\phi = 0$ and $\phi = 2\pi$ are treated numerically with periodic boundary conditions as described in Chap. 3. When referencing the geometry in the future we refer to the region blow the $\hat{x}$-axis as upstream, and the region above the $\hat{x}$-axis as downstream.

travel, as seen in Fig. 5.3. The accretion flow is assumed to only occur on the equatorial plane, $\theta = \pi/2$.

This is not expected to be a physically general setup. One would typically expect the fluid to bulge near the black hole due to extreme pressure build-up in that region. This effect is taken into consideration in several papers written about thin-disk accretion such as those cited in the introduction. This setup is a means to understand the full three dimensional evolution that is left for a future study. As described by Font *et al.* [2, 3], this is a simplifying assumption. As cited in FI99, similar Newtonian works on this problem using cylindrical coordinates may be seen in Matsuda *et al.* [86] and Benensohn *et al.* [120]. We explicitly assume that the flow has no dependence on the polar coordinate. If a flow is reflection symmetric on the equatorial plane there will be no polar pressure gradient, and the polar velocity will vanish, therein the infinitely thin disk model is justifiable. For more general configurations a full three dimensional treatment is required [3].

We initialize the variables using a similar procedure as with the axisymmetric case; however, the fluid 3-velocity, v^i, will now take the form of those used in FI99;

$$v^r(t,r,\phi) = F_1 v_\infty \cos\phi + F_2 v_\infty \sin\phi \tag{5.15}$$

$$v^\theta(t,r,\phi) = 0 \tag{5.16}$$

$$v^\phi(t,r,\phi) = -F_3 v_\infty \sin\phi + F_4 v_\infty \cos\phi. \tag{5.17}$$

We define the F_i functions written explicitly in terms of the general metric;

$$F_1 = \frac{1}{\sqrt{g_{rr}}} \tag{5.18}$$

$$F_4 = \frac{-2g_{r\phi}}{g_{\phi\phi}} F_1 \tag{5.19}$$

$$F_3 = \frac{F_1 g_{rr} + F_4 g_{r\phi}}{\sqrt{g_{rr}g_{\phi\phi} - g_{r\phi}^2}} \tag{5.20}$$

$$F_2 = \frac{F_3 F_4 g_{\phi\phi} + F_1 F_3 g_{r\phi}}{F_1 g_{rr} + F_4 g_{r\phi}}. \tag{5.21}$$

Equations (5.18) to (5.21) are a slightly simpler form of the function F_i described in Papadopoulos *et al.* [91]. The variables, g_{rr}, $g_{\phi\phi}$ and $g_{r\phi}$ are elements of the spacetime metric and are functions

of the spacetime coordinates. As with the axisymmetric case, the characteristics are independent of the thermodynamic pressure. Therefore, we will take $P_\infty = 1$ without loss of generality. For these simulations we have restricted the system to the equatorial plane which satisfies the infinitely thin-disk approximation as described in Chap. 2.7.

5.3.1 Infinitely Thin-Disk Accretion: a=0

The plot of the energy accretion rate may be seen in Fig. 5.16, where we see the dependence of the energy accretion rate on the velocity of the black hole. We also see that the faster the black hole is travelling, the longer it takes for the system to reach a steady state. This is in contrast to the axisymmetric simulations and to the findings of FI982. We perform a convergence test for the system at $v_\infty = 0.6$ to verify the results. Snapshots of these simulations may be seen in Fig. 5.22 and 5.23. We refer the reader to the appendix Fig. A.7 for the time evolution of model U12 using $r_{\max} = 50$, and Fig. A.10 for $r_{\max} = 1000$. Model U13 is seen in Fig. A.9, where we focus on the region $2 < r < 50$, and Fig. A.11 for the evolution of the full domain.

The evolution for models U12 and U13 developed a tail shock. The tail shock formed very early in the evolution, with the presence of highly evacuated regions (signified by very low relative pressure) on the edge of the tail. While the fluid accumulates on the black hole, a secondary wave begins to approach the front shock. In this configuration, the fluid collects against the black hole, and wraps around to the downstream side. However, unlike the axisymmetric setup previously discussed there is a large pressure that builds in the upstream side of the black hole that pushes more oncoming fluid back upstream. This upstream travelling bow shock is typically evidence that the tail detaches; however, in this case we see that that a tail shock remains. We conclude that the bow shock presented here results from fluid reflecting off of the matter built up in the front of the black hole. A profile of the bow shock wave is seen in Fig. 5.17. In Fig. 5.22 we see that the reflected wave extends out to the edge of the tail shock. This shock travels faster than the black hole, and will eventually reach the outer boundary of the domain. Once the shock hits the outer domain, the boundary conditions used in the simulation would be incorrect due to the fact that they were held constant. Consequently, any further evolution would become meaningless in this simulation. We see from the profiles in Fig. 5.20 that the flow pressures in the wake are much higher than those in the upstream flow.

To determine the behaviour of the accretion phenomenon, we also measure the angular mo-

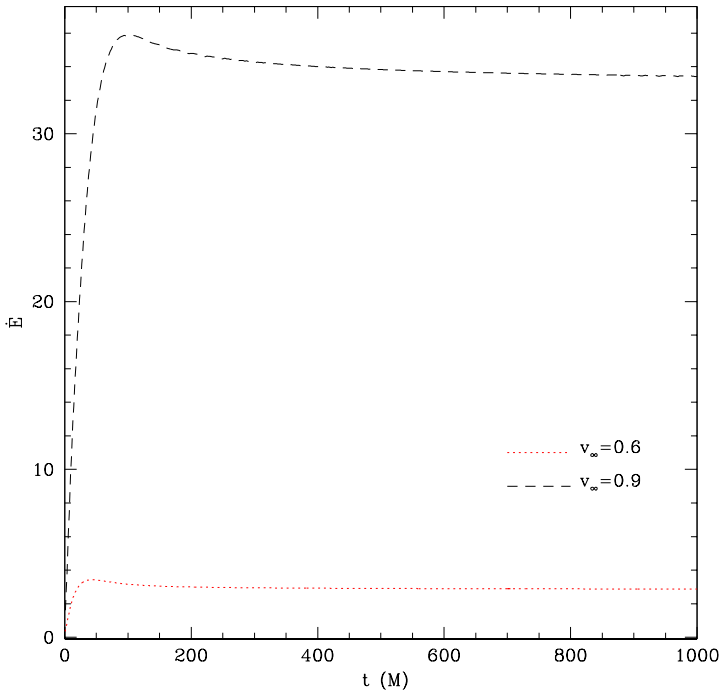

Figure 5.16: Nonaxisymmetric ultrarelativistic energy accretion rates for models U12 and U13. We see a dependence of the accretion rate on the velocity of the black hole.

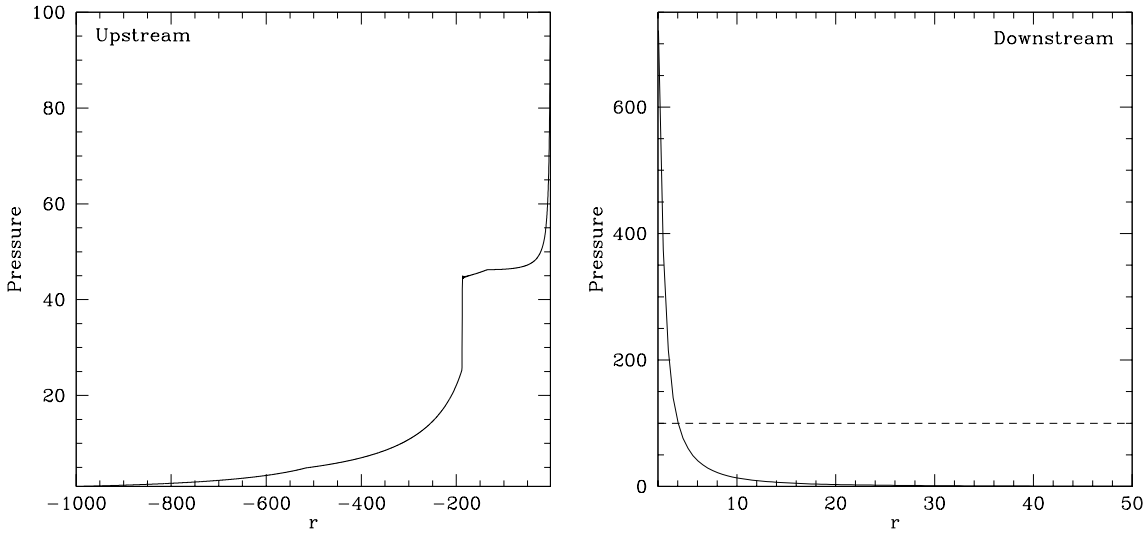

Figure 5.17: Ultrarelativistic pressure profile for model U13 at time T = 1000M. On the left we see the profile of a shock moving upstream, while on the right we see the downstream profile. The dashed line emphasizes the amplitude of the maximum upstream pressure.

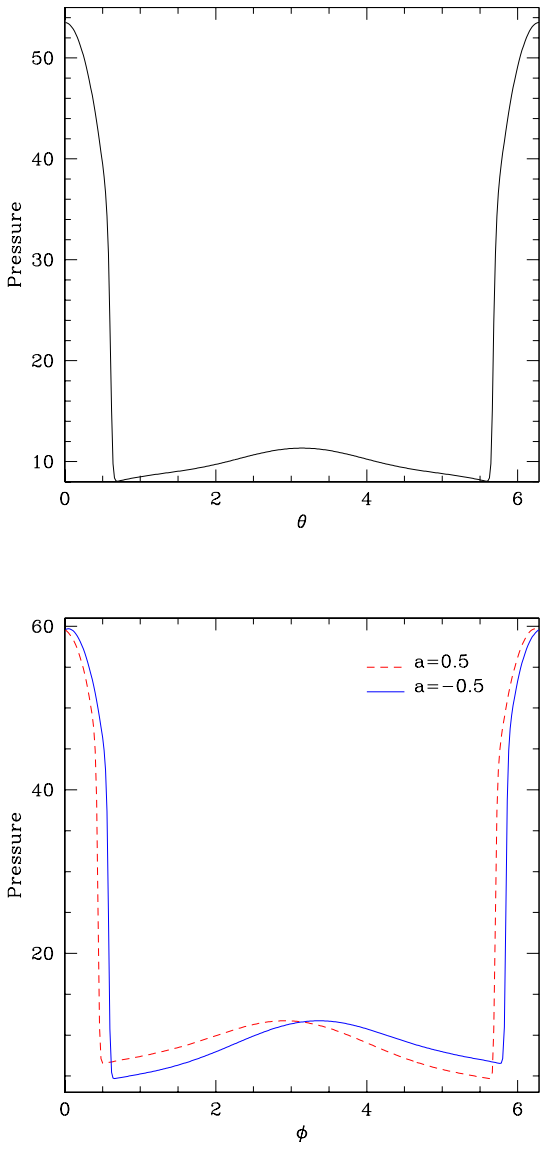

Figure 5.18: Ultrarelativistic pressure profile for the thin disk approximation for model U11 for $r_{\max} = 1000$. This cut is taken at the Schwarzschild radius. The $a = 0$ simulation at time $t = 1000M$ (top) shows symmetry around the black hole while the $a = 0.5$ and $a = -0.5$ simulations at time $t = 1000M$ (bottom) shows a deviation from the symmetry due to the rotation. The regions close to $\phi = 0$ and $\phi = 2\pi$ are downstream of the black hole. The $a = 0$ simulation shows that there is only a small pressure difference between the upstream and downstream sides of the black hole. The rotating black hole exhibits a larger pressure in the downstream region, while the pressure in the upstream part of the domain, $\pi/2 < \phi < 3\pi/2$ is similar to the $a = 0$ model.

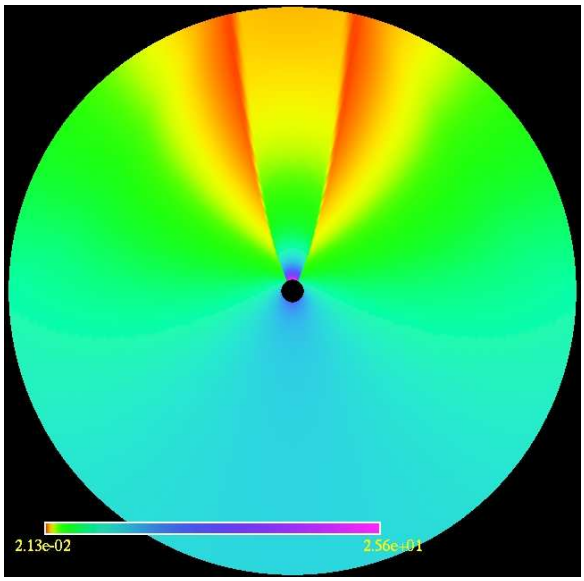

Figure 5.19: Ultrarelativistic infinitely thin-disk accretion $a = 0$. This plot shows the energy accretion rate for model U12. This image displays the result for time $t = 1000M$, long after the evolution has reached a steady-state.

mentum accretion. Previous studies by Font *et al.* [2] in the hydrodynamic regime show that the angular momentum accretion does not attain large amplitude for any simulation. Their results show the angular momentum accretion rate profile oscillating with very low amplitude around zero. The angular momentum accretion rates for $a = 0$ are seen in Fig. 5.25. We find that the angular momentum accretion rate increases as a function of resolution as seen in Fig. 5.26.

The simulations performed with different radii defining the outer boundaries had very different quantitative results which may be seen in the comparison of the two accretion rates in Fig. 5.21. The accretion process studied here must also be a function of $r_{\rm max}$. We consider $r_{\rm max} = 1000$, while holding the resolution constant. The results of these simulations are seen in Figs. 5.22, and 5.23. We present a preliminary study of this phenomenon, a more detailed study of the functional dependence of the accretion process on the quantity $r_{\rm max}$ is left for a future project.

We compare the flow morphology for the two different radii in Fig. 5.24, and find that the morphology remains similar; however, the magnitude of the pressure and other quantities are quite different.

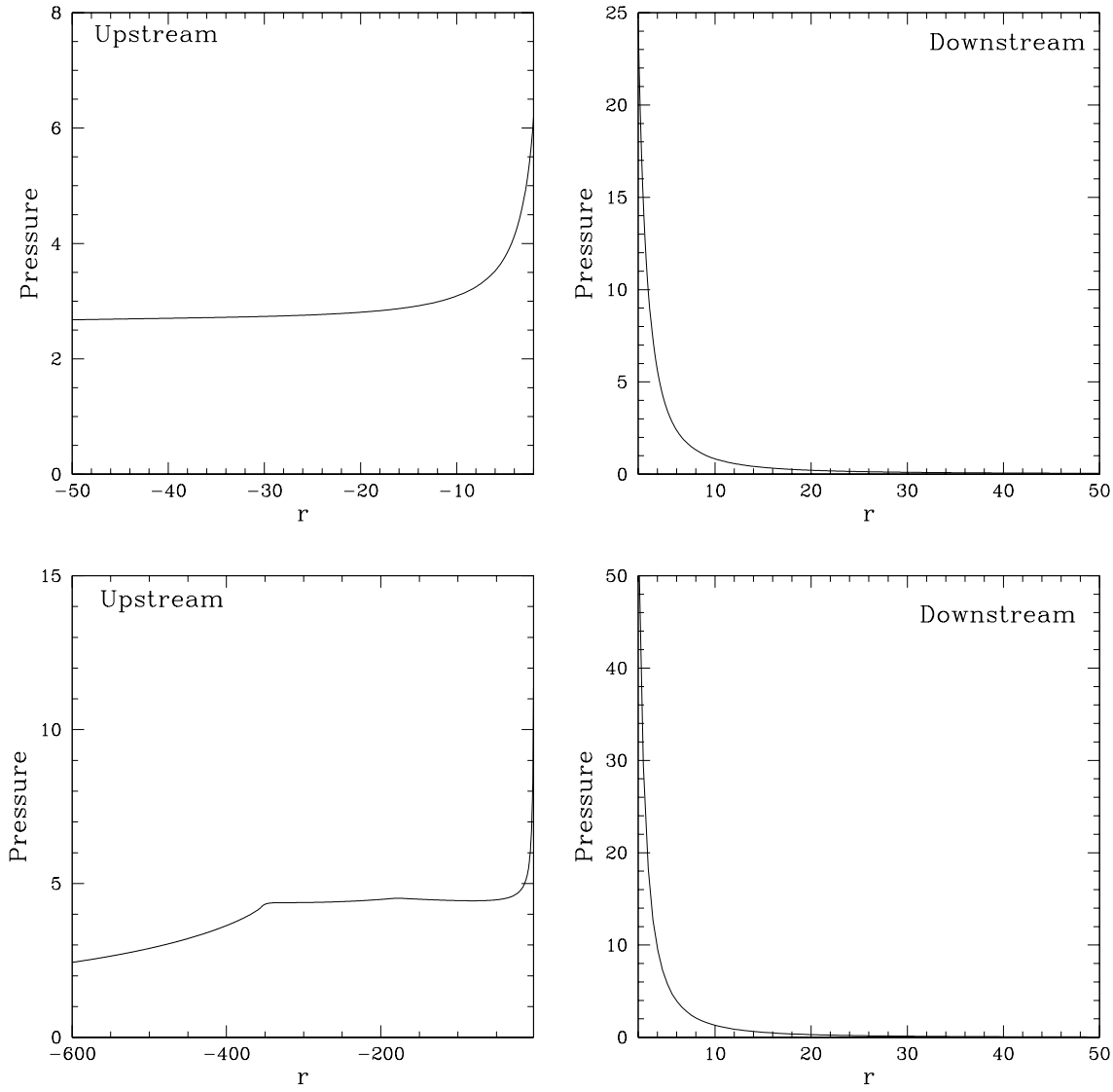

Figure 5.20: Ultrarelativistic infinitely thin-disk accretion onto a spherically symmetric black hole for model U12. This is a cross section of the domain at angle $\phi = 0$ and time $t = 1000M$. The pressure profile appears very similar to that of the axisymmetric profile. The same cut was performed along the angle $\phi = 2\pi$ to reveal the same form. In the upstream image, we see that the outer boundary is very different from the boundary condition that $P = 1$. When we push the boundary out further, we are able to capture more features of the accretion system before the boundary effects begin to disrupt the system. In the bottom plots we restrict our attention to smaller domains to aid in visualization.

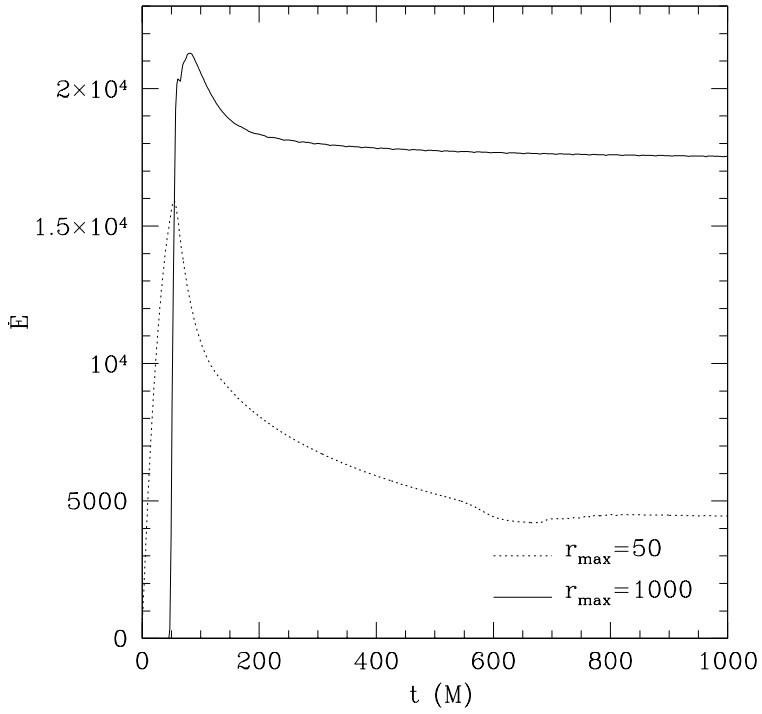

Figure 5.21: Ultrarelativistic energy accretion rates for model U13 with $r_{\max} = 50, 1000$, $a = 0$. We see from this preliminary survey that there is a dependence of the accretion rate on the maximum radius of the domain. The evolution is much smoother for the larger radius, and when we investigate the evolution of the pressure field P as seen in Fig. 5.22 and 5.23. The values presented here are not normalized.

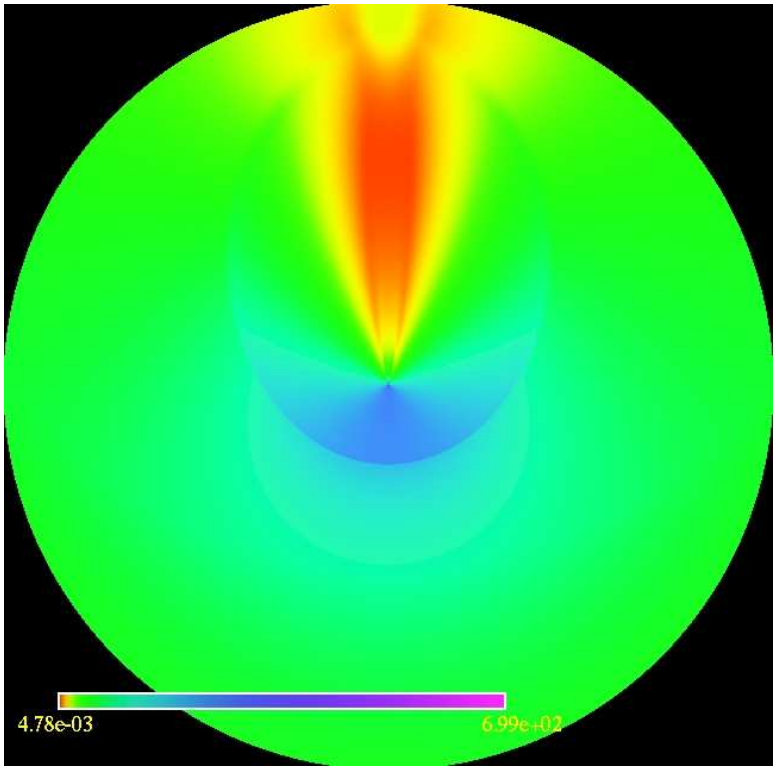

Figure 5.22: Ultrarelativistic accretion onto a spherically symmetric black hole for model U13. This is the result for $P(1000, r, \phi)$ in the infinitely thin-disk evolution with $r_{\rm max} = 1000$. The faster the asymptotic velocity, the thinner and more well defined the tail shock becomes. The point of contact between the tail shock and the black hole decreases as a function of the asymptotic velocity. Note the presence of a bow shock radiating from the black hole. It is this bow shock that forces us to extend our simulation domain out much further than those in the ultrarelativistic axisymmetric simulation, and further than the cases considered in Font *et al.* [2]. The tail, magnified in Fig. 5.23, is surrounded by low pressure regions. At the time of this snapshot the tail has not reached the outer boundary, but we do note that the tail remains well defined even out to very large distances.

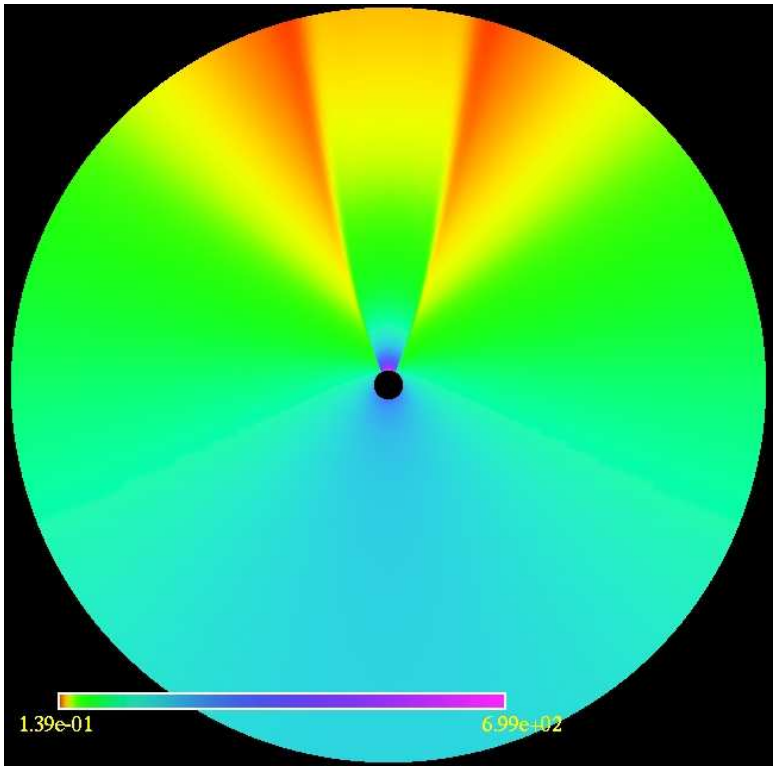

Figure 5.23: Ultrarelativistic pressure accretion onto a spherically symmetric black hole for model U13. Here, we focus on the region $2 \leq r \leq 50$. We see a well defined tail shock.

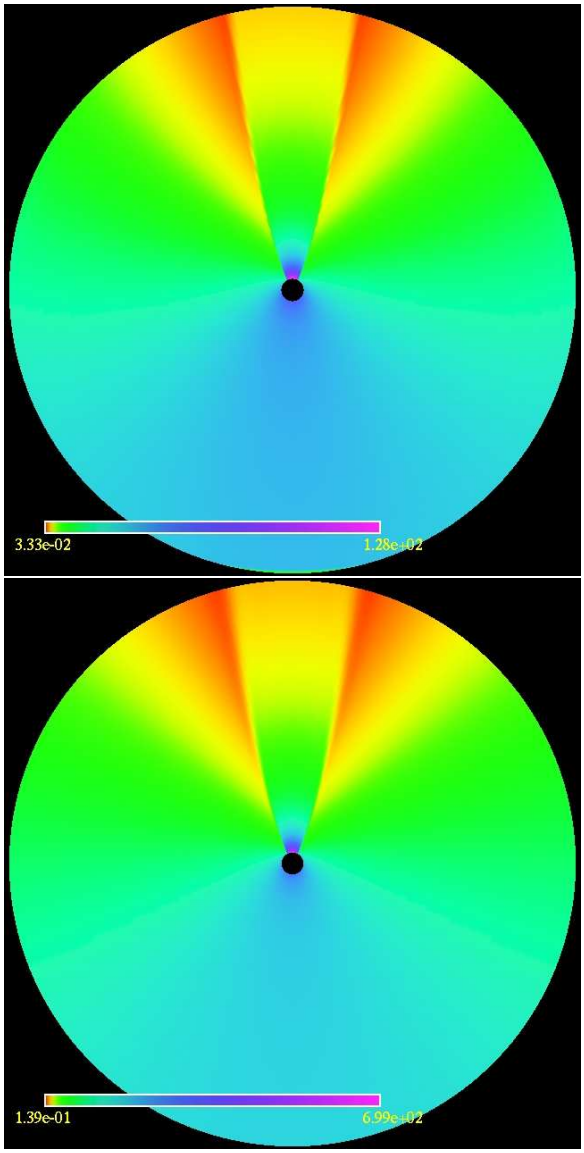

Figure 5.24: A comparison between $r_{\max} = 50$ (left) and $r_{\max} = 1000$ (right) pressure fields for model U13. In both of these images we focus on the region $2 \leq r \leq 50$, for the left image the pressure ranges $3.3 \times 10^{-2} \leq P \leq 1.3 \times 10^{2}$ while on the right $1.4 \times 10^{-2} \leq P \leq 7.0 \times 10^{2}$. We see that the pressure morphology is very similar between these two models; however, the smaller domain artificially holds the initial bow shock close to the black hole introducing unphysical waves that propagate into the black hole. The bow shock in the left image is not visible because it resides on the edge of the domain. The presence of the artificially stable bow shock explains the different range of pressures in the region displayed here. When the domain is larger the flow still develops a tail shock, but the solution is not affected by the boundary at the time when the simulation was terminated.

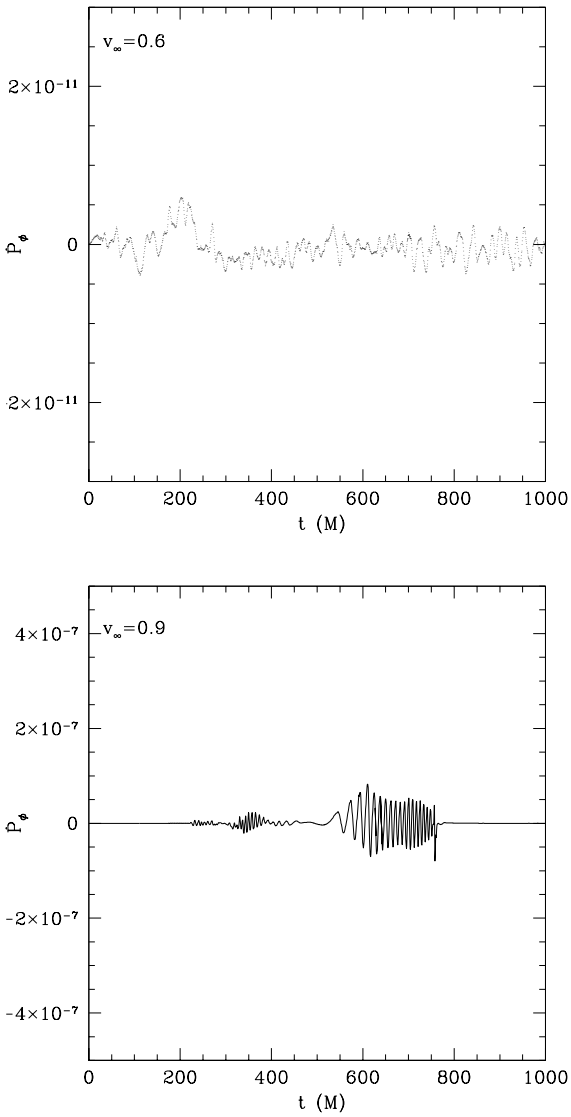

Figure 5.25: Ultrarelativistic angular momentum accretion rates for models U12 (top) and U13 (bottom) for $a = 0$. The amplitude of the result for model U12 is close to the tolerance parameter used to solve the system of equations and is considered to be an artifact of the numerical simulations. The result for model U13 shows a larger oscillation near the middle of the simulation time; however, since the larger oscillation damps out after a short time, the flow is still considered steady. The original study by Font *et al.* [1] had a similar feature and claims that this is within the numerical error and can be dismissed. Upon convergence testing, we find that the numerical values for model U12 actually increase as the evolution proceeds, as seen in Fig. 5.26, but the amplitudes remain small. Convergence testing for model U13 indicates that the oscillations decrease with increased resolution.

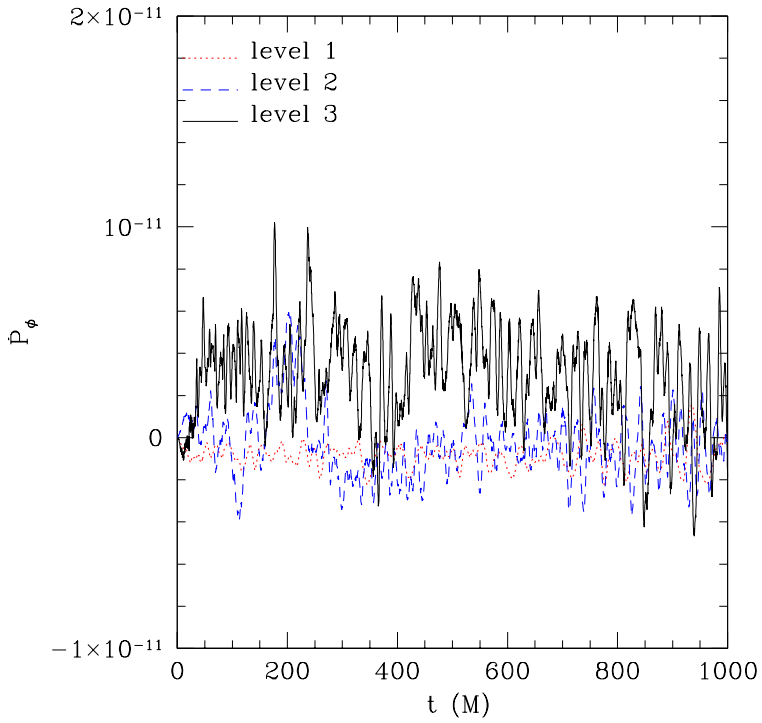

Figure 5.26: Ultrarelativistic angular momentum accretion rate convergence test for model U12 with $a = 0$. The dotted line indicates the lowest resolution $(N_r, N_\phi) = [1000, 160]$, the dashed line represents $(N_r, N_\phi) = [2000, 320]$, and the solid line represents $(N_r, N_\phi) = [4000, 640]$. We see that for each resolution the net angular momentum accretion rate remains near zero. We do note two features, first that the magnitude of the oscillation increases with resolution and second, the highest resolution oscillates around a non-zero value; however, due to the overall amplitude of the oscillation and the fact that it oscillates around a fixed value would indicate that the flow will not experience a so-called "flip-flop" instability. The oscillations presented here are too small to be seen in a visualization of the flow.

Another important observation is that in the presence of smooth flow the $a = 0$ infinitely thin-disk accretion will not experience any net angular momentum accretion. If an instability were to develop the black hole could accrete a net angular momentum from the passing fluid. In Figs. 5.25 and 5.26 we see the results of measuring the angular momentum accretion onto the black holes. We see in Fig. 5.25 that model U12 does not accrete any net angular momentum from the surrounding fluid. The fact that the momentum accretion rate oscillates around zero is indicative of numerical noise especially when considering that the amplitude of the oscillation is only two orders of magnitude larger than numerical tolerances of the code. When we perform convergence tests as seen in Fig. 5.25, we find that the amplitude of these oscillations actually increases as a function of resolution. In particular when looking at the $(N_r, N_\phi) = [4000, 6400]$ calculations we find the oscillations no longer oscillate around zero. This indicates that an instability may be forming, but, the amplitude of such an instability is very small. To verify this behaviour may require higher numerical accuracy methods, and at the very least requires higher resolution simulations. The verification of this instability is left as a future project, using methods described in Chap. 6. The angular momentum accreted in model U13, seen in the bottom of Fig. 5.25 exhibits a nontrivial momentum accretion rate; however, as the simulation continues the accretion rate returns to zero.

Due to the geometric configuration, the only way angular momentum may be transfered to the black hole is if a tangential instability develops. We see no such evidence of such an instability developing, which is in agreement with the results reported in FI982. We now describe our last parameter survey using the infinitely thin-disk approximation with a rotating black hole.

5.3.2 Infinitely Thin-Disk Accretion: a≠0

When the rotation parameter is turned on, we have a non-trivial angular momentum accretion rate as seen in figure 5.27. The accretion rates indicate that the rotating black holes investigated in this study also reach a steady state following a transition period.

The effects of rotation in the ultrarelativistic system was found to be in agreement with the results originally discovered by Font *et al.* [3]. The effects of rotation are only noticeable within a few Schwarzschild radii of the black hole.

The remaining domain has very similar features to the non-rotating black hole. To check the symmetry of the system we run two separate simulations with opposite spin. The results of this simulation may be seen in Figs. 5.28. The mirror symmetry is apparent and the resulting accretion

rates reflect this behaviour. No noticeable difference in the accretion rates exists as may be seen in the energy and radial momentum accretion rate plots in Figs. 5.30, 5.32; however, the azimuthal momentum accretion rate seen in Fig. 5.31 clearly changes sign as one may expect.

We note that, with rotation turned on, the instability that appeared to be developing for models U12 and U13 with $a = 0$ are no longer apparent. This may be due to the fact that the angular momentum accreted is much larger than that produced by the instability, that the effects are negligible. Convergence tests reveal no evidence for the presence of instabilities.

In Figs. 5.33, 5.34 we compare model U12 and U13 with $a = 0$ and $a = 0.5$. We find that the accretion rates for different quantities is a function of the spin rate. The radial momentum rates decrease as a function of spin, while the energy accretion rates increase. We should be sure not to make too strong a claim here, since the axisymmetric studies indicate that the accretion rates are non-monotonic functions of the spin rate. The axisymmetric case shows the maximum accretion rates occur when $a = 0.5$. As this is a preliminary result we will need to perform a larger parameter survey to find the correct relationship.

This ends our discussion on the ultrarelativistic fluid regime. To see the conclusions of this work we refer the reader to Sec. 6.1.1. We now describe the results from our axisymmetric accretion of a magnetofluid onto a black hole.

5.4 Magnetohydrodynamic Bondi–Hoyle Accretion Onto a Black Hole

From the work of Wald [100] and Komissarov [157], we have the electromagnetic tensor for a rotating black hole immersed in a asymptotically uniform magnetic field. The asymptotic field is aligned with the rotational axis of the black hole, defined in terms of the temporal ${}^{(t)}\xi_{\mu} = \partial_t$, and rotational, ${}^{(\phi)}\xi_{\mu} = \partial_{\phi}$, Killing vectors of an axisymmetric black hole;

$$F_{\mu\nu} = B_o \left({}^{(\phi)}\xi_{[\mu,\nu]} + 2a\, {}^{(t)}\xi_{[\mu,\nu]} \right). \tag{5.22}$$

More explicitly, we are interested in the magnetic field configuration which we may obtain from;

$$B^i = \frac{1}{2}\epsilon^{ijk} F_{jk}, \tag{5.23}$$

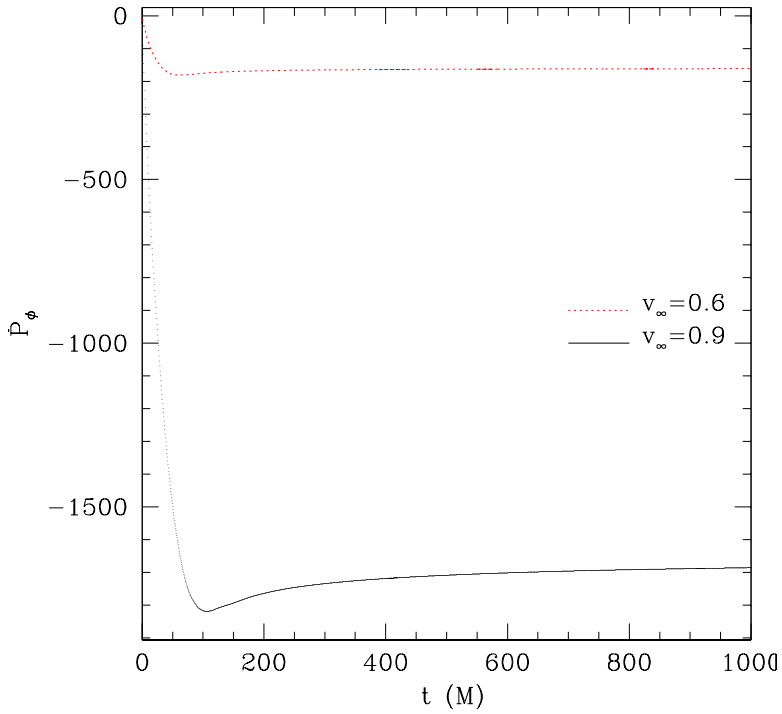

Figure 5.27: Ultrarelativistic angular momentum accretion rate for models U12 and U13 with $a = 0.5$. The trends of our accretion rates as a function of asymptotic velocity agree with the results shown in Font *et al.* [3].

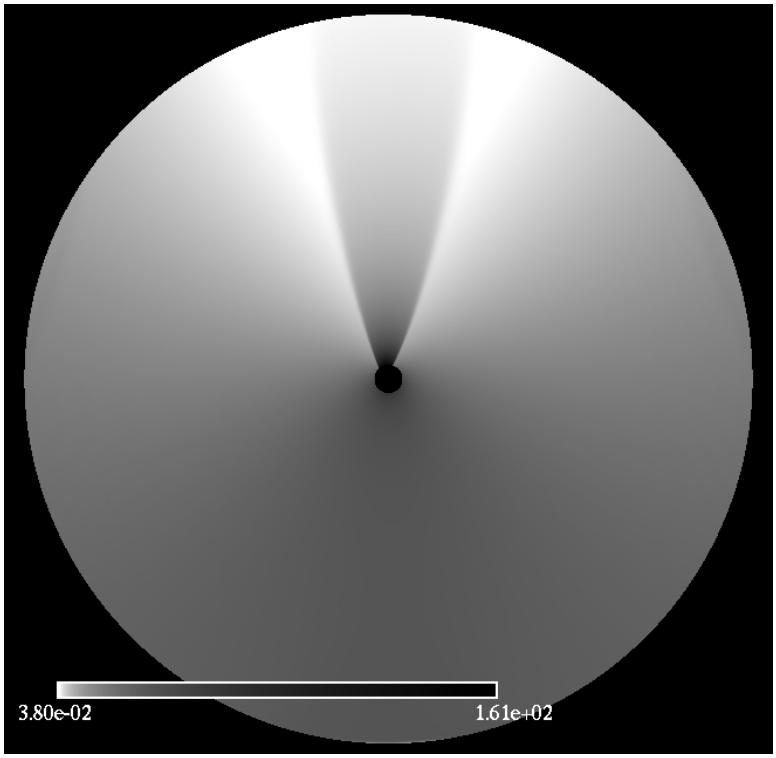

Figure 5.28: Ultrarelativistic accretion for model U13 with $a = 0.5$. For this simulation, $r_{\rm max} = 50$. This image was taken at time $t = 500M$ before the boundary effects were found to effect the accretion process. The morphology of the pressure flow rotates around the black hole. The rotational effects of the black hole was localized to a few a few Schwarzschild radii. Beyond that, the flow morphology was found to be similar to that of accretion onto a spherically symmetric black hole. The region of contact between the tail shock and the black hole decreases as a function of the asymptotic velocity; however, none of the parameters investigated exhibited a disconnection between the tail shock and the black hole. These results agrees with the findings presented in FI99.

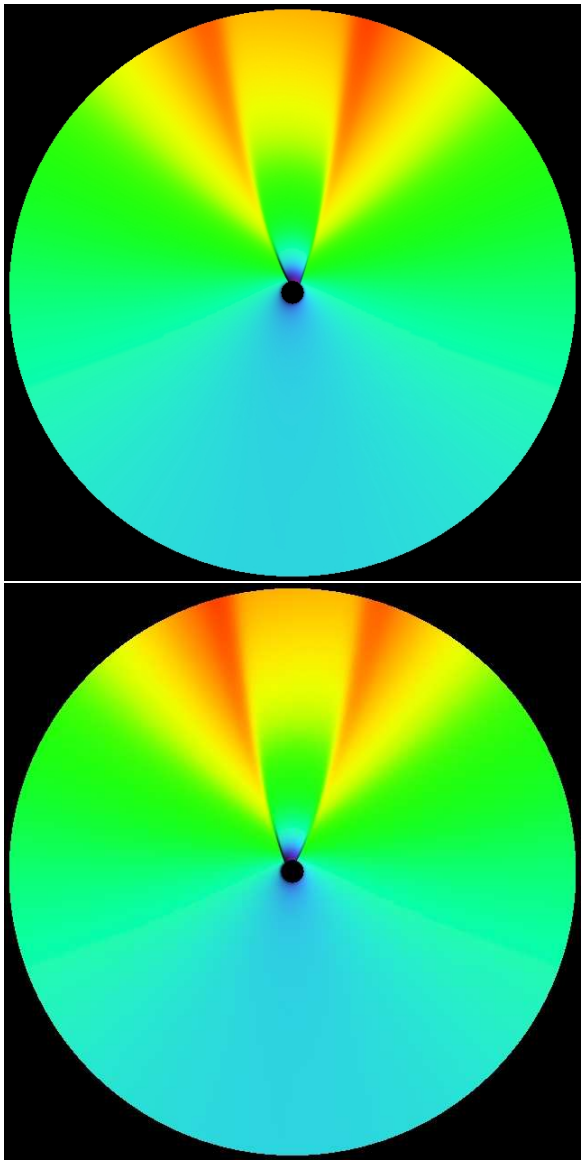

Figure 5.29: Ultrarelativistic accretion for model U13 with $a = \pm 0.5$. For this simulation, $r_{\rm max} = 1000M$, but we focus on the region $2 \leq r \leq 50$. This image was taken at time $t = 500M$ and we present the logarithm of the pressure to emphasize the tail shock. We see that near the black hole the pressure profile wraps around the black hole, however a few Schwarzschild radii away and the flow recovers a profile similar to that of the non-rotating black hole. We see that the flow morphology around an $a = 0.5$ black hole is a mirror image to the morphology around an $a = -0.5$ black hole. The similarity between rotating and counter rotating black holes is emphasized in the accretion rate plots in Figs. 5.30 and 5.32

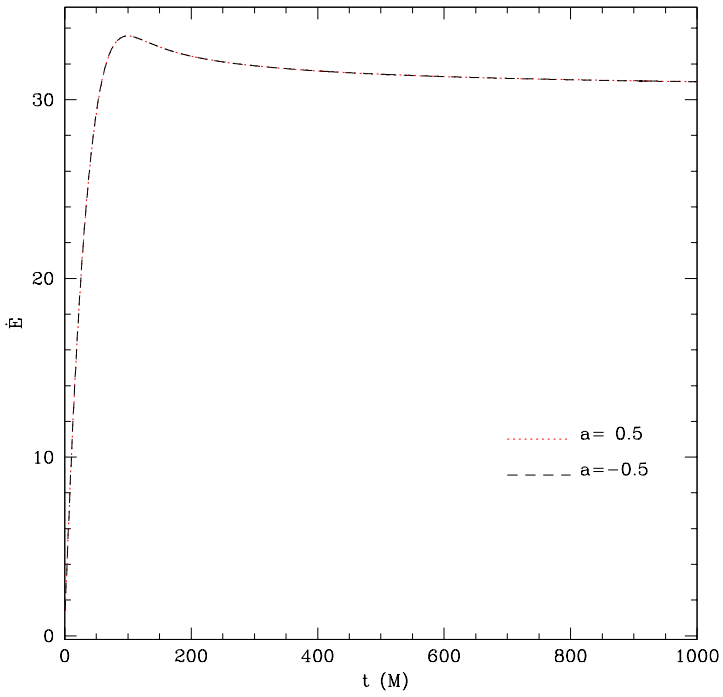

Figure 5.30: Ultrarelativistic energy accretion rates for model U13 with $a = \pm 0.5$. Due to the symmetry of the flux components with respect to the rotation rate we have that the accretion rates are identical.

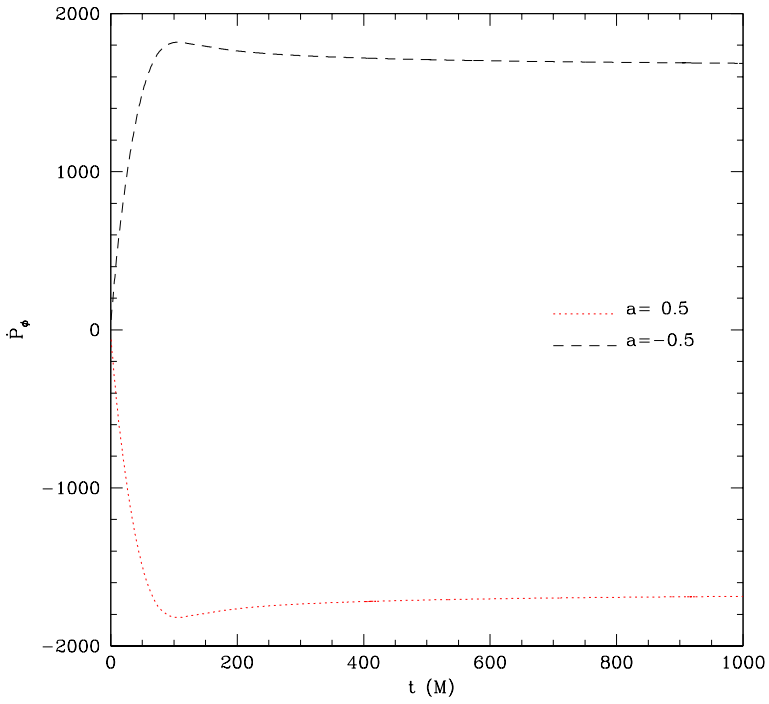

Figure 5.31: Ultrarelativistic azimuthal angular momentum accretion rates for model U13 with $a = \pm 0.5$. Due to the symmetry of the flux components with respect to the rotation rate we have that the form of the accretion rates is identical; however, the signs have been reversed.

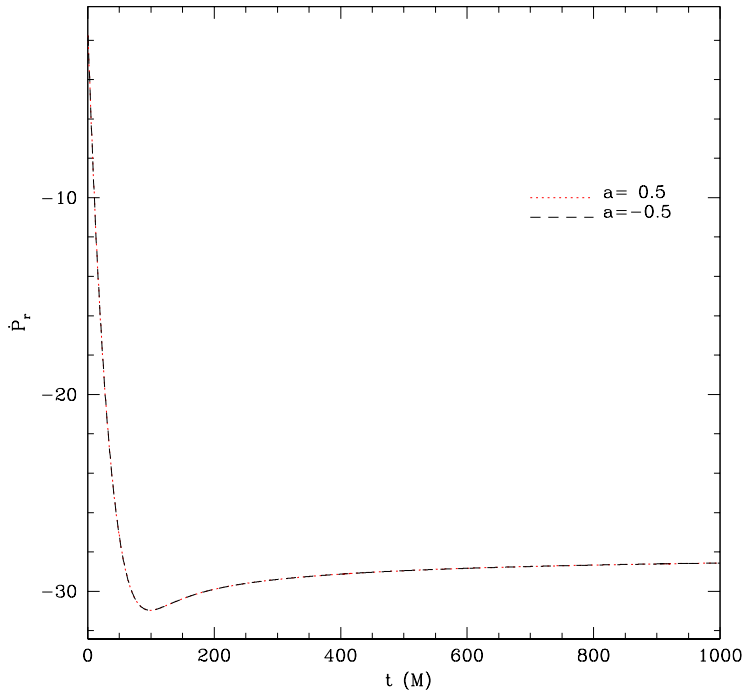

Figure 5.32: Ultrarelativistic radial momentum accretion rates for model U13 with $a = \pm 0.5$. Just like the energy accretion seen in Fig. 5.30 we see that the accretion rates are identical.

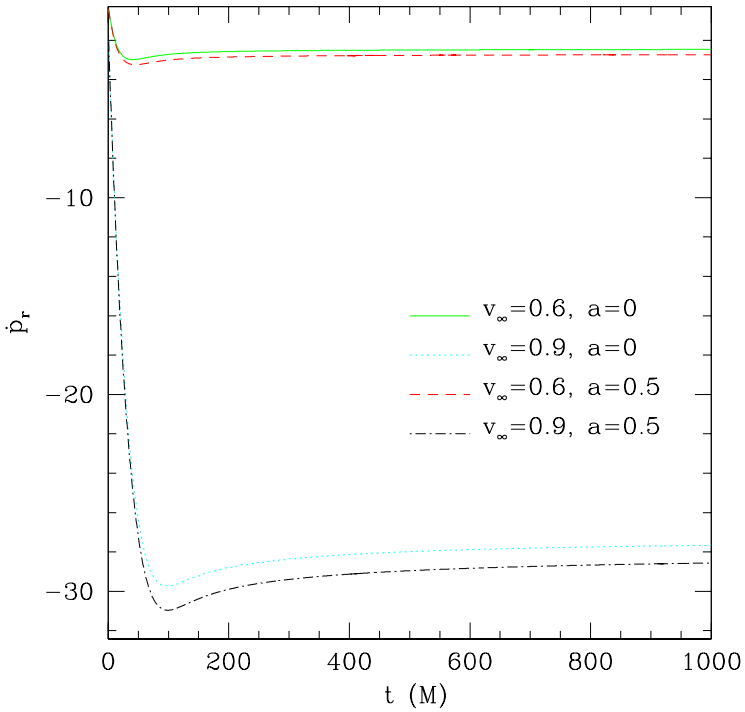

Figure 5.33: Ultrarelativistic accretion rates for models U12 and U13 with $a = 0, 0.5$. We see a similar trend to the axisymmetric $a \neq 0$ simulations, the radial momentum accretion rate decreases as a function of spin up to parameter $a = 0.5$. Further investigation is needed to see if the trend continues to be similar to the axisymmetric case. This diagnostic calculation does not reveal any instabilities forming with the parameters investigated.

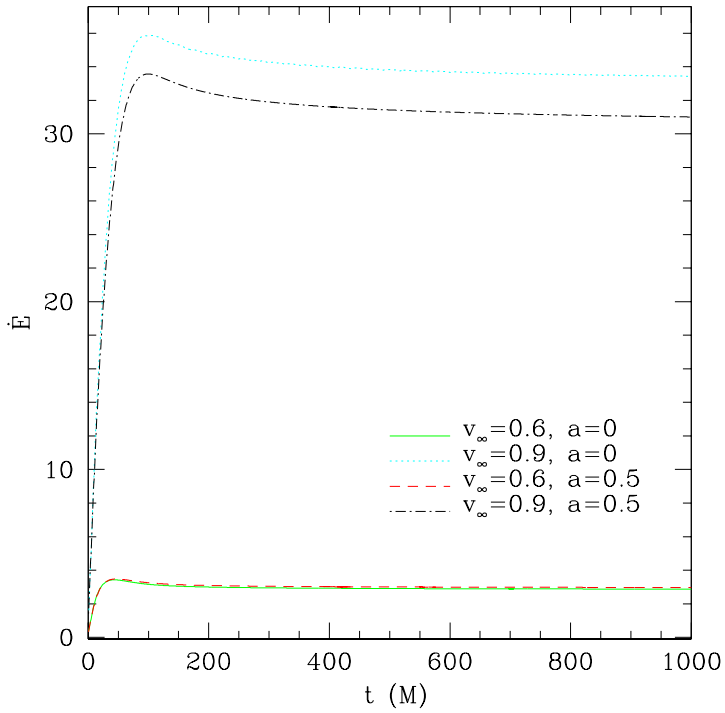

Figure 5.34: Ultrarelativistic azimuthal angular momentum accretion rates for models U12 and U13 with $a = 0, 0.5$. The energy accretion rate also increases as a function of spin up to $a = 0.5$.

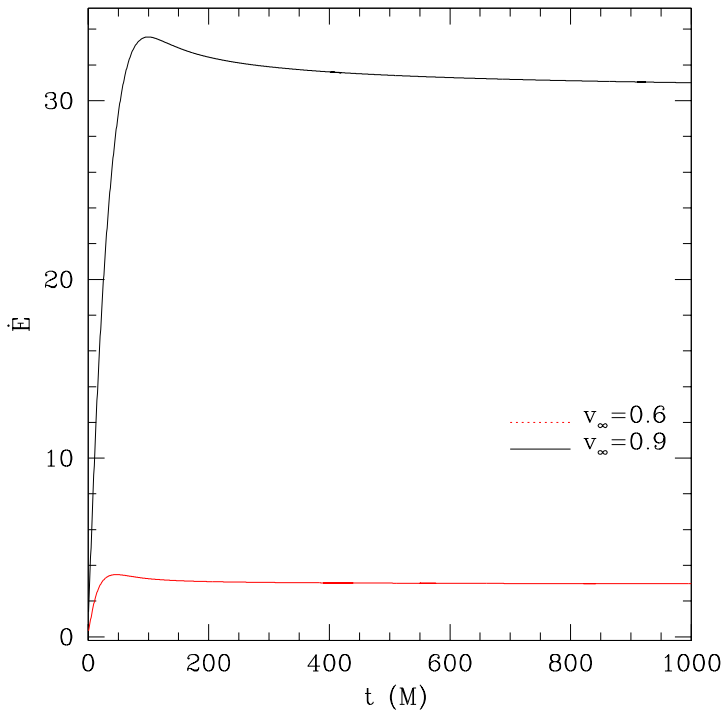

Figure 5.35: Ultrarelativistic energy accretion rates for models U12 and U13 with $a = 0.5$. Here we again have evidence that the black hole accretes energy at a steady rate while rotating. We see that, as expected, the accretion rate depends on the asymptotic velocity of the black hole.

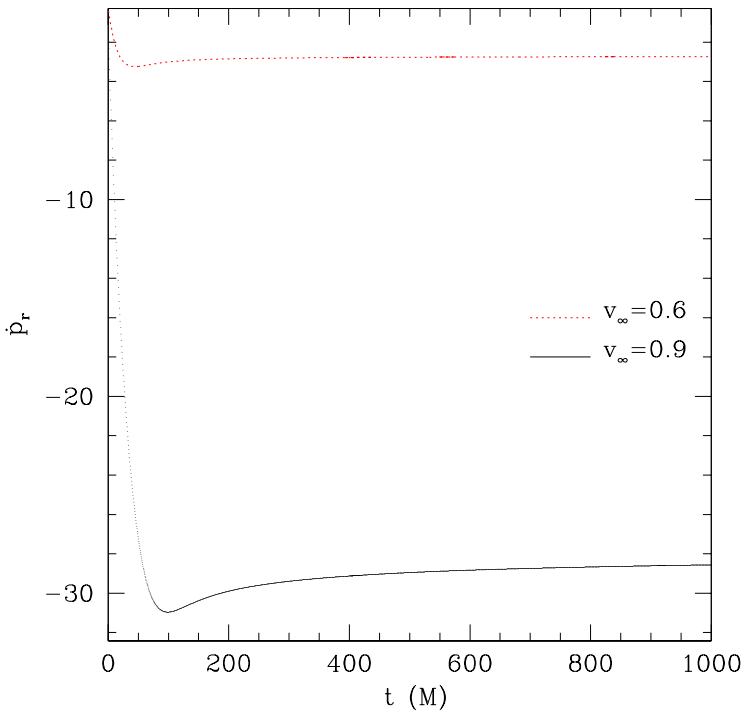

Figure 5.36: Ultrarelativistic radial momentum accretion rates for models U12 and U13 with $a = 0.5$. Here we have evidence that the radial momentum accreted by the black hole depends on the asymptotic velocity of the hole. The faster the black hole travels, the more radial momentum is accreted. As stated previously, we are not able to extract physical information from this quantity, but we do see that this is in agreement with the results from the Font *et al.* papers.

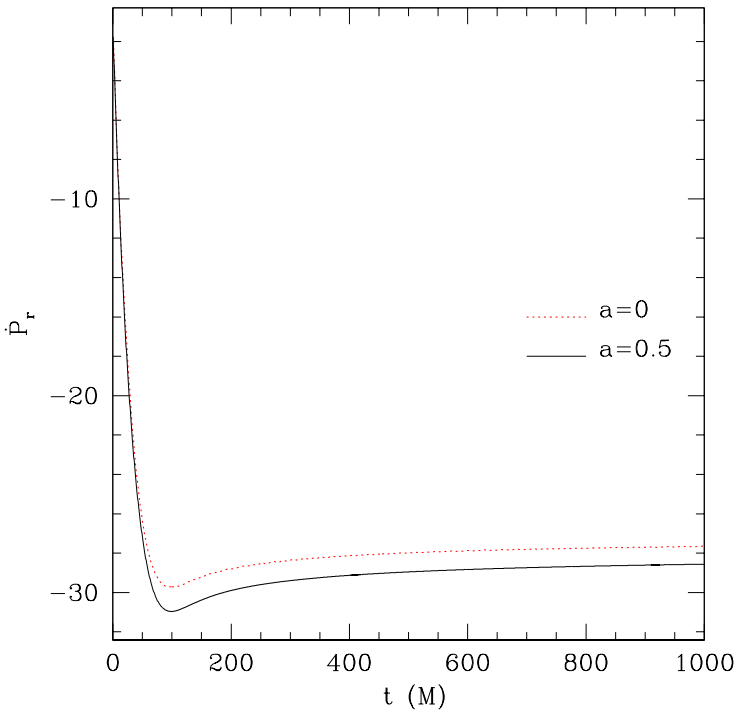

Figure 5.37: Ultrarelativistic radial momentum accretion rates for models U11 with $a = 0$ and U13 with $a = 0.5$. We see that for a moderately rotating black hole the radial accretion rate actually increases. This trend is independent of the asymptotic speed of the black hole, so we only show the case for $v_\infty = 0.9$.

where $\epsilon^{ijk} \equiv 1/\sqrt{\gamma}[ijk]$ and $[ijk]$ is the totally antisymmetric Levi–Civita tensor. In particular, we are interested in the following magnetic field;

$$\begin{aligned} B^r &= \frac{-B_o}{2\sqrt{\gamma}}\left(\gamma_{\phi\phi,\theta} + 2ag_{\phi t,\theta}\right) \\ B^\theta &= \frac{B_o}{2\sqrt{\gamma}}\left(\gamma_{\phi\phi,r} + 2ag_{\phi t,r}\right) \\ B^\phi &= \frac{B_o}{2\sqrt{\gamma}}\left(\gamma_{r\phi,\theta} + 2ag_{rt,\theta}\right), \end{aligned} \tag{5.24}$$

where γ_{ij} and $g_{\mu\nu}$ are the 3-metric, and 4-metric components respectively, $\sqrt{\gamma}$ is the determinant of the 3-metric and B_0 is a scaling factor that determines the magnitude of the magnetic field. This magnetic field satisfies (2.103) as it has zero divergence. When we travel far from the black hole, the rotational effects go as $1/r^3$ [4][17], and the magnetic field must tend to that of a field around a spherically symmetric black hole. In that case we have $g_{\phi t}, g_{r\phi} \to 0$ and (5.24) becomes,

$$\begin{aligned} B^r &= \frac{-B_o}{2\sqrt{\gamma}}\left(\gamma_{\phi\phi,\theta}\right) \\ B^\theta &= \frac{B_o}{2\sqrt{\gamma}}\left(\gamma_{\phi\phi,r}\right) \\ B^\phi &= \frac{B_o}{2\sqrt{\gamma}}\left(\gamma_{r\phi,\theta}\right). \end{aligned} \tag{5.25}$$

To determine the more general case of an asymptotically uniform magnetic field not aligned with the rotation axis of the black hole, we refer to the work performed by Bičák *et al.* [158] where they calculate the general magnetic field configurations as seen by an observer at infinity. Unfortunately, due to the symmetry considered in the axisymmetric problem, a tilted magnetic field (relative to the rotation axis) will break the symmetry.[18]

For the axisymmetric simulations, we use the Wald solution for a magnetic field parallel to the axis of rotation described in (5.24). This magnetic field configuration is sufficiently general for a spherically symmetric or axisymmetric (uncharged) black hole which is asymptotically flat. In the spherically symmetric case, the orientation of the magnetic field is parallel to the direction of black hole travel. For the axisymmetric black holes studied, the orientation of the magnetic field is parallel to the axis of rotation, which coincides with the direction of the black hole's velocity.

[17] see page 891

[18] For more detailed calculations for some geometric configurations we refer the reader to Thorne *et al.* [159] page 121. See also [160, 161, 158] as cited by Thorne.

Model	v_∞	Γ	$O(\beta_P^\infty)$	c_s^∞
M1	0.5	4/3	2	0.1
M2	0.5	5/3	1	0.1

Table 5.4: The parameters used for systems studied with an accreting magnetofluid with a magnetic field orientated parallel to the rotation axis. The third column is the order of magnitude selected for the asymptotic plasma beta parameter. The plasma beta parameters selected reflect the right order of magnitude for accretion disks around dwarf nova, [162], and have been used in Newtonian gravity studies of magnetized accretion disks by Hawley *et al.* [163, 164]. The hydrodynamic variables selected were chosen to always allow for asymptotically supersonic flow.

Using Wald's solution for models M1 and M2 we see in Figs. 5.38, 5.41, and 5.52, that the plasma beta parameter, $\beta_P(t,r,\theta)$,

$$\beta_P(t,r,\theta) = \frac{2P(t,r,\theta)}{b^2(t,r,\theta)} \tag{5.26}$$

tends to values below unity near the event horizon on the downstream side of the black hole. As we noted in Chap. 2.4.3 when the plasma beta parameter, β_P, drops too far below unity the MHD equations of motion are no longer valid. During the evolution of the magnetized system we found that the magnetic field on the downstream side of the black hole becomes large. This amplification corresponds to a relatively low $\beta_P(t,r,\theta)$ in the same region. If the amplification is too great, the solution of the equations of motion become unphysical for the model considered. Numerically this would not be a problem; however, the primitive variable solver is known to have severe numerical difficulties finding a physical solution for the primitive variables when there are extreme gradients in either the velocity or the magnetic field variables.

5.4.1 Magnetized Axisymmetric Accretion: a=0

We study the MHD accretion problem onto an $a = 0$ black hole. The resulting evolution of model M1 may be seen at time $t = 2500M$ in Fig. 5.38, and in Fig. 5.41 for model M2 at $t = 1400M$. The flow morphology for this supersonic system shows a tail shock; however, in contrast to hydrodynamic flows there is a noticeable depleted region downstream of the black hole along the axis of symmetry. In hydrodynamic flows this region has a maximum value of both the baryon density, ρ_0, and pressure P. The depletion is a result of a large value of the magnetic field in the depressed region which corresponds to an increase in the magnetic pressure. The relative strength of the magnetic pressure to the thermodynamic pressure is seen in the plasma beta function $\beta_P(t,r,\theta)$ in Fig. 5.38. We also plot the magnetic pressure $P_{\rm magnetic} = b^2/2$ along with the thermodynamic

Model	v_∞	Γ	$O(\beta_P^\infty)$	c_s^∞
M3	0.9	4/3	2	0.1

Table 5.5: The parameters used for the system studied with an accreting magnetofluid with a magnetic field orientated parallel to the rotation axis of the black hole. The fourth column is the order of magnitude selected for the asymptotic plasma beta parameter. The hydrodynamic variables selected were chosen to allow for asymptotically supersonic flow. The last column indicates the asymptotic speed of sound.

pressure, P_{thermal}, in Figs. 5.39, 5.42 and total pressure, P_{total}, in Figs. 5.40, 5.43. The material in the depleted region is being pushed out by the magnetic pressure. This type of phenomenon is also seen in the region around the earth's magnetopause where the magnetic pressure builds and the plasma drains out of the region along the magnetic field lines [165, 166]. Further research is necessary to assert that the density is draining along the field lines. To ensure that the depletion is a feature of the fluid flow and not a result of the specific resolution, we perform a convergence test focusing on a slice along $r = 2$. The results of these tests are seen in Fig. 5.46 where as the resolution increases the depletion becomes more and more apparent.

The resulting accretion rates are seen in Figs. 5.49 and 5.50. Based on the magnetic energy accretion rates, we see that the magnetic field has not reached a steady state at the time that the evolution is terminated. The evolution of the hydrodynamic variables clearly have reached a steady state. Time evolution of the baryon rest mass density for model M1 and M2 may be found in the appendix in Figs. A.13 and A.14 respectively.

5.4.2 Magnetized Axisymmetric Accretion: $a \neq 0$

We simulate magnetized axisymmetric accretion onto an $a = 0.5$ black hole. A snapshot of model M3 at $t = 2500M$ is seen in Fig. 5.51. We have a similar morphology as seen in the evolution of model M1. Model M3 has an interesting dynamical feature in that $\beta_P(t, r, \theta)$ shows oscillations along the shock front in the tail. The oscillations propagate away from the black hole out of the domain. Time evolution of the density for model M3 is found in Fig. A.15.

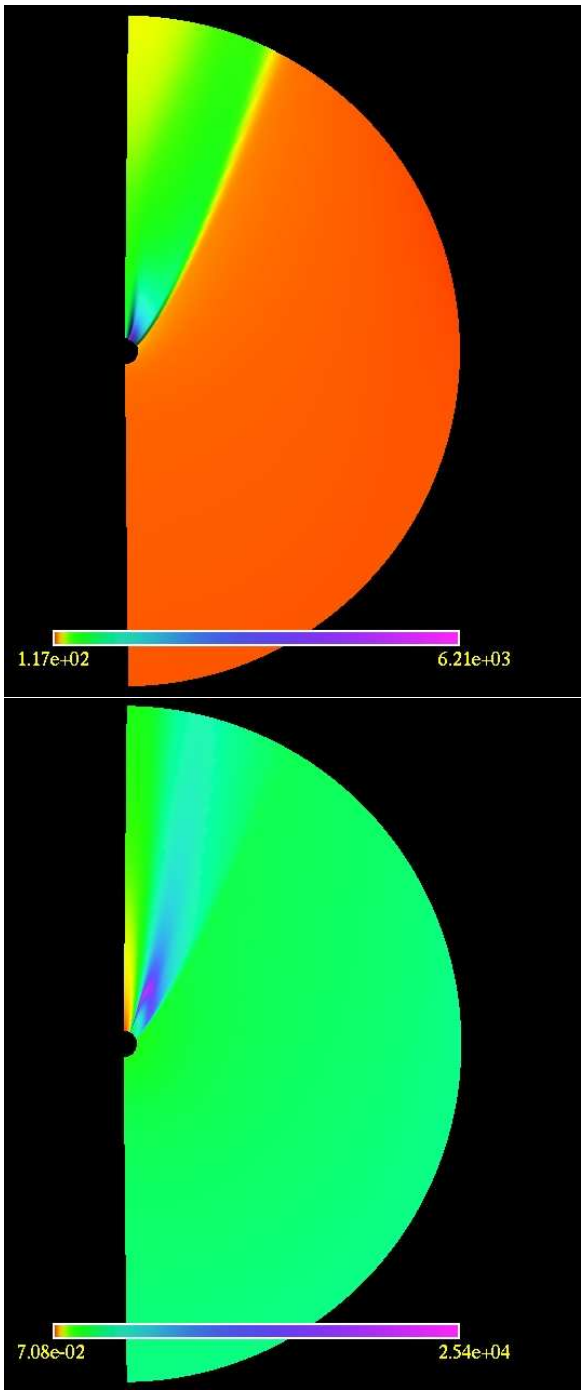

Figure 5.38: The relativistic Bondi–Hoyle accretion simulation for model M1. The black hole is travelling parallel to the background magnetic field direction as measured by an observer at infinity. Top is the logarithm of the density, $\rho_o(2500, r, \theta)$, and the bottom is the log plot of the plasma beta function $\beta_P(2500, r, \theta)$ profile. We see evidence that the magnetic field piles up on the downstream side of the black hole. The $\beta_P(t, r, \theta)$ profile indicates in the downstream side, near the black hole, the ideal MHD conditions may be breaking down, as the magnitude drops below unity. Note the high β_P values in the tail of the wake, they indicate regions where the magnetic field drops significantly.

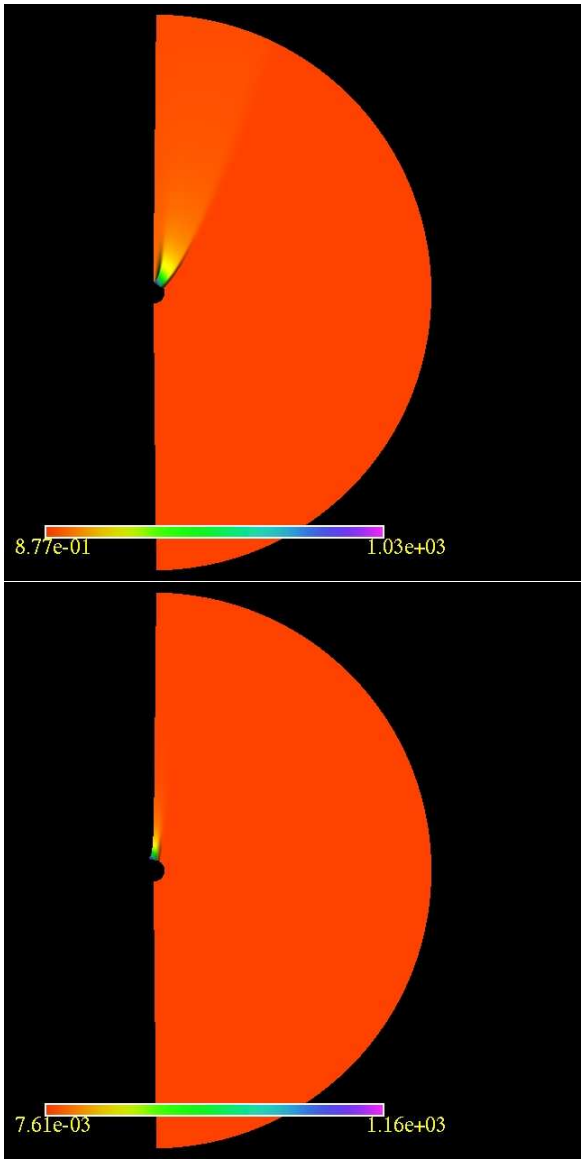

Figure 5.39: The relativistic Bondi–Hoyle accretion simulation for model M1. The black hole is travelling parallel to the background magnetic field direction as measured by an observer at infinity. The top is the thermodynamic pressure, $P_{\rm thermal}(2500, r, \theta)$, the bottom is the magnetic pressure, $P_{\rm magnetic}(2500, r, \theta)$. We see that the thermal pressure decreases significantly on the axis of symmetry near the black hole on the downstream side, exactly where the magnetic pressure is at its largest. The total pressure is presented in Fig. 5.40.

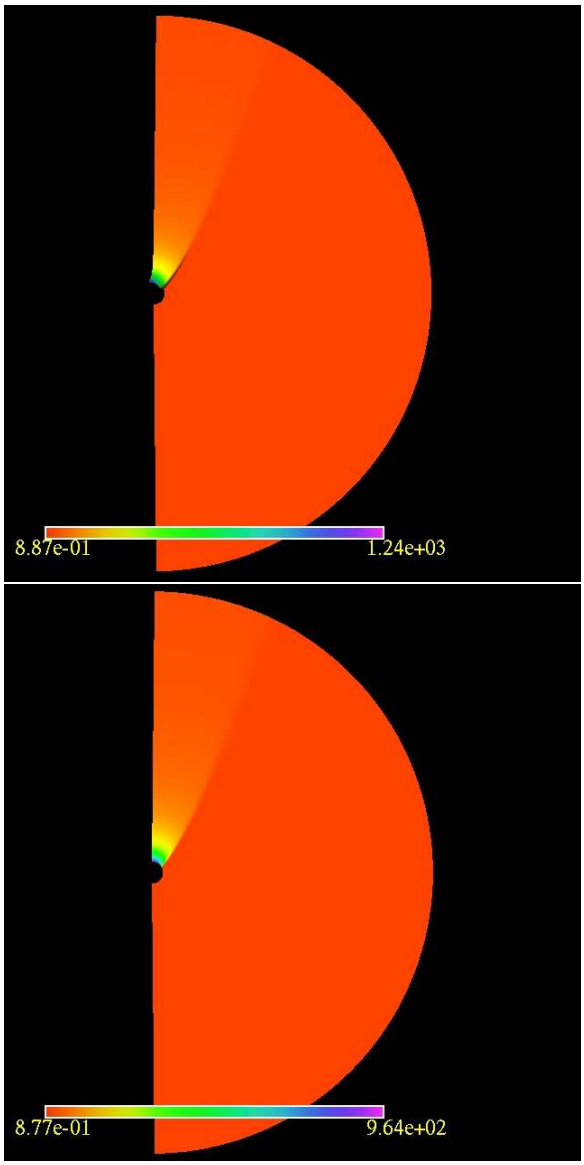

Figure 5.40: The total pressure, $P_{\rm total}(2500, r, \theta)$ (top), for the relativistic Bondi–Hoyle accretion simulation, model M1, and the hydrodynamic pressure for model M1 with $|B| = 0$ (bottom) at $t = 2500$. We see that the total pressure appears to have a similar profile to the hydrodynamic pressure in the flows studied in FI981, where a magnetic field is *not* considered.

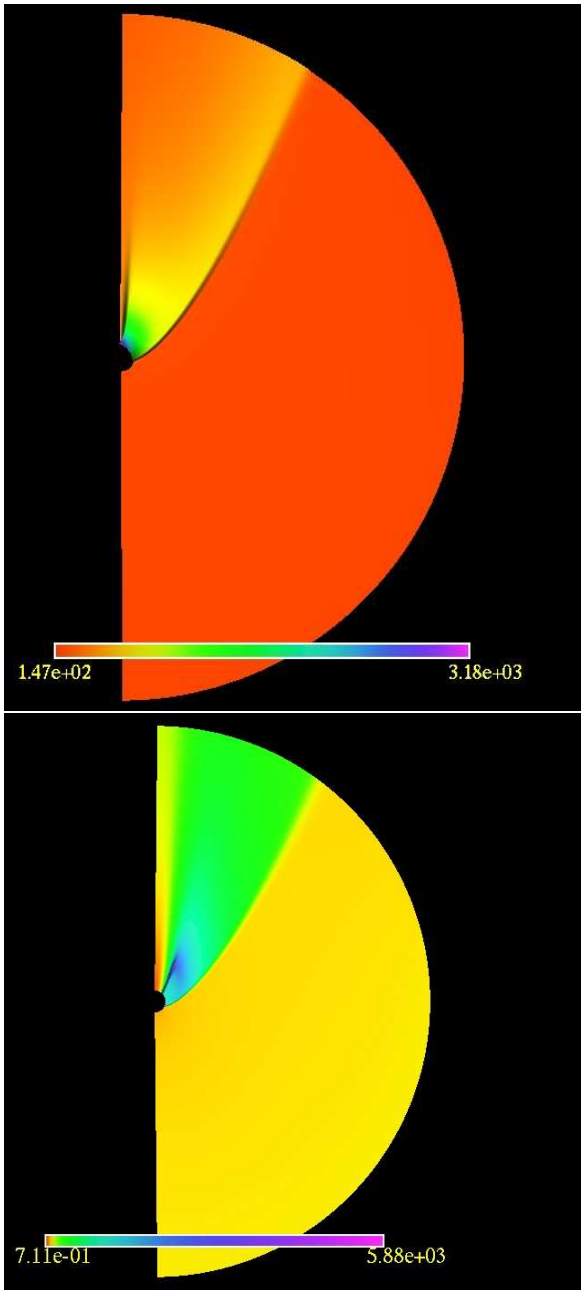

Figure 5.41: The relativistic Bondi–Hoyle accretion simulation for model M2 with $a = 0$. The black hole is travelling parallel to the magnetic field direction as measured by an observer at infinity. Top is the pressure profile, and the bottom is the plasma beta β_P profile. We see evidence that the magnetic field piles up on the downstream side of the black hole. The β_P profile indicates in the downstream side, the near the black hole, the ideal MHD conditions may be breaking down, as the magnitude drops below unity. Note the high β_P regions in the tail of the wake, which indicate regions where the magnetic field drops significantly. These regions start near the black hole and propagate out of the domain along the shock.

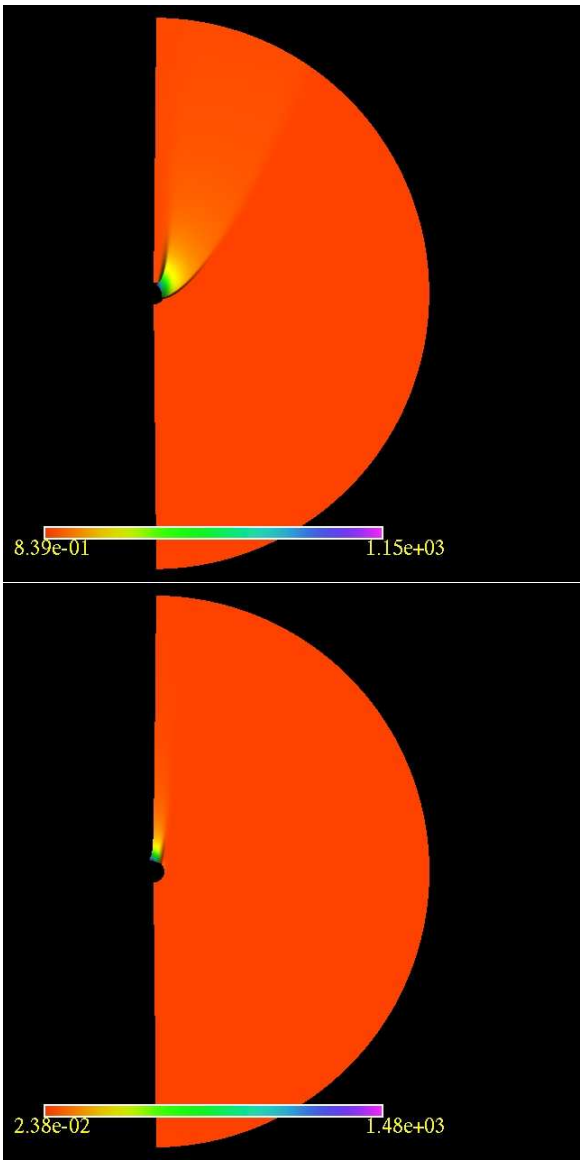

Figure 5.42: The relativistic Bondi–Hoyle accretion simulation for model M2. The black hole is travelling parallel to the background magnetic field direction as measured by an observer at infinity. The top is the thermodynamic pressure, $P_{\rm thermal}(1400, r, \theta)$, the bottom is the magnetic pressure, $P_{\rm magnetic}(1400, r, \theta)$. We see that the thermal pressure decreases significantly on the axis of symmetry near the black hole on the downstream side, where the magnetic pressure on the downstream side of the black hole is at its largest. These results are consistent with those of model M1. The total pressure is presented in Fig. 5.40.

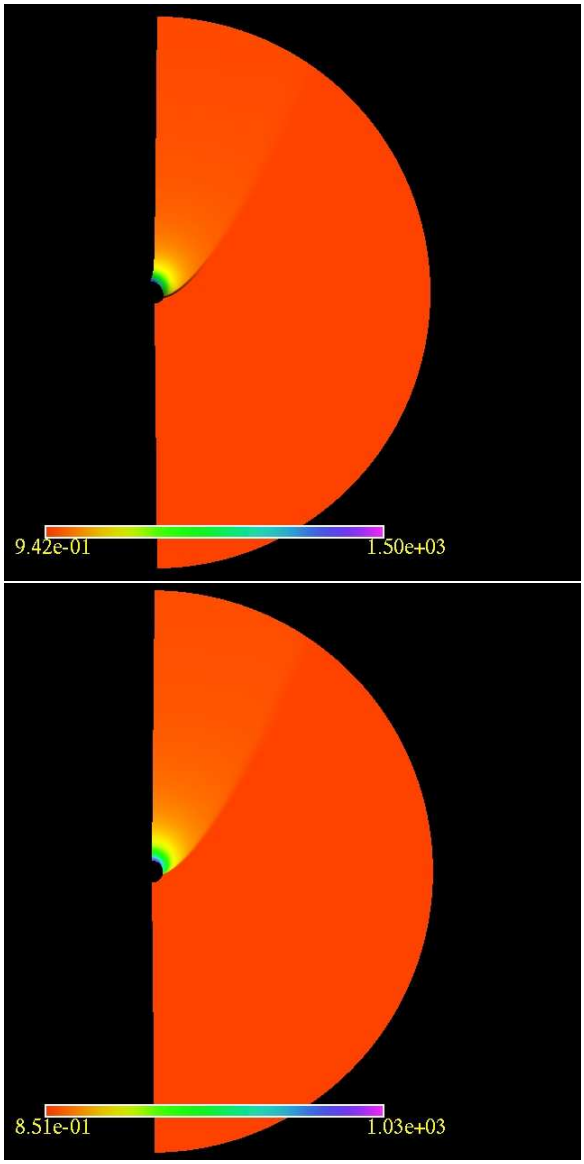

Figure 5.43: The total pressure, $P_{\rm total}(1400, r, \theta)$ (top), for the relativistic Bondi–Hoyle accretion simulation, model M2 and the hydrodynamic pressure for model M2 with $|B| = 0$ (bottom) at time $t = 1400M$. In agreement with the total pressure for model M1, we see that the total pressure on the downstream side of the black hole has a similar profile to the hydrodynamic profile, Fig. 5.45, and in the purely hydrodynamic study performed in FI981.

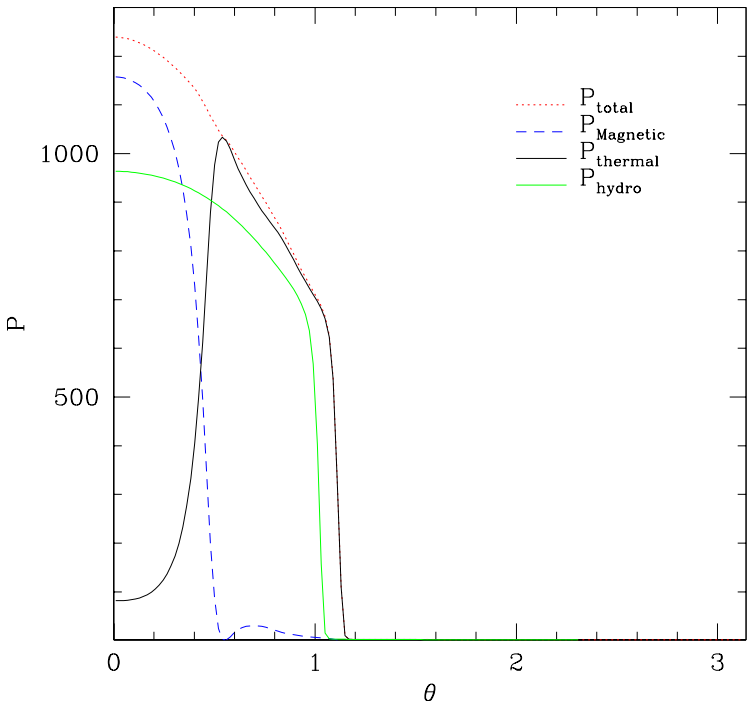

Figure 5.44: The relativistic Bondi–Hoyle accretion pressure cross section for model M1 with $a = 0$. We have plotted the three pressures, thermal, $P_{\rm thermal}(2500, 2, \theta)$, magnetic, $P_{\rm magnetic}(2500, 2, \theta)$, and total pressure, $P_{\rm total}(2500, 2, \theta)$ on the event horizon at $t = 2500$. We see that the magnetic pressure is at its greatest on the axis of symmetry and balances the thermodynamic pressure near $\theta \sim 0.4$, while the purely hydrodynamic model ($|B| = 0$) has a pressure maximum on the axis of symmetry.

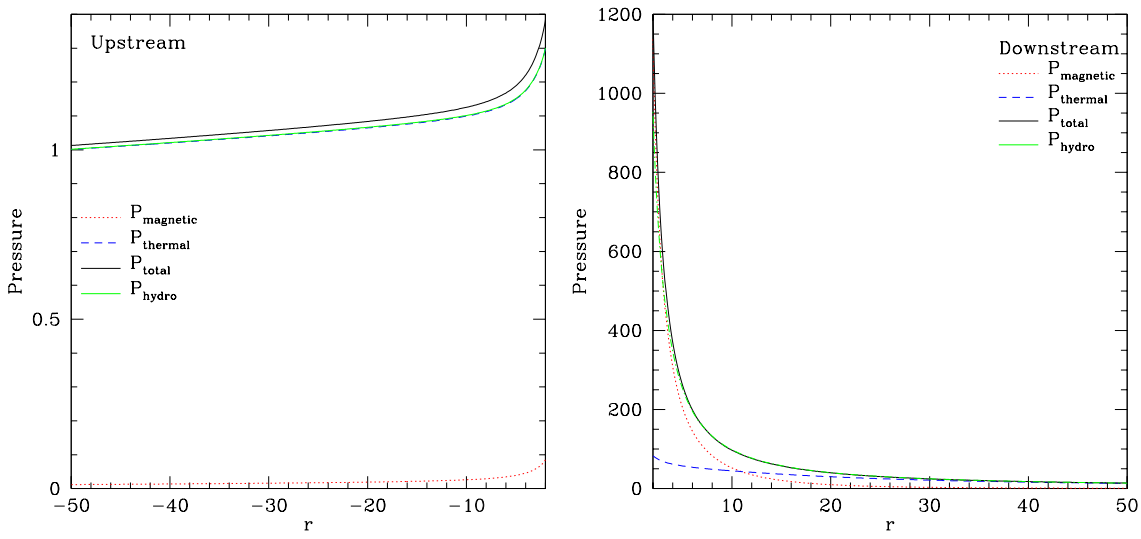

Figure 5.45: The relativistic Bondi–Hoyle accretion pressure profiles for model M1 with $a = 0$. We have plotted the three pressures, thermal, $P_{\rm thermal}(2500, r, \theta)$, magnetic, $P_{\rm magnetic}(2500, r, \theta)$, and total pressure, $P_{\rm total}(2500, r, \theta)$ for both the upstream region, $\theta = \pi$, (left) and the downstream region, $\theta = 0$ (right). In these plots we show the radial domain from the event horizon to the outer domain at $r_{\rm max} = 50$. When comparing to the purely hydrodynamic model, we see that upstream the thermal pressure matches the hydrodynamic pressures, however in the downstream region the total pressure is a closer match to the hydrodynamic pressure. The downstream pressure profile for model M1 does have a larger maximum pressure than the hydrodynamic model allows.

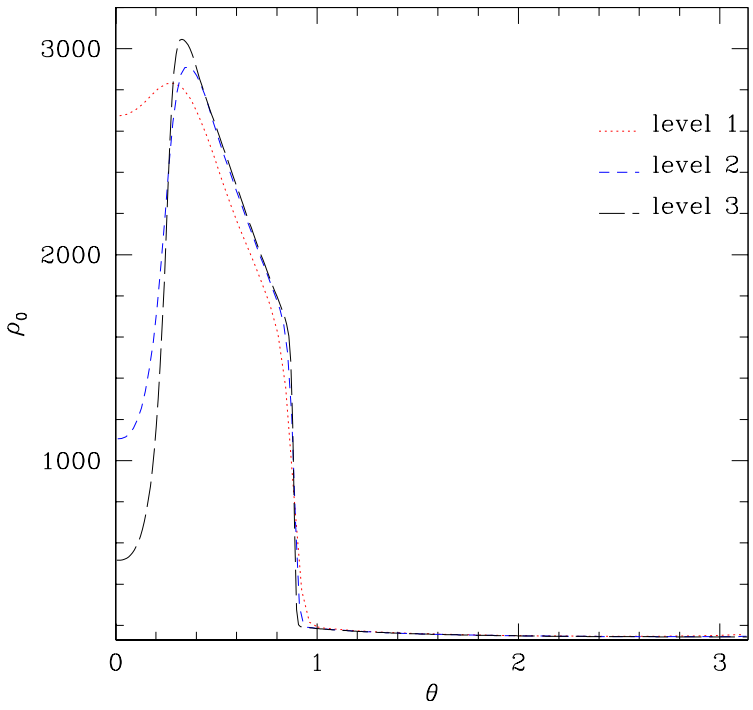

Figure 5.46: A convergence test for the relativistic Bondi–Hoyle accretion simulation for model M1. We see that the baryon rest mass density, ρ_0, is converging to a shock front at $\theta \sim 0.9$. The density profile along the axis in this simulation indicates that the fluid is evacuating the axial location. This is in contrast to the simulations performed in FI981 where the axis marked a density maximum. Level 1 uses $(N_r, N_\theta) = [200 \times 80]$, level 2 $(N_r, N_\theta) = [400 \times 160]$, and level 3 $(N_r, N_\theta) = [800 \times 320]$.

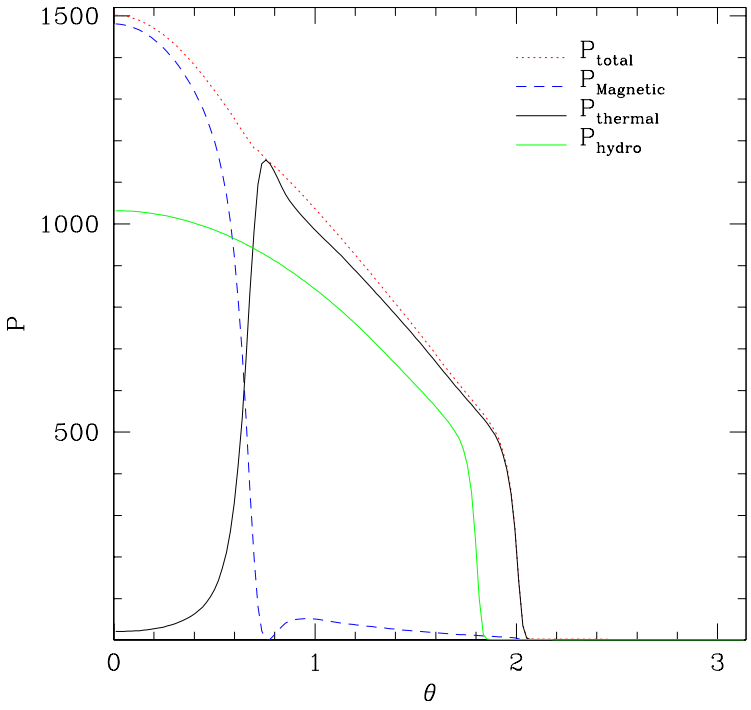

Figure 5.47: The relativistic Bondi–Hoyle accretion pressure cross section for model M2 with $a = 0$. We have plotted the three pressures, thermal, $P_{\rm thermal}(1400, 2, \theta)$, magnetic, $P_{\rm magnetic}(1400, 2, \theta)$, and total pressure, $P_{\rm total}(1400, 2, \theta)$ along the event horizon at $t = 1400$. We see that the magnetic pressure is at its greatest on the axis of symmetry and balances the thermodynamic pressure near $\theta \sim 0.6$ while, like model M1, the hydrodynamic pressure is maximal on the axis of symmetry. We also see that the presence of a magnetic field allows for a wider opening angle of the Mach cone.

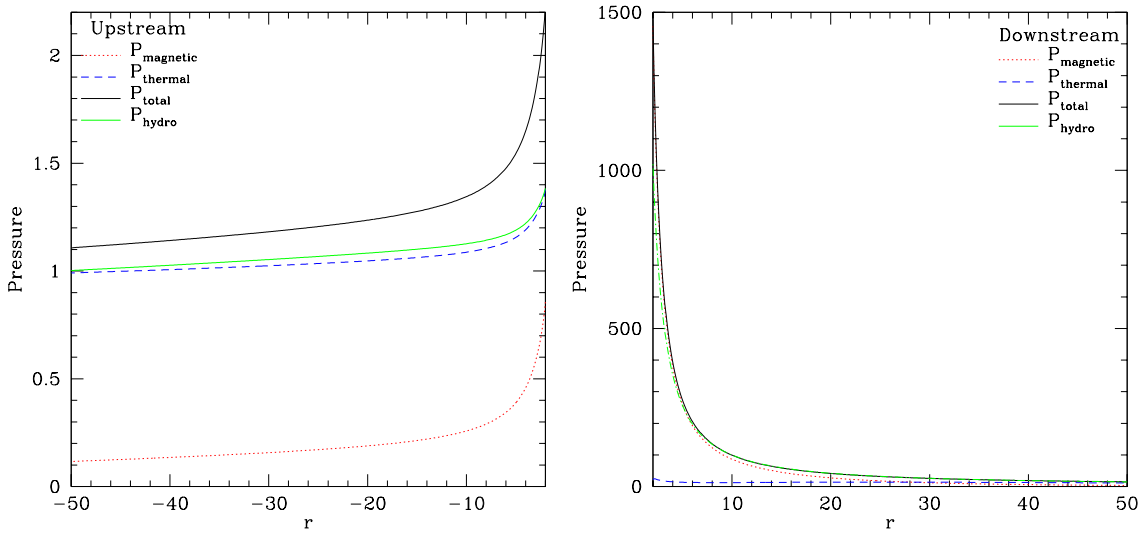

Figure 5.48: The relativistic Bondi–Hoyle accretion pressure profiles for model M2 with $a = 0$. We have plotted the three pressures, thermal, $P_{\rm thermal}(1400, r, \theta)$, magnetic, $P_{\rm magnetic}(1400, r, \theta)$, and total pressure, $P_{\rm total}(1400, r, \theta)$ in both the upstream $\theta = \pi$ (left) and downstream $\theta = 0$ (right) region. The upstream region shows a close agreement between the thermal pressure and the hydrodynamic pressure; however, it ia apparent that the two models are not in as close agreement as seen in Fig. 5.45 for model M1. The downstream pressure profiles for the hydrodynamic model and model M2 are in close agreement. Model M2 allows for a larger downstream pressure maximum than the purely hydrodynamic model allows.

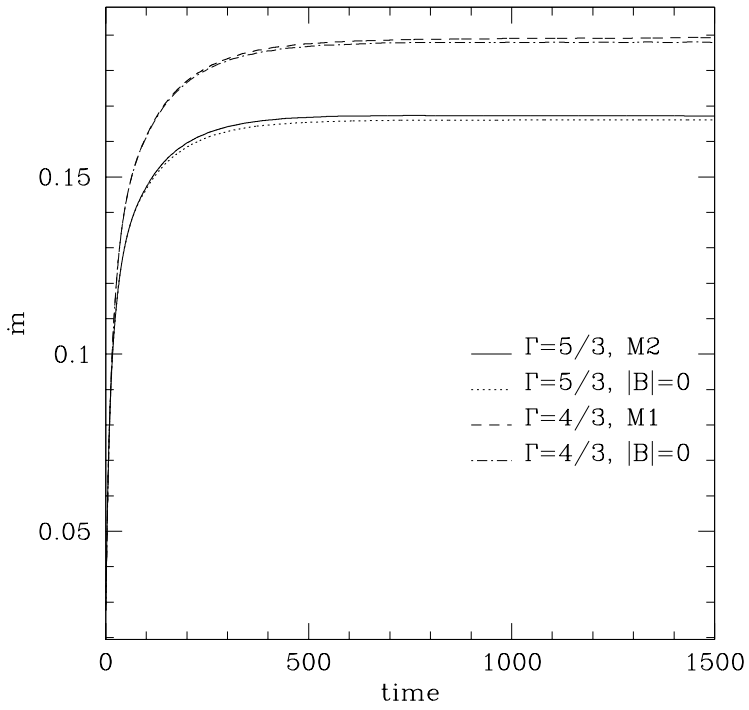

Figure 5.49: The normalized mass accretion for models M1 and M2. The flow with larger Γ accretes more mass, which is in agreement with the hydrodynamic systems studied in FI981 [1]. We have also plotted the mass accretion rates with no magnetic field present. The presence of the magnetic field has a marginal affect on the mass accretion rate.

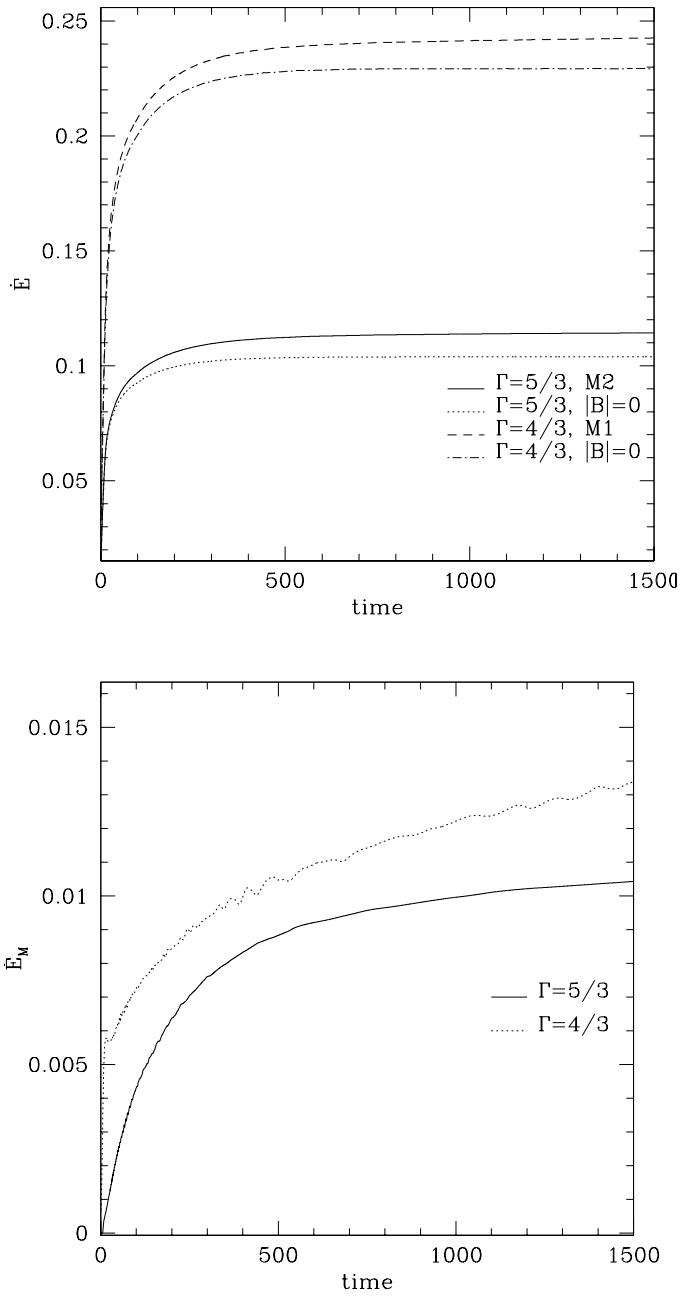

Figure 5.50: The relativistic Bondi–Hoyle energy accretion for models M1 and M2 with the corresponding simulations with no magnetic field present. The magnetic field energy accretion rate, $\dot{E}_{\rm M}$ (bottom), has not yet settled in the time shown here, but the total energy, $\dot{E}$ (top), is clearly steady, which indicates that the hydrodynamic energy contribution in this simulation dominate the system. The trend shown in the total energy accretion rate is in agreement with the hydrodynamic systems studied in Font *et al.* [1]. The oscillations in the magnetic energy accretion rate decrease as a function of resolution.

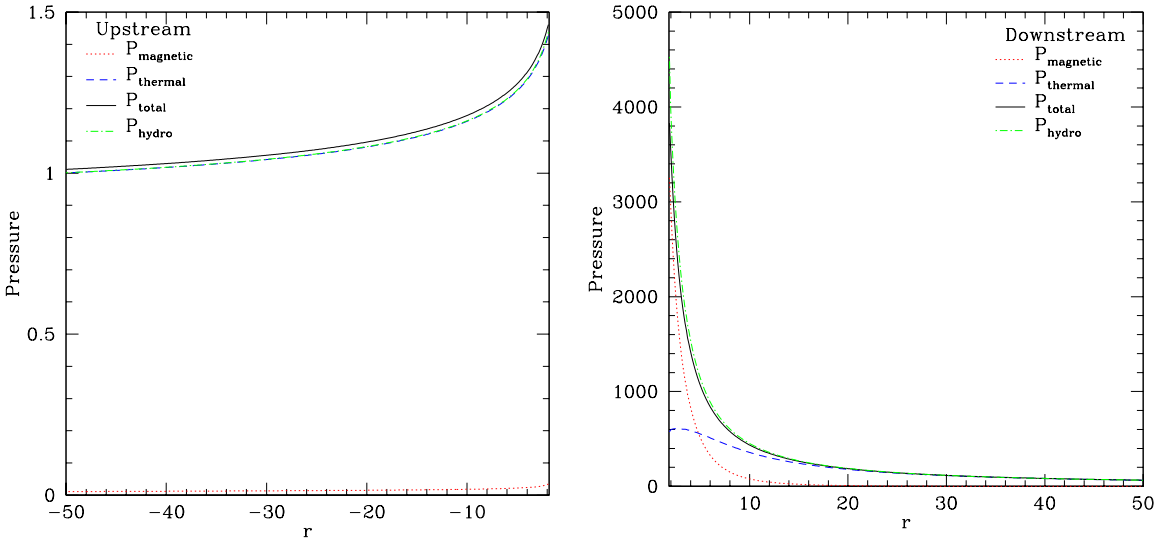

Figure 5.51: Magnetohydrodynamic pressure profiles in the upstream (left) and downstream (right) regions for model M3. We see that the thermal pressure in the upstream region of the black hole is small by comparison to the pressure in the wake in the downstream region. The image on the left shows that there is an increase in pressure as the fluid reaches the black hole, as is expected from Bondi accretion [1]. The bulk of the pressure piles up in the wake of the black hole, the thermal pressure begins to decrease near the black hole in the wake, while the magnetic pressure reaches a maxima on this slice. The above slices are recorded at time $t = 2500M$, and has not yet reached a steady state. As with model M1 the upstream pressure profile closely matches the thermal pressure profile, while the downstream pressure profile closely matches the total pressure. In this configuration, the hydrodynamic pressure profile has a larger maximum than the total pressure profile in model M3.

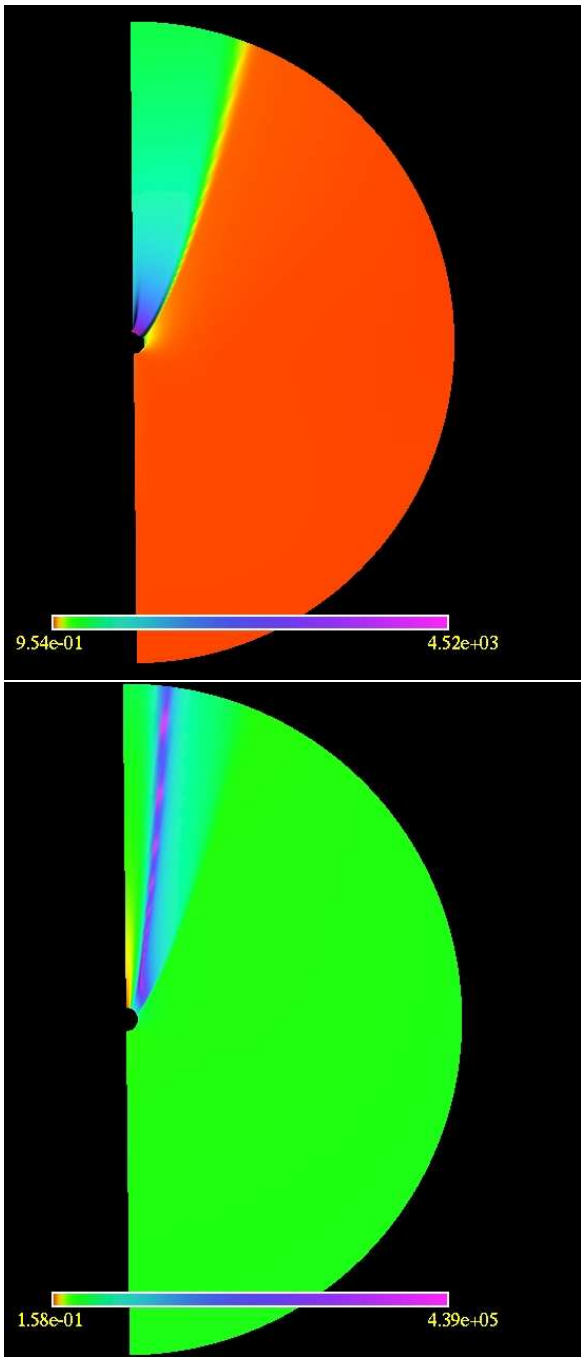

Figure 5.52: The relativistic Bondi–Hoyle accretion simulation for model M3 with $a = 0.5$. The black hole is travelling parallel to the magnetic field direction as measured by an observer at infinity. Top is the pressure profile, and the bottom is the plasma beta β_P profile. We see evidence that the magnetic field piles up on the downstream side of the black hole. The β_P profile indicates in the downstream side, the near the black hole, the ideal MHD conditions may be breaking down, as the magnitude drops below unity. Note the high β_P nodes in the tail of the wake, they indicate regions where the magnetic field drops significantly. These regions start near the black hole and propagate out of the domain along the shock front.

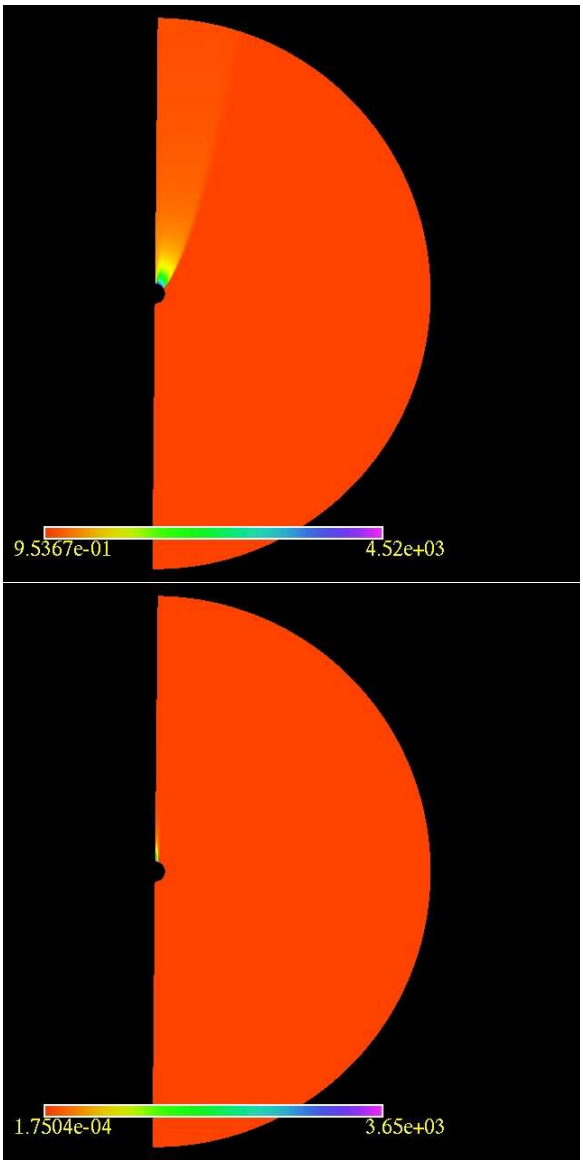

Figure 5.53: The relativistic Bondi–Hoyle accretion simulation for model M3. The black hole is travelling parallel to the background magnetic field direction as measured by an observer at infinity. The top is the thermodynamic pressure, $P_{\rm thermal}(2500, r, \theta)$, the bottom is the magnetic pressure, $P_{\rm magnetic}(2500, r, \theta)$. We see that the thermal pressure decreases on the axis of symmetry near the black hole on the downstream side, where the magnetic pressure on the downstream side of the black hole is at its largest. These results are consistent with those of model M1. The total pressure is presented in Fig. 5.54.

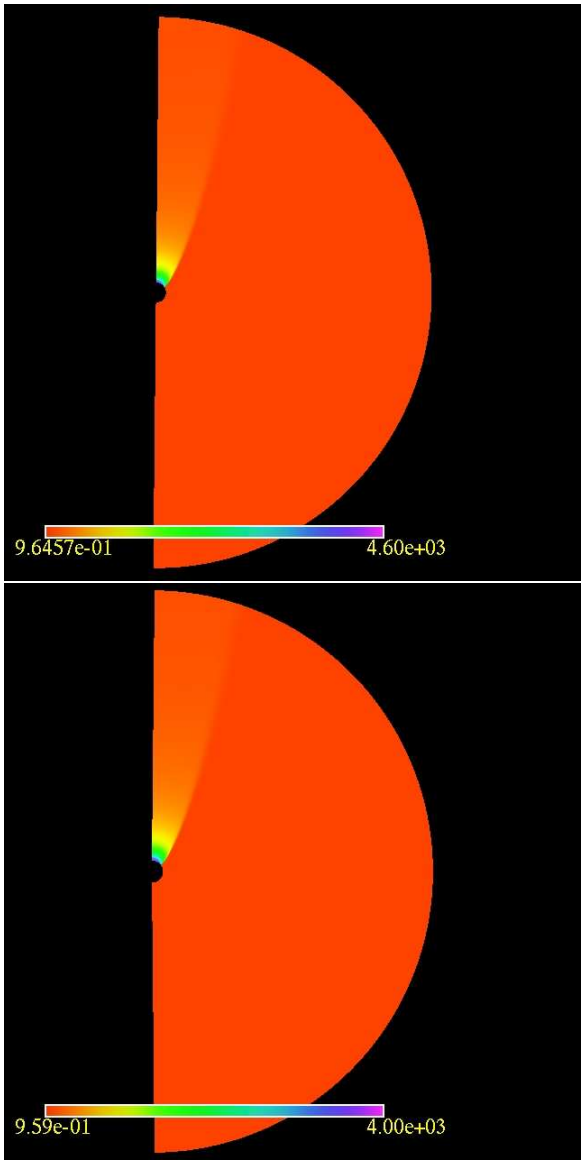

Figure 5.54: The total pressure, $P_{\rm total}(2500, r, \theta)$ (top), for the relativistic Bondi–Hoyle accretion simulation, model M3 and the hydrodynamic pressure for model M3 with $|B| = 0$ (bottom) at time $t = 2500M$. As with the total pressure for models M1 and M2, we see that the total pressure on the downstream side of the black hole takes on a similar profile as the hydrodynamic pressure profile.

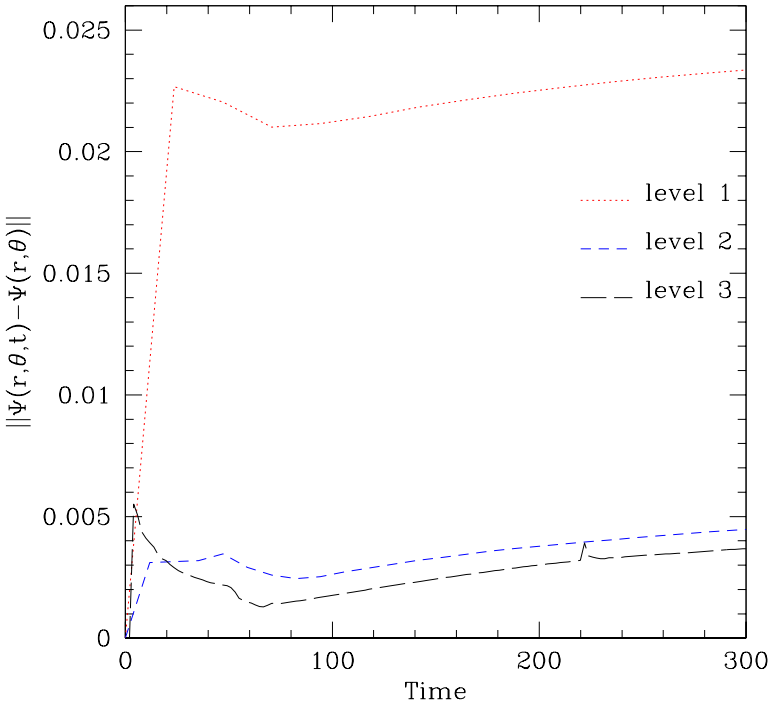

Figure 5.55: The L_2-norm of the auxiliary function $\Psi(t, r, \theta)$ for the relativistic Bondi–Hoyle accretion simulation model M3. This trend shows a small increase of the auxiliary function Ψ, which indicates that there is an increase in the $\nabla \cdot B = 0$ violations. However, with higher resolution we see that the $\nabla \cdot B = 0$ violations are reducing to zero. The slow may account for the accretion of magnetic energy not reaching a steady state.

In Figs. 5.58, 5.59, and 5.60 we see the accretion rates for the magnetized relativistic Bondi–Hoyle accretion flow model M3. In these figures, the asymptotic magnetic field is parallel to the trajectory of the black hole. The magnetic field flux is embedded in the accreting fluid, and consequently also builds in the tail shock. The build-up of the magnetic field strength leads to a decrease in the accretion rate for matter onto the black hole, which is seen in the accretion plots in Figs. 5.59 and 5.60.

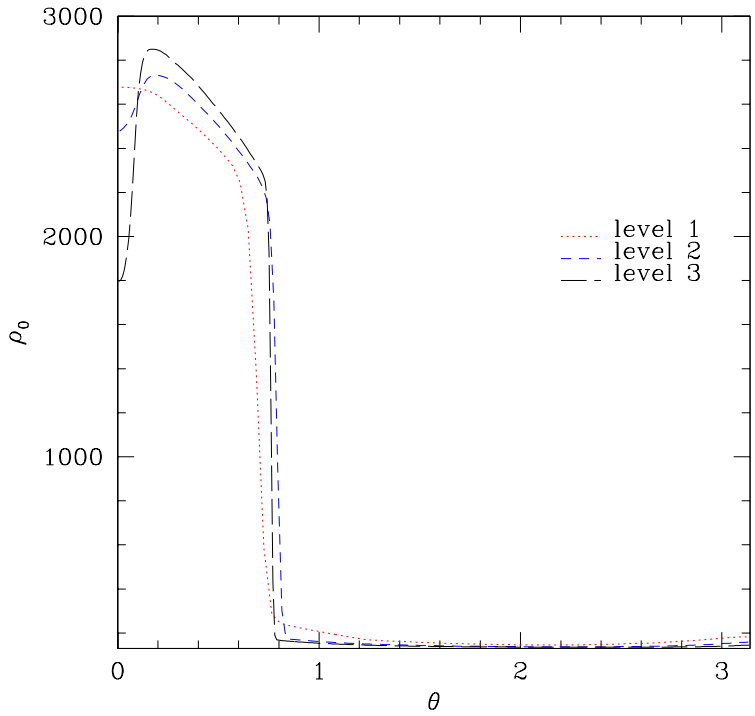

Figure 5.56: A convergence test for the relativistic Bondi–Hoyle accretion simulation for model M3 with $a = 0.5$ at time $t = 300M$. The cross section is taken at $r = 2$M We see that the system is converging to a shock front at $\theta \sim 0.8$.

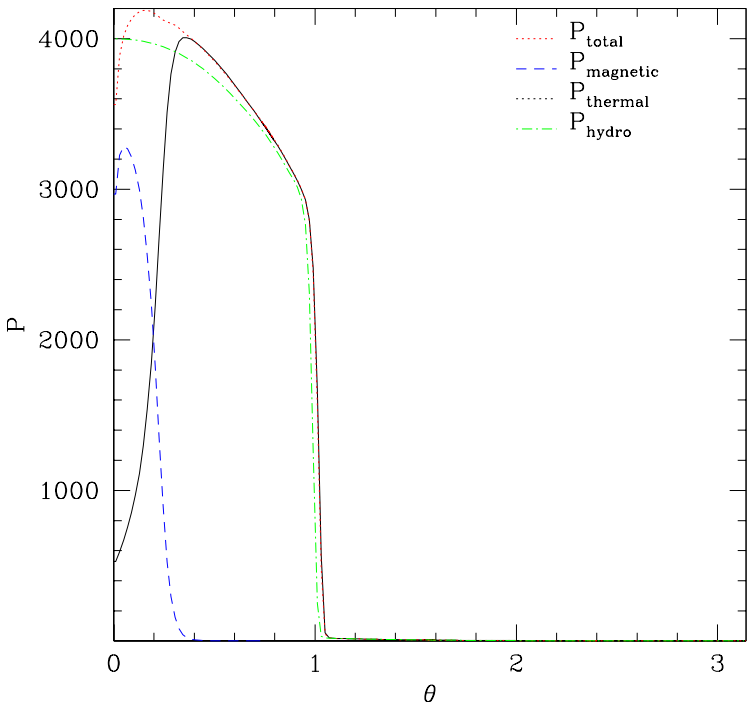

Figure 5.57: Pressure cross section at $r = 2\mathrm{M}$ for model M3 with $O(\beta) = 2$, and $|B| = 0$. We see that the cross section is completely different between the two models. The hydrodynamic model does not experience a depletion region, and we see that with a rotating black hole the pressure in the purely hydrodynamic model is different than exhibited in model M3, including a smaller Mach cone opening angle.

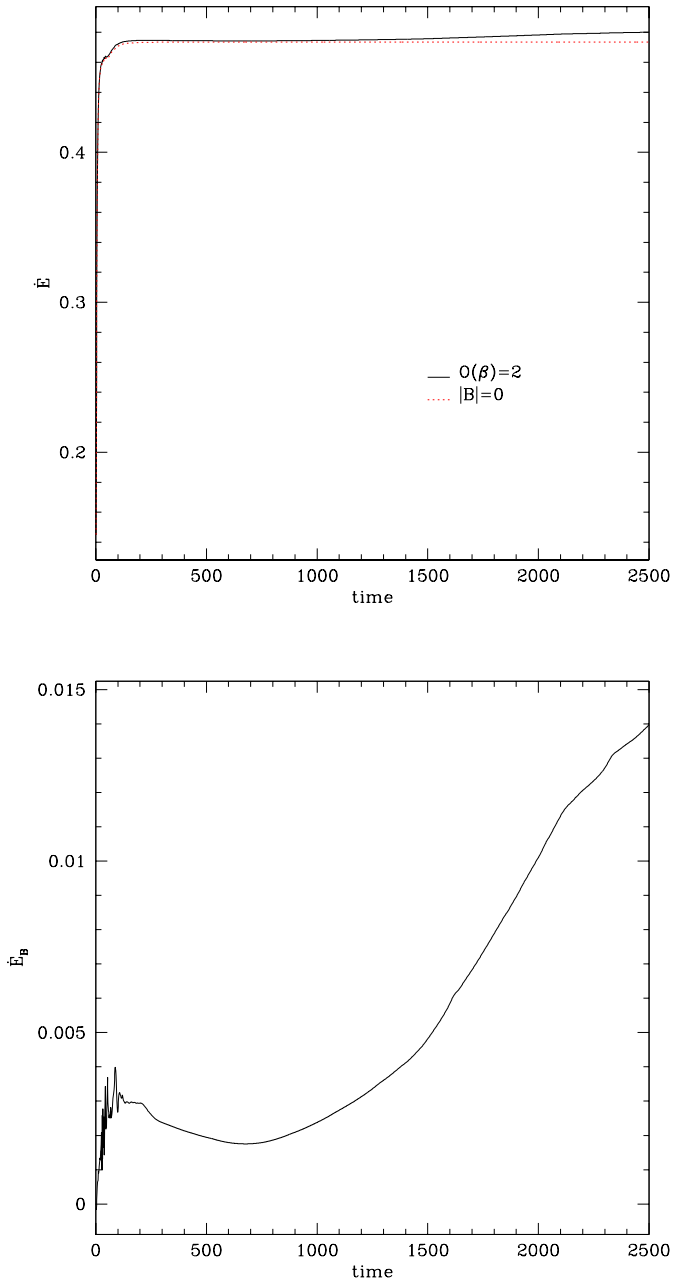

Figure 5.58: The relativistic Bondi–Hoyle energy accretion for model M3. The magnetic field has not settled in the time shown here, but the total energy is clearly steady, which indicates that the hydrodynamic energy contribution in this simulation dominate the system.

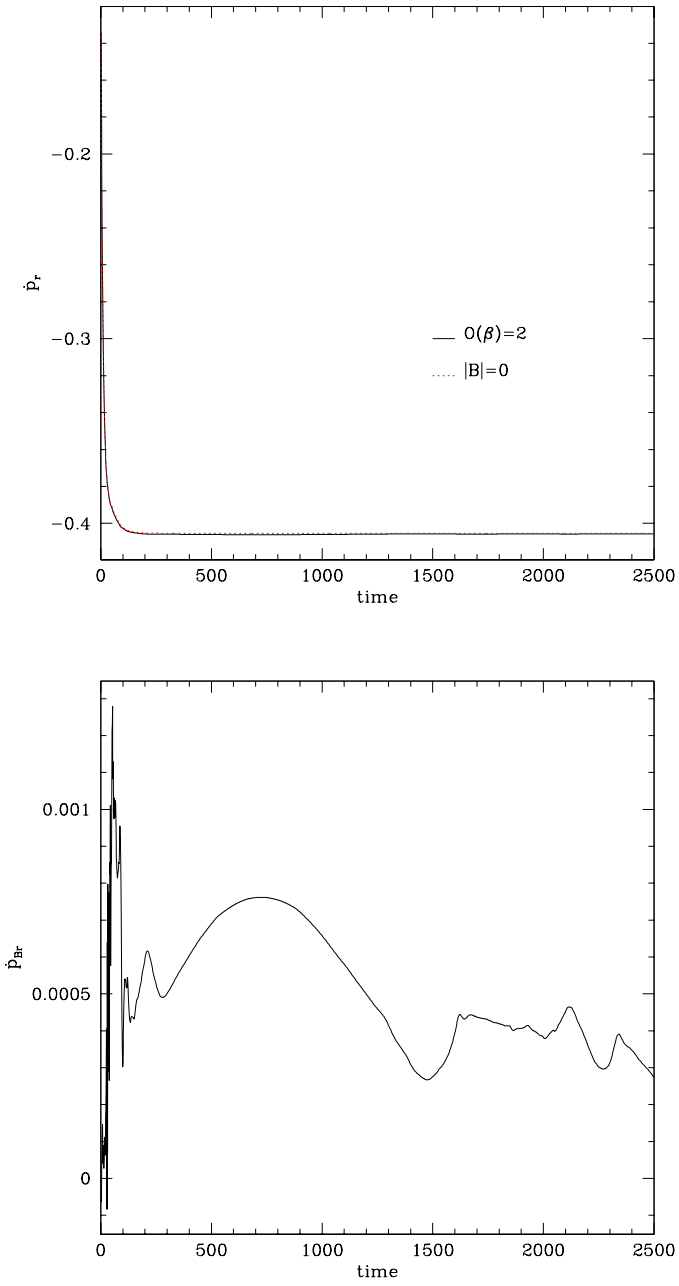

Figure 5.59: The relativistic Bondi–Hoyle accretion simulation for model M3 with $a = 0.5$. The magnetic field has not settled in the time shown here, but the hydrodynamic variables are clearly steady. The top plot shows the radial momentum accretion rate with and without the presence of the magnetic field. It is evident that the magnetic field does not have a large impact on the momentum accretion rate. The bottom plot is the difference between the hydrodynamic radial momentum accretion rate and the total radial momentum accretion rate, which clearly shows unsettled behaviour between the two different systems. We see from this diagnostic calculation that the accretion flow does not indicate that instabilities are forming.

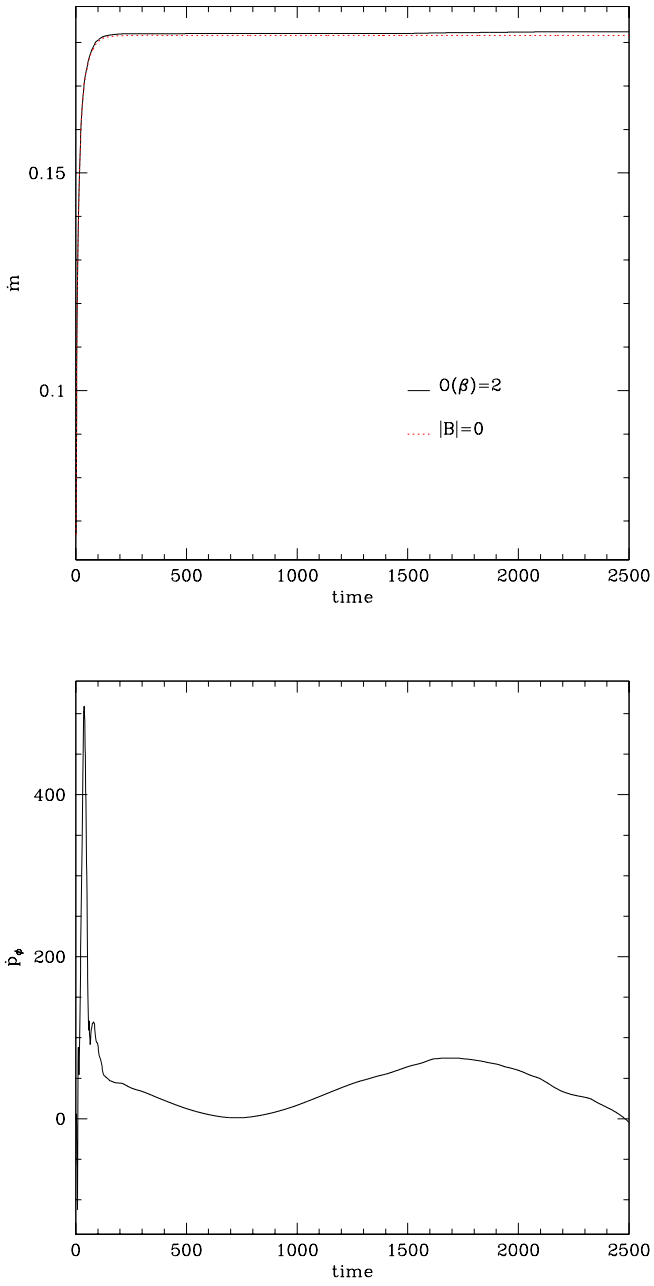

Figure 5.60: The relativistic Bondi–Hoyle accretion simulation for model M3 with $a = 0.5$. The magnetic field has not settled in the time shown here, but the hydrodynamic variables are clearly steady. In the top plot we present the mass accretion rate with and without a magnetic field. There is a slight difference between the accretion rates towards the end of the simulation. This is attributed to the evolution of the magnetic field. In the bottom plot we present the difference between the angular momentum accretion with and without the presence of the magnetic field. We see that a net azimuthal accretion rate is oscillatory. During the transition period there is a large spike in the angular momentum accretion. This is attributed to the initialization of the fluid variables to their asymptotic uniform values and is deemed a numerical artifact.

CHAPTER 6

CONCLUSIONS AND FUTURE DIRECTIONS

6.1 Conclusions

Our studies revealed several interesting new results for the Bondi–Hoyle accretion problem when using different models for the background fluid. We recapitulate these results below and draw our conclusions.

6.1.1 Ultrarelativistic Hydrodynamics

For our investigation of the ultrarelativistic hydrodynamic Bondi–Hoyle accretion problem we conclude that all flows of this configuration and set of boundary conditions are stable for long-term evolution.

In the axisymmetric UHD accretion problem, all flows develop a steady state after a short transition period and maintained stability well after the steady state is established. Unlike the original study by Font *et al.* [1, 2] that used $r_{\rm max} = 50$, this simulation required at a minimum $r_{\rm max} = 100$ to capture the evolution without interference by domain boundaries. A parameter survey where we test the functional dependence of the accretion rate on the value of $r_{\rm max}$ is a future direction for this project. Only preliminary dependence has been investigated so far, and there is evidence that the domain does impact the accretion rate for our system. Font *et al.* used the usual hydrodynamic equations of motion (Eqn. (2.108) using (2.118), (2.119) and (2.120) with $\mathcal{B}^i = 0$) to study fluids with speeds of sound in the ultra relativistic regime, $v_\infty > \sqrt{\Gamma - 1}$. Our study focused on a fluid with an internal energy sufficiently large that we are able to neglect the conservation of the baryon rest mass density entirely, therein solving a different set of hydrodynamic equations. The studies performed by Font *et al.* set the outer radial boundary at $r_{\rm max} = 50$, and assumed that this is sufficiently far from the black hole to prevent numerical artifacts from disrupting the calculations even for their ultrarelativistic study. Our studies of the ultrarelativistic regime show that using $r_{\rm max} = 50$ results in a stable accretion flow that is marred with numerical artifacts. Our

results show that the domain must be carefully monitored to prevent artificial numerical results. Furthermore, when studying the axisymmetric evolution of our formulations of the ultrarelativistic hydrodynamic system we discovered that marginally supersonic flows exhibit a detached shock. The detached shock formation was not achieved in previous simulations.

When larger asymptotic velocities were studied, the flow morphology changed dramatically. The bow shock did not form instead the tail shock that forms early in the simulation remained attached to the black hole. This is in agreement with previous studies presented in [1].

The infinitely thin-disk approximation has a different evolution. The flow, even at large velocities, produces an outward travelling shock wave, propagating upstream. To study this problem effectively we required the use of a much larger domain than those used in the axisymmetric study. In the simulations where the domain size was small, the shock wave would quickly reach the upstream boundary, and alter the boundary conditions in the upstream boundary. The leading shock was found to behave similar to the bow shock found in the axisymmetric $v_\infty = 0.6$ evolution. A tail shock developed, and remained attached to the black hole. The accretion rates were stable and steady in these simulations when a larger domain was used.

6.1.2 Magnetohydrodynamic Accretion

The magnetized fluid background configuration used in our study did not result in a steady accretion flow. We performed a preliminary parameter survey by studying studied a small range of plasma beta parameters, and found that only larger plasma beta parameters would reach a steady state. We were restricted to plasma beta parameters above unity due to the numerical methods used as discussed in Chaps. 2 and 3. Considering larger field strengths require the development of new methods to handle modified equations of motion. Although the flows did not reach a steady state, we can conclude that the flows up to time of termination were stable.

Ultimately, there is a question of how we should maintain the magnetic field constraint. We used the diffusive hyperbolic divergence cleaning method which allowed the violations of the no-divergence constraint to be treated as a flux for an auxiliary field which we could quench as necessary. In this study we considered a quenching parameter of $c_p = 12$ which is used for strong shock conditions [114], and used $c_h = 1$ such that the violations will propagate out of the domain as fast as possible, without the need to decrease the Courant factor to keep the results meaningful.

We investigated both the total field contributions, as well as the magnetic field contributions.

The total field accretion rates achieve a steady rate; however, the magnetic field contributions were relatively small, and did not reach equilibrium. The simulations were pushed to long time evolution, and a steady state was not achieved. Further research considering larger asymptotic magnetic fields will be necessary.

The morphology of the ideal MHD accretion shows a rather significant impact by the presence of a magnetic field. The downstream axial location shows evidence of a depleting density, whereas in the hydrodynamic models presented by Font *et al.* [1], this region has a maximum density. When we studied the accretion onto a rotating black hole, the profile of $\beta_P(t, r, \theta)$ indicated that the magnetic field experienced deficits along the shock front along the tail which propagate out of the domain.

During the simulations, the auxiliary field, Ψ, remained well below unity, and by checking the convergence of this field we saw that it tends to zero, but would slowly grow as the evolution proceeded. During the simulations presented here the constraint violations did not grow sufficiently large to disrupt the system.

The fluid rest mass density and thermal pressure evacuate the region immediately downstream of the black hole. The depleted region corresponds exactly with the region where the magnetic field, and magnetic pressure is at its largest. The large magnetic pressure leads us to consider that the fluid is being evacuated in a similar fashion to the plasma depletion layer near the earths magnetopause. More research is required to know for certain that this is the same effect.

6.2 Summary

The key results from our investigation are

- UHD systems are highly sensitive to the location of the boundary of the domain of integration.
- UHD axisymmetric systems are capable of producing a bowshock.
- UHD non-axisymmetric infinitely thin-disk models produce both bowshocks and tail shocks.
- Both of the UHD configurations studied are stable.
- MHD axisymmetric systems produce a density depletion region immediately downstream of the black hole.

- Although the MHD flows did not reach a steady state, the flows were stable.
- A new field, Ψ, may be used to monitor the convergence rates of MHD systems.

These results were not previously known, and thus are not found in the literature.

We now discuss the future directions that numerical codes can be modified to investigate.

6.3 Future Directions

From our research alone there are several open questions, the first of which is the combination of the ultrarelativistic evolution with the presence of a magnetic field. This would be a useful simulation to determine the accretion rates for early universe black holes where the surrounding fluid is thought to be sufficiently hot to justify the ultrarelativistic approximation, while at the same time we expect the presence of a strong background magnetic field. The codes developed for the UHD simulations are sufficiently generalized to also allow for the evolution of a background magnetic field. In a future paper we expect to analyze such a system in three dimensions. By extending the study to three dimensions will allow us to study any configuration of the black hole relative to the asymptotic magnetic field. Another open question is the dependence the accretion rates have on the value of $r_{\rm max}$ denoting the outer domain of the system. Our studies show that $r_{\rm max}$ has an impact on the accretion rates, and on the flow morphology.

The use of ideal magnetohydrodynamics limited our study to cases where the magnetic field strength was insufficient to significantly affect the accretion rates. If we extend our numerical method to allow for a transition to force-free electrodynamics (FFED) [119], in particular near the black hole, we will be able to increase the asymptotic magnetic field strength and study the strong field limit.

Further, there has been some unpublished development of methods that allow hydrodynamic codes to capture a true vacuum. Implementing such effects in an MHD code will aid in the understanding of true (magneto)fluid dynamics.

Research into relativistic plasma astrophysics is still in its infancy, with the advent of high powered supercomputers and the persistent study of higher accuracy approximate solutions to the (magneto)hydrodynamic equations of motion we are able to probe closer and closer to the true behaviour of fluid systems. Only in the last decade have the numerical tools used to study relativistic magnetized fluid systems been developed. Because of this we have only scratched the

surface of all the different effects and possible configurations that observation may one day detect. I list a few of the extensions that I find to be the most interesting. This is not a complete list of all the possibilities but does offer a sample of how much more there is to do in the field of fluid dynamics and magnetohydrodynamics.

Force-Free Electrodynamics

In the regime where the magnetic field strengths are sufficiently large that the hydrodynamic contributions are negligible we are to consider force free electrodynamics, wherein one uses the force free idea described above and apply it to the electrodynamic equations [167, 151]. This reduces the system to the study of the full complement of the electrodynamics equations and the three momentum/velocity fields. Such a system is necessary when the plasma beta parameter is much less than unity, so the magnetic field energy and pressure dominate the hydrodynamic quantities. If at any point the ideal MHD system develops a plasma beta that drops well below unity the ideal MHD conditions break down and a new set of equations of motion are necessary.

Viscous Hydrodynamics

Theories of relativistic viscous hydrodynamics, such as those presented in Misner, Thorn and Wheeler's Gravitation [4] are not in agreement with the kinetic theory of relativistic viscous hydrodynamics. I intend to continue my study of hydrodynamic systems by investigating a more general case of heat transport beyond the idealized cases. Some research into thermodynamic effects has been studied by investigating thermodynamic radiation from a Stephan-Boltzmann law for black-body radiation. This is a necessary process to study if one is in the lower energy limit. If we deviate too far from the IR spectrum we usually have to leave the black-body treatments as a mild effect relative to other more dominating radiation effects [168, 169]. More recent work on this effort are considered in Romatschke [170, 171].

Full Electromagnetic hydrodynamics

Recently, the study of MHD systems has given us the tools needed to study the full electromagnetic hydrodynamic systems. In these systems conductance is no longer infinite, and consequently electric fields are not longer explained using the ideal MHD condition. Some of the leading authors on this material are Palenzuela, [116] and Komissarov [167]. Each group have formulations for the full

electromagnetic hydrodynamics still in the ideal fluid limit, and expressed for special relativistic metrics. It would be of great interest to study the effects of the full system in general relativity even with stationary metrics.

Equation of State

Finally, there has been an effort by some members of the MHD community to attempt to study more "realistic" equations of state. The range of possible equations of state is quite large and it is a difficult task to review all expressions here. Most of the research in (magneto)hydrodynamic flows performed to date uses the ideal gas equation of state as a means to use a well known and well understood equation of state to determine what kind of dynamics ensue. By adhering so closely to such an approximation is limiting. In some cases the idealization is used for the ease of closed form calculations or for ease of numerical computation. An example of a more general equation of state was studied by Synge to describe what is now known as a Synge gas [172]. For consistency with the kinetic theory of gases, in the limit of negligible mean free path, Taub determined that we cannot treat the specific heat ratio as a constant [106]. With modern computers and algorithms, this type of generalization, although more expensive that the current approximations, is worth pursuing.

BIBLIOGRAPHY

[1] J.A. Font and J.M. Ibáñez. A Numerical Study of Relativistic Bondi–Hoyle Accretion onto a Moving Black Hole: Axisymmetric Computations in a Schwarzschild Background. *The Astrophysical Journal*, 494:297–316, (1998).

[2] J.A. Font and J.M. Ibáñez. Non-axisymmetric Relativistic Bondi–Hoyle Accretion onto a Schwarzschild Black Hole. *MNRAS*, 298:835–846, (1998).

[3] J.A. Font, J.M. Ibáñez, and P. Papadopoulos. Non-axisymmetric Relativistic Bondi–Hoyle Accretion onto a Kerr Black Hole. *MNRAS*, 305:920–936, (1999).

[4] C. W. Misner, K. S. Thorne, and J. A. Wheeler. *Gravitation*. W.H. Freeman and Company, New York, (1973).

[5] M. Camenzind. *Compact Objects in Astrophysics*. Springer-Verlag, Berlin Heidelberg, (2007).

[6] S.L. Shapiro and S.A. Teukolsky. *Black Holes, White Dwarfs and Neutron Stars: The Physics of Compact Objects*. Wiley-Interscience, (1983).

[7] H. Bondi and F. Hoyle. On the Mechanism of Accretion by Stars. *MNRAS*, 104:273, (1944).

[8] L.I. Petrich, S.L. Shapiro, R.F. Stark, and S.A. Teukolsky. Accretion onto a Moving Black Hole - A Fully Relativistic Treatment. *Astro. & Astrophys.*, 336:313–349, (1989).

[9] Scott Charles Noble. *A Numerical Study of Relativistic Fluid Collapse*. PhD thesis, University of Texas at Austin, (2003).

[10] G. Birkhoff. Numerical Fluid Dynamics. *SIAM Review*, 25:1–34, (1983).

[11] O. Darrigol. Empirical Challenges and Concept Formation in the History of Hydrodynamics. *Centaurus*, 50:214–242, (2008).

[12] S. Goldstein. Fluid Mechanics in the First Half of This Century. *Annual Review of Fluid Mechanics*, 1:1–129, (1969).

[13] M.M. May and R.H. White. Hydrodynamic Calculations of General-Relativistic Collapse. *Phys. Rev.*, 141(4):1232–1241, (1966).

[14] M.M. May and R.H. White. Stellar Dynamics and Gravitational Collapse. *Methods Comput. Phys.*, 7:219–258, (1967).

[15] Ignacio (Iñaki) Olabarrieta. *Relativistic Hydrodynamics and Other Topics in Numerical Relativity*. PhD thesis, University of British Columbia, (2004).

[16] J.R. Wilson. Numerical Study of Fluid Flow in Kerr Space. *Ap.J.*, 173:209–219, (1971).

[17] J.R. Wilson. A Numerical Method for Relativistic Hydrodynamics. *Sources of Gravitational Radiation, ed. L. Smarr*, pages 423–445, (1978).

[18] R.D. Richtmyer and K.W. Morton. *Difference Methods for Initial-Value Problems, Second edition*. Interscience Publishers, (1967).

[19] J.M. Martí, J.M. Ibáñez, and J.A. Miralles. Numerical Relativistic Hydrodynamics: Local Characteristic Approach. *Phys.Rev.D*, 43:3794–3801, (1991).

[20] J.A. Font. Numerical Hydrodynamics and Magnetohydrodynamics in General Relativity. *Living Reviews, http://relativity.livingreviews.org/Articles/lrr-2008-7/index.html*, (2008).

[21] J.M. Martí and E. Múller. Numerical Hydrodynamics in Special Relativity. *Living Reviews, http://relativity.livingreviews.org/Articles/lrr-2003-7/index.html*, (2003).

[22] F.C. Michel. Accretion of Matter by Condensed Objects. *Astrophysics amd Space Science*, 15:153–160, (1972).

[23] S.A. Balbus and J.F. Hawley. Instability, Turbulence, and Enhanced Transport in Accretion Disks. *Reviews of Modern Physics*, 70:1–53, (1998).

[24] J.F. Hawley. *A Numerical Study of Nonspherical Black Hole Accretion.* PhD thesis, Illinois Univ., Urbana-Champaign, (1984).

[25] J.F. Hawley, L.L. Smarr, and J.R. Wilson. A Numerical Study of Nonspherical Black Hole Accretion I. equations and test problems. *Ap.J.*, 277:296–311, (1984).

[26] J.F. Hawley, L.L. Smarr, and J.R. Wilson. A Numerical Study of Nonspherical Black Hole Accretion II. finite differencing and code calibration. *Ap.J. Supp*, 55:211–246, (1984).

[27] J. Frank, A.R. King, and D.J. Raine. *Accretion Power in Astrophysics, Third Ed.* Cambridge University Press, (2002).

[28] J-P. DeVilliers and J. Hawley. Three-Dimensional Hydrodynamic Simulations of Accretion Tori in Kerr Spacetime. *Ap.J.*, 577:866–879, (2002).

[29] J.C.B. Papaloizou and J.E. Pringle. The Dynamical Stability of Differentially Rotating Discs with Constant Specific Angular Momentum. *MNRAS*, 208:721–750, (1984).

[30] B.W. Carroll and D.A. Ostlie. *An Introduction to Modern Astrophysics.* Addison Wesley, San Francisco, CA, (2007).

[31] R.M. Wald. *General Relativity.* University of Chicago Press, Chicago IL, (1984).

[32] D. Neilsen and M.W. Choptuik. Ultrarelativistic Fluid Dynamics. *Class. Quantum Grav.*, 17:733–759, (2000).

[33] M.S. David Wayne Neilsen, B.S. *Extremely Relativistic Fluids in Strong-Field Gravity.* PhD thesis, University of Texas at Austin, (1999).

[34] M. Snajdr. Critical Collapse of an Ultrarelativistic Fluid in the $\gamma \rightarrow 1$ Limit. *Class. Quantum Grav.*, 23:3333–3352, (2006).

[35] L.I. Petrich, S.L. Shapiro, and S.A. Teukolsky. Accretion onto a Moving Black Hole: An Exact Solution. *Phys. Rev. Lett.*, 60:1781–1784, (1988).

[36] J-P. De Villiers and J.F. Hawley. Global General Relativistic Magnetohydrodynamic Simulations of Accretion Tori. *Ap.J.*, 592:1060–1077, (2003).

[37] P. Anninos, P.C. Fragile, and J.D. Salmonson. COSMOS++: Numerical Relativistic Magnetohydrodynamics on Unstructured Grids With Local Adaptive Refinement. *Ap.J.*, 635:723–740, (2005).

[38] P.C. Fragile, O.M. Blaes, P. Anninos, and J.D. Salmonson. Global General Relativistic Magnetohydrodynamic Simulation of a Tilted Black Hole Accretion Disk. *Ap.J.*, 668:417–429, (2007).

[39] M.H.P.M. van Putten. A Numerical Implementation of MHD in Divergence Form. *Journal of Computational Physics*, 105:339–353, (1993).

[40] M. Brio and C.C Wu. An Upwind Scheme for the Equations of Ideal Magnetohydrodynamics. *Journal of Computational Physics*, 75:400–422, (1988).

[41] J.S. Hesthaven, S. Gottlieb, and D. Gottlieb. *Spectral Methods for Time-Dependent Problems*. Cambridge University Press, (2007).

[42] M.H.P.M. van Putten. A Two-Dimensional Numerical Implementation of Magnetohydrodynamics in Divergence Form. *SIAM J. Numer. Anal.*, 32(5):1504–1518, (1995).

[43] S.S. Komissarov. A Godunov-type Scheme for Relativistic Magnetohydrodynamics. *MNRAS*, 303:343–366, (1999).

[44] D. Balsara. Total Variation Dimisnishing Scheme for Relativistic Magnetohydrodynamics. *Ap.J. Supp.*, 132(83), (2001).

[45] L. Del Zanna, N. Bucciantini, and P. Londrillo. An Efficient Shock-capturing Central-type Scheme for Multidimensional Relativistic Flows. II. Magnetohydrodynamics. *Astron. & Astro.*, 400:397–413, (2003).

[46] J.M. Marti and E. Müller. The Analytical Solution of the Riemann Problem in Relativistic Hydrodynamics. *J. Fluid Mech.*, 258:317–333, (1994).

[47] J.A. Pons, J.M. Martí, and E. Müller. The Exact Solution of the Riemann Problem with Nonzero Tangential Velocities in Relativistic Hydrodynamics. *J. Fluid Mech.*, 422:125, (2000).

[48] L. Rezzolla and O. Zanotti. An Improved Exact Riemann Solver for Relativistic Hydrodynamics. *J. Fluid Mech.*, 449:395–411, (2001).

[49] B. Giacomazzo and L. Rezzolla. The Exact Solution of the Riemann Problem in Relativistic Magnetohydrodynamics. *J. Fluid Mech.*, 562:223–259, (2006).

[50] A.M. Anile. *Relativistic Fluids and Magnetofluids: With applications in astrophysics and plasma physics*. Cambridge University Press, (1989).

[51] C.F. Gammie and J.C. McKinney. HARM: A Numerical Scheme for General Relativistic Magnetohydrodynamics. *Ap.J.*, 589:444–457, (2003).

[52] S.S. Komissarov. Observations of the Blandford-Znajek Process and the Magnetohydrodynamics Penrose Process in Computer Simulations of Black Hole Magnetospheres. *MNRAS*, 359:801–808, (2005).

[53] L. Antón, O. Zanotti, J. Miralles, J. Martí, J. Ibáñez, J. Font, and J. Pons. Numerical 3+1 General Relativistic Magnetohydrodynamics: A Local Characteristic Approach. *Ap.J.*, 637:296–312, (2006).

[54] P.J. Montero, O. Zanotti, J.A. Font, and L. Rezzolla. Dynamics of Magnetized Relativistic Tori Oscillating Around Black Holes. *MNRAS*, 378:1101–1110, (2007).

[55] C.D. Ott. The Gravitational-wave Signature of Core-Collapse Supernovae. *Classical and Quantum Gravity*, 26:063001, (2009).

[56] S.J. Smartt. Progenitors of Core-Collapse Supernovae. *Annual Review of Astronomy and Astrophysics*, 47:63–106, (2009).

[57] M. Duez. Numerical Relativity Confronts Compact Neutron Star Binaries: a review and status report. *Class. Quantum Grav.*, 27:114002, (2010).

[58] C. Fryer and K. New. Gravitational Waves from Gravitational Collapse. *Living Reviews, http://relativity.livingreviews.org/Articles/lrr-2003-2/index.html*, (2003).

[59] J.M. Stone and S.A. Balbus. Angular Momentum Transport in Accretion Disks by Convection. *Ap.J.*, 464:364, (1996).

[60] S.A. Balbus, J.F. Hawley, and J.M. Stone. Hydrodynamical Turbulence, Nonlinear Stability, and Transport in Disks. *Ap.J.*, 467:76, (1996).

[61] S.A. Balbus and J.F. Hawley. A Powerful Local Shear Instability in Weakly Magnetized Disks. I - linear analysis. ii - nonlinear evolution. *Ap.J.*, 376:214–233, (1991).

[62] J.F. Hawley and J.M. Stone. MOCCT: A Numerical Technique for Astrophysical MHD. *Comp. Phys. Comm.*, 89:127–148, (1995).

[63] R. Edgar. A Review of Bondi–Hoyle–Lyttleton Accretion. *New Astronomy Reviews*, 48:843–859, (2004).

[64] S. Rosswog and M. Brüggen. *Introduction to High-Energy Astrophysics*. Cambridge University Press, Cambridge, UK, (2007).

[65] H.J.G.L.M. Lamers and J.P. Cassinelli. *Introduction to Stellar Winds*. Cambridge University Press, (1999).

[66] M. Harwit. *Astrophysical Concepts*. John Wiley & Sons, Inc., (1973).

[67] J.I. Castor, D.C. Abbott, and R.I. Klein. Radiation-Driven Winds in Of Stars. *Ap.J.*, 195:157–174, (1975).

[68] B.D. Farris, Y.T. Liu, and S.L. Shapiro. Binary Black Hole Mergers in Gaseous Environments: "Binary Bondi" and "Binary Bondi–Hoyle–Lyttleton" Accretion. *Phys. Rev. D*, 81:084008, (2010).

[69] M.S. Longair. *High Energy Astrophysics, Volume 2 Second Edition*. Cambridge University Press, Cambridge, (1994).

[70] F. Hoyle and R.A. Lyttleton. The Effect of Interstellar Matter on Climatic Variation. *Proc. Camb. Phil. Soc.*, 35, (1939).

[71] F. Hoyle and R.A. Lyttleton. On the Accretion of Interstellar Matter by Stars. *Proc. Camb. Phil. Soc.*, 36, (1940).

[72] F. Hoyle and R.A. Lyttleton. On the Physical Aspects of Accretion by Stars. *Proc. Camb. Phil. Soc.*, 36, (1940).

[73] F. Hoyle and R.A. Lyttleton. On the Accretion Theory of Stellar Evolution. *MNRAS*, 101, (1941).

[74] H. Bondi. On Spherically Symmetric Accretion. *MNRAS*, 112:195, (1952).

[75] M. Ruffert. Hydrodynamic Calculations of Axisymmetric Accretion Flow. *MNRAS*, 217, (1985).

[76] M. Ruffert. Three-Dimensional Hydrodynamic Bondi–Hoyle Accretion, I. code validation and stationary accretors. *Ap.J.*, 427, (1994).

[77] M. Ruffert. Three-Dimensional Hydrodynamic Bondi–Hoyle Accretion, II. homogeneous medium at mach 3 with $\gamma = 5/3$. *Ap.J.*, 427, (1994).

[78] M. Ruffert. Three-Dimensional Hydrodynamic Bondi–Hoyle Accretion, III. mach 0.6, 1.4 and 10; $\gamma = 5/3$. *Astro. & Astrophys. Supp.*, 106, (1994).

[79] M. Ruffert. Three-Dimensional Hydrodynamic Bondi–Hoyle Accretion, IV. specific heat ratio 4/3. *Astro. & Astrophys. Supp.*, 113, (1995).

[80] M. Ruffert. Three-Dimensional Hydrodynamic Bondi–Hoyle Accretion, V. specific heat ratio 1.01, nearly isothermal flow. *Astro. & Astrophys. Supp.*, 106, (1995).

[81] T. Foglizzo, P. Galletti, and M. Ruffert. A Fresh Look at the Unstable Simulations of Bondi–Hoyle–Lyttleton Accretion. *Astron. & Astrophys.*, 435, (2005).

[82] T. Foglizzo, P. Galletti, and M. Ruffert. A Fresh Look at the Unstable Simulations of Bondi–Hoyle–Lyttleton Accretion. *Astro. & Astrophys.*, 435:397–411, (2005).

[83] J. Blondin and C. Pope. Revisiting the "Flip-Flop" Instability of HoyleLyttleton Accretion. *Astron. & Astrophys.*, 700, (2009).

[84] M. Ruffert. Simulations of Coalescing Neutron Star and Black Hole Binaries. *Progress of Theoretical Physics*, 136:287–299, (1999).

[85] K. Sawada, T. Matsuda, U. Anzer, G. Börner, and M. Livio. Inhomogeneous Wind Accretion - Comparison Between 3D and 2D Computations. *Astro. & Astrophys.*, 231:263, (1989).

[86] T. Matsuda, N. Sekino, K. Sawada, K. Shima, M. Livio, U. Anzer, and G. Börner. On the Stability of Wind Accretion. *Astro. & Astrophys.*, 248:301, (1991).

[87] M. Livio, N. Soker, T. Matsuda, and U. Anzer. On the "Flip-Flop" Instability of Bondi–Hoyle Accretion Flows. *MNRAS*, 253:633, (1991).

[88] M. Ruffert. Non-axisymmetric Wind-accretion Simulations I. Velocity gradients of 3% and 20% over one accretion radius. *Astro. & Astrophys.*, 317:793–814, (1997).

[89] M.R. Krumholz, C.F. McKee, and R.I. Klein. Bondi–Hoyle Accretion in a Turbulent Medium. *Ap.J.*, 638:369–381, (2006).

[90] M.R. Krumholz, C.F. McKee, and R.I. Klein. Bondi Accretion in the Presence of Vorticity. *Ap.J.*, 618:757–768, (2005).

[91] P. Papadopoulos and J.A. Font. Relativistic Hydrodynamics Around Black Holes and Horizon Adapted Coordinate Systems. *Phys. Rev. D*, 58, (1998).

[92] C.M. DeWitt and J.A. Wheeler. *Battelle Rencontres - 1967 Lectures in Mathematics and Physics*. W.A. Benjamin, Inc., New York/Amsterdam, (1968).

[93] R.M. Kulsrud. *Plasma Physics for Astrophysics*. Prineton University Press, Princeton, (2005).

[94] R. Arnowitt, S. Deser, and C.W. Wheeler. The Dynamics of General Relativity. *In Gravitation, ed. L. Witten*, pages 227–265, (1962).

[95] J.W. York Jr. Kinematics and Dynamics of General Relativity. *Sources of Gravitational Radiation, Proceedings of the Battelle Seattle Workshop*, pages 83–126, (1978).

[96] M. Choptuik. 3+1 ADM Decomposition. Lecture Notes.

[97] E. Poisson. *A Relativist's Toolkit*. Cambridge University Press, (2004).

[98] M. Choptuik. Phy 387nl Relativity Theory II Spring 1998 Project 2. Class Homework.

[99] B.F. Schutz. *A First Course in General Relativity*. Cambridge University Press, (1985). pp.200.

[100] R.M. Wald. Black Hole in a Uniform Magnetic Field. *Phys. Rev. D*, 10(6):1680–1685, (1974).

[101] J. Hartle. *Gravity: An Introduction to Einstein's General Relativity*. Benjamin Cummings, (2003).

[102] A. Lichnerowicz. *Relativistic Hydrodynamics and Magnetohydrodynamics*. Benjamin, New York, (1967).

[103] L. Landau and E. Lifshitz. *Fluid Mechanics Second Edition: Volume 6*. Butterworth-Heinemann; 2 edition, (1987).

[104] D. Prialnik. *Introduction to the Theory of Stellar Structure and Evolution*. Cambridge University Press, Cambridge, (2000).

[105] S. Motta A. Lanska, J.C. Miller. Relativistic Shocks in a Synge Gas. *Lettere Al Nuovo Cimento*, 35(10):309–314, (1982).

[106] A.H. Taub. Relativistic Rankine–Hugoniot Equations. *Phys. Rev.*, 74:328–334, (1948).

[107] A. Mignone and J. McKinney. Equation of State in Relativistic Magnetohydrodynamics: Variable Versus Constant Adiabatic Index. *MNRAS*, 378:1118–1130, (2007).

[108] J.D. Jackson. *Classical Electrodynamics*. Wiley, (1998).

[109] H. Alfvén. Existence of Electromagnetic-Hydrodynamic Waves. *Nature*, **150**:405–406, (1942).

[110] A. Dedner, F. Kemm, D. Kröner, C.D. Munz, T. Schnitzer, and M. Wesenberg. Hyperbolic Divergence Cleaning for the MHD Equations. *J. Comp. Phys.*, **175**:645–673, (2002).

[111] C. Evans and J. Hawley. Simulation of Magnetohydrodynamic Flows - A Constrained Transport Method. *Ap.J.*, 332:659–677, (1988).

[112] G. Toth. The $\nabla \cdot B = 0$ Constraint in Shock-capturing Magnetohydrodynamics Codes. *Journal of Computational Physics*, Vol.**161**:605–652, (2000).

[113] J.F. Hawley and J.M. Stone. MOCCT: A Numerical Technique for Astrophysical MHD. *Computer Physics Communications*, **89**:127–148, (1995).

[114] M. Anderson, E.W. Hirschmann, S.L. Liebling, and D. Neilsen. Relativistic MHD with Adaptive Mesh Refinement. *Class. Quantum. Grav.*, **23**:6503–6524, (2006).

[115] M. Anderson, E.W. Hirschmann, S.L. Liebling, and D. Neilsen. Relativistic MHD and Excision: Formulation and Initial Tests. *Class. Quantum. Grav.*, **23**:S505–S527, (2006).

[116] C. Palenzuela, L. Lehner, O. Reula, and L Rezzolla. Beyond Ideal MHD: Towards a More Realistic Modelling of Relativistic Astrophysical Plasmas. *MNRAS*, 394:1727–1740, (2008).

[117] S.C. Noble, C.F. Gammie, J.C. McKinney, and L. Del Zanna. Primitive Variable Solvers for Conservative General Relativistic Magnetohydrodynamics. *Ap.J.*, 641:626–637, (2006).

[118] A. Königl. Relativistic Gasdynamics in Two Dimensions. *Phys. Fluids*, 23(1083), (1980).

[119] S.S. Komissarov. Multidimensional Numerical Scheme for Resistive Relativistic Magnetohydrodynamics. *MNRAS*, 382:995–1004, (2007).

[120] J.S. BENENSOHN and D.Q. LAMB. Hydrodynamical Studies of Wind Accretion onto Compact Objects: Two-Dimensional Calculations. *Ap.J.*, 478:723–733, (1997).

[121] S.K. Godunov. A Difference Method for Numerical Calculation of Discontinuous Solutions of the Equations of Hydrodynamics. *Mat.Sb.*, 47:271–306, (1959).

[122] R. LeVeque. *Finite Volume Methods for Hyperbolic Problems*. Cambridge University Press, (2002).

[123] A. Bressan. *Hyperbolic Systems of Conservation Laws the One-dimensional Cauchy Problem*. Oxford University Press, (2000).

[124] M.H.P.M. van Putten. Uniqueness in MHD in Divergence Form: right null vectors and well-posedness. *J. Math. Phys.*, 43:6195–6206, (2002).

[125] K.O. Friedrichs. On the Laws of Relativistic Electro-Magneto-Fluid Dynamics. *Commun. Pure Appl. Math.*, 28:749–808, (1974).

[126] T. Ruggeri and A Strumia. Main Field and Convex Covariant Density for Quasi-linear Hyperbolic Systems: Relativistic Fluid Dynamics. *Annales de l'I. H. P.*, 34(1):65–84, (1981).

[127] G.K. Batchelor. *An Introduction to Fluid Dynamics*. Cambridge University Press, (2000).

[128] J. Pringle and A. King. *Astrophysical Flows*. Cambridge University Press, (2007).

[129] E. Anderson, Z. Bai, C. Bischof, S. Blackford, J. Demmel, J. Dongarra, J. Du Croz, A. Greenbaum, S. Hammarling, A. McKenney, and D. Sorensen. *LAPACK Users' Guide*. Society for Industrial and Applied Mathematics, Philadelphia, PA, third edition, (1999).

[130] R. Vainio. (solar) MHD and Shock Waves. Lecture Notes, (2009).

[131] A. Majorana. Analytical Solutions of the Rankine–Hugoniot Relations for a Relativistic Simple Gas. *Nuovo Cimento*, 98(2):111–118, (1987).

[132] E.F. Toro. *Riemann Solvers and Numerical Methods for Fluid Dynamics: A Practical Introduction Third Edition*. Springer, (2009).

[133] C.B. Laney. *Computational Gasdynamics*. Cambridge University Press, Cambridge, (1998).

[134] L. Rezzolla, O. Zanotti, and J. Pons. An Improved Exact Riemann Solver for Multidimensional Relativistic Flows. *J. Fluid Mech.*, 479:199–219, (2003).

[135] J.M. Martí and E. Müller. Extension of the Piecewise Parabolic Method to One-Dimensional Relativistic Hydrodynamics. *Journal of Computational Physics*, Vol.**123**:1–14, (1996).

[136] P.L. Roe. Approximate Riemann Solvers, Parameter Vectors, and Difference Schemes. *J. Comp. Phys.*, 135:250–258, (1997).

[137] A. Frank, T. Jones, D. Ryu, and J. Gaalaas. The Magnetohydrodynamic Kelvin–Helmholtz Instability: A two-dimensional numerical study. *Ap.J.*, 460:777–793, (1996).

[138] A. Harten, P. Lax, and B. vanLeer. On Upstream Differencing and Godunov-type Schemes for Hyperbolic Conservation Laws. *SIAM Review*, 25:35–61, (1983).

[139] J.J. Quirk. A Contribution to the Great Riemann Solver Debate. *ICASE Report*, 92-64, (1992).

[140] R. Courant, K. Friedrichs, and H. Lewy. On the Partial Difference Equations of Mathematical Physics. *IBM Journal*, 11:215–234, (1967).

[141] R. Courant, K. Friedrichs, and H. Lewy. On the Partial Difference Equations of Mathematical Physics. *Mathematische Annalen*, 100:32–74, (1928).

[142] Neilsen. Private communication. (2008).

[143] M. Choptuik. Lecture notes. (2004).

[144] M.W. Choptuik. Consistency of Finite-Difference Solutions of Einstein's Equations. *Phys. Rev. D*, 44:3124–3135, (1991).

[145] M. Brio and C.C. Wu. An Upwind Differencing Scheme for the Equations of Ideal Magnetohydrodynamics. *J. Comp. Phys.*, 75:400–422, (1988).

[146] N. Aslan. Two-dimensional Solutions of MHD Equations With an Adapted Roe Method. *International Journal for Numerical Methods in Fluids*, 23:1211–1222, (1996).

[147] D. Biskamp. *Magnetiohydrodynamic Turbulence*. Cambridge University Press, (2003).

[148] A.B. Mikhailovskii. *Electromagnetic Instabilities in an Inhomogeneous Plasma*. IOP Publishing, (1992).

[149] L.F. Wang, W.H. Ye, Z.F. Fan, Y.J. Li, X.T. He, and M.Y. Yu. Weakly Nonlinear Analysis on the Kelvin–Helmholtz Instability. *Letters Journal Exploring the Frontiers of Physics*, 86:15002, (2009).

[150] R.V.E. Lovelace, M.M. Romanova, and W.I. Newman. Kelvin–Helmholtz Instability of the Magnetopause of Disc-Accreting Stars. *arXiv:0911.3590*, (2009).

[151] L. Del Zanna, O. Zanotti, N. Bucciantini, and P. Londrillo. ECHO: a Eulerian Conservative High-Order Scheme for General Relativistic Magnetohydrodynamics and Magnetodynamics. *Astron. & Astro.*, 473:11–30, (2007).

[152] S. Chandrasehkar. Dynamical Friction. I. General Considerations: the Coefficient of Dynamical Friction. *Ap.J.*, 97:255–262, (1943).

[153] S. Chandrasehkar. Dynamical Friction. II. The Rate of Escape of Stars from Clusters and the Evidence for the Operation of Dynamical Friction. *Ap.J.*, 97:263–273, (1943).

[154] S. Chandrasehkar. Dynamical Friction. III. A More Exact Theory of the Rate of Escape of Stars from Clusters. *Ap.J.*, 98:54–60, (1943).

[155] J. Binney and S. Tremaine. *Galactic Dynamics*. Princeton University Press, (1994).

[156] F. Pretorius and M. Choptuik. Adaptive Mesh Refinement for Coupled Elliptic-Hyperbolic Systems. *J. Comp. Phys.*, 218:246–274, (2006).

[157] S.S. Komissarov. Electrodynamics of Black Hole Magnetospheres. *MNRAS*, 350:427–448, (2004).

[158] J. Bičák and V. Janiš. Magnetic Fluxes Across Black Holes. *MNRAS*, 212:899–915, (1985).

[159] K.S. Thorne, R.H. Price, and D.A. Macdonald. *Black Holes: The Membrane Paradigm*. Yale University Press, (1986).

[160] T. Damour. Black-hole Eddy Currents. *Phys. Rev. D*, 18(10):3598–3604, (1978).

[161] A.R. King and J.P. Lasota. Magnetic Alignment of Rotating Black Holes and Accretion Disks. *Astron. & Astrophys.*, 58:175–179, (1977).

[162] T. Sano and J.M. Stone. A Local One-Zone Model of MagnetoHydroDynamic Turbulence in Dwarf Nova Disks. *Ap.J.*, 586:1297–1304, (2003).

[163] J.F. Hawley, C.F. Gammie, and S.A. Balbus. Local Three-dimensional Magnetohydrodynamic Simulations of Accretion Disks. *Ap.J.*, 440:742–763, (1995).

[164] J.F. Hawley, C.F. Gammie, and S.A. Balbus. Local Three-dimensional Simulations of an Accretion Disk Hydromagnetic Dynamo. *Ap.J.*, 464:690–703, (1996).

[165] V. Florinski, A. Balogh, J.R. Jokipii, D.J. McComas, M. Opher, N.V. Pogorelov, J.D. Richardson, E.C. Stone, and B.E. Wood. The Dynamic Heliosphere: Outstanding Issues. *Space Sci. Rev.* , 143:57–83, (2009).

[166] Y.L. Wang, J. Raeder, and C.T. Russell. Plasma depletion layer: Magnetosheath flow structure and forces. *Annales Geophysicae*, 22:10011017, 2004.

[167] S.S. Komissarov and M.V. Barkov. Activation of the Blandford-Znajek Mechanism in Collapsing Stars. *MNRAS*, 397:1153–1168, (2009).

[168] G.S Denicol, T. Kodama, T. Koide, and P. Mota. Causal Theory of Relativistic Dissipative Hydrodynamics. *Braz. J. Phys.*, 37, (2007).

[169] G.S Denicol, T. Kodama, T. Koide, and P. Mota. Causality, Memory Effect, and Relativistic Dissipative Hydrodynamics. *Braz. J. Phys.*, 37, (2007).

[170] P. Romatschke. New Developments in Relativistic Viscous Hydrodynamics. *arxiv:0902.3663v3*, (2009).

[171] P. Romatschke. Relativistic Viscous Fluid Dynamics and Non-Equilibrium Entropy. *arxiv:0906.4787v1*, (2009).

[172] J.L. Synge. *The Relativistic Gas.* (1957).

APPENDIX A

TIME EVOLUTION

In this appendix we present the time evolution of the relativistic Bondi–Hoyle accretion simulations studied in this thesis. Specifically we present,

1. A.1 presents axisymmetric UHD accretion on an $a = 0$ black hole for model U2
2. A.2 presents axisymmetric UHD accretion on an $a = 0$ black hole for model U4
3. A.3 presents axisymmetric UHD accretion on an $a = 0.5$ black hole for model U7
4. A.5 presents axisymmetric UHD accretion on an $a = 0.99$ black hole for model U11
5. A.7 presents thin-disk UHD accretion on an $a = 0$ black hole for model U12, $r_{\rm max} = 50$
6. A.9 presents thin-disk UHD accretion on an $a = 0$ black hole for model U13, $r_{\rm max} = 50$
7. A.10 presents thin-disk UHD accretion on an $a = 0$ black hole for model U12, $r_{\rm max} = 1000$
8. A.11 presents thin-disk UHD accretion on an $a = 0$ black hole for model U13, $r_{\rm max} = 1000$
9. A.13 presents axisymmetric MHD accretion on an $a = 0$ black hole for model M1
10. A.14 presents axisymmetric MHD accretion on an $a = 0$ black hole for model M2
11. A.15 presents axisymmetric MHD accretion on an $a = 0.5$ black hole for model M3

We also present one image which shows the shock capturing properties of the UHD code we developed in Fig. A.12.

The visualization was produced using a program called Data Vault created by F. Pretorius, M. Choptuik, M. Snajdr, and R. Stevenson. One of the features of this program is that it automatically selects the scale for each time frame based on the maximum and minimum of the data set at each timestep.

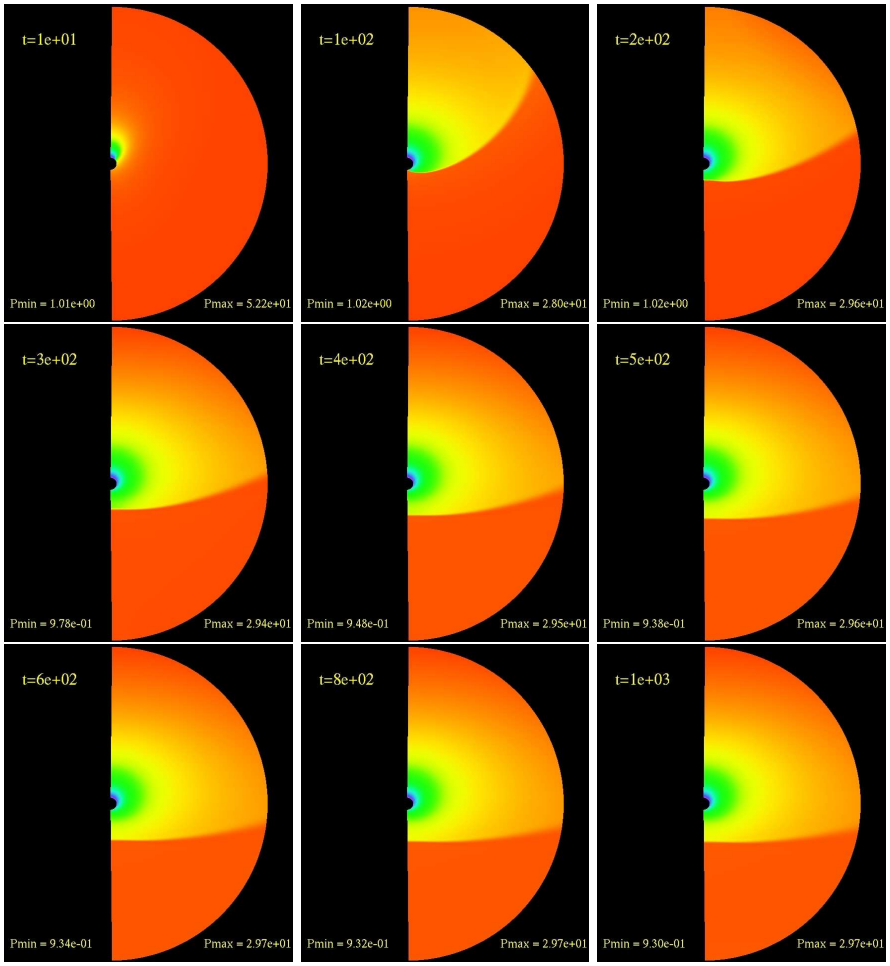

Figure A.1: Time evolution of $P(t, r, \theta)$ for model U2 with $a = 0$, we see the evolution of the ultrarelativistic fluid as it flows past the black hole. The formation of the a tail shock is evident in the first two frames. This shock expands quickly and eventually detaches from the black hole by the 4th frame. In the last two frames we see the detached shock flow upstream.

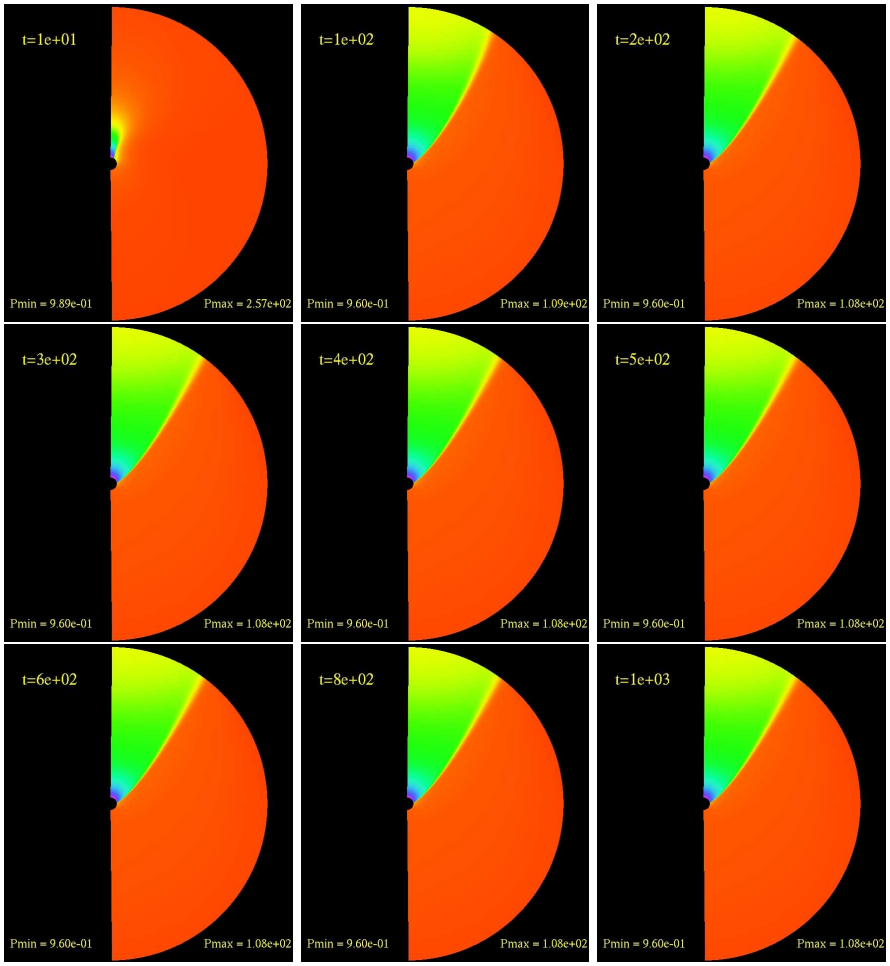

Figure A.2: Time evolution of $P(t, r, \theta)$ for model U4 with $a = 0$, we see the evolution of the ultrarelativistic fluid as it flows past the black hole. The formation of the a tail shock is evident in the first two frames. This shock begins to expand, but does not break contact with the black hole. The last several frames show that the fluid flow is steady.

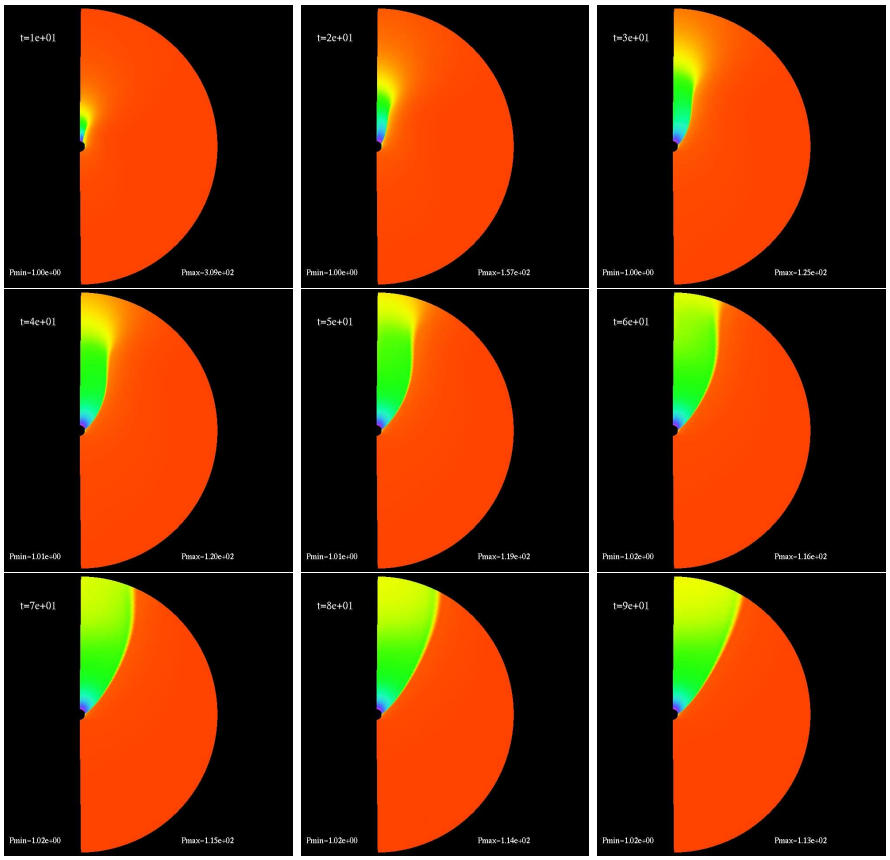

Figure A.3: Time evolution of $P(t, r, \theta)$ for model U7 with $a = 0.5$, we see the evolution of the ultrarelativistic fluid as it flows past the rotating black hole does not change morphology significantly when compared to the $a = 0$ black hole. Once again we have a tail shock and a steady flow.

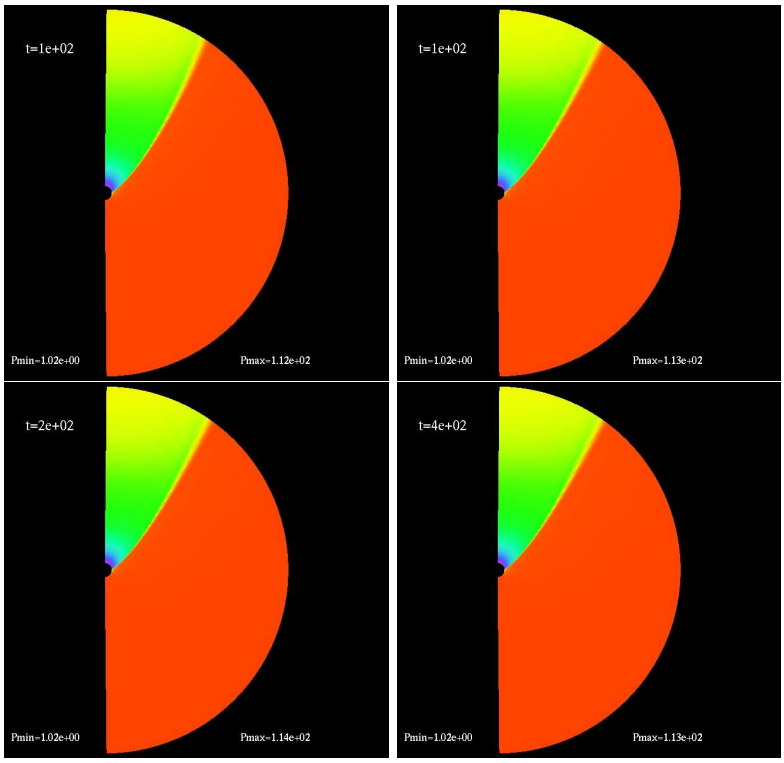

Figure A.4: Longer time evolution for model U7 with $a = 0.5$.

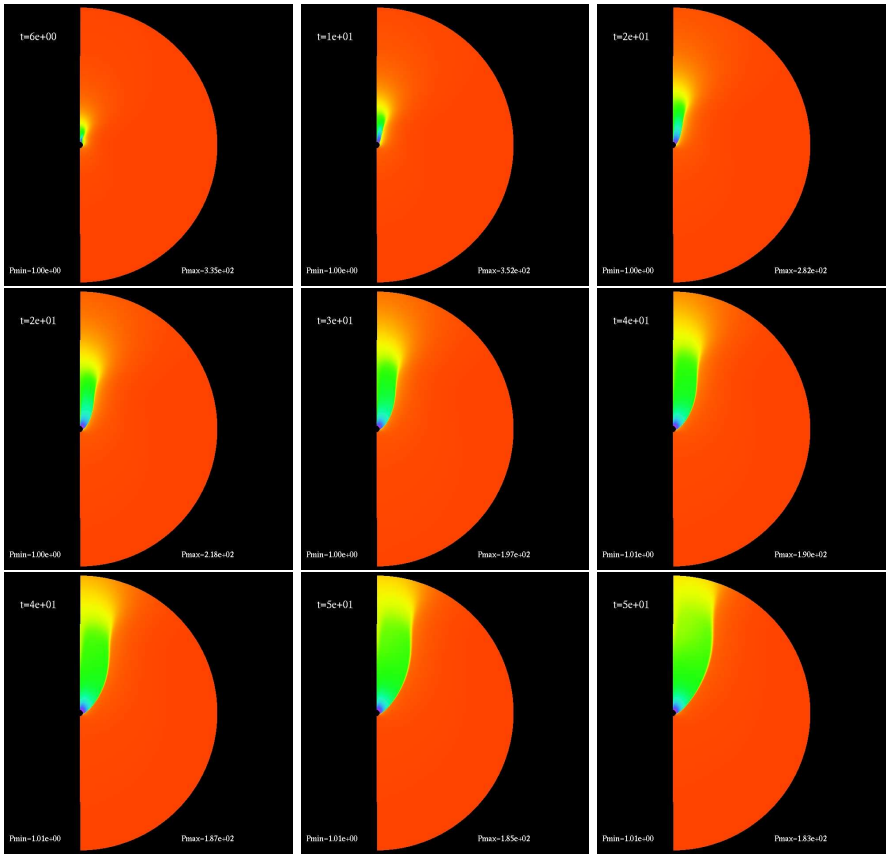

Figure A.5: Time evolution of $P(t, r, \theta)$ for model U11 with $a = 0.99$. As with other models the tail shock forms; however, here we see that the shock attaches to the black hole much closer to the upstream side.

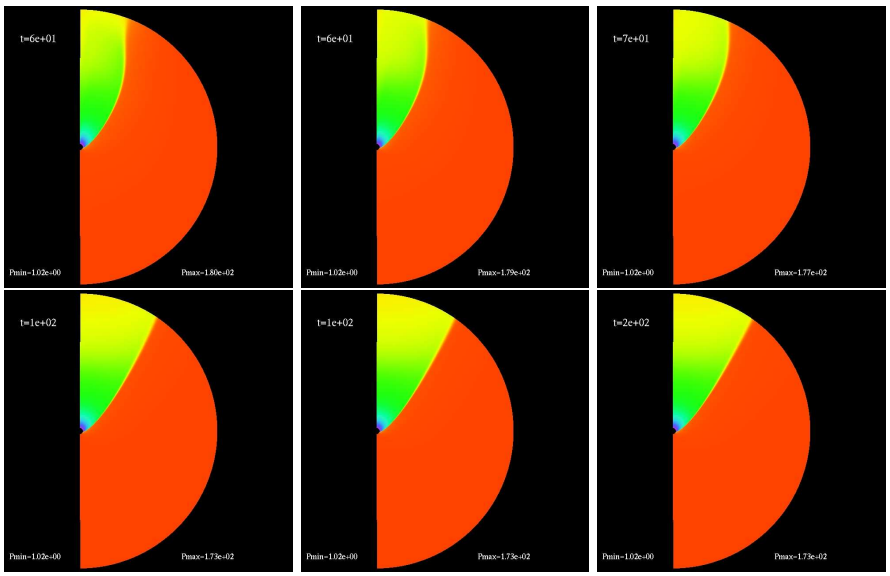

Figure A.6: Longer time evolution of $P(t, r, \theta)$ for model U11 with $a = 0.99$. The flow reaches a steady state.

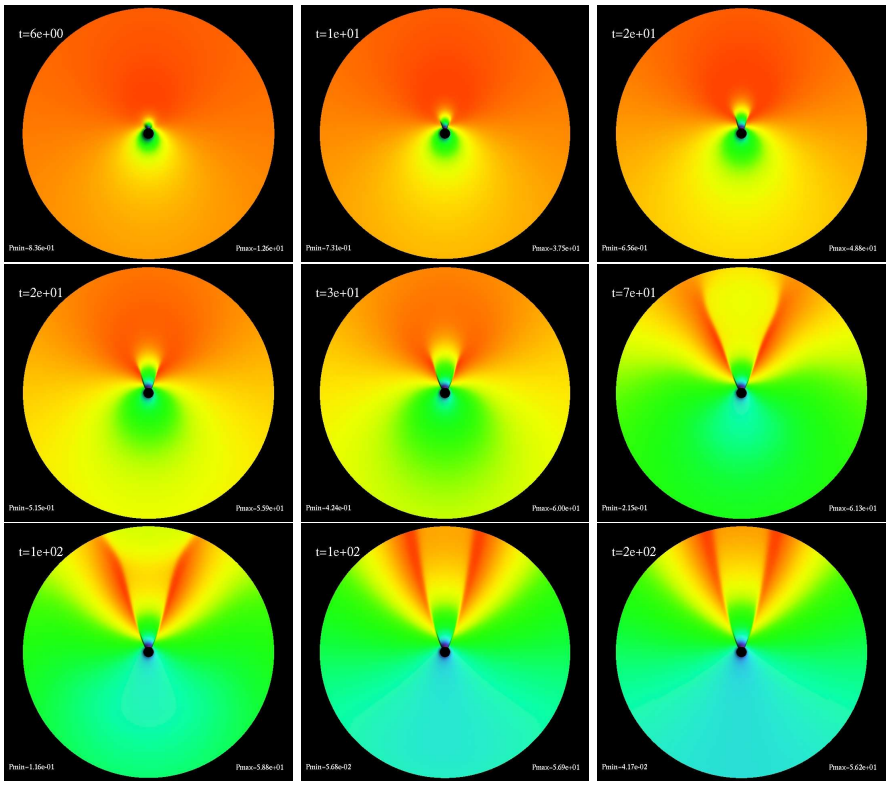

Figure A.7: Time evolution of the thin-disk accretion of $P(t, r, \phi)$ for model U12 with $a = 0$. We plot the logarithm of the pressure profile here, other scalar fields have a similar profile. The tail shock is clearly visible.

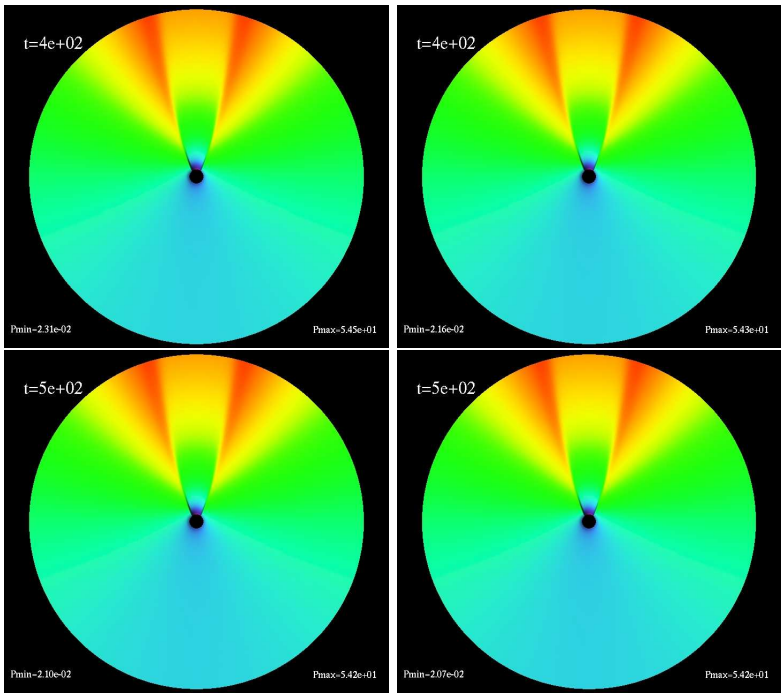

Figure A.8: Time evolution of the thin-disk accretion of $P(t, r, \phi)$ for model U12 with $a = 0$. We plot the pressure profile here, other scalar fields look similar. The last several frames shows that the evolution has become steady state.

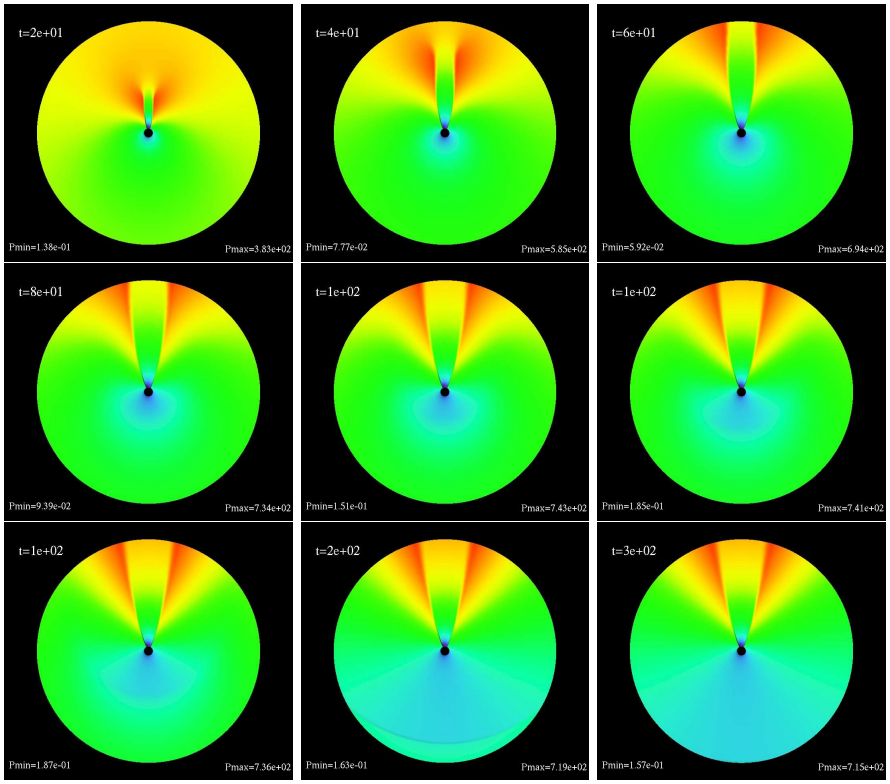

Figure A.9: Time evolution of the thin-disk accretion if $P(t, r, \phi)$ for model U13 with $a = 0$. When the flow is faster the width of the tail shock decreases. Notice the wave impinging on the upstream boundary in the second last frame. When this makes contact with the boundary we expect an amplification of the boundary effects to enter the simulation.

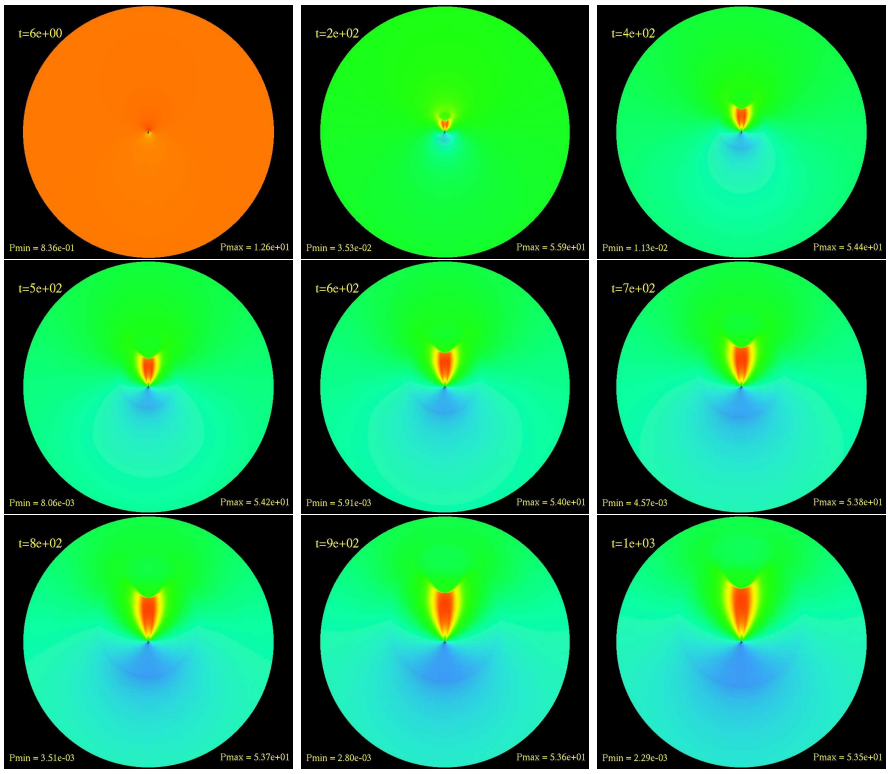

Figure A.10: Time evolution of the thin-disk accretion of $P(t, r, \phi)$ for model U12 with $r_{\max} = 1000$ and $a = 0$. We plot the logarithm of the pressure profile here, other scalar fields have a similar profile. The tail shock is clearly visible.

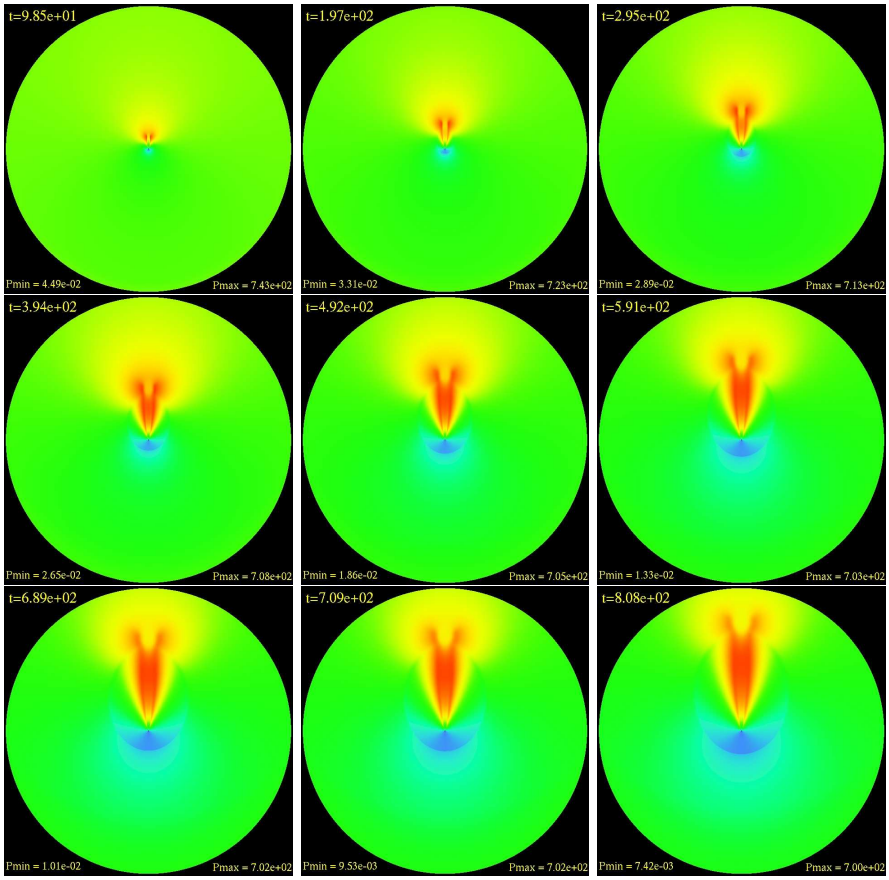

Figure A.11: Time evolution of the thin-disk accretion of $P(t, r, \phi)$ for model U13 with $r_{\max} = 1000$ and $a = 0$. When the flow is faster the width of the tail shock decreases. Notice the wave impinging on the upstream boundary in the second last frame. When this makes contact with the boundary we expect an amplification of the boundary effects to enter the simulation.

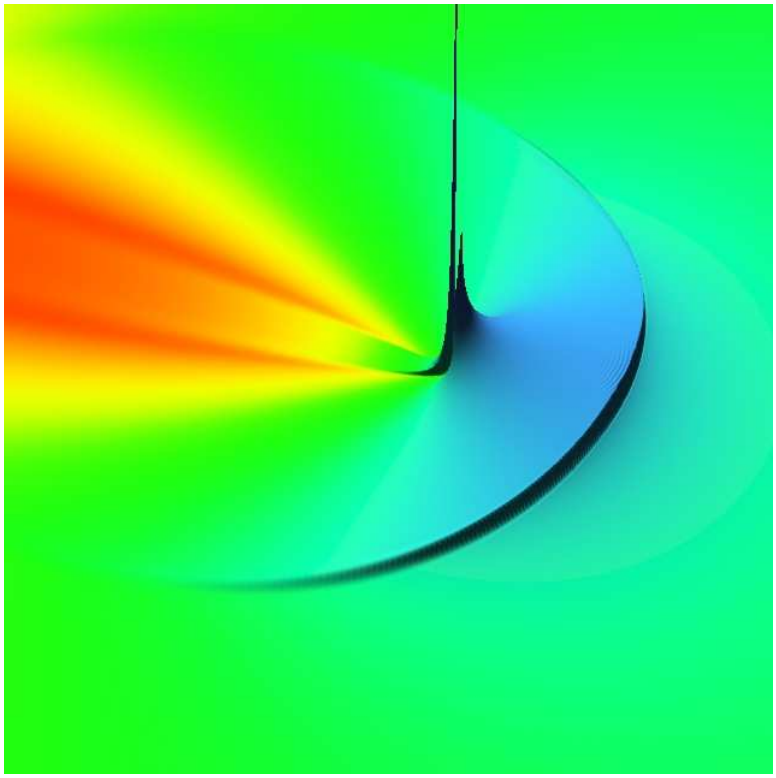

Figure A.12: A snapshot of model U13 at time $t = 500M$. The bow shock moving upstream is sharply defined with resolution even with a low resolution $\Delta r = 0.25$.

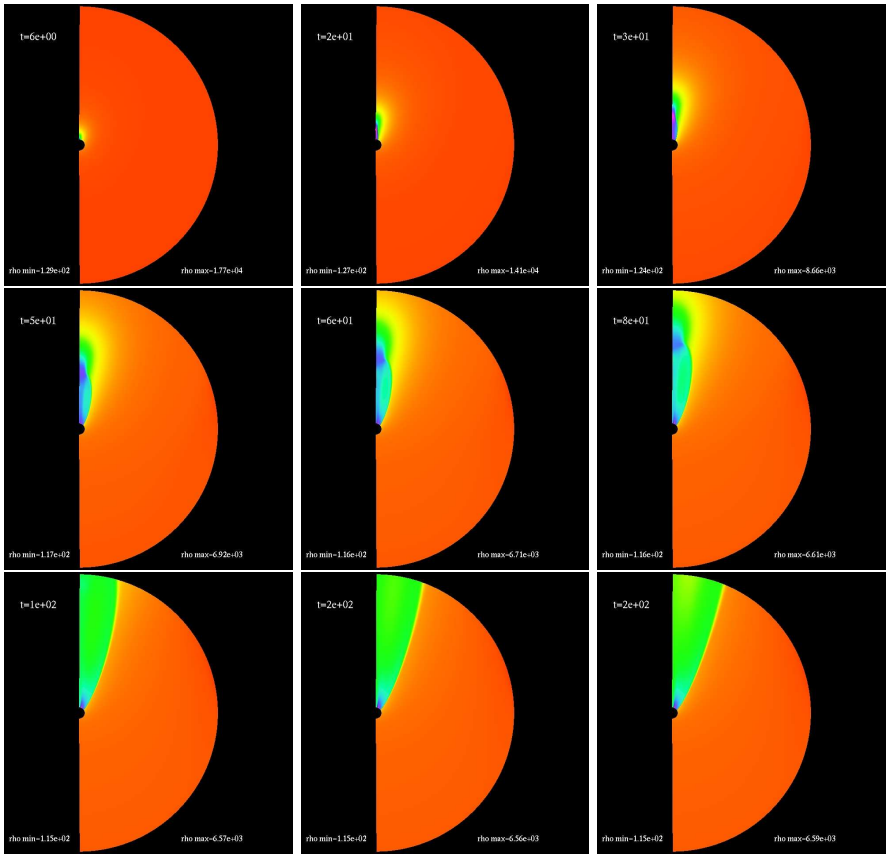

Figure A.13: Time evolution of the axisymmetric of $\rho_0(t, r, \theta)$ accretion for model M1 with $a = 0$. We plot the log of the density profile here. The last several frames shows that the density evolution has reached a steady state.

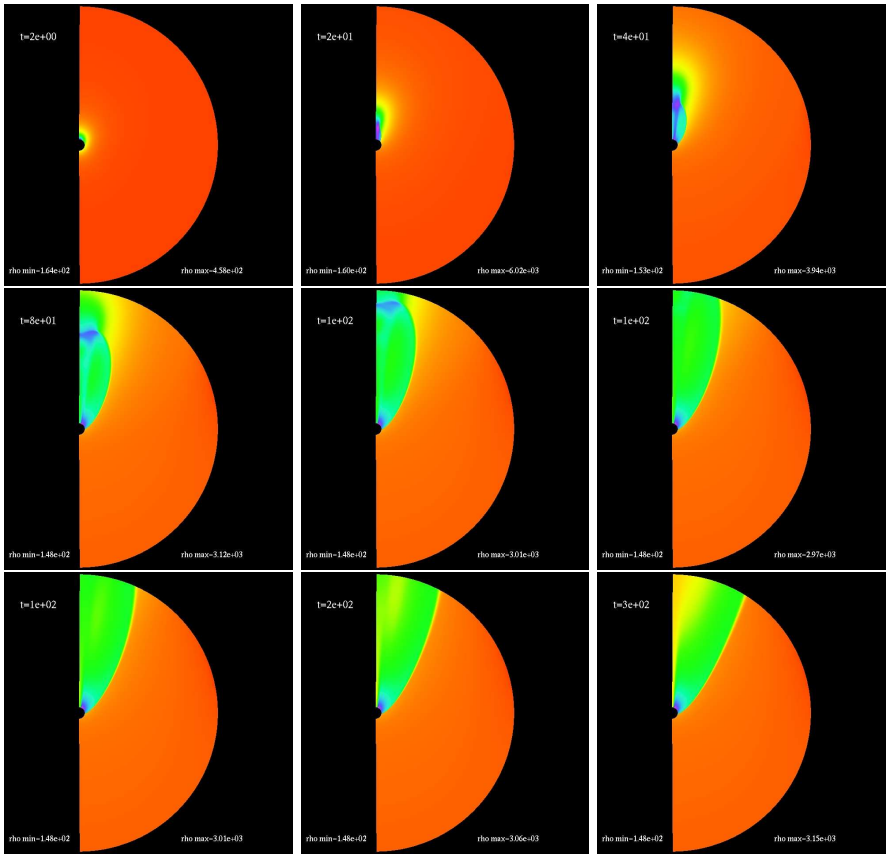

Figure A.14: Time evolution of the axisymmetric accretion of $\rho_0(t, r, \theta)$ for model M2 with $a = 0$. We plot the log of the density profile here. The last several frames shows that the density evolution has reached a steady state.

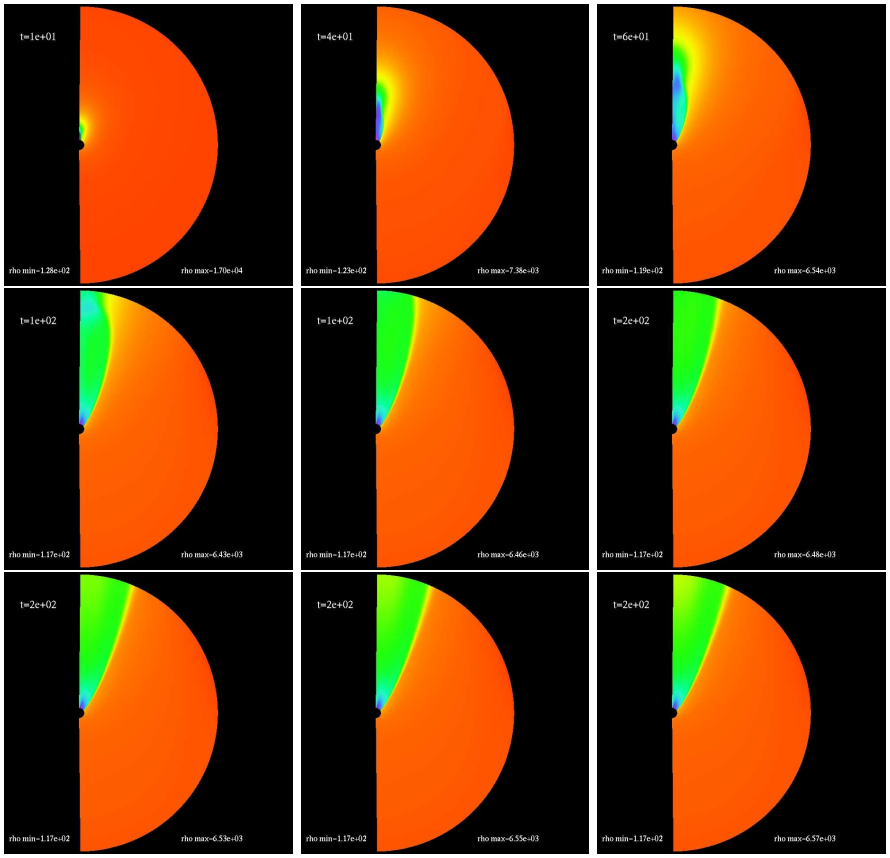

Figure A.15: Time evolution of the axisymmetric accretion of $\rho_0(t, r, \theta)$ for model M3 with $a = 0.5$. We plot the log of the density profile here. The last several frames shows that the density evolution has reached a steady state.